STUDIES OF AND MODELLING OF THE FRACTURE BEHAVIOUR OF COMPOSITE MATERIALS

David Griffin BSc, MSc

A thesis submitted in part fulfilment of the requirements for the degree of
Doctor of Philosophy

School of Engineering
Surface Engineering Research Centre
University of Northumbria at Newcastle
Newcastle upon Tyne

February 1998

Abstract

The programme of work involved creating a new method of modelling to realistically predict failure in a unidirectional, fibre-reinforced material and some experimental studies of the fatigue behaviour of Al_2O_3/CPAl and Al_2O_3/6061Al* composites.

For the modelling, a traditional linear elastic fracture mechanics stress intensity factor approach was initially used, in conjunction with finite element analysis, to predict crack growth. The limitations of conventional micromechanical models to single mode type failure was demonstrated and a more novel approach was used whereby a model which incorporated bonded surface algorithms was constructed; this model was capable of simulating multi-mode failure mechanisms.

The investigation was carried out using three different finite element analysis programmes: *Display 3*, *Applied Structure* and *ABAQUS*.

On running the simulation it was found that the fibre/matrix bond strength played a key rôle in determining the dominant failure mechanisms in the composite: a low bond strength resulted in debonding/fibre bridging as the dominant mode of failure, whereas a high bond strength indicated that catastrophic fracture in mode I failure was the more dominant mechanism.

The fatigue behaviour of the Al based MMCs was conducted at ambient temperatures. It was found that the Al_2O_3/6061 had the better fatigue properties and further work was carried out on this material in air and a simulated sea water environment. The sea water environmental tests showed that a reduction of approximately 4 % in fatigue life compared to the results for fatiguing in air could be expected.

*6061 Al = Al 96.62%, Cu 0.28%, Mn 0.15%, Cr 0.25%, Mg 1.0%, Zn 0.25%, Si 0.6% Fe 0.7%, Ti 0.15%

Contents

Nomenclature for Chapters 5 and 6

a crack length

$\frac{da}{dN}$ increase in crack length, a, wrt number of fatigue cycles, N

ΔK increase in stress intensity factor

$\frac{\partial U}{\partial A}$ partial change in energy release rate wrt area

E_f Young's modulus of fibre

E_m Young's modulus of matrix

F force applied to three-point bend specimen

F_0 fracture force of three-point bend specimen

f fracture criterion

f_{tol} fracture criterion tolerance

G energy release rate

J contour integral around crack tip

K_I stress intensity factor for mode I failure

μ one micron

N number of cycles performed in fatigue test

$\mathbf{N}$ normal vector

v Poisson ratio

r two-dimensional radial axis

σ tensile stress

$\hat{\sigma}_n$ normal component of stress

σ^f tensile failure stress

τ shear stress

τ^f shear failure stress

U strain energy at the tip of a centre crack

W width of interphase

x axial direction

y axial direction

List of Tables

List of Figures

Acknowledgement

I would like to express my thanks to my two supervisors Professor P K Datta and Dr A Daadbin for the assistance given to me during the course of my research. I would also like to thank Dr J S Burnell-Gray for the numerous times he has proof read both this thesis and various technical publications.

I would also like to acknowledge the Surface Engineering Research Centre and the School of Engineering at the University of Northumbria for the use of facilities. And finally, my sincere thanks to DRA who provided me with the materials for the experimental studies.

Author's declaration

Part of the work contained in this thesis has been published in two technical papers which are attached as appendices 5 and 6.

1 Introduction

Engineering of modern composite materials has had a significant impact on the technology of design and construction. By combining two, or more, materials, it is possible to tailor-make advanced composites which are lighter, stiffer and stronger than conventional structural materials.

There are essentially, three broad categories of composite material at present: dispersion-strengthened, particle reinforced and fibre- (whisker) reinforced. *Dispersion-strengthened composite* materials are characterised by a microstructure which consists of an elemental or alloy matrix within which fine particles of 0.01 to 0.1 μm in diameter are uniformly dispersed in a volume concentration of ~1–15%. *Particle-reinforced composites* differ from dispersion-strengthened composites since the particle size exceeds 1.0 μm and particle concentration ranges from ~5–40%. The reinforcing phase in *fibre composite* materials spans a range of sizes from a fraction of a micron to several microns in diameter and ranges of volume fraction from a few percent to over 70%. Fibre-reinforced materials are microstructurally different in that the fibre reinforcement has one long dimension, whereas the reinforcement of the other two composites does not.

In forming composites, conventional materials are modified through the addition of extra constituents to obtain specific performance characteristics not available in the unmodified material. The second phase may be added to provide strength and stiffness; to enhance toughness or to control thermal expansion. As the different constituents are mixed or combined, there is always a contiguous region. It may simply be an interface, that is the surface forming the common boundary of the constituents. In some cases, however, the contiguous region is a distinct added phase, called an "interphase". When such an interphase is present, there are two interfaces, one between each surface on the interphase and its adjoining constituent. In yet other composites, e.g. metal matrix composites (MMC), the surfaces of the dissimilar constituents interact to produce an interphase.

Metal matrix composites consist of a metal matrix (in most cases, an alloy is the metal matrix) and a reinforcement (in general an intermetallic compound – an oxide, carbide or nitride). MMCs have been under development for more than twenty five years. They were

first developed for application in the aerospace industry, followed by engineering-base applications. As fabrication and material prices decreased, MMCs expanded into non-military and non-aerospace applications. Over the last thirty years, several metallic systems have been considered for matrix materials for MMCs, the most important being the non-ferrous lightweight materials for structural use – such as aluminium, titanium and magnesium – because specific properties for these materials can be enhanced to replace heavier monolithic materials. Aluminium is the most attractive non-ferrous matrix material used particularly in the aerospace and transportation industries where weight of structural components is critical. Typically, in a commercial airliner, every pound of material saved translates into savings of about $250 in fuel costs over the projected life of the aircraft, at present day fuel prices. Development of newer generation aircraft has placed stringent requirements on performance of aluminium alloys because the temperatures to which they are exposed is steadily increasing.

Fibre-reinforced materials, unlike most metals and alloys, are anisotropic. The degree of anisotropy depends primarily on the degree of fibre orientation. The prime rôle of the fibres is to carry the load, while the metal matrix serves to transfer and distribute the load to the fibres. The efficiency with which the loads are transferred from the matrix to the fibres depends on the bonding interface between them.

Many theories on the effect of bonding materials exist [1], suggesting either chemical and/or mechanical bonding as the primary function of coupling agents. Mechanical bonding is significant only in the case of fibre-reinforced composites, when fibres have rough or faceted surfaces. Whereas, chemical bonding is important for all kinds of reinforcements, e.g. fibres, whiskers and particulates. Weak or incomplete bonding between fibre and matrix can be a cause of early failure. The matrix bond is often in a state of shear when the material is under load. When the bond is broken, the fibre separates from the matrix and leaves discontinuities that may cause failure.

The nature of the interfacial bonding between fibre and matrix has a very important bearing on the strength of the composite. A strong fibre/matrix bond facilitates load transfer from the matrix to the reinforcement. In such composites fracture takes place in the composite via the fibre and not along the interface. This leads to high strength properties of the composite

in the case where the fibre is stronger than the matrix, because load will also be borne by the fibre. Conversely, if the fibre/matrix interface is weak, then a crack will nucleate in the interface and propagate in the matrix. As a result, the fibre will not act as a load-bearing constituent and the composite will fail at lower stress.

An intuitively logical explanation of the adhesion between the composite phases, based on the surface area and roughness of the fibre has been proposed: the greater the surface area and rougher the reinforcement, the better the matrix can adhere. However, studies on carbon fibres have shown no correlation between *short beam shear strength* (SBSS) and fibre surface area. In fact there are some indications that increasing roughness may actually reduce fibre/matrix bonding. For fracture toughness, in the case of ceramic-matrix composites, the interface is intentionally weak, minimizing the chemical coupling of reinforcement to matrix which could destroy the two-phase structure. When the composite is deformed, cracks propagate through the matrix until they meet a whisker. As the interface between phases is weak, the separating matrix causes the whisker to pull out from either side of the advancing crack front, rather than allowing the crack to continue through the whisker. The friction resulting from this pull-out dissipates a large amount of energy, as well as deflecting the crack along the fibre. These phenomena result in substantial toughening of the composite, in some cases doubling the fracture toughness relative to the un-reinforced ceramic.

The properties of a composite are not simply a weighted average of the properties of the reinforcement and matrix. The strength and stiffness of the reinforcement are the most important factors in the properties of a composite, while the matrix determines much of the shear and compressive properties. However, the overall performance of a composite also depends to a large extent on the nature of the bond between matrix and fibre.

The interface or if there is a fibre/matrix reaction zone, interphase, determines how impact energies or strains are transferred from matrix to fibre, thus controlling the mechanical performance.

One of the major problems in analysing the crack propagation behaviour of composite materials is the inability of the *Rule of Mixtures* to characterise their fracture behaviour. In

general, for composites:

$$G_{Ic} \text{ composite} \neq G_{Ic} \text{ matrix } V_m + G_{Ic} \text{ fibre } V_f \qquad \{1\}$$

where G_{Ic} = critical strain energy release rate, and V_m, V_f = volume fraction of matrix and fibres respectively.

Because of the expense of fabricating composite materials it is desirable to be able to predict the mechanical behaviour of these materials without recourse to expensive destructive testing. One of the simplest way of predicting how the composite will behave under varying loading conditions is to construct a mathematical model of the material. How accurate the model will be at predicting the mechanical properties of the composite is dependent on how complex the model is and the type of analysis chosen.

Generally, there are two approaches to modelling stress/strain behaviour of fibre-reinforced composites. The *macro-mechanical approach* treats a composite as an homogeneous, orthotropic, elastic-plastic, continuum. Although the *macro-mechanical approach* offers simplicity, it is not possible to identify the differing stress states in the fibre or supporting matrix. The *micromechanical approach*, on the other hand, uses models that retain the identities of the fibre and matrix. With this approach, the overall composite properties are determined in terms of the individual constituent properties, their volume fraction and the mutual constraints between the phases associated with the geometry of the microstructure. Two differing analysis methods can be employed for both macro- and micro-scale approaches: one uses *analytical methods* and the other uses numerical techniques such as *finite element analysis* (FEA).

The elastic behaviour of fibrous composites is reasonably well understood, although of course linear-elastic analysis methods are only acceptable for the initial part of the stress/ strain behaviour of metal-matrix composites. Most metal-matrix composites exhibit non-linear stress/strain responses as a consequence of plastic deformation of the matrix. Thus, the elastic-plastic behaviour of the matrix should be included in the analysis models.

Micromechanical models that lead to an analytical solution, under simple loading cases, include the *composite cylinder model* which consist of a series of concentric cylinders

each representing a composite phase, these models seek to study: for example, the yielding and shakedown of unidirectional composites under axisymmetric loading. Fibre/matrix interfacial effects can be incorporated into an analytical model using the *vanishing fibre diameter model*; although the model is limited to purely fracture mechanics analysis and cannot incorporate any thermal studies. Analytical models have been built which incorporate several packed fibres, usually in a rectangular array. This type of model is a compromise between the single fibre/matrix micro-scale approach and the macro-scale approach. Such models usually have rectangular fibre cross-sections in order to reduce the complexity of the analysis; volume average properties can be calculated for the composite, and comparisons made with experimental results. Square fibre cross-section analytic models have been used to describe the elastic-plastic behaviour of fibrous composites, and thus fibre/matrix separation and the non-linear off-axis, stress/strain curves.

Analytical, micromechanical models are usually restricted to simplified model geometries and stress/strain assumptions to achieve closed-form solutions, as such it is difficult to obtain a detailed description of stresses at the micro-scale. A further limitation of the analytic approach is that each time the geometry is changed, the model may have to be completely rebuilt, involving a great deal of work.

In general, while analytical methods offer a simple tool for obtaining the overall response of composites, numerical techniques, such as the finite element method, provide more accurate and detailed characterisation of composite properties for complicated geometries and constituent property variations. Various effects that influence the stress/strain response, fibre/matrix deformation and crack propagation in composite materials are readily modelled using finite element techniques.

The finite element technique became a feasible method of characterising fracture behaviour with the availability of relatively cheap, powerful computers. Until this time, the use of computationally intensive techniques, such as finite element analysis was limited to those establishments with the highest budget, notably the defence industries.

During the late 1960s and early 1970s a great deal of work was carried out investigating suitable elements to model embedded defects in a material. Although special and highly

esoteric elements were evolved to model crack tips these elements tended to be computationally slow and inefficient. The adaptation of the conventional eight-noded isoparametric elements, to model crack tips and calculate such parameters as the maximum principal stress distribution around these tips, as well as stress intensity factors for a propagating crack was something of a breakthrough. The use of these modified "conventional" elements led to a large saving on both computing and data preparation time and is now the accepted convention when modelling defects.

Finite element analysis has recently been used to model stress transfer through the reaction zone (or interphase) of a ceramic-matrix composite, although only the stress distributions on the fibre/interface and interface/matrix were analysed, the stress distribution over the entire interphase was not addressed. Axisymmetric FEA models of a composite with the material properties of the interphase obtained from shear lag analysis have been constructed, but as with all models both analytic and numerical discussed so far, incorporating an interphase which was assumed to be axisymmetric, with uniform modulus and fixed dimensions.

Some composite reinforcements are surrounded not only by an interphase region, but also an additional radial variation in microstructure (and by implication, microproperties) in the surrounding matrix material as a function of distance from the centre of each fibre. No representation of this property behaviour has yet been reported and to model the spatial variations, a three-dimensional model of some refinement would be essential.

Typical damage in an unidirectional metal-matrix composite includes fibre fracture in longitudinal tension and interface debonding in transverse tension. Special interface elements now exist in finite element packages which can simulate the interface debonding process; such elements represent a perfect interface until a certain state of stress is reached when the interface is assumed to fail, by node decoupling.

The modelling of MMC failure mechanisms is usually limited to the prediction of one particular mode, e.g. mode I, II or III failure*. Models to predict multi-mode failure have, until recently, been difficult, if not impossible to produce, due to the lack of both the sophisticated software required and the computing power needed.

*See Appendix 2

The objectives of this programme of work are to create a numerical model which will simulate multi-mode failure mechanisms in metal matrix composites using novel modelling methods; also, the fatigue properties of two differing long fibre metal matrix composites will be investigated in air and simulated seawater environments.

The multi-mode failure model will use interface elements built, in conjunction with conventional axisymetric finite element models, to simulate multi-mode composite failure and the effect that differing fibre/matrix interfacial bonding has on this failure.

This project thus consists of two areas of work – finite element modelling and experimental studies of some important mechanical properties. The experimental work was undertaken mainly to obtain an insight into the actual load transfer and fracture behaviour on SiC/Al, Al_2O_3/Al and Al_2O_3/6061 Al composites under cyclic loading. The objective was that finite element modelling of the load transfer and static fracture behaviour, together with the experimental studies of the fatigue behaviour will provide a comprehensive picture of the response of MMCs to stress.

Initially, the behaviour of the stress distributions around an embedded defect in the reaction zone of an MMC has been investigated; this work then was used to further investigate the rôle differing fibre/matrix bond strengths have on the differing failure mechanisms.

The results of the simulation have been compared to published experimental results carried out on MMC samples.

The thesis is presented in seven chapters. The second chapter is a review of the literature applicable to this study, which includes an overview of analytical and numerical modelling and an introduction to the *finite element analysis* (FEA) method of modelling failure mechanisms in composites. Chapter three presents an introduction to the theoretical and experimental work and the techniques employed. Modelling and experimental methods adopted are dealt with in Chapter four. Chapter five contains the results derived from the study. The implications of the results are discussed in Chapter six while in Chapter seven the main conclusions drawn from the present study are given, together with suggestions for future work in the same area.

2 Literature Review

2.1 Introduction

2.1.1 Structure of Chapter

Section 2.2 deals with the differing approaches to analytical modelling of unidirectional composite MMCs. Section 2.3 compares the two main numerical techniques – finite differences and finite elements – used in modelling MMC failure mechanisms, while Section 2.4 describes the differing ways in which FEA has been applied to modelling MMCs over the past three decades. Important characteristics which should be included in composite FEA models are discussed in Section 2.5. The next section describes the approaches to modelling local stress distributions in MMCs and Section 2.7 draws attention to the varying ways damage initiation and propagation have been modelled. The incorporation of distinct phases – such as an interphase – in an MMC have been investigated in Section 2.8, while Section 2.9 reports the possibilities of modelling multiple failure mechanisms. Finally, Sections 2.10 and 2.11 respectively deal with the fatigue crack growth behaviour of long fibre MMCs, and the effects sea water have on MMC fatigue properties.

The review presented here will outline the work carried out over the last few years in the field of composite failure prediction and the various modelling and experimental methods used. In particular, the area of numerical modelling will be examined as this is the area which has undergone the most fundamental changes, primarily due to the decreasing cost of computing power over the last twenty years, and the availability of sophisticated modelling tools such as *graphical user interface* (GUI) finite element packages. The review will show that while analytical models offer a simple tool for obtaining the overall response of composites, numerical techniques such as *finite element analysis* provide more accurate and detailed characterisation of composite properties for complicated geometries and constituent property variations.

When modelling failure in composite materials, a primary concern is the prediction of the macroscopic behaviour from the basic mechanical properties of the constituent materials. There are, generally, two approaches to modelling stress/strain behaviour of fibre-reinforced

composites. The first of these is the *macromechanical approach*, which treats the composite as being wholly homogeneous, where the individual composite constituent properties are "averaged", using some form of rule of mixtures, into a single set of properties; while such an approach is simple to model, it is not possible to identify stress states in the fibre or matrix since these individual properties no longer exist. The *micromechanical approach*, on the other hand, uses a model which retains the individual constituent phases by concentrating on only a few of these constituents – typically one repeating (or fundamental) segment, usually by using the symmetrical properties of the material, one quarter of a fibre and its surrounding matrix. Using this approach, the overall composite properties are determined in terms of the constituent properties, their volume fraction and the mutual constraints between the phases associated with the geometry of the microstructure.

Two differing analysis methods can be employed for both macro- and micro-scale approaches. One is the *analytical, or closed form, method* and the other is the *numerical method.*

2.2 Analytical Modelling of Unidirectional Fibre-Reinforced Metal Matrix Composites

Of the many types of micromechanical models that lead to an analytical solution under simple loading cases, the Hashin-Rosen concentric cylinder model [2] (Figure 2.1) is one of

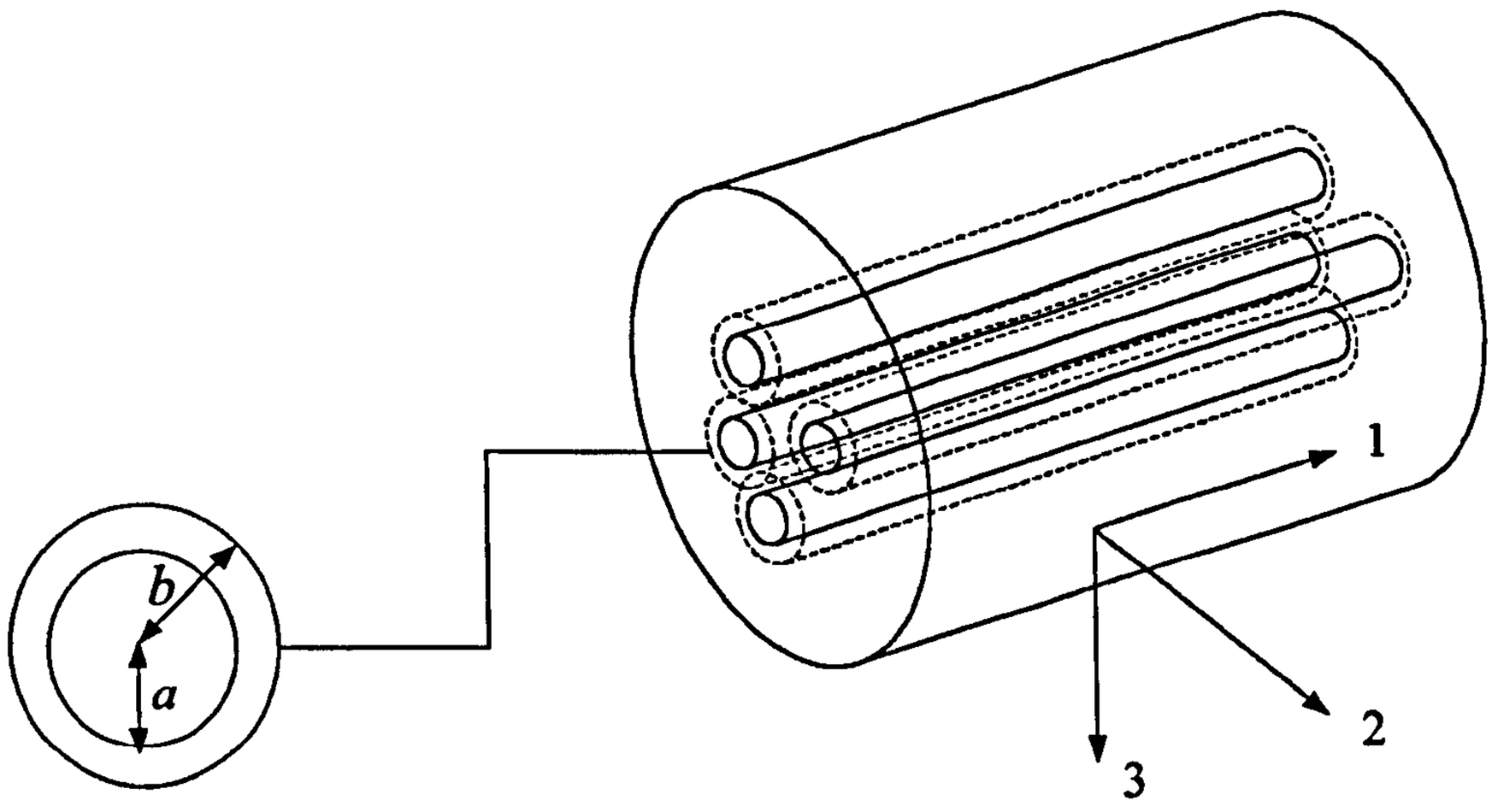

Figure 2.1 *Composite cylinder model [2]*

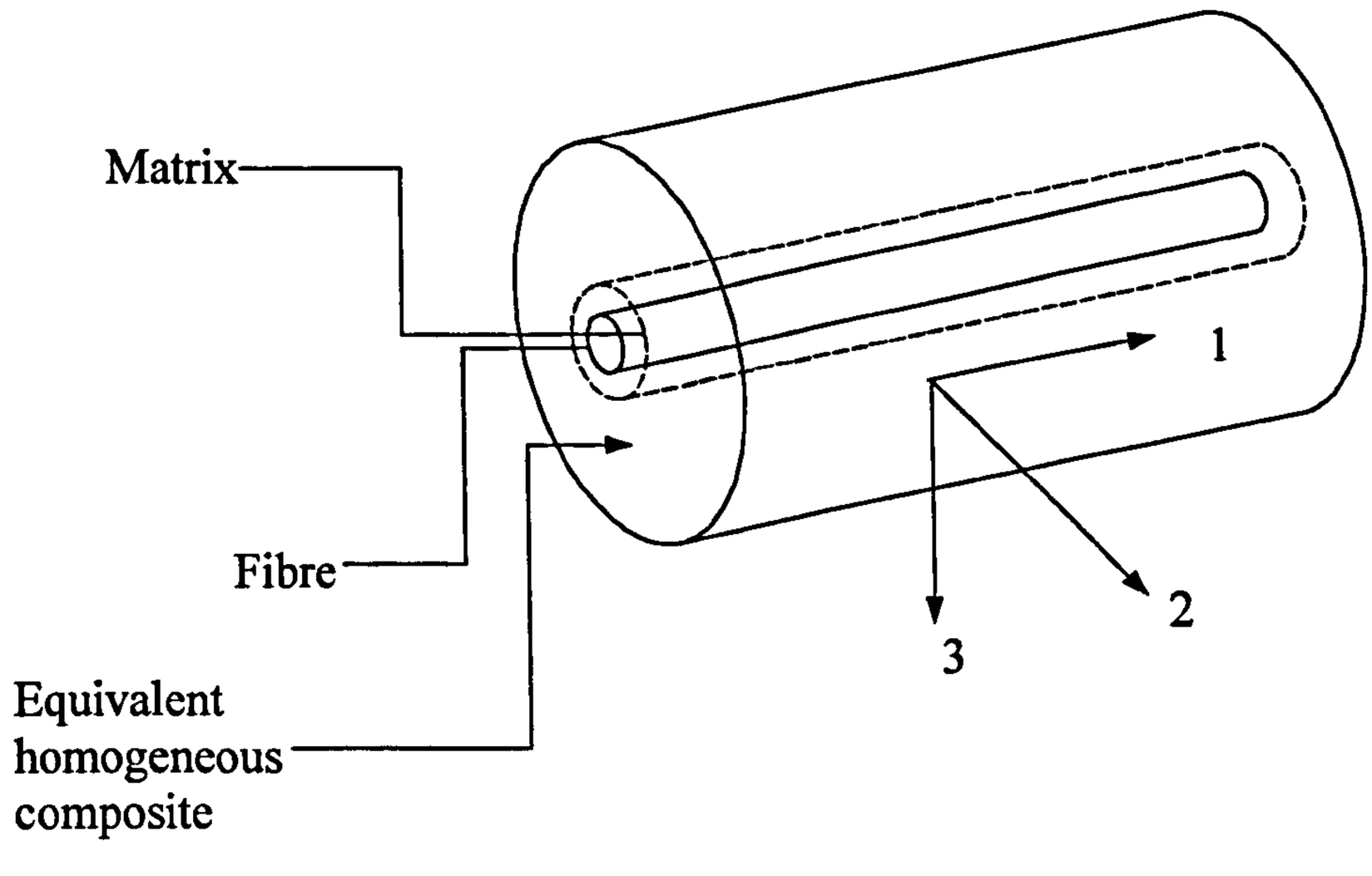

Figure 2.2 *The three-phase cylinder model [4]*

the most widely used. In this model, a unidirectional fibrous composite can be regarded as a transversely isotropic, macroscopically homogeneous solid consisting of an elastic-perfectly plastic matrix, and elastic fibre. The composite microstructure can thus be modelled as a system of right circular cylinders consisting of fibres surrounded by uniform layers of the matrix material, i.e. each individual fibre of radius a, has an associated annulus of matrix material, of radius b. Each of the individual cylinder combinations in Figure 2.1 are referred to as composite cylinders with the absolute values of a and b varying from each composite cylinder, so that a volume filling configuration is obtained. However, the ratio a/b is required to be constant for all the composite cylinders in order to keep the volume fraction constant. The composite cylinder model can determine the effective uniaxial Young's modulus E_{11} and the effective Poisson's ratio ν_{12}*, but results for other moduli, e.g. the transverse shear modulus μ_{23} cannot be accurately obtained, except for very high and very low volume fractions [2,3]. Because of the difficulty in obtaining μ_{23}, there is a variation on the composite cylinder model, the *three-phase cylinder model* [4], whereby all but a single composite cylinder is replaced by a homogeneous media (Figure 2.2). The results for μ_{23} can be calculated perfectly using this model, although to date it has not been proven that the results can be perfectly extrapolated to the composite cylinder model; this is interesting to note since two- and three-phase cylinder models are often referred to as "the composite

*Note: the first subscripts denotes the direction of the imposed stress or strain and the second the response direction)

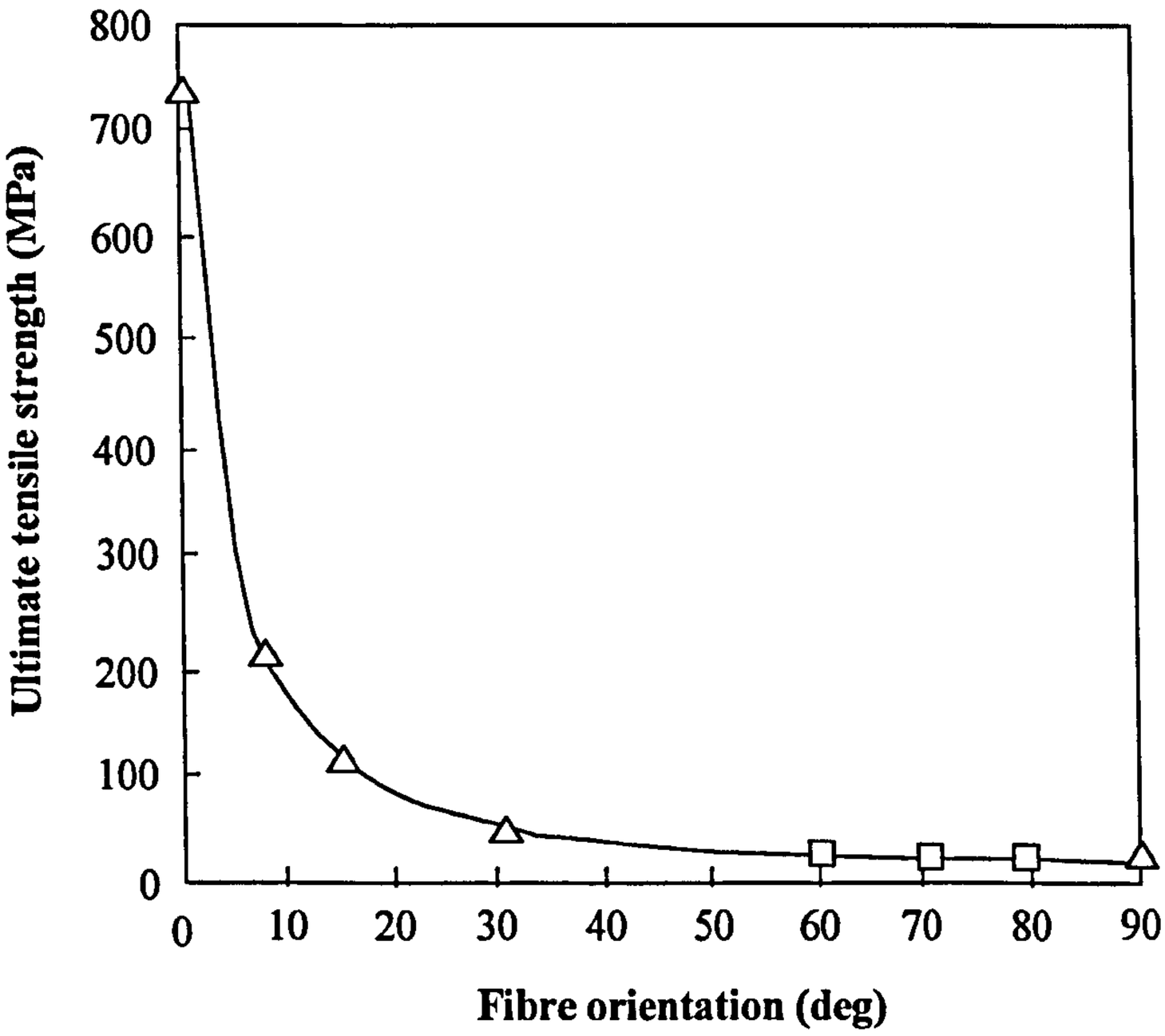

Figure 2.3 *Effect of orientation (with respect to the loading direction) on the UTS of a unidirectional 0.42Gr/6061Al composite – the composite exhibits pronounced anisotropy[6]*

cylinder model" by many authors [5].

For a unidirectionally reinforced long fibre composite, the longitudinal strength, i.e. the fibre direction, can be determined from a two-phase model with fibre volume fraction V_f and external radius b, containing a concentric cylindrical fibre of radius a, has $V_f = (a/b)^2$ [6]. For a strong fibre/matrix interfacial bond strength, the longitudinal strength (σ_L, at $\theta = 0$, Figure 2.3) obeys a simple rule of mixtures:

$$\sigma_L = V_f\sigma_f + (1 - V_f)\sigma_m \qquad \{2.1\}$$

where: σ_f = the strength of the fibre, and

σ_m = the strength of the matrix

σ_m is taken as the UTS value of the unreinforced matrix material, processed in the same manner as the composite [6].

Because of the differing materials comprising the phases in a composite material, the two materials may exhibit a thermal miss-match and, depending on how the material was constructed, may have internal residual stresses due to cooling from the process temperature

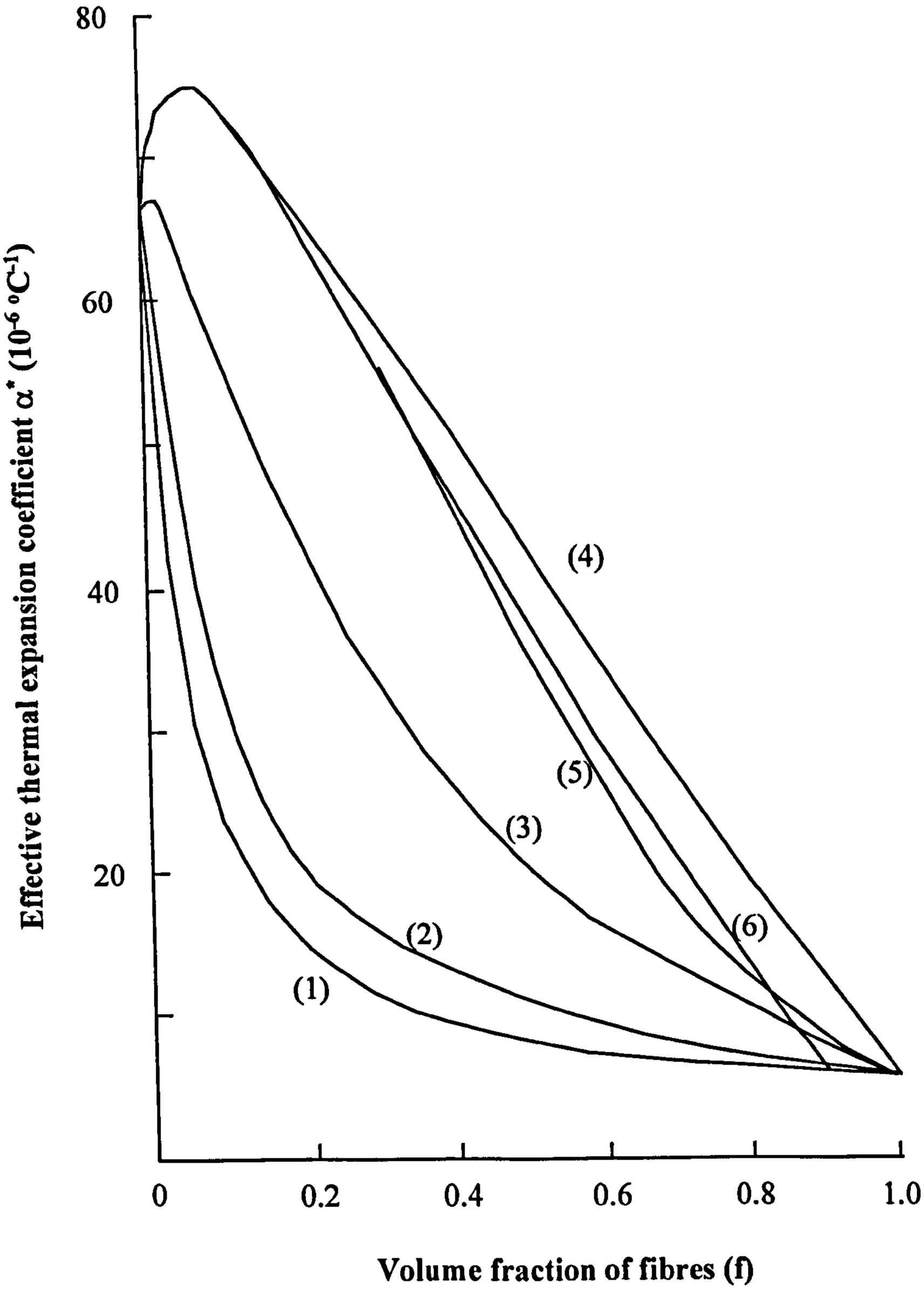

Figure 2.4 *ETEC as a function of volume fraction of fibres for glass-fibre-reinforced epoxy resin and comparison to other published results: (1) result of model from [7] and lower bound for a_z^* [9], (2) upper bound for a_z^* [9] (3) lower bound for a_t^*, [9], (4) result from [7] and upper bound a_t^*, [9], (5) self-consistent scheme for a_t^* [10], (6) Schneider's equation for a_t^**

to room temperature. Hsueh and Becher [7] investigated the possibility of using a two-phase composite cylinder model to calculate effective thermal expansion coefficients (ETEC), α_t^* (transverse) and α_z^* (axial) from the total strains consisting of strains due to temperature changes, and strains induced by the presence of internal stresses. The particular composite was glass-fibre-reinforced, epoxy-resin matrix, with the following properties: E_f = 71.59 GPa, v_f = 0.25, $\alpha_t = \alpha_z = 4.8 \times 10^{-6}\ ^\circ C^{-1}$, E_m = 3.14 GPa, v_m = 0.4, and $\alpha_m = 66 \times 10^{-6}\ ^\circ C^{-1}$. The results obtained from the composite cylinder model were compared with existing results [8–10] and revealed that when the composite constituents had the same effective elastic constants (EEC) the rule of mixtures could be used to obtain thermal expansion coefficients of the composite.

The elastic-plastic behaviour of continuous fibre, unidirectional MMCs was investigated by Dvorak and Bahei-El-Din [11] who formulated a "vanishing fibre diameter model" whereby the composite was modelled as a continuum reinforced by cylindrical fibres of vanishingly small diameter occupying a finite volume fraction.

Comparisons were made between the two types of model [12–14] to illustrate the differences between the bilinear form of the vanishing fibre model and the elliptical, initial yield surface for the composite cylinder model in the $\bar{\sigma}_1\bar{\sigma}_2$-plane (Figure 2.5).

The axisymmetric stress $\bar{\sigma}_1 = \left(\frac{\bar{\sigma}_{11} + \bar{\sigma}_{22}}{2}\right)$, $\bar{\sigma}_2 = \bar{\sigma}_{33}$ where $\bar{\sigma}_{11}$, $\bar{\sigma}_{22}$ are stresses in the transverse plane and $\bar{\sigma}_{33}$ in the fibre direction.

For a B/Al composite, the yield surfaces coincided quite well for low values of $\bar{\sigma}_1/Y$ (Y = tension yield stress of matrix) particularly in the case of plane stress loading of the lamina, where the composite model limited the transverse hydrostatic stress to $|\bar{\sigma}_1/Y| \leq 1/\sqrt{3}$. Conversely, there was poor agreement between the models in the presence of high hydrostatic stress.

Although the modelling method accounted for the mechanical interaction between fibre and matrix, the model favoured composites with low-to-moderate volume fractions – the higher volume fraction materials exhibited overestimation of the overall magnitude of plastic strains. The effects of thermal residual stresses could also not be incorporated into the

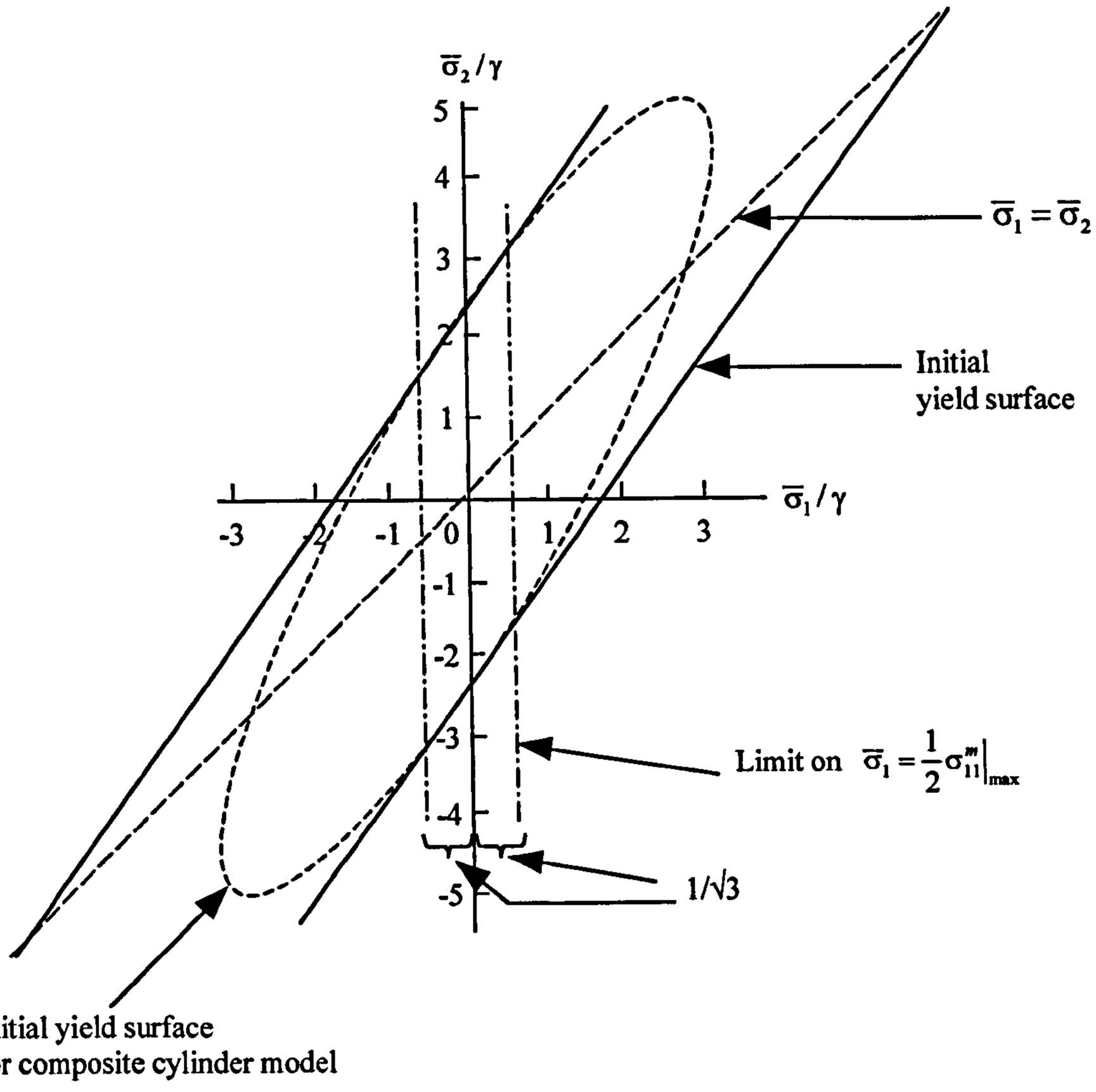

Figure 2.5 *Initial yield surfaces of the vanishing fibre model compared to those of the composite cylinder model, in the axisymmteric overall stress plane for a B/Al composite[11]*

modelling process. Min and Crossman [15, 16] presented a deformation analysis of unidirectional composites subjected to both thermal and mechanical loading using a plane stress mechanics of materials model which allowed for non-hardening matrix behaviour. Experimental tests were conducted on a high modulus graphite (VS0054)/aluminium (6061) unidirectional composite to characterise its thermomechanical properties as influenced by the thermomechanical history. The experiments included:

- tension tests under monatonically increasing loads followed by unloading,
- measurement of the cyclic thermal expansion in the longitudinal and transverse directions, and
- tests on the thermal expansion behaviour of specimens simultaneously.

The tension test results showed that the yield strength of the composite was greatly

influenced by the residual stress which may have varied with the thermomechanical loading history. For thermal cycling, the aluminium matrix of the annealed specimen underwent elastic and plastic deformation owing to fibre/matrix thermal mismatch.

For interpretation of the results, an engineering material model (*MET*MAT*) was developed to characterise the salient features of the above deformation. The model considered the aluminium as an elastic perfectly plastic material with temperature-dependent yield and thermal expansion properties. The model permitted calculation of residual stresses during thermal and mechanical loading. The theoretical model was based on a two-dimensional continuum model which assumed that the strains in the fibre direction were the same in the fibre as in the matrix (Figure 2.6), and that the stresses in the direction transverse to the fibre were equal in both of the constituents. The model allowed for the input of orthotropic elastic properties for the matrix and fibre, thus taking account of the highly anisotropic elastic and thermal properties of the fibre, and for the deformation-induced orthotropic response of the matrix.

Figure 2.7 shows the predicted and measured stress-strain behaviour for a VS0054/6061-T6 composite at –144°C for an assumed initial residual stress of 106 MPa. Figure 2.8 shows the predicted and measured cyclic thermal expansion behaviour of the above composite in the longitudinal direction, and Figure 2.9 shows the predicted and measured thermomechanical strain during a repeated step loading and thermal cycling for an assumed

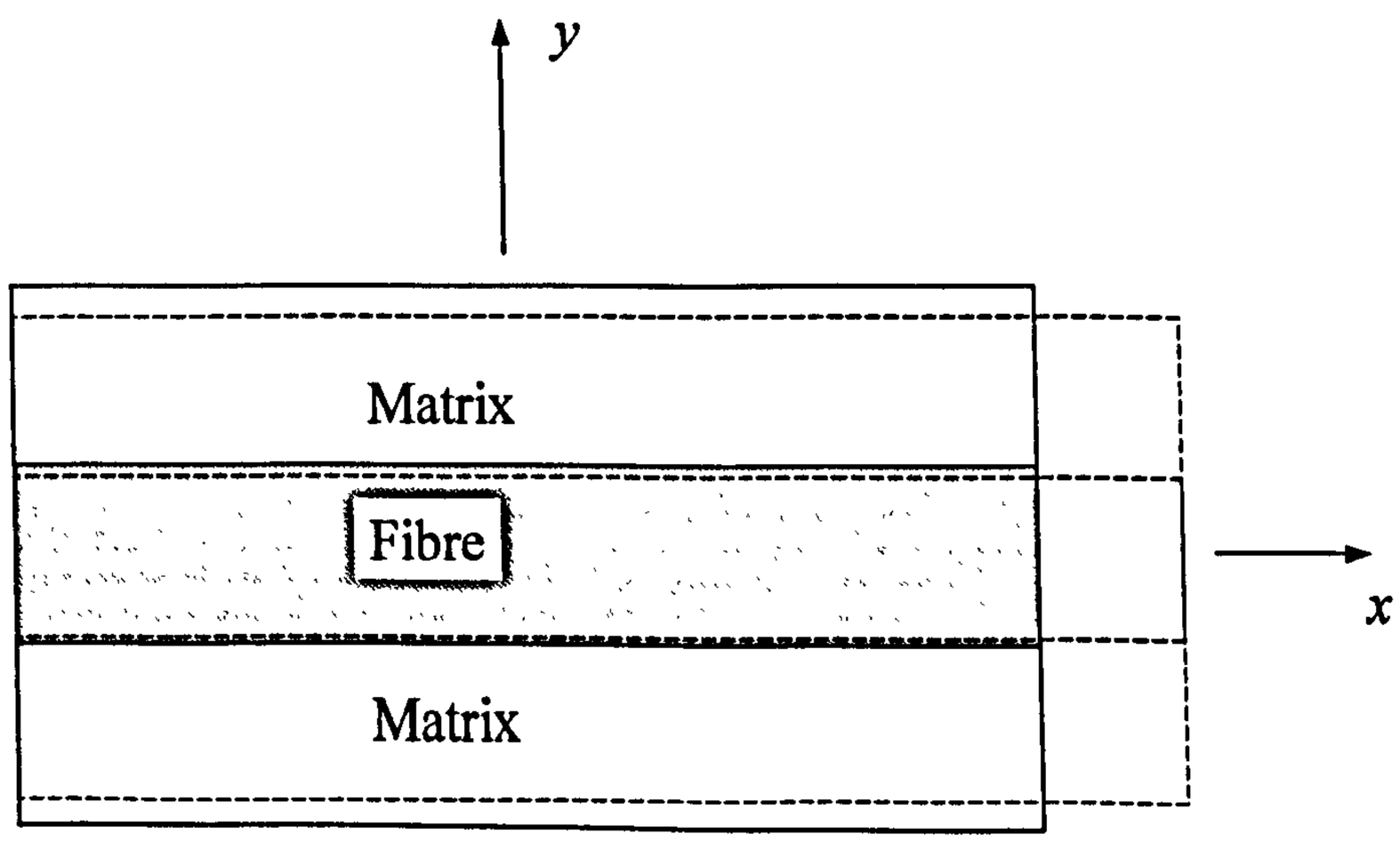

Figure 2.6 *Continuum model for unidirectional composites*

residual stress of 0 MPa.

The model suggested that the strong history dependency was a consequence of change in matrix yield strength and residual stress with respect to temperature and loading history. However, because the model was simplified in that it assumed that the strains in the longitudinal (fibre) direction were the same in the fibre as in the matrix, i.e. neglected the detailed micromechanics of a heterogeneous deformation of the fibre/matrix system, further investigation in these areas was warranted.

Aboudi [17–19] developed a sophisticated analytical model in which a regular rectangular packing of the fibres was modelled explicitly. The elastic-plastic behaviour of the individual composite constituents was incorporated into the model. The modelled fibre cross-section had a rectangular shape (assumed in order to reduce the complexity of the analysis) whose area was equal to the circular cross-sectional area of the actual fibre (Figure 2.10).

By denoting (x_1,x_2,x_3) to be a cartesian system of co-ordinates, with x_1 oriented in the fibre direction the constitutive law for the effective transverse isotropic behaviour of the composite was presented in the form of equations which were derived from a micromechanical analysis in which the fibres of square cross-section h_1^2 were arranged in the matrix phase in a double periodic array at distance h_2 apart (Figure 2.10 (a)).

The fibre and matrix constituents, were both assumed to be transversly isotropic, with x_1 being the direction of isotropy. The stresses in the sub-cells were obtained and the average stresses were calculated based on them. For the strength of the composite it was assumed that the failure of the composite was controlled by the stresses in the fibre and matrix constituents. A general expression for the failure criterion in terms of the stress components in the sub-cells of the representative cell of the model was written which determined the adopted failure criterion.

Based on the Aboudi model, for a unidirectional boron/aluminium composite whose parameters were reported by Becker et al. [20] the strengths of the composite in the principal material directions were $X = 1292.6$ MPa, $Y = 117.9$ MPa and $S = 137.2$ or 108.2 MPa. The first value in the in-plane shear strength was obtained from a 10° off-axis test, while the other was from a 0° Iosipescu shear test. X_f(longitudinal ultimate stress of the fibres in

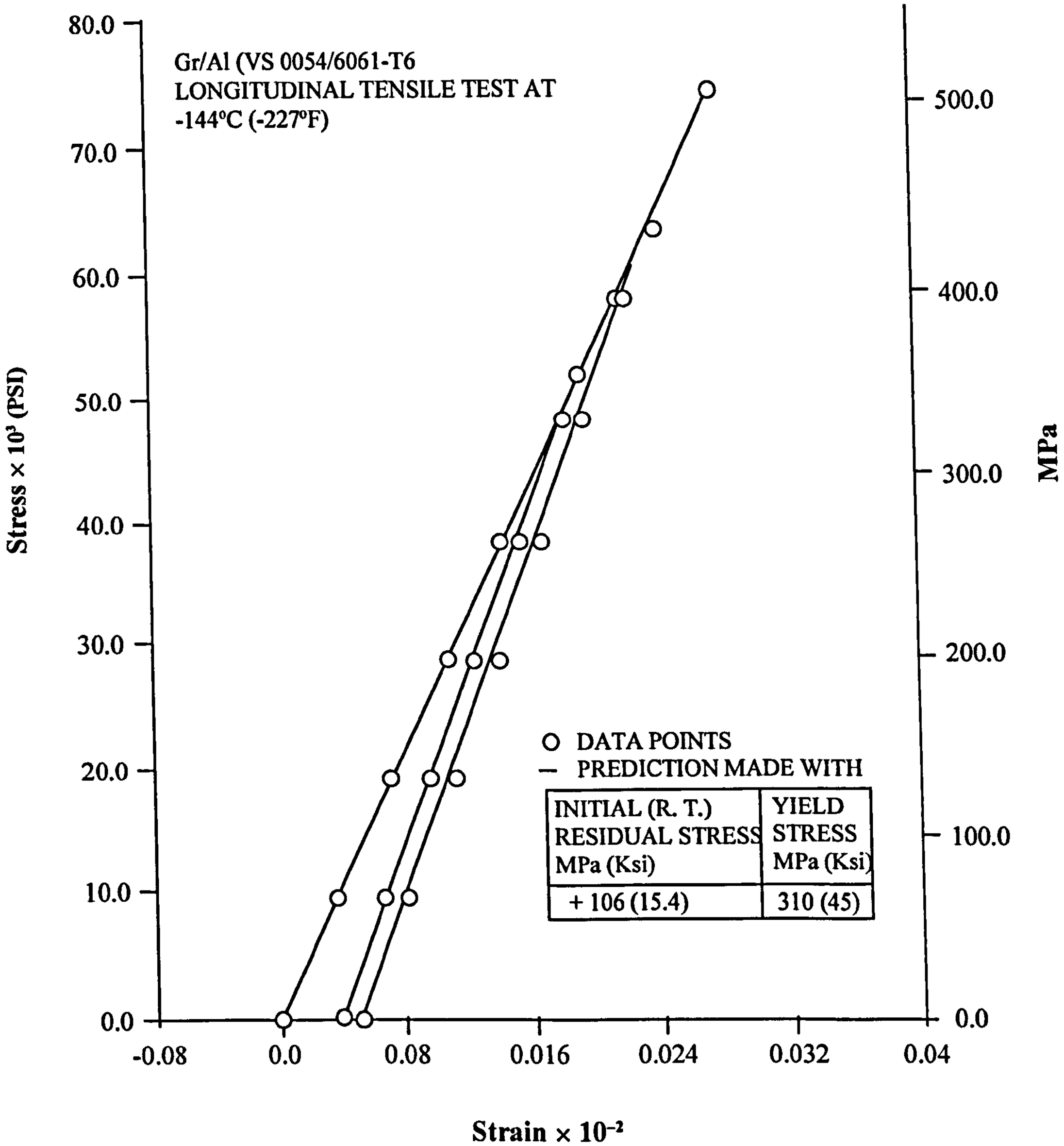

Figure 2.7 *Predicted and measured tensile stress-strain behaviour of a VS0054/6061-T6 composite at –144°C for an asssumed initial residual stress of 106 MPa[15]*

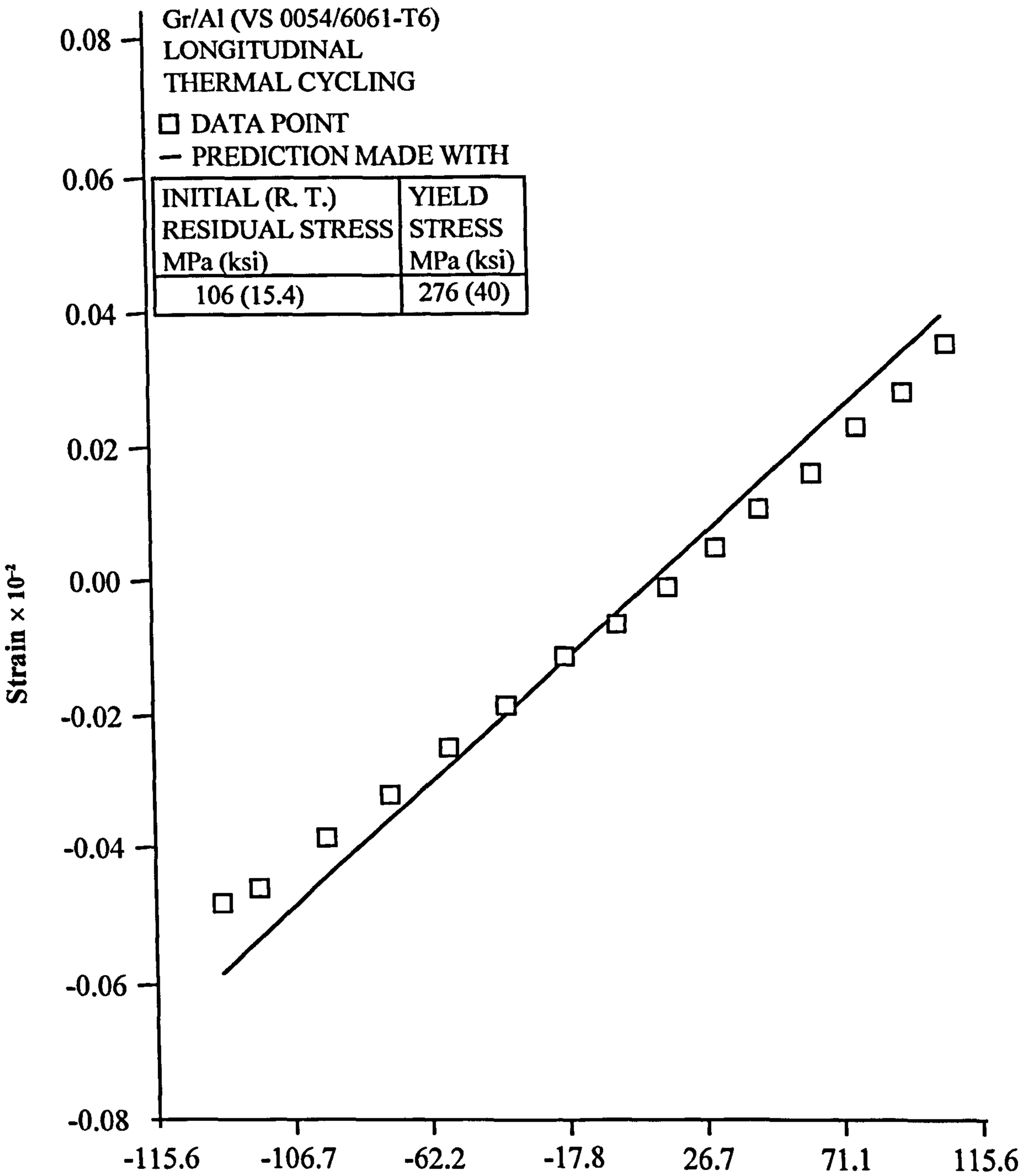

Figure 2.8 *Predicted and measured cyclic thermal expansion behaviour of VS0054/ 6061-T6 in the longitudinal direction[15]*

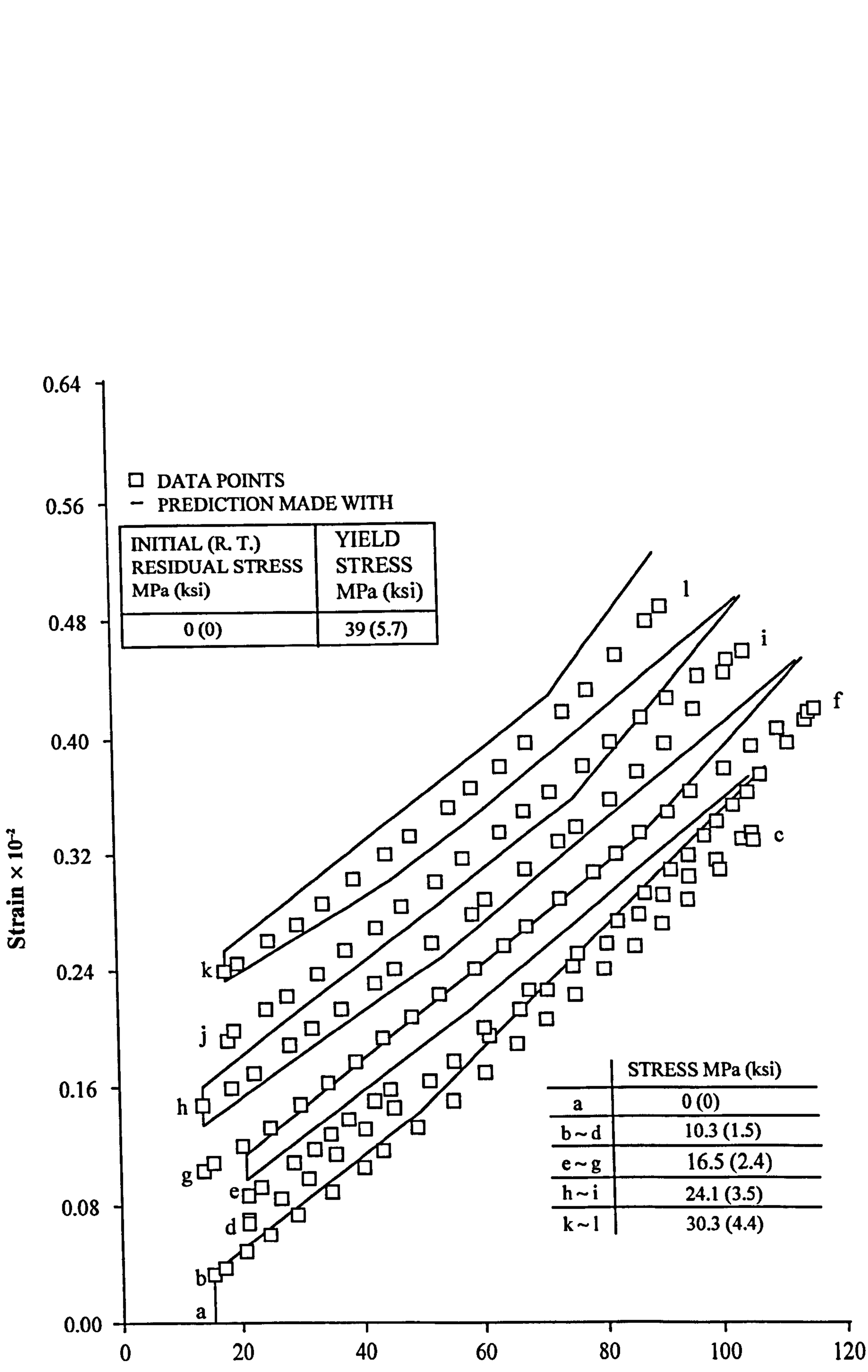

Figure 2.9 *Predicted and measured thermomechanical strain during repeated step loading and thermal cycling, for an assumed residual stress of 0 MPa [15]*

Table 2.1 *Parameters of boron/aluminium composite (the volume fraction is 0.44)[17]*

	Young's modulus E (GPa)	Poissons ratio v	X_f (MPa)	X_m (MPa)	S_m (MPa)
Boron	400	0.2	2313.8	-	-
Aluminium	72.5	0.33	-	155.6	167.4 132

tension), X_m (matrix tensile strength) and S_m (matrix shear strength) were calculated and the results can be seen in Table 2.1. Figure 2.11 shows a comparison between the predicted values of the off-axis strengths against orientation angle of the fibres, and the measured values. As can be seen there was reasonable agreement with the lower values of the in-plane strength, measured from the 0° Iosipescu shear test.

More recently, a simple micromechanical model was developed by Sun and Chen [21] to describe the elastic-plastic behaviour of fibrous composites; in the model the fibre was assumed to be linearly elastic and the matrix elastic-plastic. This model was then used to predict the fibre/matrix separation and non-linear off-axis stress/strain curves of a SiC-fibre-reinforced titanium alloy [22, 23]. As with the Aboudi model the fibres were assumed to have square cross-sections, with cross-sectional area equal to that of the actual fibre circular cross-section. Despite its sophistication, the Aboudi model, and its variants, is still

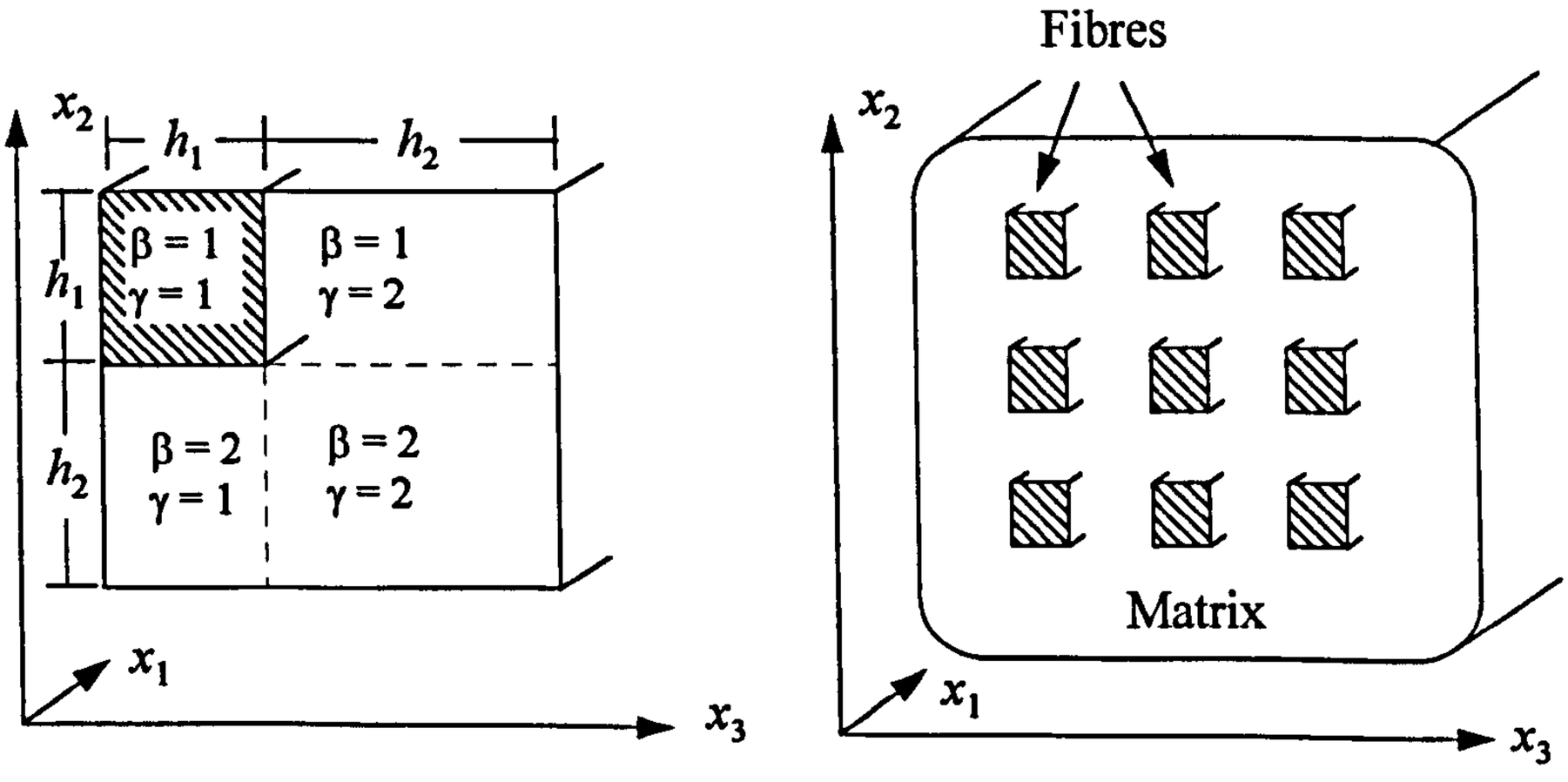

Figure 2.10 *(a) Representative unit cell of (b) composite [17–19]*

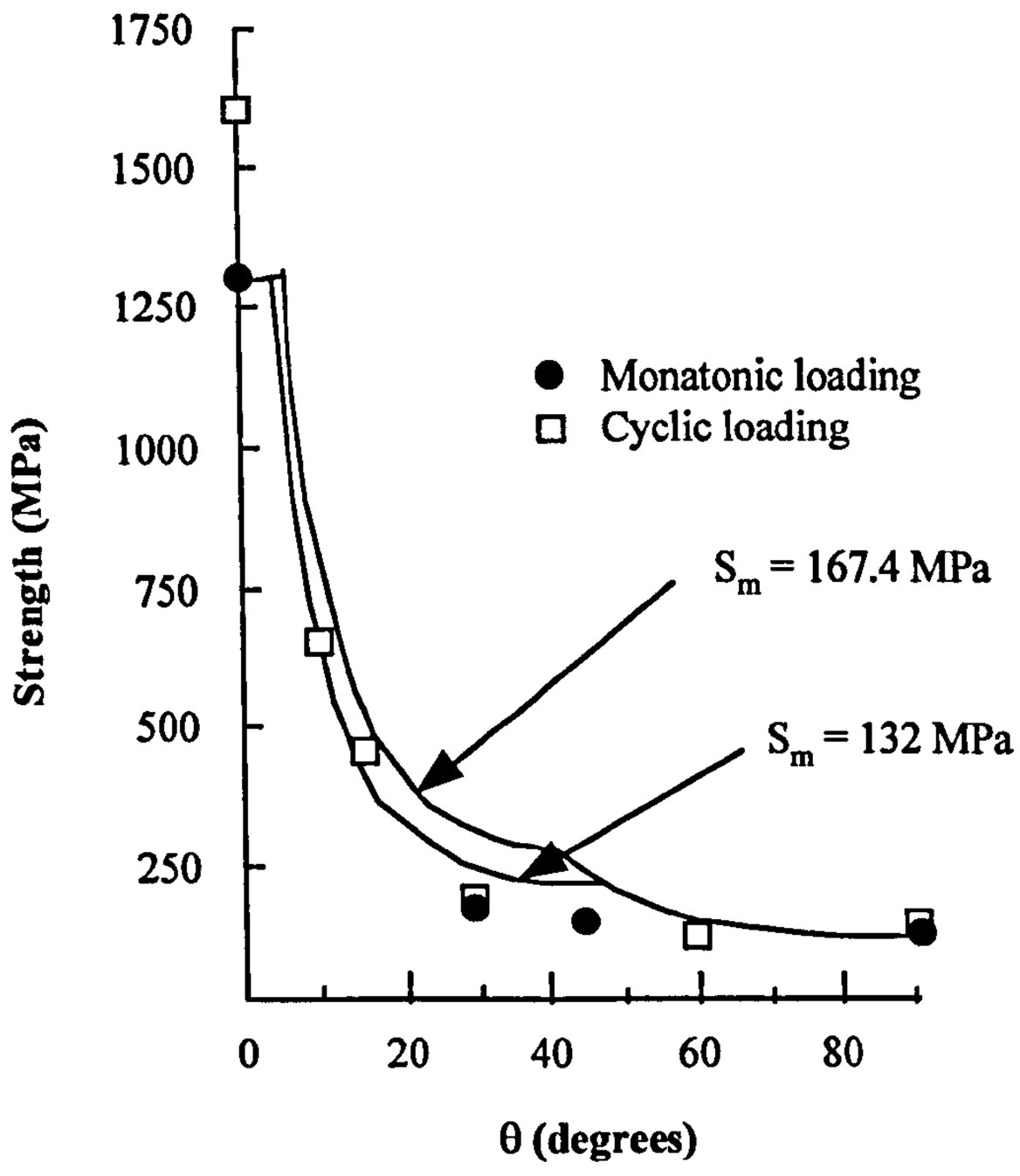

Figure 2.11 *Comparison between predicted and measured off-axis strength of a boron/ aluminium composite [18]*

limited in its application, the greatest limitation being the assumed perfectly bonded fibre matrix interface.

Begley and McMeeking [24] very recently produced a semi-analytic, semi-numerical procedure which modelled the effect of fibres bridging a matrix crack using line spring models for long, unidirectional fibres. The procedure was generic in that both ceramic and metal matrix composites could be modelled (Figure 2.12).

The bridging laws that Begley and McMeeking used were based on a shear lag analysis [25, 26] of a cell model. The model assumed that there existed a region where fibre and matrix were debonded and frictional sliding occurred; referred to as the *slip length*, this region extended from the matrix crack, to a length determined by the strain in the intact composite. Also assumed in the model, was that the stress resisting sliding was constant, and did not degrade with cyclic loading. The total opening $\delta_t(x)$ between the crack faces was related to the bridging tractions supplied by the fibres through the bridging law. The relation was given by*:

*See Appendix 1 for a complete nomenclature

$$\delta_t(x) = \lambda[\sigma_b(x)]^2 \qquad \{2.2\}$$

where

$$\lambda = \frac{D(1-f)^2 E_m^2}{4 f \tau E_f E_l^2} \qquad \{2.3\}$$

λ being the bridging law coefficient, D the diameter of the fibres, f the volume fraction, E_f and E_m the Young's modulus of fibres and matrix respectively, τ the shear sliding stress of

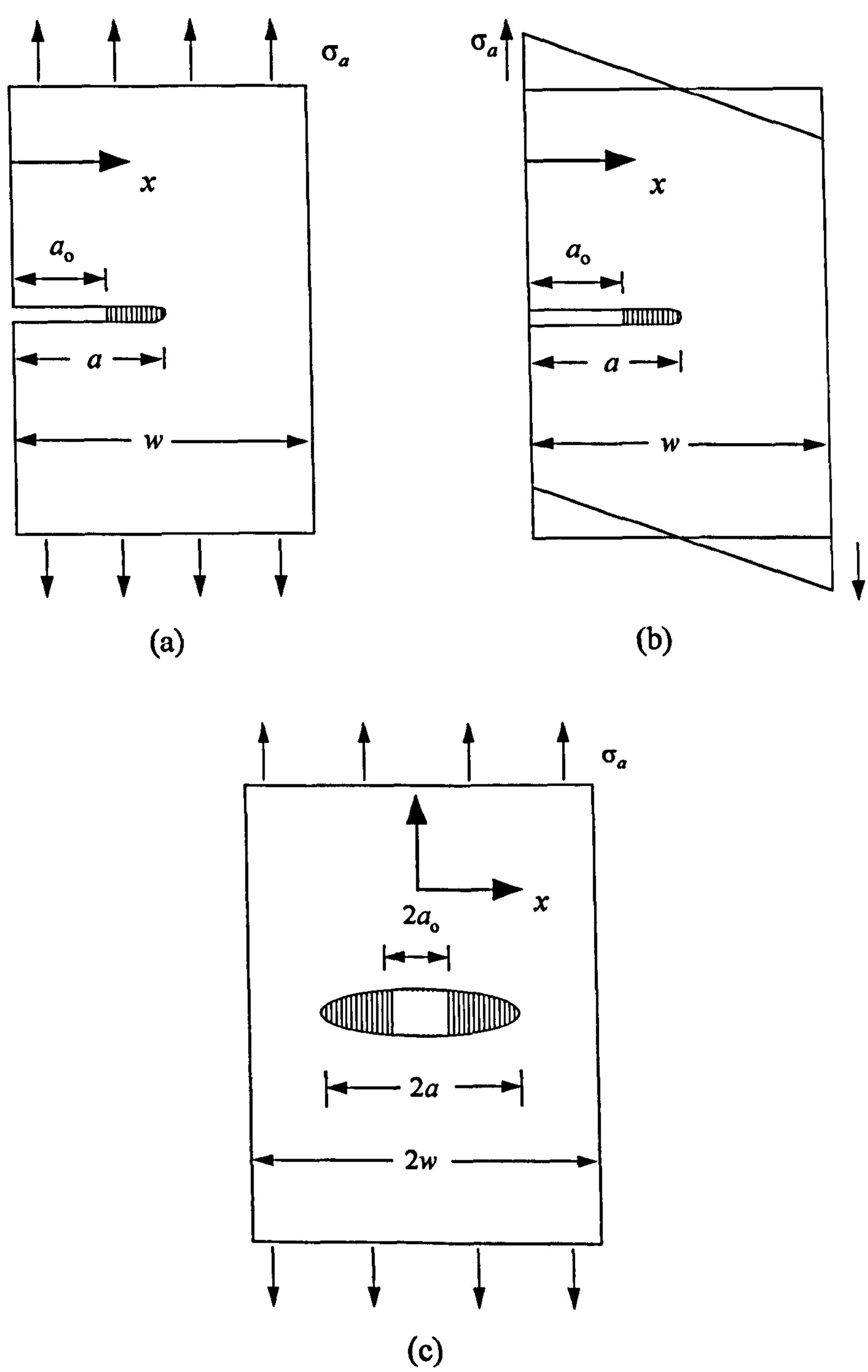

Figure 2.12 *Bridged crack geometries for (a) edge crack – tension loading, (b) edge crack – bending loading and (c) centre crack – tension loading [24]*

the fibre/matrix interface, E_L the global composite modulus found from the rule of mixtures given by:

$$E_L = fE_f + (1-f)E_m.$$

For cyclic loading McMeeking and Evans [27] found that the following similar bridging law resulted for {2.2}:

$$\Delta\delta_t(x) = \pm\frac{1}{2}\lambda[\Delta\sigma_b(x)]^2 \qquad \{2.4\}$$

where $\Delta\delta_t(x)$ was the total change in the crack face opening and $\Delta\sigma_b(x)$ was the change in bridging traction. Although {2.4} was the appropriate relation for considering fatigue of metal matrix composites, the assumptions outlined for monotonic loading in {2.2} were appropriate here as well.

The model described in [24] dealt with the monatonic loading case only, with the transformations in [27, 28] the integral equations for cyclic loading were of an identical form. The obtained formulation was for the tractions in the bridged zone, rather than the crack openings.

The total opening between crack faces at a point x in the bridged region, $\delta_t(x)$, could be expressed as the sum of the opening due to applied load, $\delta_a(x)$ and the opening due to the bridging tractions supplied by the fibres, $\delta_b(x)$, i.e.:

$$\delta_t(x) = \delta_a(x) + \delta_b(x) \qquad \{2.5\}$$

If the opening due to the applied load could be written as:

$$\delta_a(x) = \frac{2}{\overline{E}}\int_x^a K_a(\bar{a})\frac{\partial K_P(x,\bar{a})}{\partial P}d\bar{a} \qquad \{2.6\}$$

where K_a was the stress intensity factor* for the applied load, K_P was the stress intensity factor for a pair of point forces of magnitude P applied to the crack face at x, $\overline{E}$ was the composite modulus that accounted for orthotropy, a was the crack length and $\bar{a}$ a dummy integration variable. The opening due to the tractions supplied by the fibres could similarly be written as:

$$\delta_b(x) = \frac{2}{\overline{E}} \int_x^a K_b(\bar{a}) \frac{\partial K_P(x,\bar{a})}{\partial P} d\bar{a} \qquad \{2.7\}$$

where K_b was the stress intensity factor from the bridging traction distribution [29].

K_b was determined by integrating the effect of the bridging traction along the bridged zone. The opening due to the bridging traction distribution then became:

$$\delta_b(x) = \frac{2}{\overline{E}} \int_x^a \int_{a_0}^{\bar{a}} \sigma_b(t) \frac{\partial K_P(t,\bar{a})}{\partial P} \frac{\partial K_P(x,\bar{a})}{\partial P} dt\, d\bar{a} \qquad \{2.8\}$$

where a_0 is the length of the unbridged region (Figure 2.12) [29]. Since the unbridged region could be referred to as the notch, the analysis was applicable to both machined notches, and regions were the fibres had failed. The combination of equations {2.2}, {2.6} and {2.8} resulted in the following general integral equation for bridging traction distribution:

$$\lambda[\sigma_b(x)]^2 + \frac{2}{\overline{E}} \int_x^a \int_{a_0}^{\bar{a}} \sigma_b(t) \frac{\partial K_P(t,\bar{a})}{\partial P} \frac{\partial K_P(x,\bar{a})}{\partial P} dt\, d\bar{a} = \frac{2}{\overline{E}} \int_x^a K_a(\bar{a}) \frac{\partial K_P(x,\bar{a})}{\partial P} d\bar{a} \qquad \{2.9\}$$

Equation {2.9} had the generality in the sense that it applied to any bridged crack geometry and any type of loading. If the stress intensity factor due to a pair of point forces were known for every position along the crack, and every crack length, (i.e. $K_P(x,a)$), and the stress intensity factor due to the applied load was known as a function of crack length (i.e. $K_P(a)$), then {2.9} could be used to describe the effect of fibres bridging the matrix crack for that geometry. For the stress intensity factors in {2.9}, finite width effects could be incorporated by using appropriate functions, i.e. for the centre crack (Figure 2.12 (c)) of length $2a$, in a specimen of width $2w$, under uniform tension, $K_a = \sigma_a(\pi a)^{1/2}F(a/w)$, where $F(a/w)$ was the finite width correction term given in [29].

By normalizing equation {2.9} it was possible to obtain solutions for a variety of material and crack configurations. For the finite body specimens which [27] McMeeking and Evans were concerned with, the specimen width, w, was used as a normalizing factor, giving:

$$\lambda[\sigma_b(x)]^2 + \frac{2w}{\overline{E}} \int_x^{a/w} \int_{a_0/w}^{\bar{a}} \sigma_b(\bar{t}) \frac{\partial K_P(\bar{t},\bar{a})}{\partial P} \frac{\partial K_P(\bar{x},\bar{a})}{\partial P} d\bar{t}\, d\bar{a} = \frac{2w}{\overline{E}} \int_x^{a/w} K_a(\bar{a}) \frac{\partial K_P(\bar{x},\bar{a})}{\partial P} d\bar{a}$$
{2.10}

with the normalized position along the crack being $\bar{x} = x/w$ and the integration variable along the crack face being $\bar{t} = t/w$.

For a centre and edge cracks, the solutions for the stress intensity factor due to a pair of point forces of magnitude P, applied at position x, were:

$$K_P = \frac{2P}{\sqrt{\pi a}} G\left(\frac{x}{a}, \frac{a}{w}\right)$$

$$= \frac{2P}{\sqrt{\pi a}} \frac{f\left(\frac{x}{a}, \frac{a}{w}\right)}{\left(1-\frac{a}{w}\right)^{3/2} \sqrt{1-\left(\frac{x}{a}\right)^2}} \qquad \{2.11\}$$

where $f(x/a, a/w)$ was non-singular [29]. Substituting {2.11} into {2.10} an integral equation that was general to both centre and edge cracks was obtained. Multiplying both sides of this equation by $\lambda \bar{E}^2 / w^2$ resulted in the following general integral equation, in terms of non-dimensional variables:

$$\frac{\left(\sum(\bar{x})\right)^2}{16} = \frac{2}{\pi} \int_{a_0/w}^{a/w} \int_{\max(\bar{x},\bar{t})}^{a/w} \frac{1}{\bar{a}} G\left(\frac{\bar{x}}{\bar{a}}, \bar{a}\right) G\left(\frac{\bar{t}}{\bar{a}}, \bar{a}\right) \sum(\bar{t}) d\bar{a}\, d\bar{t} = \sum_a \int_{\bar{x}}^{a/w} F(\bar{a}) G\left(\frac{\bar{x}}{\bar{a}}, \bar{a}\right) d\bar{a}$$

{2.12}

where the normalized bridging traction is $\sum = 4\lambda \bar{E} \sigma_b / w$ and the normalized applied load is $\sum_a = 4\lambda \bar{E} \sigma_a / w$.

Equation {2.12} was solved numerically, with Figure 2.13 showing the solution to the integral equation for a given applied load level and several notch sizes for an edge crack loaded in three-point bending. The bridging traction illustrated in Figure 2.13 also represents the change in bridging tractions for an applied cyclic load, due to the simple conversion from monotonic to cyclic results; thus Figure 2.13 shows results for both monotonic and cyclic loading.

It was noted that the bridging traction in each distribution always occurred at the notch tip due to the large stress concentration from the unbridged region. When considering fibre failure, the bridging stress at the edge of the bridged region was the critical value. For a

deterministic fibre strength, it was assumed that fibres always began failing at this location. The bridging tractions in Figure 2.13 were used to predict the stress intensity factor of the matrix crack tip for each bridged crack geometry; the results are shown in Figure 2.14. As the crack extended across the specimen, the length of the bridged zone increased, resulting in the greater shielding effect of the fibres. As before, the results shown were for monotonic and cyclic loading, so that the curves in Figure 2.14 could be used to calculate the critical stresses for matrix crack extension for a given crack length for monotonic loading or fatigue crack growth.

Figure 2.15 shows the crack growth curves for a centre crack with a variety of load levels and normalized fibre strengths, using a Paris law exponent of $n = 2$. As the matrix crack extended, the shielding effect of the fibre lowered the crack tip stress intensity factor and crack growth slowed. At some point, depending on fibre strength, the maximum bridging traction is high enough to begin failing fibres, resulting in a rapid increase in the rate of crack growth. Once the fibres fail, increasing the notch size will increase the maximum bridging traction. Once all the fibres in the bridging zone failed, the crack growth of the composite was identical to that of the composite material. The above behaviour is shown

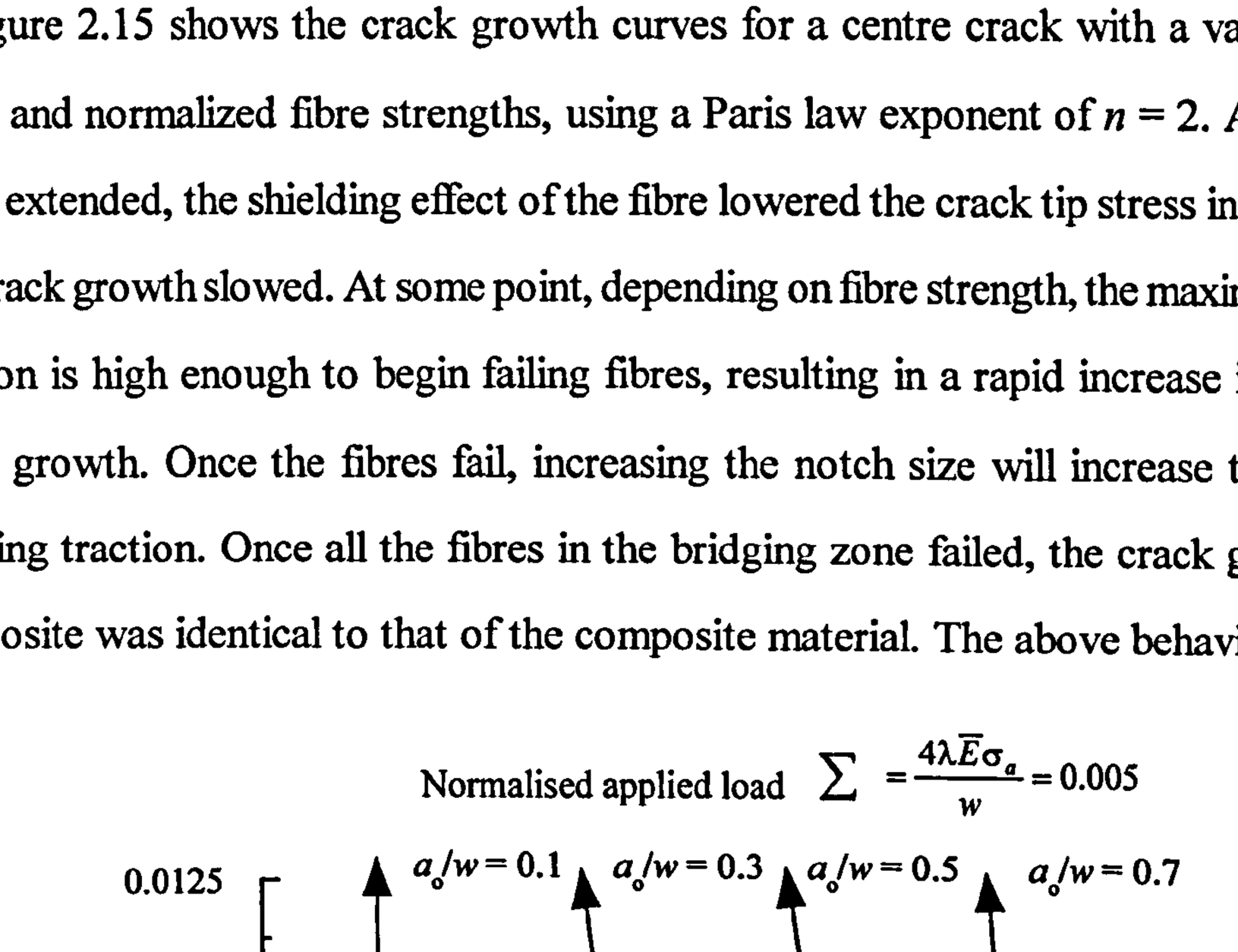

Figure 2.13 *Bridging stress distribution for an edge crack in bending [24]*

by the nearly vertical positions of the growth curves in Figure 2.15.

Due to the nature of the governing system of integral equations, the method by which this model was implemented was by no means elegant. Also, the following underlying assumptions used in the line spring model to describe fibre bridging in the fatiguing of metal matrix composites meant that the results could only be valid for a limited number of composite materials:

i. the specimen was perfectly elastic,
ii. the shear sliding stress of the fibre matrix interface was constant and did not degrade with cyclic loading,
iii. the solutions for the stress intensity factors for point loads generated for an isotropic material were valid for the anisotropic composite,
iv. the matrix fatigue crack growth could be described using the Paris law, and

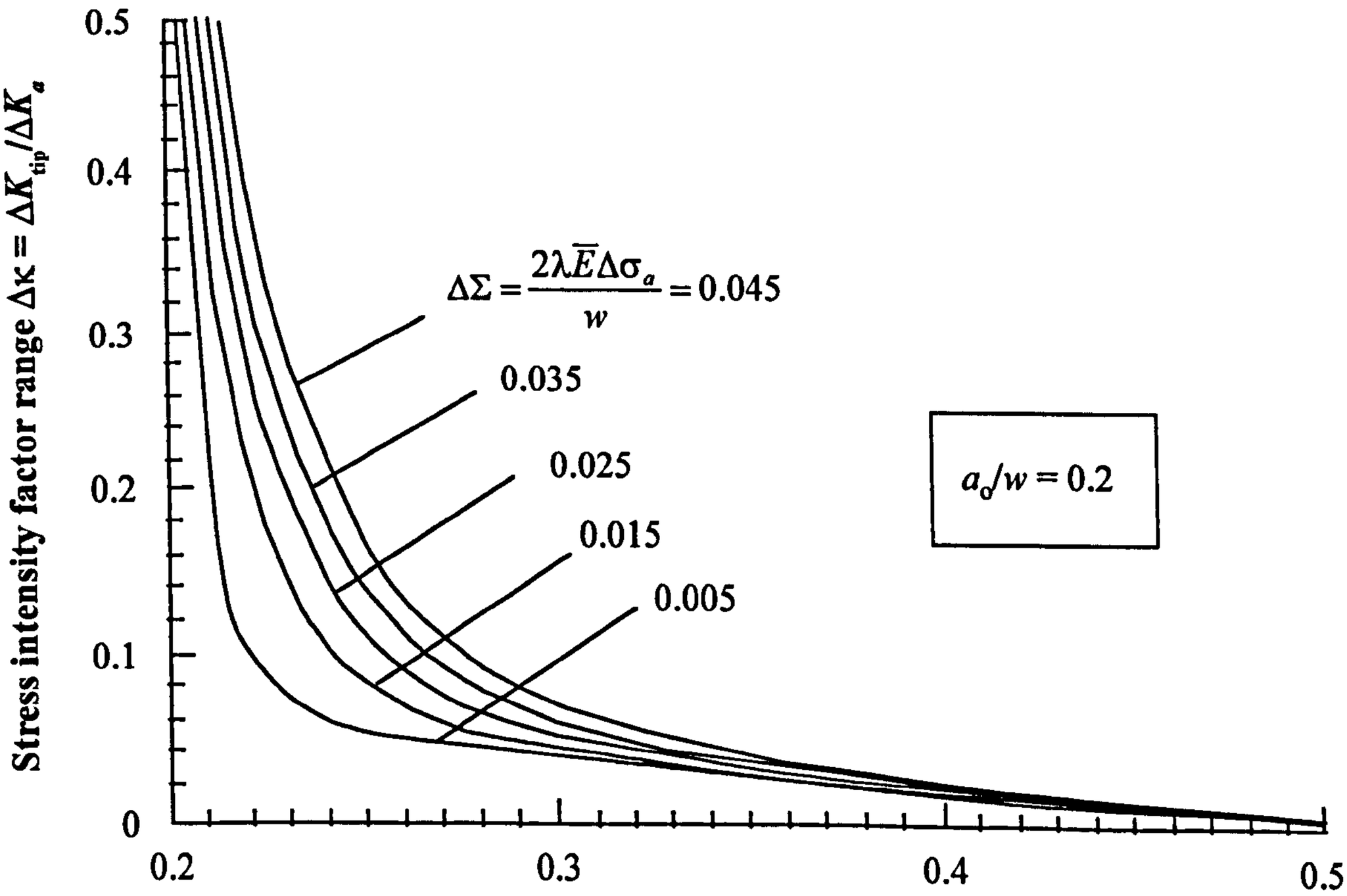

Figure 2.14 *Normalized stress intensity factor range at the matrix crack tip for an edge crack in three-point bending. (This can also be interpreted as the stress intensity factor at the matrix crack tip for monotonic loading) [24]*

v. that the strength of the fibres was deterministic, and they broke in the crack and not ahead of the crack tip.

Micromechanical analytical models are usually restricted to simplified model geometries and stress/strain assumptions to achieve closed-form solutions. For bulk properties of a unidirectional composite – i.e. those properties which represent average material response over its entire volume, such as elastic stiffness, coefficients of thermal and moisture expansion and thermal conductivity – the phenomenological approaches are quite adequate. However, fracture of a composite is a point property, i.e. the fracture initiates at one or a number of local points in the material. These cracks then grow with increasing applied stress, or cycles of stress in the case of fatigue loading, and eventually propagate over a great enough distance to coalesce; thus reducing the cross-sectional area sufficiently to cause total failure of the composite. Therefore, a detailed micromechanical stress analysis is required to model

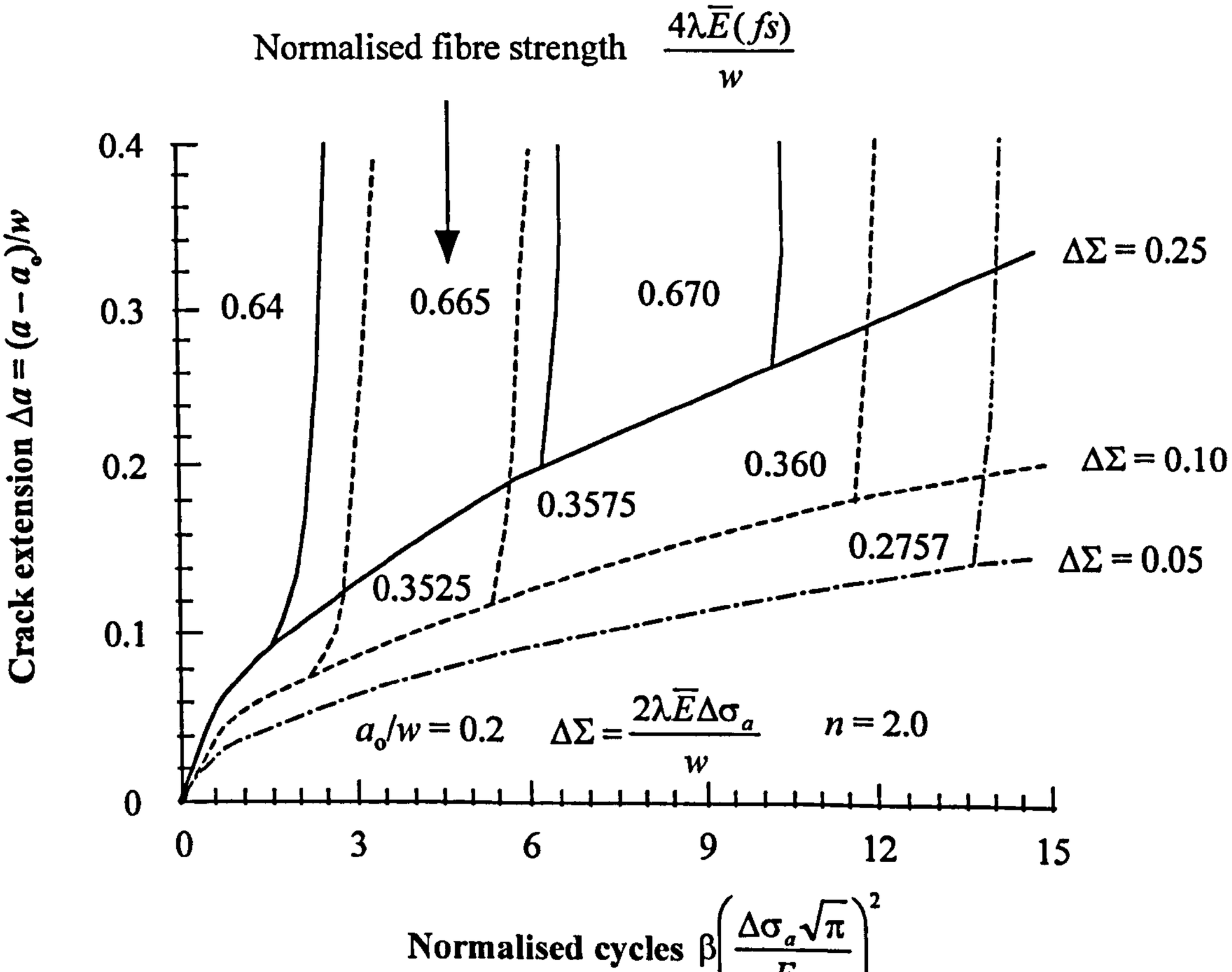

Figure 2.15 *Predictions for fatigue crack growth with fibre failure for a centre crack loaded in three point bending – nearly vertical portions of curves indicate fibre failure [24]*

this behaviour. This translates into a complex boundary value problem, not amenable to closed-form solution. Thus, numerical approaches such as finite difference and finite element techniques are required.

2.3 Numerical Techniques

For micromechanical modelling of composite behaviour there are two main numerical techniques which can be used to determine the complex stress distributions within the composite [24]. These are:

i. finite difference methods, and

ii. finite element methods.

Adams and Doner [30] first analysed the transverse tensile loading of a unidirectional composite using a finite difference method. A linear elastic plane strain analysis of a doubly repeating square array of fibres was performed and the stiffness and stresses investigated. The residual stresses due to an imposed temperature difference were also analysed.

The composite material was assumed to consist of a rectangular array of unidirectionally oriented elastic fibres perfectly bonded to an infinite elastic matrix (Figure 2.16). By assuming a regular packing arrangement, a fundamental or repeating unit could be isolated by symmetry, as indicated by the dashed lines in Figure 2.16. Because of the desirability of establishing symmetry conditions in the solution, the fibre was assumed to have two axes of symmetry, these axes being oriented parallel to the x and y axes of the fundamental shape.

The body was assumed to be loaded at infinity by uniform normal stresses $\overline{\sigma}_x$ and $\overline{\sigma}_y$ in the x an y coordinate directions as shown in Figure 2.16. The stresses could each be of arbitrary magnitude in tension or compression. The influence of thermal stresses induced by a uniform temperature change, T, in the composite material were also included in the analysis.

Because of the double periodicity of the fibre geometry and spacing, only one quadrant of the fundamental region needed to be considered, as shown in Figure 2.17. The problem was treated as one of plane elasticity and either a condition of plane stress or plane strain being assumed, as was appropriate to the analysis.

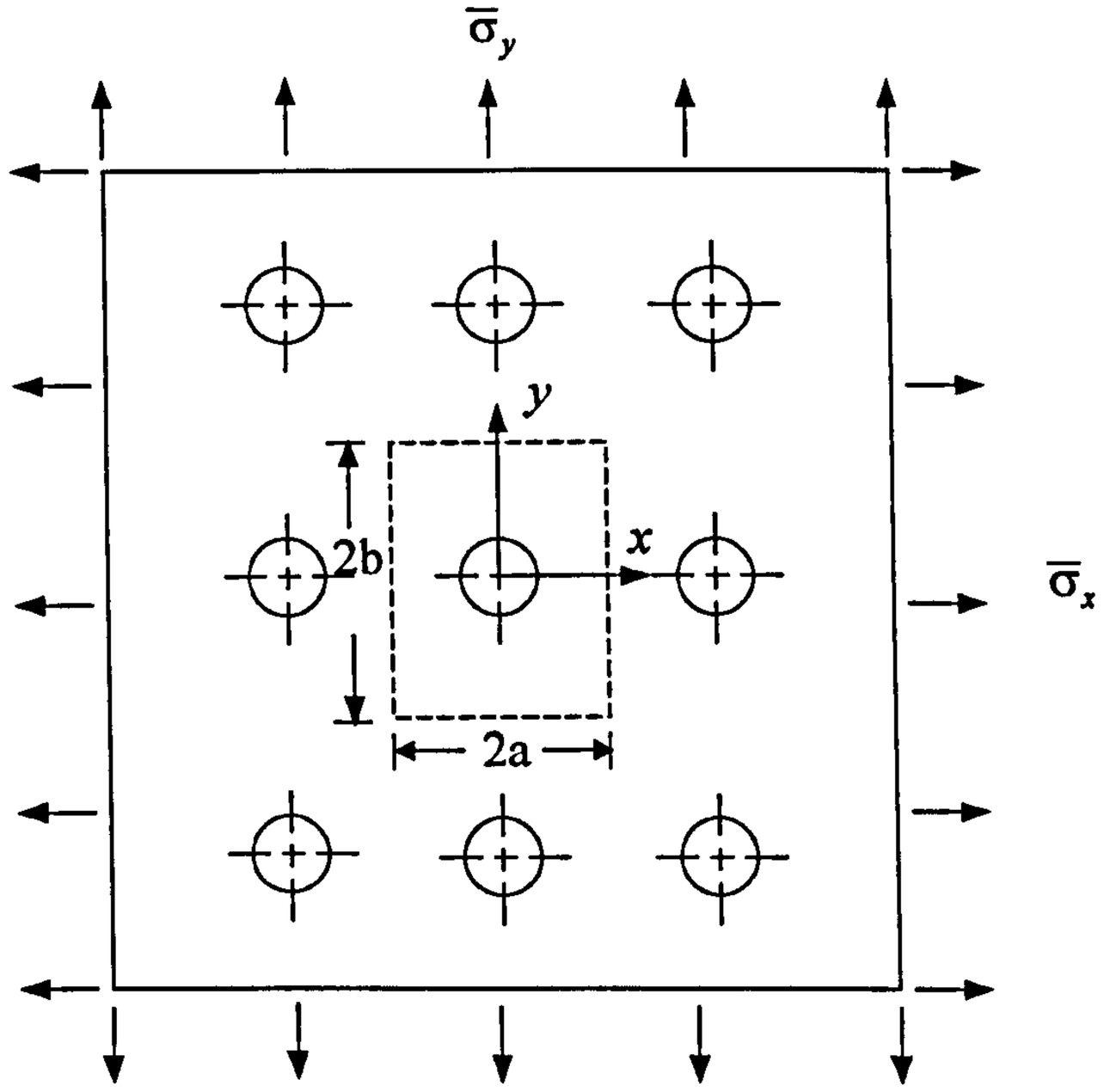

Figure 2.16 *Composite containing a rectangular array of fibres embedded in an elastic matrix and subjected to uniform transverse normal stress at infinity [30]*

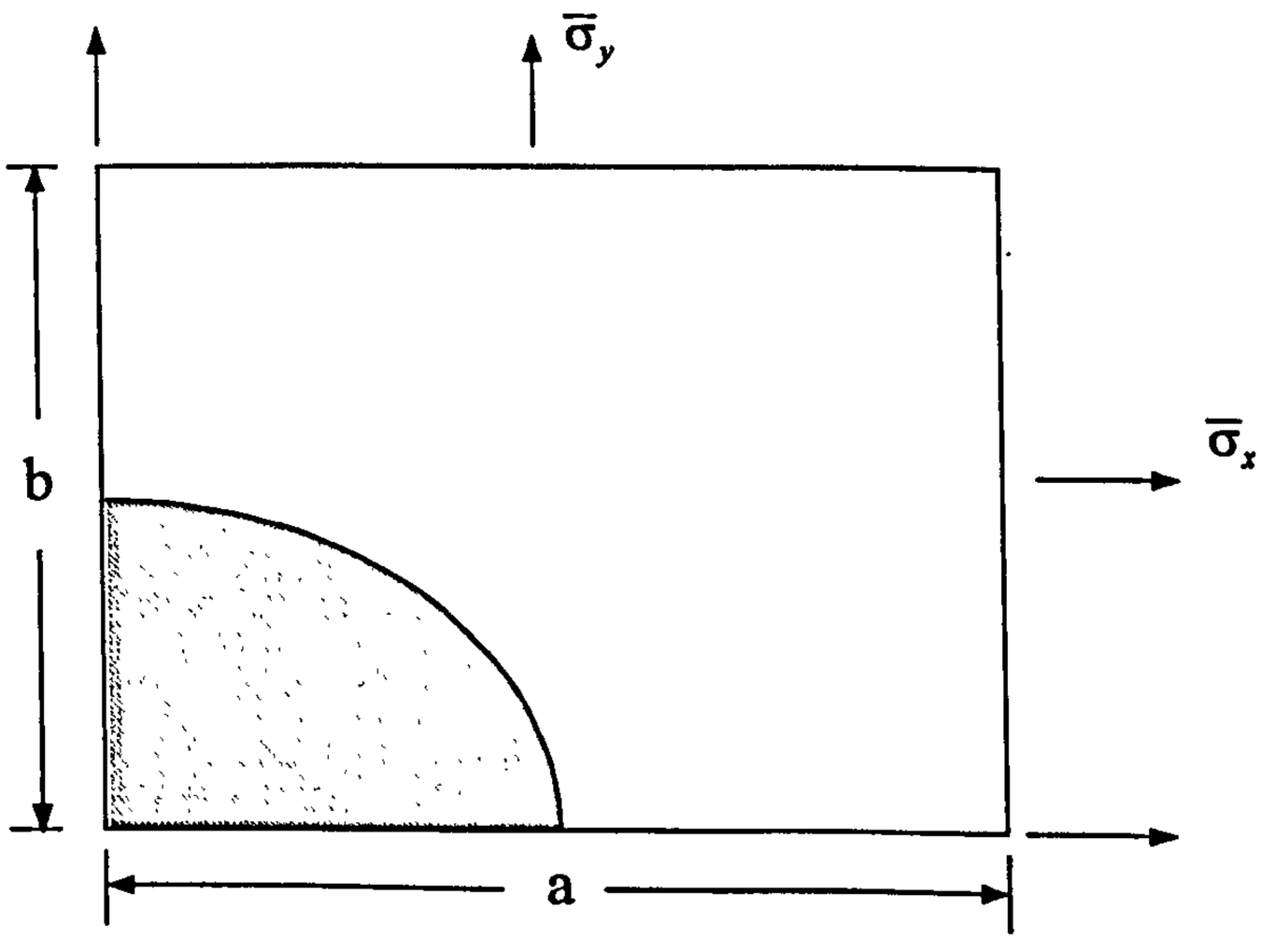

Figure 2.17 *First quadrant of the fundamental region [34]*

A finite difference model using a combination of, central, forward and backward difference techniques was written in FORTRAN. Numerical results were obtained for various cross-sectional shapes, together with differing fibre and matrix material properties and a range of fibre volume fractions.

The construction of the finite difference grid was such that, those areas requiring stress accuracy, e.g. in areas of high stress concentration, had a close grid spacing, whereas less critical regions had a coarser grid spacing.

A plot of the normalised maximum principal stress distribution versus the constituent stiffness ratio E_f/E_m subjected to an average transverse tensile stress component $\overline{\sigma}_x$ only, is shown in Figure 2.18. The plotted results are for various fibre volume fractions v_f with relative fibre spacing δ/r also shown. It is apparent from Figure 2.18, the highest values of principal stress occurred in the matrix at the interface at the point of closest proximity

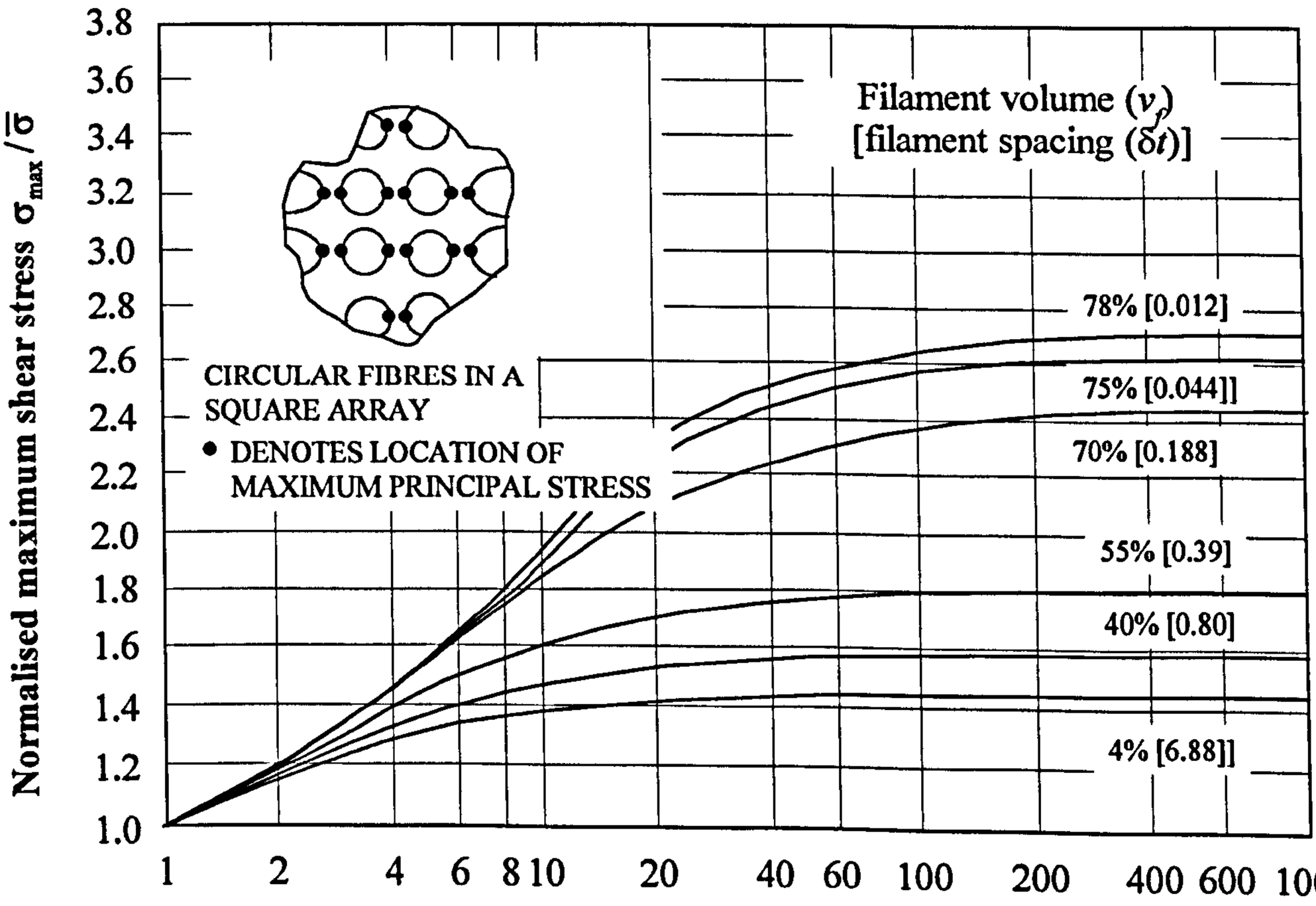

Figure 2.18 *Normalised maximum principal stress in matrix for circular fibres in a square array subjected to an average transverse normal tensile stress component* $\overline{\sigma}_x$ *only* ($\overline{\sigma}_y = 0$, $T = 0$, *and the Poisson ratios of the fibre and matrix being* $v_f = 0.2$, $v_m = 0.35$)

between adjacent fibres. The composite transverse stiffness increased with increasing fibre volume fraction or fibre stiffness, but a corresponding increase in local stress concentration, represented by the plots of maximum principal stress, indicated a decrease in composite strength.

The finite difference methodology used by Adams and Doner [30] was very similar to finite element techniques used today, particularly the grid refinement over the fundamental region of interest. It would be impractical to produce a similar model nowadays using the finite difference method, purely because of the time and effort required to set up the governing equations. It is probably true to say that had more user-friendly methods of using finite element techniques, such as the GUI methods, existed in 1967 Adams and Doner would have used this as their preferred method of numerical analysis.

Composite materials readily lend themselves to FEA because of FEA's ability to accurately discretize a complex geometrical shape and analyse in detail, the complex stress distributions within the material. For composites, the use of the finite difference method, on the other hand, is almost analogous to using analytical techniques in that discretization has to be "done by hand", with the analysis written from scratch as either a computer program (in FORTRAN, say) or as a spreadsheet. Thus, the model must be kept as simple as possible in order to save time in construction and avoid the errors that will inevitably occur when a complex model is "coded up".

Because composite materials lend themselves to FEA modelling so well, this is where the vast majority of work has been carried out; the present study will therefore concentrate on the FEA work on composites to date.

2.4 Finite Element Modelling of Composites

In order to apply finite element techniques to *micromechanical analysis* of unidirectional fibre composites, a number of assumptions and idealisations have to be introduced. The actual composite is normally replaced by a regularly spaced array of parallel cylindrical fibres embedded in an homogeneous matrix material of infinite dimensions; this array is then reduced to the smallest, fully informative, repeating segment – usually one quarter

fibre and its surrounding matrix. This segment is then replaced by an assemblage of elements. The resolution of the internal loads and deformations within this network, corresponds to a sequence of applied stress or strain states, and yields sufficient information to obtain the overall stress/strain behaviour of the composite and the details of the stress and strain distributions within the fibre and matrix materials corresponding to any applied stress state.

Early studies adopted a plane strain formulation, which precluded any Poisson ratio strain or thermal strain in the fibre direction. A more widely used assumption is the generalised plane strain formulation which allows a constant strain in the fibre direction over the 2-D domain modelled. This represents the situation at a cross-section through a continuous, infinitely long composite. Variations of stress and strain along the fibre, and the shear stresses and strains on the planes parallel to the fibres, are assumed to be zero.

The use of finite element methods to predict the mechanical properties of unidirectional composites was initiated in the 1960s. One of the earliest applications of plane strain finite element analysis to composite materials was used by Adams [31] who used a square and rectangular array of fibres (Figure 2.19). A perfect fibre/matrix interface bond was assumed and the effect of residual stresses was not taken into account. A non-linear analysis of boron/aluminium subject to transverse tension including the effect of matrix plasticity was performed. Later, the analysis was extended, again by Adams [32], to include crack initiation and propagation; different fibre packing geometries were considered (Figure 2.19). However, since the focus of the study was on developing the concept of crack initiation and propagation, the simpler rectangular array was again used; in this analysis a finite element scheme was used whereby once an element reached its ultimate stress, it was removed from the model – element removal is the simplest form of modelling crack propagation in FEA – this was achieved by setting the material properties, i.e. stress and stiffness, of the "failed element" to zero. The crack was thus assumed to have dimensions of the failed element. Clearly, unless a model of some refinement was used, in an actual material the width of the crack would typically be considerably smaller.

Figure 2.20 shows the FE mesh used for the analysis, and Figure 2.21 (a)–(d) shows the

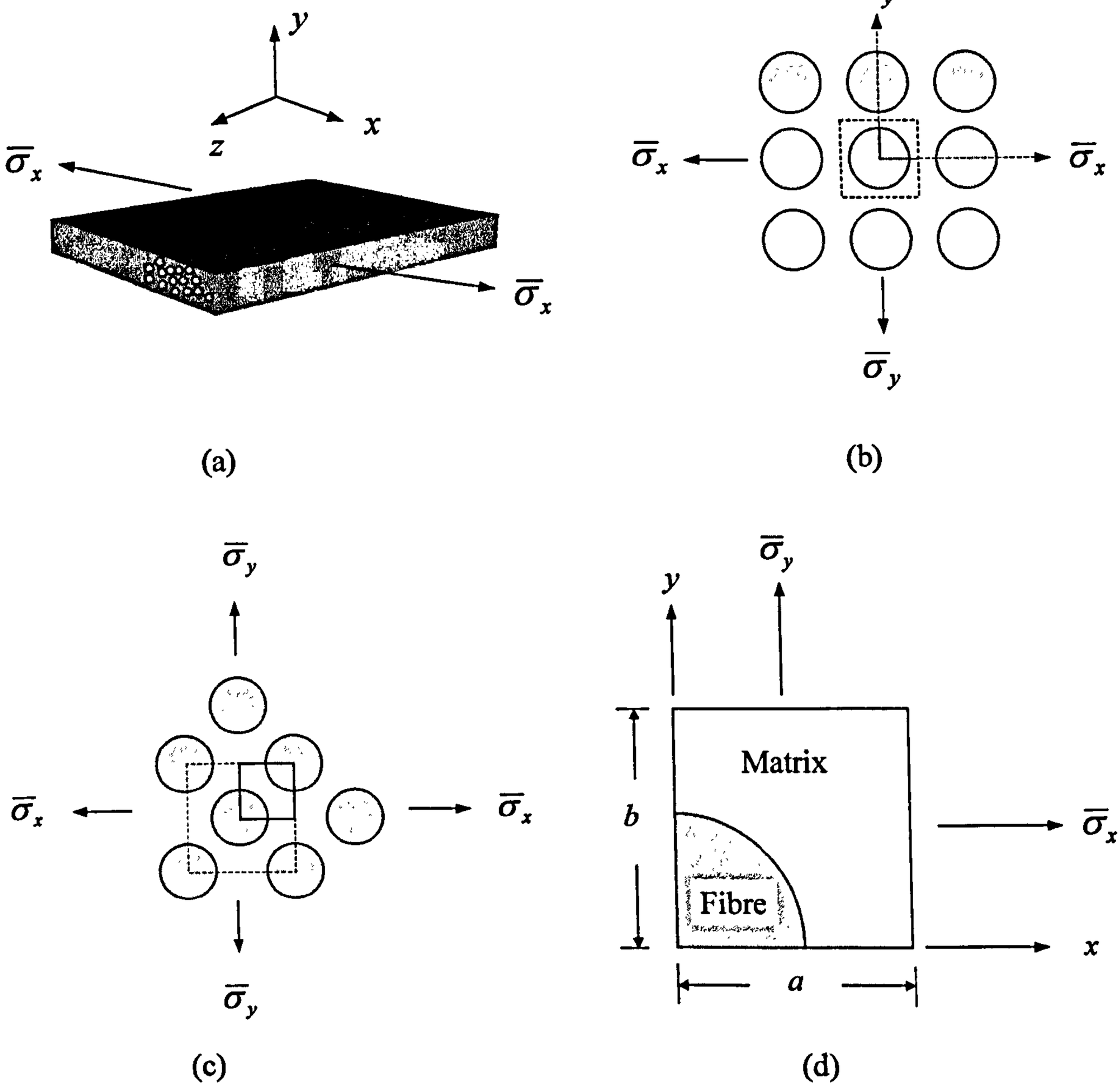

Figure 2.19 *(a) Transverse normal loading of a unidirectionally reinforced composite, (b) fibre rectangular array, (c) fibre diamond array and (d) first quadrent of a typically repeating unit [32]*

path of the crack. As can be seen from Figure 2.21 a crack initiated in the fibre/matrix interface, propagated partially round the fibre and then across the matrix. The crack starting at the interface was due to the failure of the matrix, the interface itself was assumed to be perfectly bonded.

The shortcomings of this model were that the typically repeating unit was in itself an average of the differing fibre spacing/radii/distribution within the matrix. Also, the size of the elements representing the crack/crack "tip", and the assumption that an element with zero material properties could actually represent a crack, e.g. consider what happens when

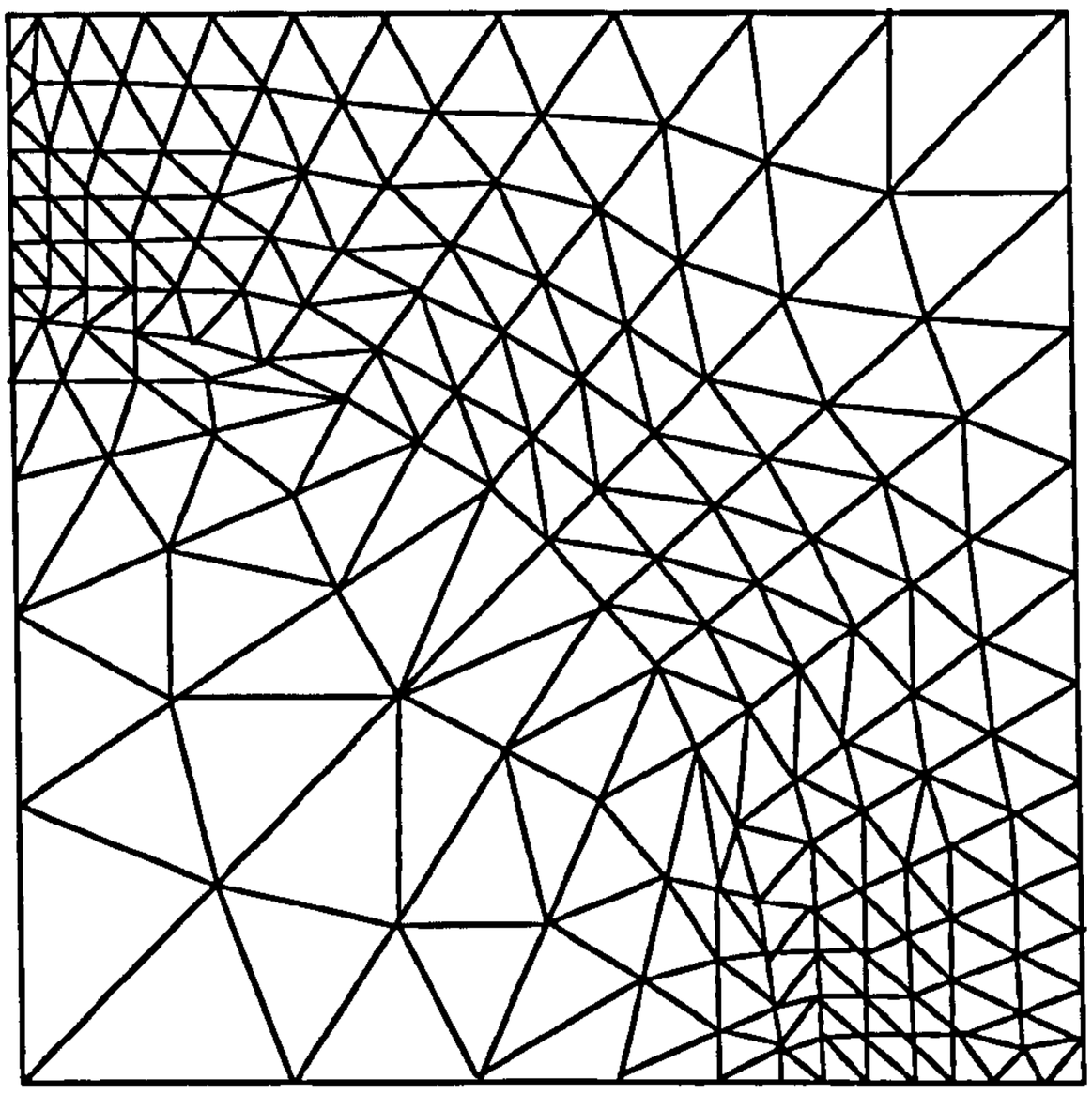

Figure 2.20 *The finite element mesh used in [32]: 40% fibre volume fraction containing 176 nodes and 304 elements*

a composite material is subject to an increasing monotonic load: when the material in a local region is stressed to its ultimate value, as defined in its stress-strain response, it will fail; if this occurs in a region of a high stress gradient, such as typically exists in a composite material, the surrounding material may be able to absorb the redistribution of stresses caused by the local failure without additional failure occurring at that level of applied stress. If this is the case, the local failure becomes a dicontinuity – a crack – within the material. As additional loading is applied the crack may grow in size and/or additional cracks may be initiated and eventually the material will fail. Since the material region is being represented by elements of finite size, in each of which the stresses and strain are assumed constant, a local failure is identified with a particular element and has the same dimensions of that element. In the actual material, the crack will typically be considerably smaller than this element. Also, by setting the material properties of the element to zero, to simulate a crack, a finite amount of material is assumed to be removed from the system which is not actually the case.

The above analysis was first used for the transverse loading of boron/aluminium and has more recently been applied to graphite/aluminium [33]. In addition to the transverse loading

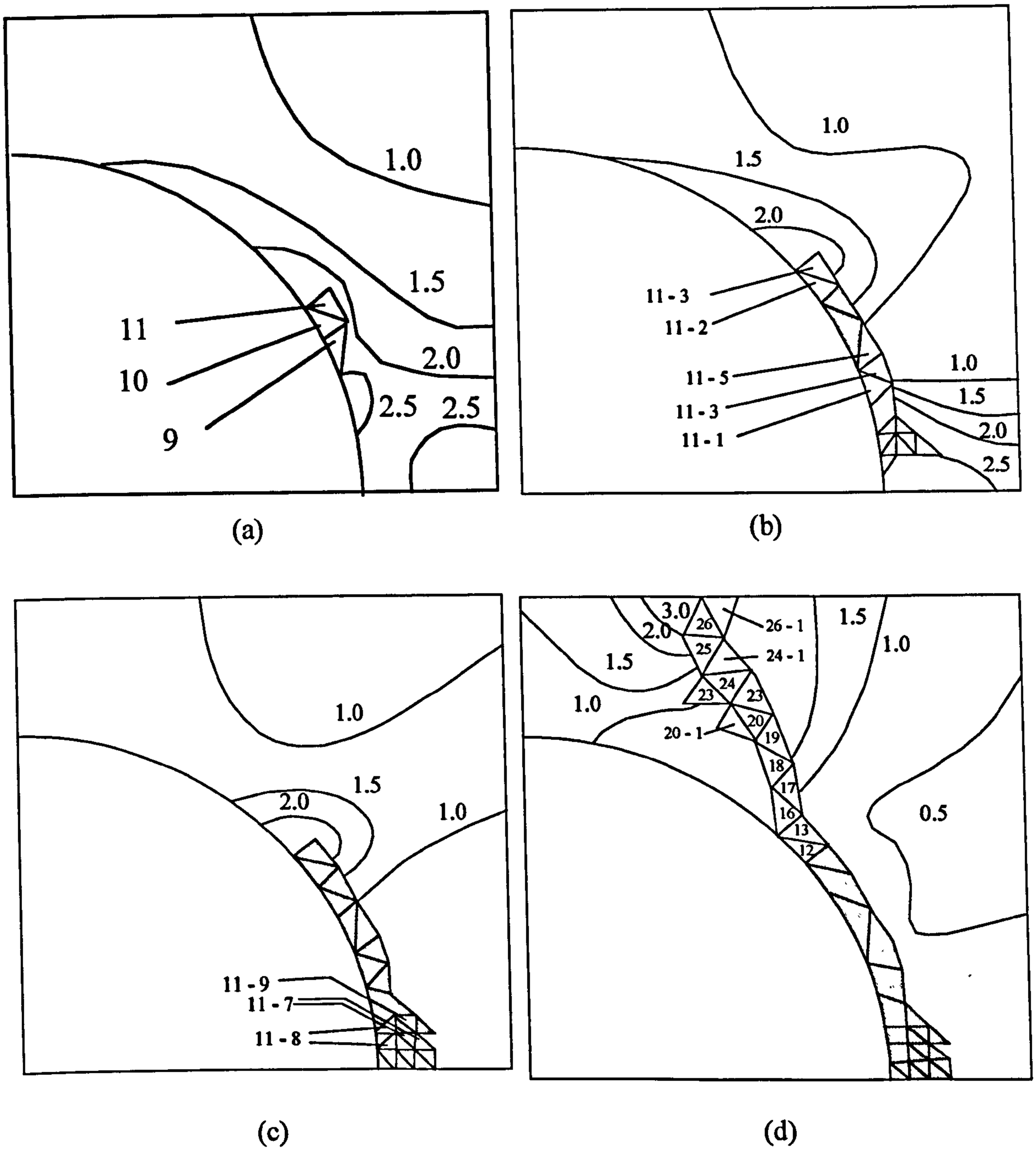

Figure 2.21 *Applied stress (σ_x), (a) increment 11, (b) increment 11-6, (c) increment 11-9 and (d) increment 26-2. In the case of a hyphenated increment number, the first digit indicates the applied stress increment number, and those after the increment indicate the adjustment increment within the applied stress increment during which the element failed [32]*

case, Adams et al. [34, 35] have also studied thermal- and moisture-induced stresses and longitudinal shear. The combination of all these differing loading conditions including thermal effects has also been given [36].

Dvorak et al. [37–40] developed a *periodic hexagonal array* (PHA) model, where the fibres were assumed to be periodically distributed throughout the matrix material in a

typological hexagonal configuration (Figure 2.22) as an approximation to large cross-section continuous fibres arranged in a regular array. Based on the vanishing fibre model of Dvorak and Bahei-El-Din [11] the PHA model overcame the inaccuracies sometimes encountered in calculating initial yield stress, and plastic strains, by explicitly modelling the microstructure of the composite.

Under the above assumptions, the smallest representative volume element that could be isolated for analysis was a triangular prism created by connecting the centres of adjacent fibres (Figure 2.22). The PHA model was then integrated into the general purpose finite analysis program *ABAQUS* [41], via a *user-defined material* (*UMAT*) subroutine.

In a similar micro-macro approach taken by Wu et al. [40] the analysis of general composite structures was performed by again combining the PHA constitutive model with *ABAQUS* [41] through the *UMAT* routine. The data provided to *UMAT* were strain and temperature increments which had been found from a macromechanical analysis in *ABAQUS* for the current load increment. The *UMAT* routine then updated the instantaneous stiffness and stresses for the given increment, returning the information to the macromechanical

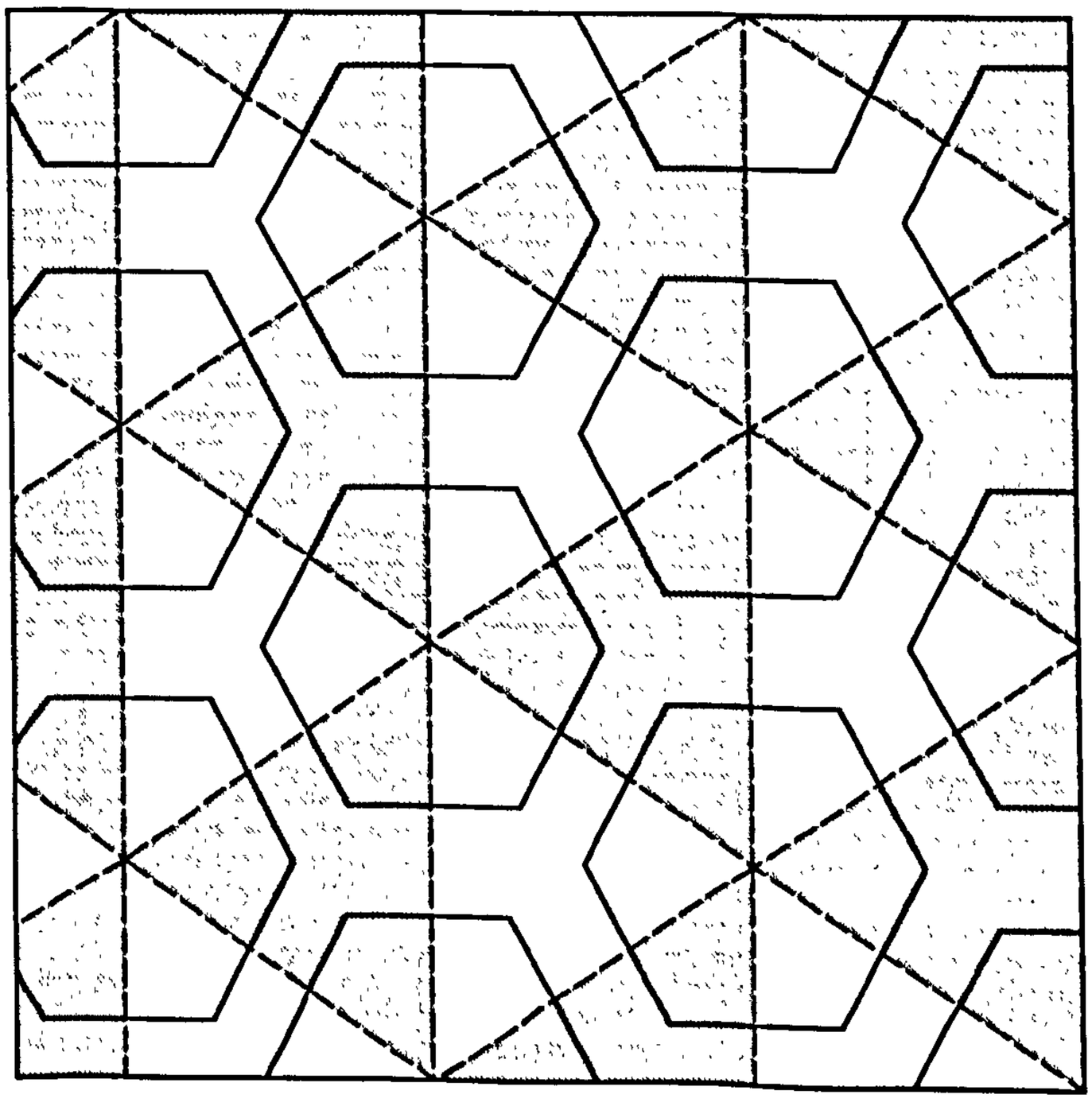

Figure 2.22 *Transverse cross-section of periodic hexagonal array [37–40]*

level finite element model. This effectively took into account the micromechanical level plasticity of the matrix material for a composite structure. Wu et al. [40] modelled the response of a laminated graphite/aluminium plate consisting of many alternating layers under thermal loading.

Figure 2.23 shows the response of the Gr/Al composite under thermal cyclic loading (20 °C, 120 °C, –120 °C, 120 °C) versus axial strain. The solid line indicates the response of a unidirectionally reinforced plate ($\theta = 0°$) and the dashed line represents laminate response. In the elastic range the laminate was dimensionally stable, and hence no overall strain was caused when the temperature changed from 20 °C to 60 °C, which marked the onset of initial yielding in the plate. After that, the plate was seen to undergo axial contraction while the temperature increased to 120 °C. The reversal of the direction of thermal change caused elastic unloading and therefore brought back dimensionally stable response. Plastic loading set in again at 50 °C and continued until –120 °C. No dimensional stability was seen in the response of the unidirectionally reinforced plate. However, the rate of plastic strain change was much lower in the unidirectionally reinforced plate and therefore the amplitude of the

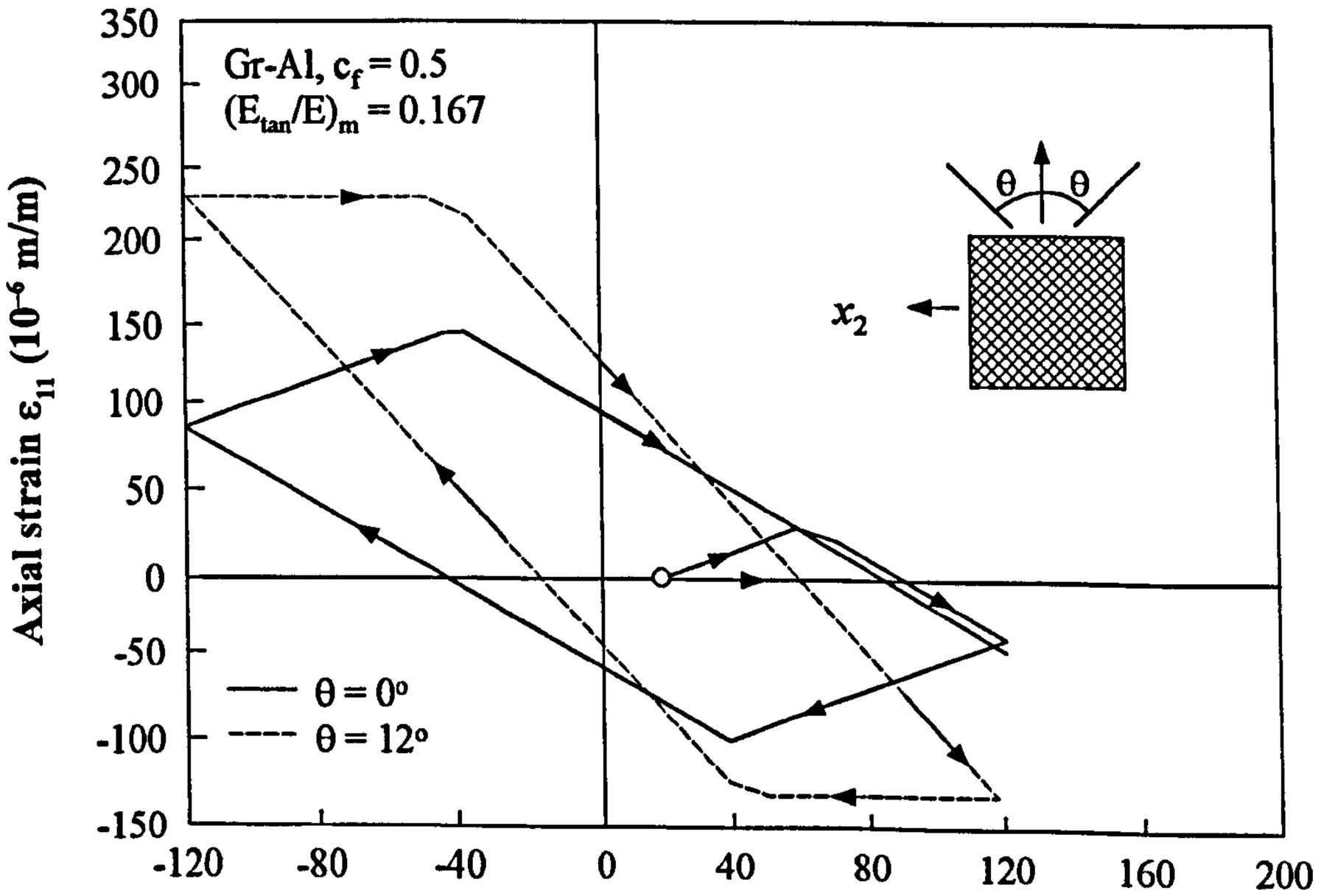

Figure 2.23 *Temperature-axial strain response of angle-ply composite with* $(E_{tan}/E)_m = 0.167$

total strain caused by the thermal change cycle was actually smaller in the unidirectional plate.

The response of a laminated composite structure to thermal and/or mechanical loads has been shown to be predicted by the use of the above specific micromechanical model associated with a general purpose finite element program. However, a problem with this approach is that the constitutive model is a six-dimensional stress-space formulation which must be used with solid brick elements. Thus the amount of computational resources required for the problems were sizable, being dominated by the PHA material evaluations. Considering that the models were relatively simple, they were, even by today's standards, computationally too expensive for general application.

2.5 Important MMC Characteristics to be Included in Models

The failure mechanisms of MMCs are strongly dependent on the constituent phases, heat treatment, environment and fabrication process, e.g. under transverse tension, SiC/titanium suffers from fibre/matrix interface debonding well before matrix yielding, while SiC/ aluminium shows considerable matrix plasticity before interface debonding [42, 43]. The effects of heat treatment on composite properties have been studied experimentally and analytically [44]. Most metal matrix composites are designed to be used in a high temperature environment, for example as components of turbine engines. The property changes due to such thermal exposure include creep, reduction in stiffness and yield stress, interface reaction and oxidation.

Metallurgical effects are important for metal matrix composites. The matrix properties are sensitive to heat treatment such as annealing and ageing. Residual stress relaxation is significant not only at elevated temperatures, but at room temperature [45]. In order to optimise composite properties, fibre treatment or the inclusion of additional phases between the fibre and matrix are often necessary. This, of course, complicates the microstructure and makes the stress analysis very difficult. For MMCs, large reinforcing fibres are usually used. The shape and distribution of such fibres may affect the composite properties, and need to be considered.

Another feature of MMCs is the interaction of the constituent phases. Li et al. [45] have shown that for SiC-fibre-reinforced 6061 Al, the cooling from fabrication temperature produces plastic deformation in the matrix, which reduces the amount of precipitation in the aluminium alloy. Interfacial reaction phenomena are a major concern for SiC/titanium MMCs; this type of composite contains much thicker interfacial reaction zones than aluminium-matrix composites due to the higher temperatures and the reactivity of the titanium alloy.

Many studies have been devoted to the characterisation of the structure and chemical composition of the interfacial reaction zones as well as the growth kinetics of the interfacial reaction [46–48]. It was found that the major reaction products were titanium carbides as a result of the reaction between the matrix and carbon-rich layer at the surface of the fibres. Yang, Jeng and Yang [48–50] measured the interfacial bond strength and frictional stress for fibre-reinforced titanium alloy matrix composites using the indentation technique and fragmentation test. The results indicate that mechanical properties and failure characteristics of the interfacial region are influenced by the fibre surface chemistry, matrix microstructure and residual stresses at the interface. The inclusion of interfacial effects is indeed a challenge for the micromechanical modelling of MMCs.

2.6 Modelling Local Stress Distributions

One of finite element's most powerful functions is to generate, in detail, the distribution of stresses and strains in the fibre and matrix – essential for understanding the mechanical behaviour of the composite, e.g. the point where matrix yielding is initiated can easily be located by *finite element analysis*. In addition, matrix yielding is a gradual process; the yield region expands progressively as the applied load increases – this is also best modelled by FEA.

Bigelow and Naik [51] performed a macro-micro-mechanics analysis to determine the matrix and fibre stresses near the notch tip in a centre-notched boron/aluminium composite. The macro-level analysis modelled the entire notched specimen using a three-dimensional homogeneous, orthotropic finite element program which used the *vanishing fibre diameter*

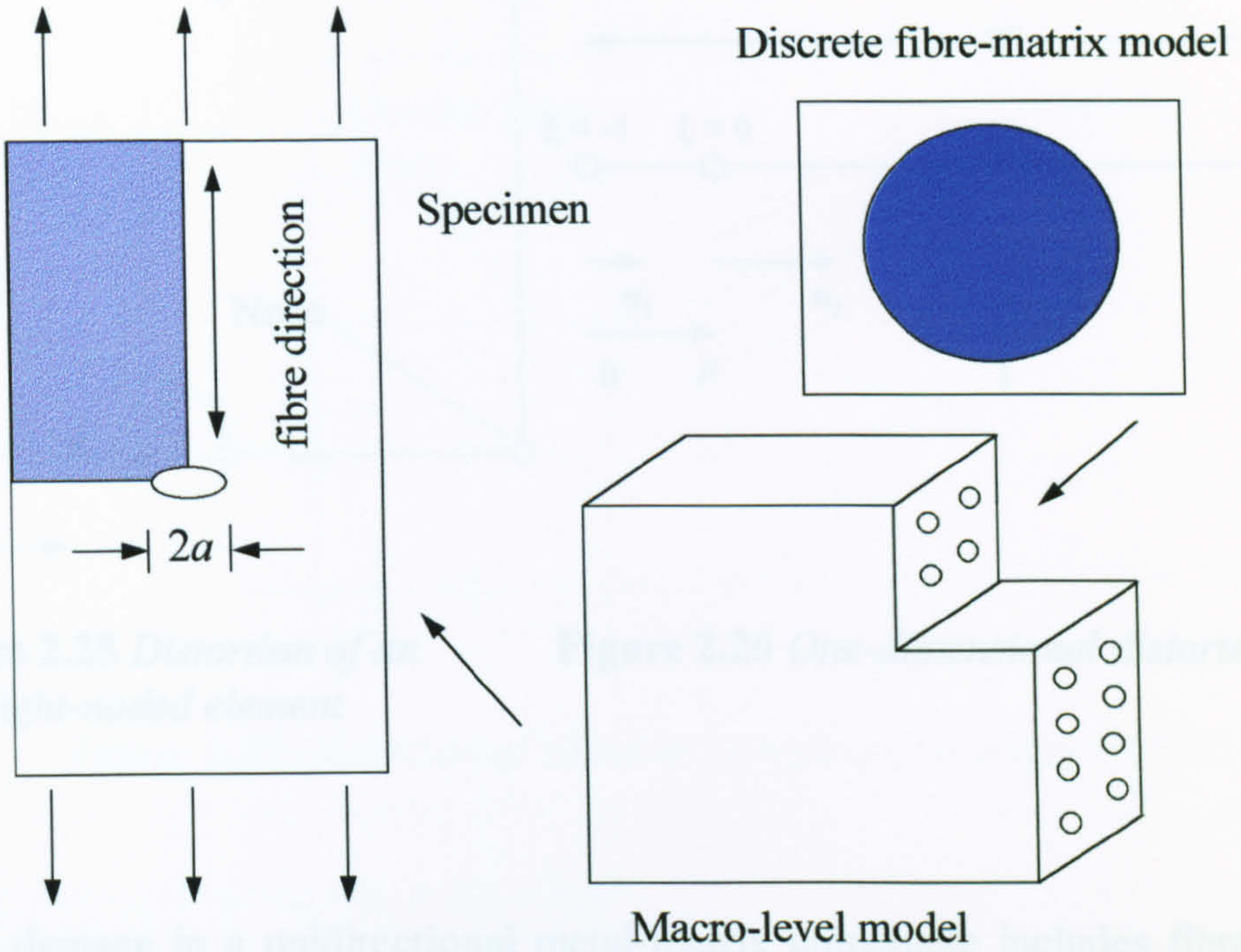

Figure 2.24 *Discrete two-dimensional, axisymmetric fibre model of composit [51]*

(VFD) material model developed by Bahei-El-Din and Dvorak [11]. The model was formed of constant-strain, eight-noded, hexahedral elements. Each hexahedral element represents a unidirectional composite material whose fibres could be oriented in the appropriate direction in the structural coordinate system. The micro-level analysis used a *discrete fibre/matrix* (DFM) model containing one fibre and the surrounding matrix at the notch tip. Instead of applying the boundary conditions corresponding to some assumed array of fibres, the unit cell of the DFM model used the displacement boundary conditions that were obtained from the global or macro-level analysis of the notched specimen. The specimen and finite element idealisations of the macro- and micro-level models are shown in Figure 2.24. The analysis showed that the stresses in the fibre and matrix at the notch tip were significantly higher than the remote applied stress and their distributions were very non-uniform. The DFM analysis also indicated that matrix yielding was initiated at the free surface next to the notch tip, and progresses uniformly through the notch tip element in a direction away from the notch tip.

2.7 Modelling Damage Initiation and Propagation

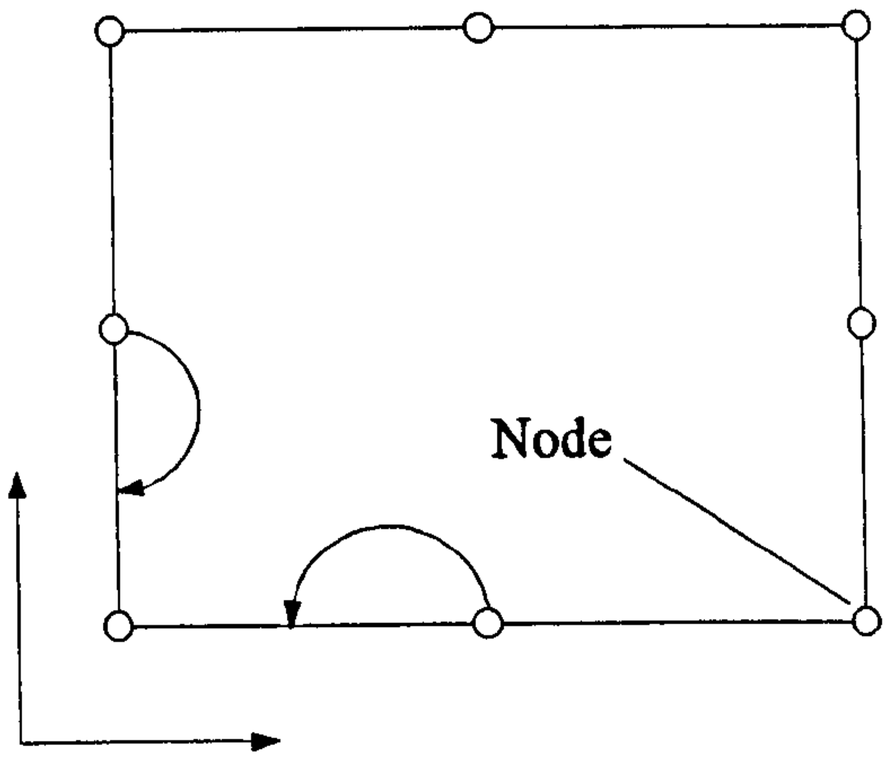

Figure 2.25 *Distortion of an eight-noded element*

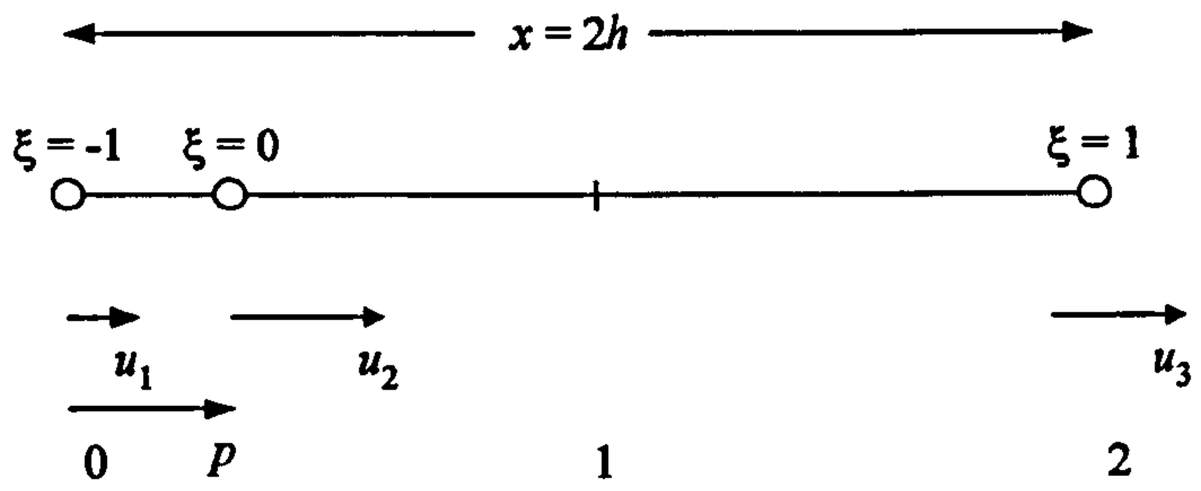

Figure 2.26 *One-dimensional distorted element*

Typical damage in a unidirectional metal-matrix composite includes fibre fracture in longitudinal tension and interface debonding in transverse tension.

One of the problems associated with modelling a discontinuity in both composite and conventional materials, is obtaining an optimal element size to give a reasonable representation of a crack tip. At the crack tip, the tensile stress is infinite and in order that this stress be numerically catered for, very small elements are required in the model. However, the use of many small elements can be computationaly very "expensive" and a more elegant solution to this problem was independently developed by Barsoum [52] and Henshell and Shaw [53] who suggested a "quarter point" method for stress intensity calculations at a crack tip. A standard eight-noded isoparametric finite element existing in xy space was transformed to a square in $\xi\eta$ space, with vertices at $(\pm 1, \pm 1)$, the behaviour of the mid-side nodes as they were being moved away from their usual position being of interest(Figure 2.25). The mathematics were simplified so that just one of the sides of the element was considered, thus reducing the problem to that of a one dimensional element. The one-dimensional element (Figure 2.26) had nodes at $x = (-1, 1)$ and $r = 0, p, 2$. The undistorted element corresponded to $p = 1$. The assumptions for transformation and displacement took the form:

$$r = a_1 + a_2\xi + a_3\xi^2 \qquad \{2.13\}$$

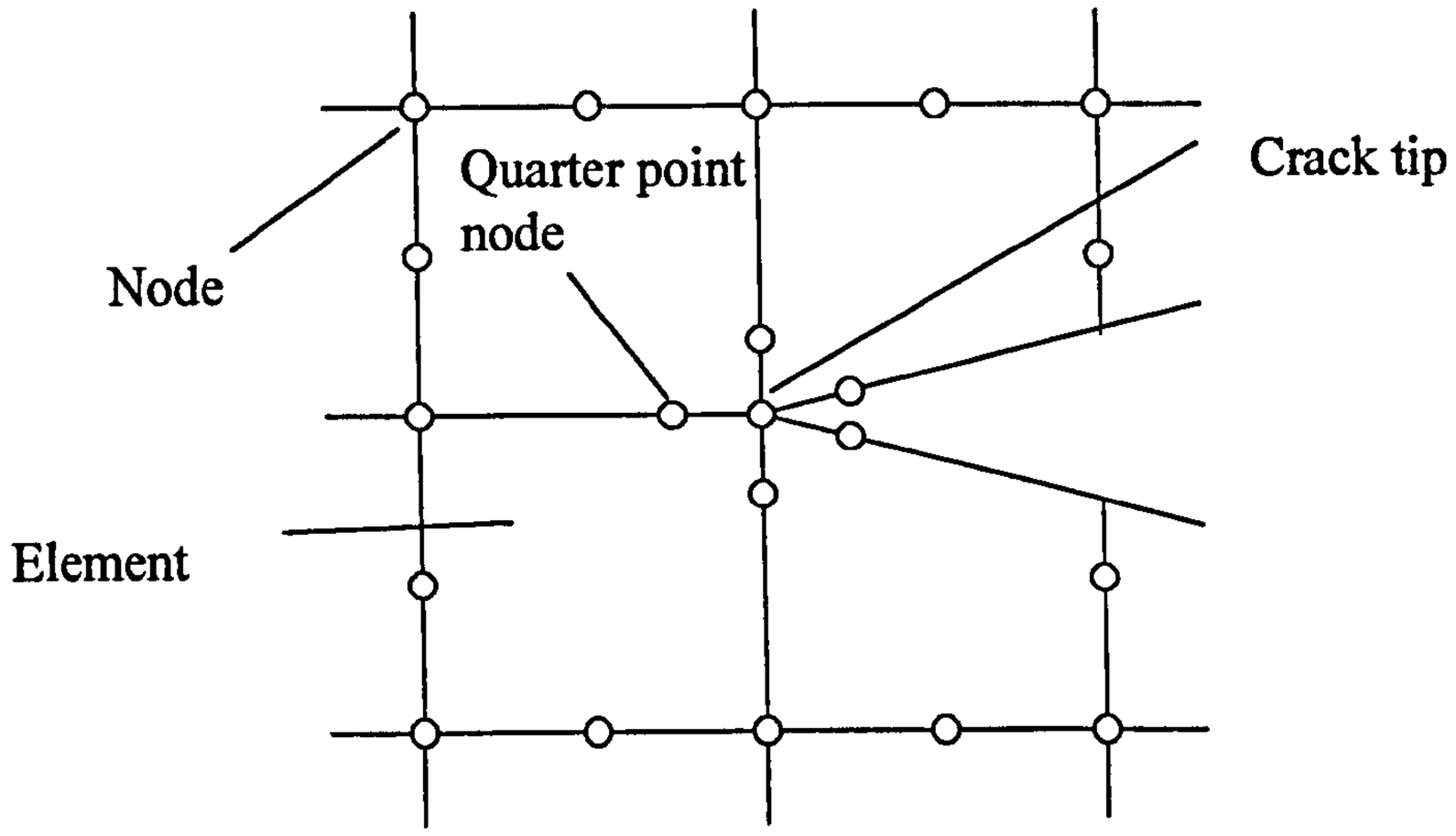

Figure 2.27 *Distortion of elements in region of a singularity [53]*

$$u = b_1 + b_2\xi + b_3\xi^2 \qquad \{2.14\}$$

where a_i and b_i were constants and $r = x/h$.

By writing {2.13} in terms of the nodal values of r to eliminate a_i and solving for ξ, gave:

$$\xi = \frac{-1 \pm \sqrt{[1-4p+4p^2+4(1-p)r]}}{2(1-p)} \qquad \{2.15\}$$

taking the positive square root as the correct one, the derivative of {2.15} was:

$$\xi'(r) = [1-4p+4p^2+4(1-p)r]^{-\frac{1}{2}} \qquad \{2.16\}$$

which had a singularity when $\xi'(r) = 0$, i.e.

$$r = \frac{(1-2p)^2}{4(p-1)}$$

The singularity occurred at the $r = 0$ end of the element, giving $p = 1/2$, thus yielding:

$$\xi = -1 + \sqrt{(2r)} \qquad \{2.17\}$$

$$\xi'(r) = (2r)^{-\frac{1}{2}} \qquad \{2.18\}$$

$$u = u_1 \frac{2-3\sqrt{2r}+2r}{2} + 2u_2\left(-r+\sqrt{2r}\right) + u_3 \frac{2r-\sqrt{2r}}{2} \qquad \{2.19\}$$

where the constants b_i in {2.14} were evaluated in terms of the expression for the nodal values of u.

Since it was the stresses that were of interest, and these are proportional to strains, in the one-dimensional element the longitudinal strain was given by:

$$u'(r) = u_1\left[1-\frac{3}{2}(2r)^{-\frac{1}{2}}\right] + 2u_2\left[-1+(2r)^{-\frac{1}{2}}\right] + u_3\left[1-\frac{1}{2}(2r)^{-\frac{1}{2}}\right] \qquad \{2.20\}$$

Equation {2.20} clearly showed that the singularity was the order of $r^{-1/2}$, as required by the Westergaard solutions [54, 55]. A simple rule was thus suggested; when elements with one mid-side node were used at a crack tip, the mid-side nodes should be moved from their usual position at the centre of each side, to the 1/4 position as shown in Figure 2.27.

Thus, by simply moving the mid-side node positions on standard eight-noded isoparametric elements so that the singularity occurred at the element corner (the crack tip), it became possible to obtain accurate stress intensity solutions [56] without recourse to using numerous small elements.

Wisnom [57] developed an interface element to simulate the interface debonding process (this element was superseded by the contact pair approach in version 5.5, and later, of *ABAQUS*). Implemented in *ABAQUS*, the element represented a perfect interface until a certain state of stress was reached, when the interface was assumed to fail. Pairs of nodes on each side of the interface were coupled with stiff springs. Normal and tangential stresses across the interface were monitored. The springs between node pairs were released when the combination of normal and shear stresses at the nodes reached a pre-defined criterion. This element was used to study the transverse properties of aluminium matrix composites. The interface failure criterion takes an elliptical form:

$$\left(\frac{\sigma}{\sigma_0}\right)^2 + \left(\frac{\tau}{\tau_0}\right)^2 = 1 \qquad \{2.21\}$$

where σ and τ are the normal and shear stresses across the interface and σ_0 and τ_0 are the failure stresses for the interface in pure tension and shear. A similar approach was also used

to study the effect of placing un-reinforced aluminium interlayers between the composite plies.

Wisnom [45] has studied the factors that affect the transverse tensile strength of continuous SiC-fibre-reinforced 6061 aluminium through a micro-mechanics approach using generalised plane strain non-linear finite element analysis. The above interface element was used, enabling separate shear and tensile interface strengths to be assigned, with a quadratic interaction equation [44]. Residual stresses due to manufacturing were included in the analysis. Li and Wisnom [45] also used this interface element to model the transverse tensile behaviour of SiC/Ti with some modification to the interface criterion. This was because the manufacturing process generated very large compressive normal residual stresses due to the high modulus and high yield point of the titanium matrix. This made the expression on the left hand side of equation {2.21} initially greater than unity if σ_0 was assumed the same in tension and compression. It assumed that the interface did not fail due to shear if the normal stress was compressive, the shear stress would be so high when the normal stress becomes tensile that the whole interface would debond immediately. Therefore, the interface failure criterion was assumed to be:

$$\left(\frac{\sigma}{\sigma_0}\right)+\left(\frac{\tau}{\sigma_0}\right)^2=1 \qquad \{2.22\}$$

where σ and τ are the normal and shear stresses across the interface and σ_0 is the interface tensile strength.

Equation {2.22} is an empirical interactive equation with no rigorous theoretical basis. However, it happens to be in the same form as that from the expression for the maximum principal stress for a plane stress state with one normal stress and one shear stress:

$$\sigma_1=\frac{\sigma}{2}+\sqrt{\left(\frac{\sigma}{2}\right)^2+\tau^2} \qquad \{2.23\}$$

with $\sigma_1 = \sigma_0$. This failure criterion is for an infinitely thin interface, the failure is determined

by the normal and shear stresses only. The hoop stress and longitudinal stress in the material around the interface are not relevant due to the assumption that the interface is dimensionless.

This failure criterion was further developed by Li and Wisnom [58,59] in their models to account for the effect of the fibre coating on the transverse properties of the SCS-6/Ti-6-4. It was assumed that the interfacial failure was initiated in the coating and, since the coating is relatively thick and brittle, the failure was assumed to be controlled by the principal stress, i.e.

$$\sigma_1 = \frac{\sigma_r + \sigma_\theta}{2} + \sqrt{\left[\frac{\sigma_r - \sigma_\theta}{2}\right]^2 + \tau_{r\theta}^2} \qquad \{2.24\}$$

where σ_r, σ_θ and $\tau_{r\theta}$ are the interfacial radial, hoop and shear stresses. This criterion is for the material in the coating immediately adjacent to the interface. The result of the simulated interface debonding is discussed in the next section.

2.8 Multiple Phase Modelling

Robertson and Mall [60] studied the interfacial effects of metal matrix composites using a unit cell comprised of fibre and matrix along with an interphase region as a third phase material, possessing its own unique elastic-plastic properties. The interphase was incorporated in an effort to model the energy dissipation mechanisms and additional constraints that cannot be obtained using a vanishingly weak interface. Transverse tensile stress/strain response was studied using a one-dimensional analytical model and finite element modelling. The finite element analysis was conducted using the *MSC/NASTRAN* program. A regular square array of fibres was assumed. The interphase was modelled with two layers of elements.

All parameters associated with the interphase were studied to determine their effects on composite transverse properties. These included interphase zone yield stress, strain hardening, Young's modulus, thermal coefficients of expansion and thickness. It was found that the

plastic properties of the interphase had the greatest effect on the transverse characteristics of the composite. Increasing the yield stress resulted in increasing the point of non-linearity, and increasing the strain hardening resulted in increasing the secondary slope. A stiffer interphase yields a higher transverse modulus. As the interphase coefficient of thermal expansion is increased, the stress at which non-linearity begins decreases. This results from the interphase zone with a higher expansion coefficient contracting more during cooling from the processing temperature. Hence the matrix experiences less resistance when it contracts, so that the compressive residual stresses in the interphase zone are decreased.

In addition to possessing the capability for modelling a partially bonded interface, an advantage in introducing an interphase is that it allows for significant energy dissipation during a loading and unloading sequence. Robertson and Mall [60] stated that modelling the interface as a third phase elastic-plastic zone allowed for additional constraints at the interface region that may be tailored to match a particular composite's characteristics. No comparison, however, was given between the models and experimental results. Whilst the assumption of an elastic-plastic interphase may be reasonable for some materials, it is less realistic for MMCs such as SiC/Ti because the interphase is actually brittle. The energy dissipation can be due to friction at the failed interphase rather than plasticity at the interphase zone.

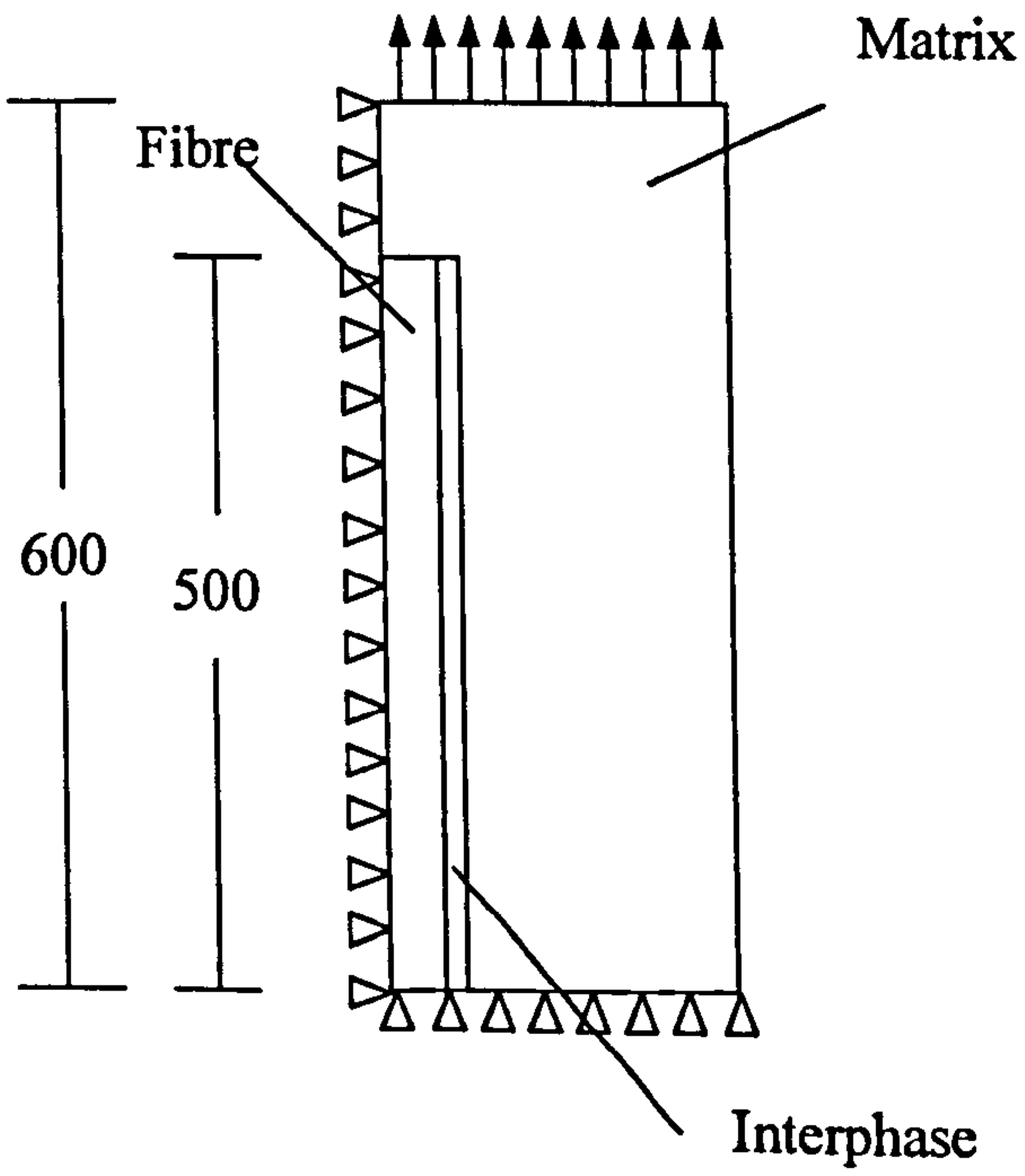

Figure 2.28 *Quarter model for finite element modelling (all dimensions in μm) [61]*

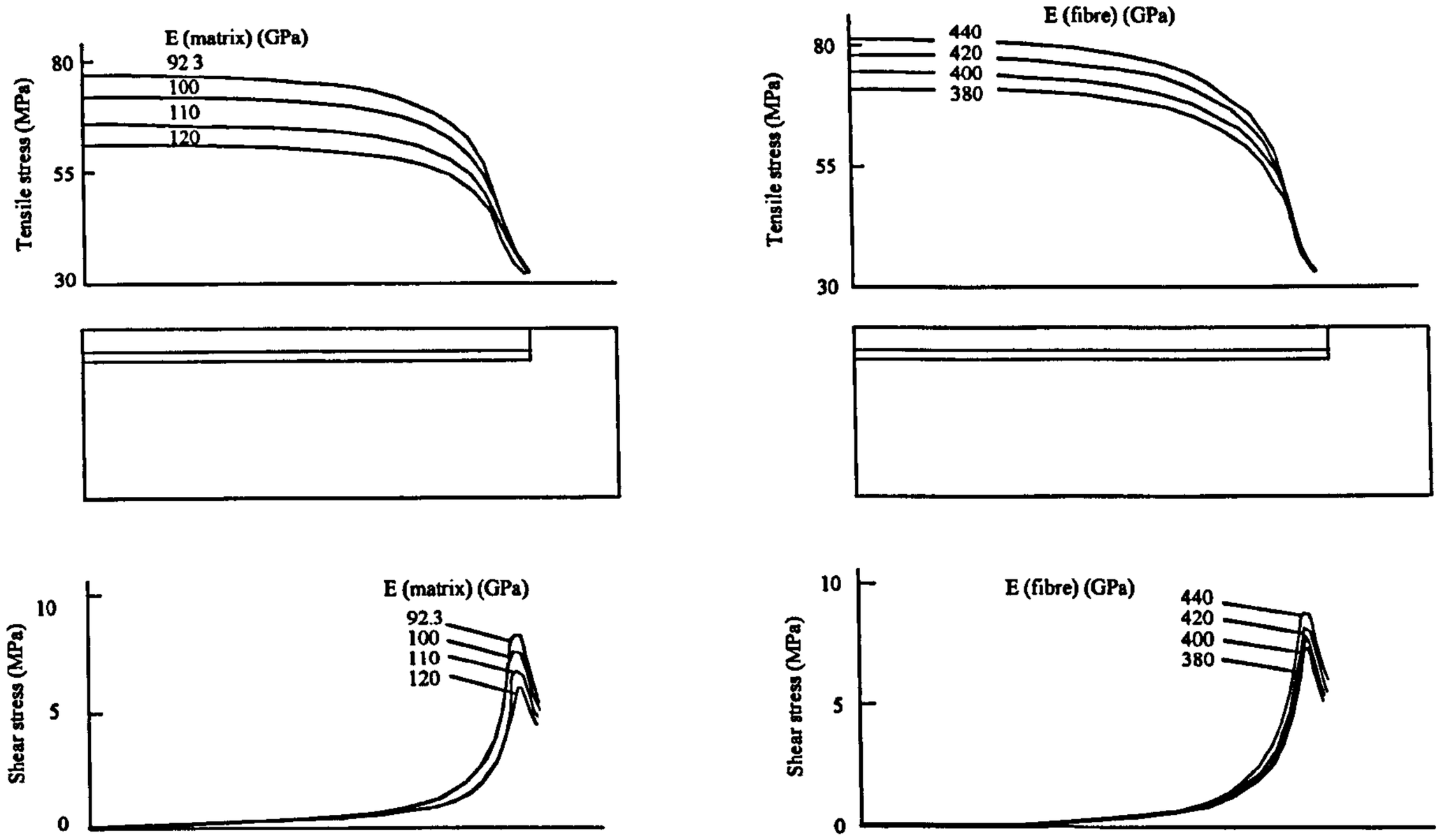

Figure 2.29 *Left: effect of Young's modulus of matrix on the tensile and shear stresses at the interphase.* $E_{intephase}$ *= 360 GPa;* E_{fibre} *= 400 GPa. Right: effect of Young's modulus of the fibre on tensile and shear stresses at the interphase.* $E_{interphase}$ *= 360 GPa;* E_{matrix} *= 92.3 GPa [61]*

Daadbin et al. [61] investigated the stress transfer through the interphase of a Ti/SiC short fibre unidirectional MMC (Figure 2.28). A quarter model of a single 1000 μm SiC fibre embedded in a 1200 μm titanium matrix was constructed using the finite element package *ANSYS*. Between the fibre and matrix was an interphase 5 μm in width with its own mechanical characteristics. The material properties of each constituent in the model were varied to show their effect on load transmission. In the interphase, embedded defects were created by initiating cracks at specific points to demonstrate load transfer; this was achieved by removing elements from the finite element model on either side of the interphase.

Figure 2.29 demonstrates the effect of varying either the matrix or fibre Young's modulus on load transfer. If the fibre Young's modulus were increased, the load to the fibre was also increased, but at the expense of increasing the shear stress at the interphase. Conversely, increasing the Young's modulus of the matrix had the reverse effect, reducing load transfer to the fibre and decreasing shear stress at the interface. The results indicated that for a particular selection of fibre and matrix materials, the maximum value of the shear stress at

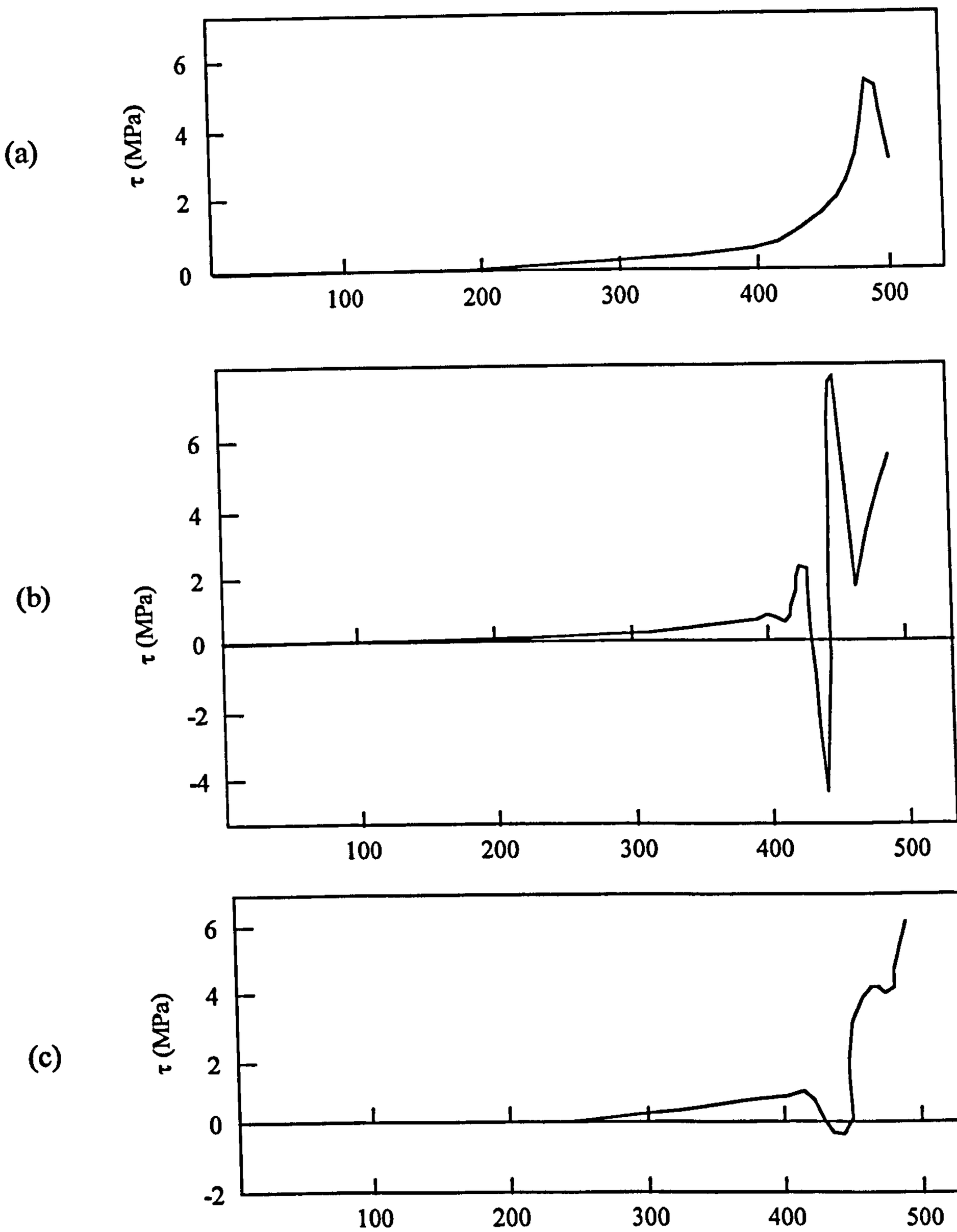

Figure 2.30 *Shear stress distribution along the fibre/interphase interface for (a) perfect interphase, (b) crack at the fibre interphase interface and (c) crack at the interphase/ matrix interface [61]*

the interphase could be reduced with the possibility of an optimum value being obtained. It was also found that the maximum shear stress at the boundary of the fibre/interphase was larger than that at the interphase/matrix boundary. The importance of the fibre/interphase border, was thus emphasised, with the conclusion that the interphase would be more vulnerable on the fibre side.

The embedded defects in the interphase (Figure 2.30) changed the pattern of the shear stresses along the interphase, and if the crack was on the fibre side of the interphase, the shear stress concentration was more severe.

The model of the interphase was only two elements wide, which meant that the tensile and shear stress distributions could only be measured at the interphase boundaries or in the longitudinal middle of the interface. It would have been interesting to see the radial and longitudinal distributions of stresses across the entire interphase, i.e. a surface, using many elements. The cracks initiated in the interphase were not representative of true defects, since they were simply removed elements, and as discussed in Section 2.4 such defects cannot represent the true stress distributions at the crack tips.

2.9 Multiple Failure Mechanisms in MMCs

It is quite clear that although much work has been carried out to study the crack growth mechanisms in composite materials, both analytically and via numerical techniques, most investigations are tailored to study only one particular type of dominant failure mechanism, and usually a crack path must also be assumed in order to model the progression of the damage. In order to gain a more comprehensive understanding of the individual failure mechanisms, and the effect their interaction has on the way a composite fails, a finite element model, which allows for multiple failure mechanisms to occur simultaneously is required.

Bakuckas et al. [62] used a finite element numerical simulation technique to predict crack path and the differing modes of damage for B/Al-5/6061-T6 and SiC/Ti/Ti-6Al-4V MMCs. The simulation incorporated elastic-plastic analysis, micromechanics analysis, failure criteria and a special "node splitting/relaxation" algorithm was developed to simulate the damage evolution in a composite with either linear or non-linear properties.

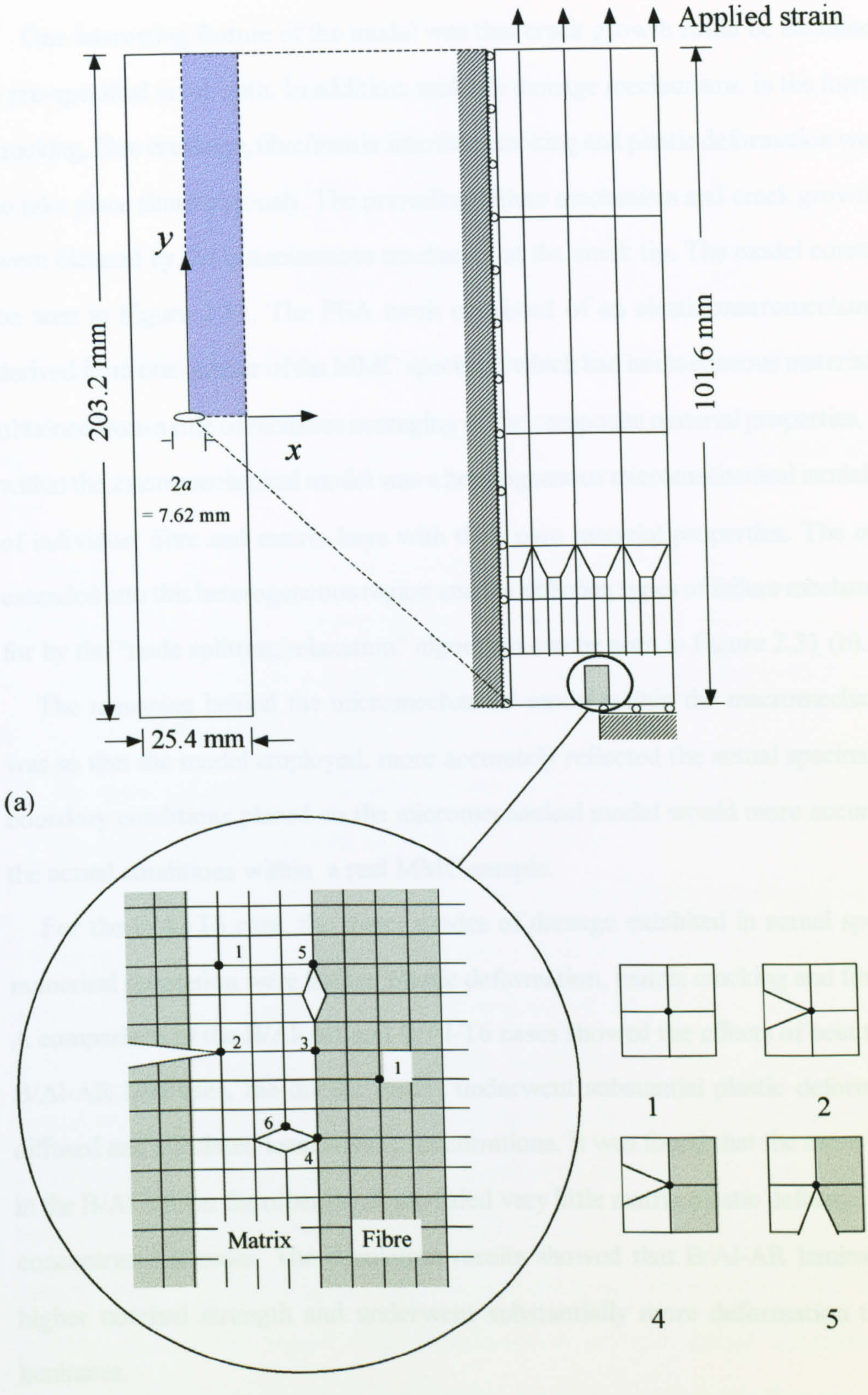

Figure 2.31 *(a) left – shows a centre crack in an MMC sample. Right – shows the quarter model mesh of the composite with homogeneous rule of mixtures properties with the exception of the shaded region which is (b) left – a heterogeneous region containing discrete fibre and matrix bays. Right – the different type of node classifications: (1) interior (homogeneous), (2) crack-tip, (3) interior (heterogeneous), (4) transverse crack-tip, (5) interface crack-tip and (6) surface [62]*

One interesting feature of the model was that crack growth could be simulated without a pre-specified crack path. In addition, multiple damage mechanisms, in the form of matrix cracking, fibre breakage, fibre/matrix interface cracking and plastic deformation were allowed to take place simultaneously. The prevailing failure mechanism and crack growth direction were dictated by the instantaneous mechanics at the crack tip. The model constructed can be seen in Figure 2.31. The FEA mesh consisted of an elastic macromechanical model derived from one quarter of the MMC specimen which had homogeneous material properties obtained from a rule of mixtures averaging of the composite material properties. Contained within the macromechanical model was a heterogeneous micromechanical model, consisting of individual fibre and matrix bays with their own material properties. The centre crack extended into this heterogeneous region and the differing types of failure mechanism catered for by the "node splitting/relaxation" algorithm can be seen in Figure 2.31 (b).

The reasoning behind the micromechanical model within the macromechanical model was so that the model employed, more accurately reflected the actual specimen; thus, the boundary conditions placed on the micromechanical model would more accurately reflect the actual conditions within a real MMC sample.

For the B/Al-T6 case, the major modes of damage exhibited in actual specimens and numerical simulation were limited plastic deformation, matrix cracking and fibre breakage. A comparison of the B/Al-AR and B/Al-T6 cases showed the effects of heat treatment. In B/Al-AR laminates, the ductile matrix underwent substantial plastic deformation which diffused and alleviated local stress concentrations. It was found that the more brittle matrix in the B/Al-T6, on the other hand, provided very little matrix plastic deformation to relieve concentrated stresses. The simulation results showed that B/Al-AR laminates exhibited higher notched strength and underwent substantially more deformation than B/Al-T6 laminates.

For SiC/Ti-6Al-4V, there was good agreement with experimental results, with initial matrix cracking propagating stably to the interface of the first intact fibre and then matrix splitting took place, causing the crack to turn and propagate along the interface; after propagating approximately the length of one fibre diameter the crack turned horizontal

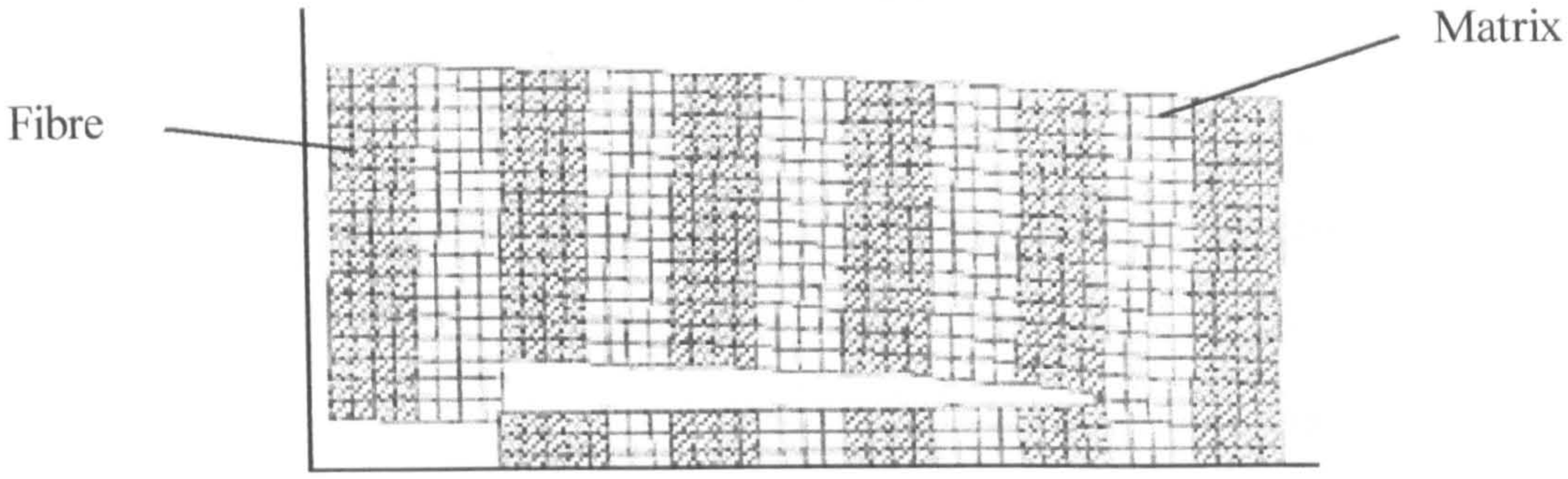

Figure 2.32 *Final simulated damage stages of SiC/Ti-6Al-4V [62]*

again and continued to propagate in mode I through the composite until total failure (Figure 2.32).

Despite some good experimental correlation, there were differences between the simulated and experimental results. These could be attributed to several factors:

i. a plane stress analysis was performed, which ignored through-the-thickness variables
ii. a perfect fibre/matrix interface was assumed and,
iii. the statistical nature and inherent variability in constituent properties made it difficult to obtain reliable values for the material properties.

To conclude the modelling review, analytical models offer a relatively simple means for obtaining the overall macroscopic response of composite materials, but lack the ability to give detailed information on the micromechanical behaviour of the material, which ultimately governs the failure mechanisms. Conversely, numerical techniques such as FEA are able to retain the individual constituent material phases, and by concentration on the smallest fully informative, repeating, segment, the resolution of internal loads and deformations, and behaviour of defects such as microcracks can be obtained. However, most FEA models to date are usually limited to predicting one specific failure mechanism. What is required is a comprehensive FEA model which incorporates multiple failure mechanisms for both monotonic and cyclic loading and which can be constructed using the currently commercially available analysis tools. By predicting the mechanical behaviour of many differing composite material combinations it will thus be possible to optimise its macroscopic behaviour, by choosing a given combination of constituent materials for a given task.

2.10 Fatigue Crack Growth of Composite Materials

Metal matrix composites are popular materials to use in the aerospace industries where weight savings lead to fuel cost savings. Where a composite is to be used in a safety-critical situation, as part of a wing structure, or an engine component working at elevated temperatures for instance, it is important to know its fatigue behaviour.

Composites exhibit complex failure behaviour under cyclic loading compared to homogeneous materials. Fatigue damage tends to consist of various combinations of matrix cracking, debonding, delamination crack growth, and fibre breakage. In an homogeneous material, for example, crack growth plays a key failure rôle; in composite materials cracks and failure zones may be formed in the very first few cycles, and indeed there are often defects such as microcracks in the material before cycling even begins.

Cotterill and Bowen [63, 64] found that, for an unidirectionally reinforced, SCS6/Ti-15-3 metal matrix composite, subjected to three-point bending, after an initial period of relatively fast crack growth, fatigue crack propagation rates diminished as the length of the matrix crack increased. This effect was explained by the concept of fibre bridging, whereby intact fibres in the wake of the growing crack bore much of the applied load, thus reducing the effective nominal stress intensity factor, ΔK [65], at the crack tip. With no fibre breakage, as the matrix crack grew, more intact fibres were left in its wake. Thus ΔK, and hence crack growth rate, either continued to diminish or reached a steady state value. Cotteril and Bowen [66] further investigated the fatigue crack growth properties, at ambient and elevated temperatures, of a long-fibre, unidirectionally reinforced, SCS6/Ti-15-3 metal matrix composite. The aim of this work was to assess effects of varying the test temperature, and load range on the aforementioned bridging mechanism. A point of particular interest was whether the deceleration of crack growth, observed in their previous work, noted at low cycling frequencies, would continue until complete crack arrest.

The SCS6/Ti-15-3 metal matrix composites used for the experimental work were bend bars of dimension 2 × 4 × 70 mm, cut from large 2 mm thick plates, with the fibres oriented as shown in Figure 2.33. Fibre diameter was ~ 140 μm and centre-to-centre spacing of the fibres was ~ 180 μm. The approximate fibre volume fraction was 33%. Each of the specimens

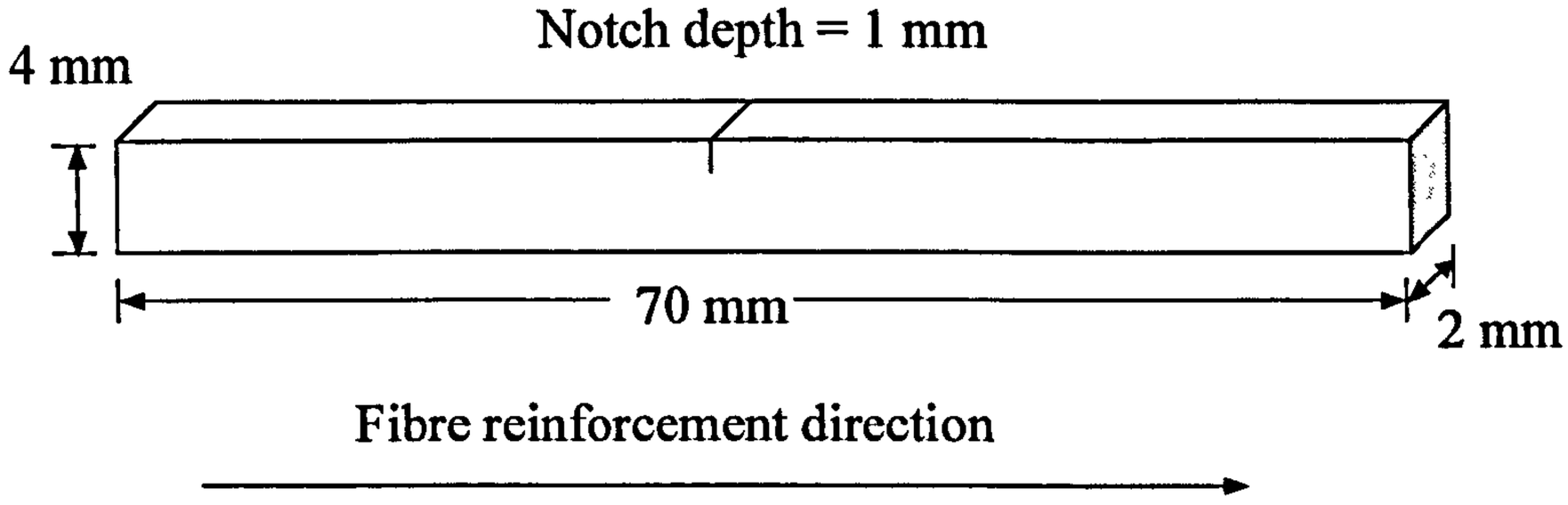

Figure 2.33 *Schematic of single-edge notched bend specimen [66]*

was notched half way along its length to an approximate depth of 1 mm using *electrical discharge machining* (EDM), thus allowing fatigue crack to be grown perpendicular to the direction of the reinforcement. During testing, the specimens were surrounded by an environmental chamber, allowing crack growth rates to be measured at temperatures of up to 700°C. Each test used a constant load range, ΔP = 105 N, initial ΔK = 16 MPa $m^{1/2}$, and at temperatures, 25, 200, 350 and 500°C. The frequencies of fatigue used were 0.5, 2 and 10 Hz.

Figure 2.34 shows fatigue crack growth data from tests performed on the composite at

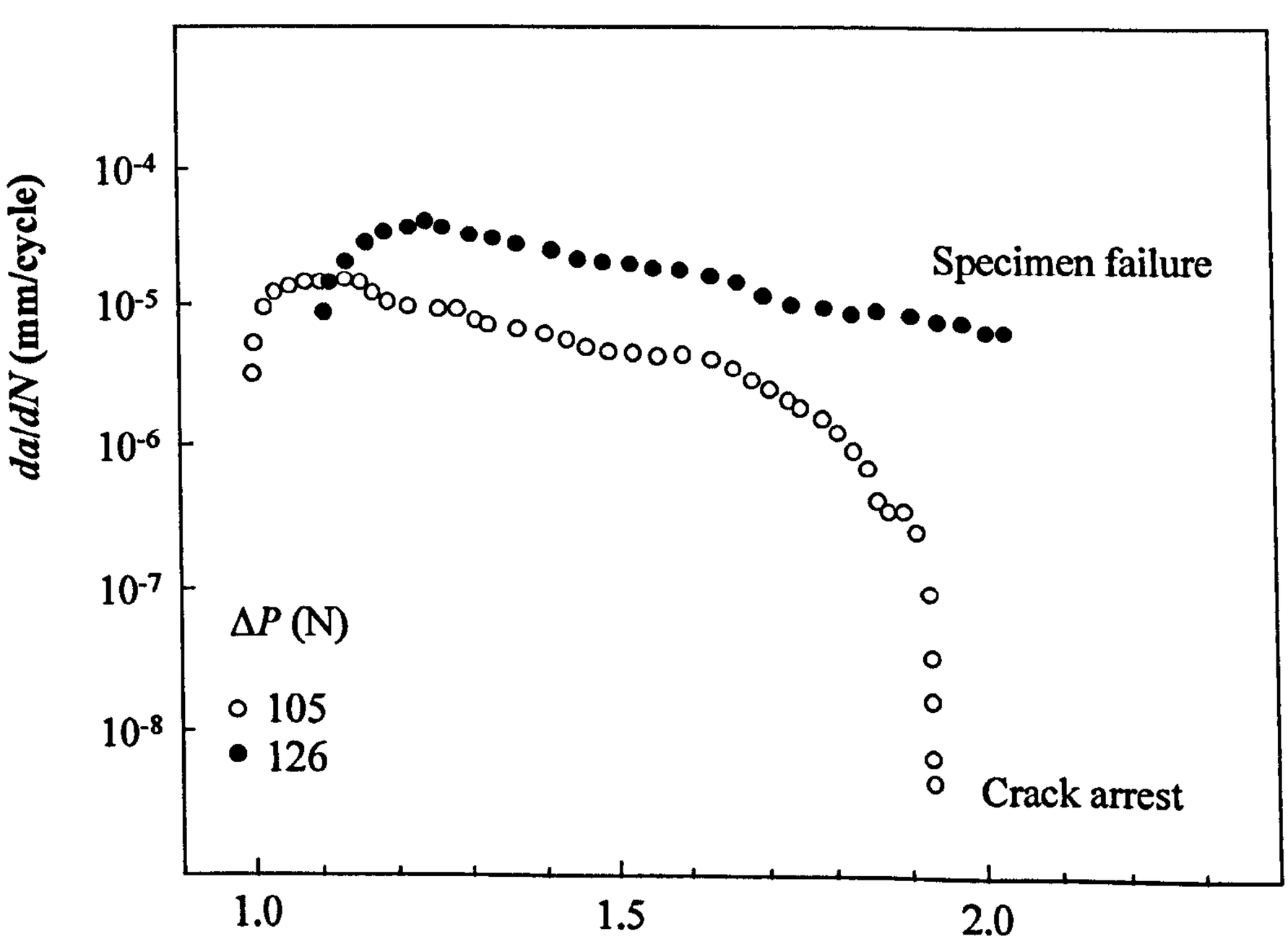

Figure 2.34 *Effect of changing applied load on fatigue crack growth rates in the SCS6/ Ti-15-3 composite at 25°C and a frequency of 10Hz [66]*

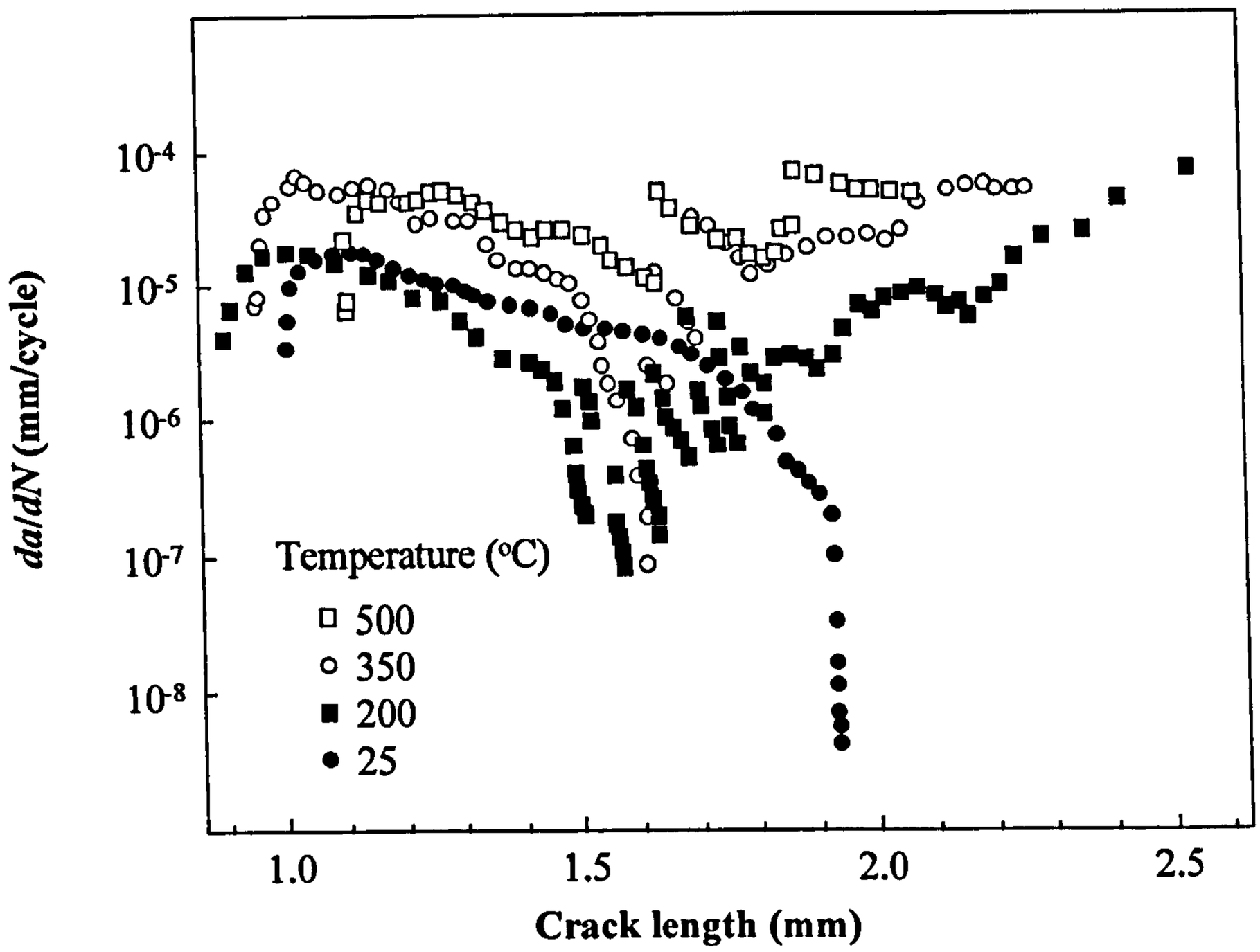

Figure 2.35 *Fatigue crack growth rates measured in the SCS6/Ti-15-3 composite at 25 °C, ΔP = 105 N and at a frequency of 10 Hz [66]*

room temperature with a frequency of 10 Hz. At ΔP = 105 N (initial ΔK = 16 MPa $m^{1/2}$) crack growth rates were initially high, but as the crack propagated, fell until zero crack growth at approximately 200,000 Hz, after 0.93 mm of growth. For a higher load range of ΔP = 126 N (initial ΔK = 19.2 MPa $m^{1/2}$) there was less crack deceleration and the specimen failed when the crack reached a total length of 2.03 mm.

It was observed that (Figure 2.35) after crack arrest, an increase in ΔP sufficient to break one or more bridging fibres caused a resumption in crack growth.

At elevated temperatures (200–500°C) it was found that crack deceleration was interrupted by discrete events of fibre failure which caused instantaneous rises in *da/dN*, preventing crack arrest, this together with a temperature-enhanced matrix fatigue crack growth rate resulted in a shorter specimen lifetime (Figure 2.36).

More recent fatigue work by Cotterill and Bowen [67] compared tension-tension loading of Ti-15-3/SCS-6 to previous data [63–66] for the same composite using three-point bending. A significant difference in crack growth behaviour between the two types of test was initially demonstrated, Figure 2.37. However, examination of the nominal stress intensity at the

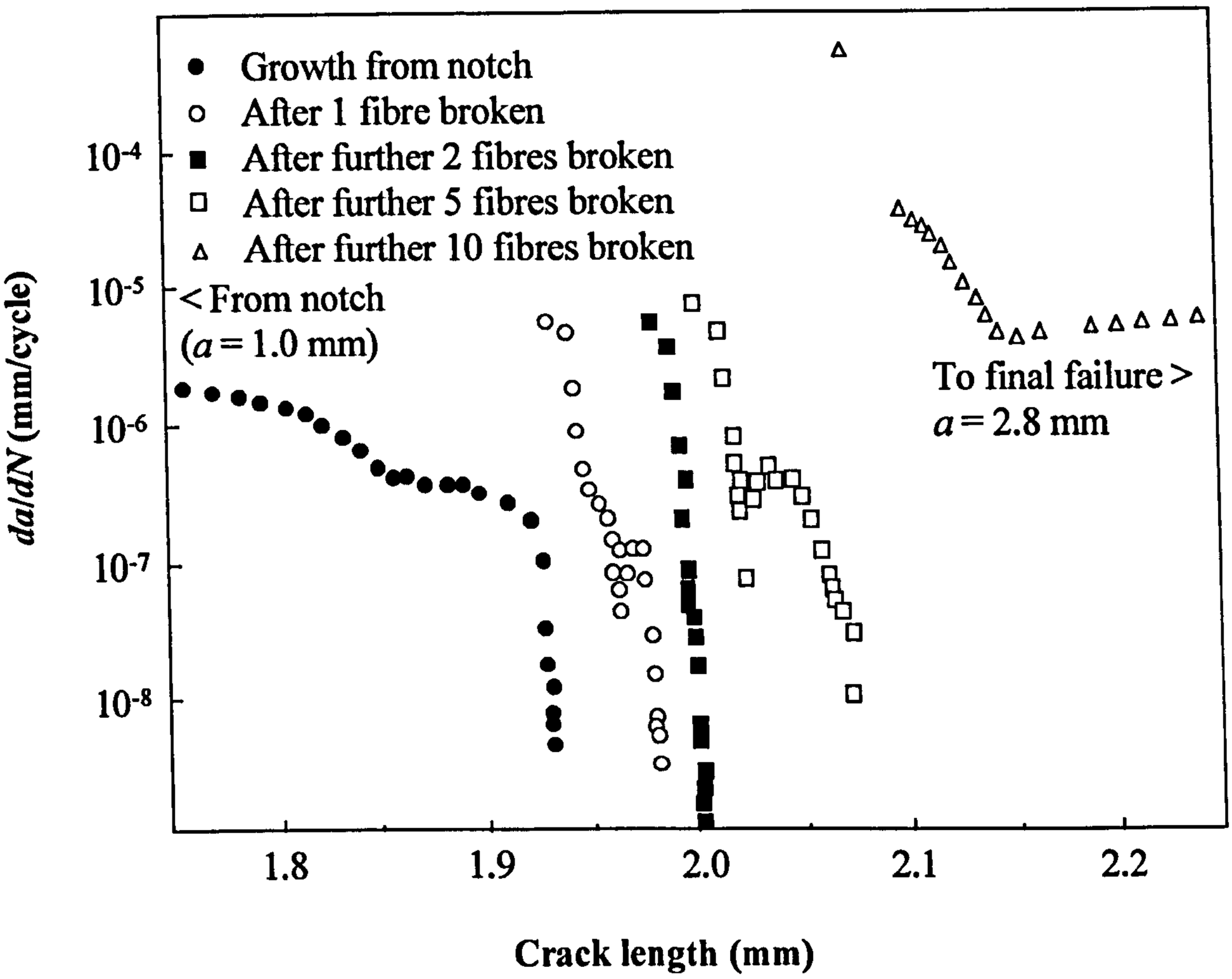

Figure 2.36 *Effect of changing temperature (200–500 °C) on fatigue crack growth rates in the SCS6/Ti-15-3 composite with ΔP = 105 N and at a frequency of 10 Hz [66]*

crack tip, ΔK, for tension-tension specimens showed a more rapid increase in ΔK than that for three-point bending. It transpired that the difference in ΔK between the two types of test was due to differing compliance functions for the two configurations. The compliance effect was removed by simulating the change in ΔK for one configuration so as to match that experienced using the other. This required a careful load shedding procedure to be used during tension-tension testing, in order to simulate the slower increase in applied ΔK with crack length, which occurs under three-point bending, and conversely, a load increase procedure was used during three-point bending in order to simulate the faster increase in applied ΔK with crack length which occurs under tension-tension loading.

It was then found that there were no major mechanistic differences between crack growth under the two loading configurations with the effects of load range and temperature being similar in each case (Figure 2.37).

However, it was discovered that the dimensions of the specimen had a marked effect on the fatigue crack growth resistance. In monolithic materials, changing the width W of the

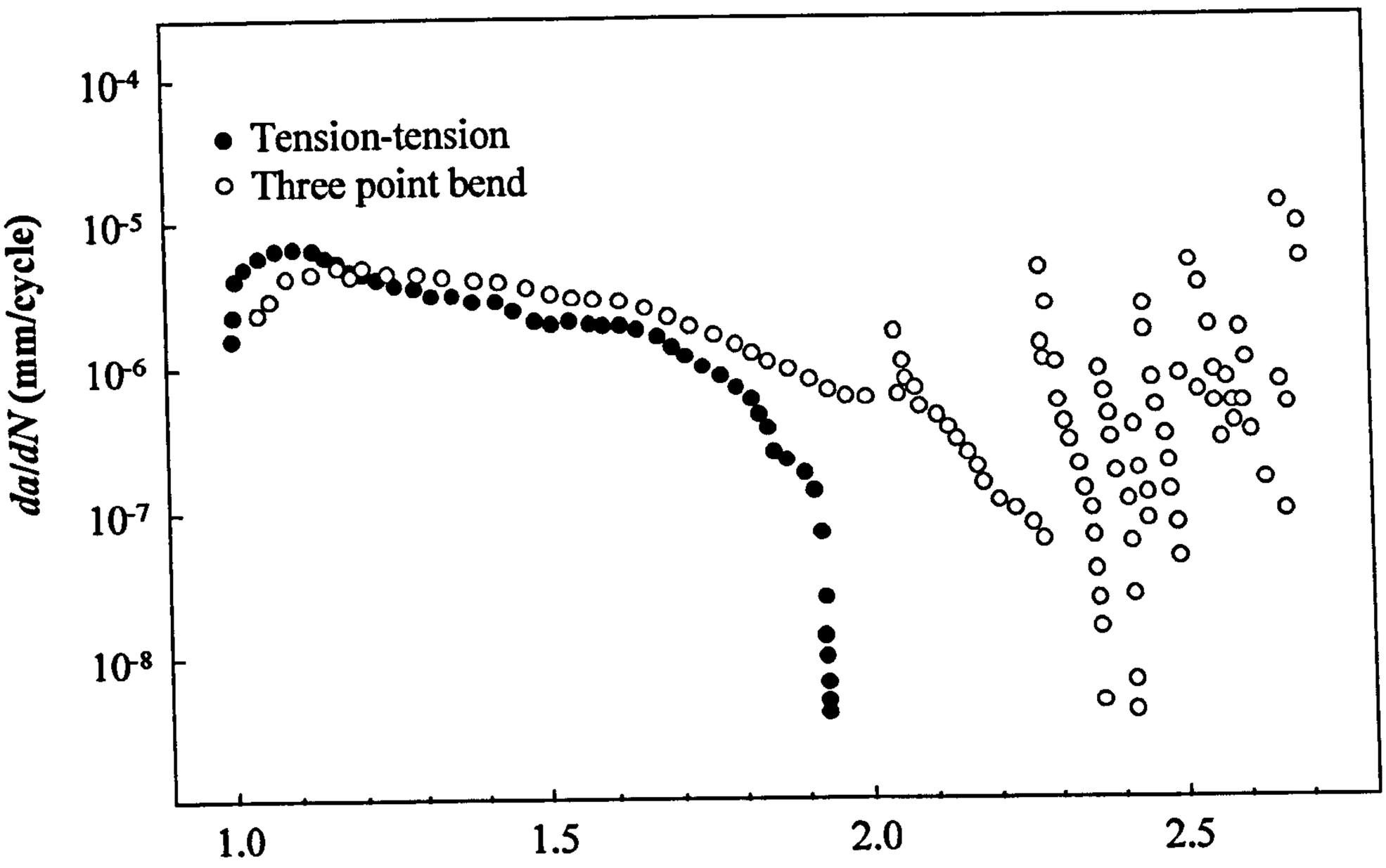

(a)

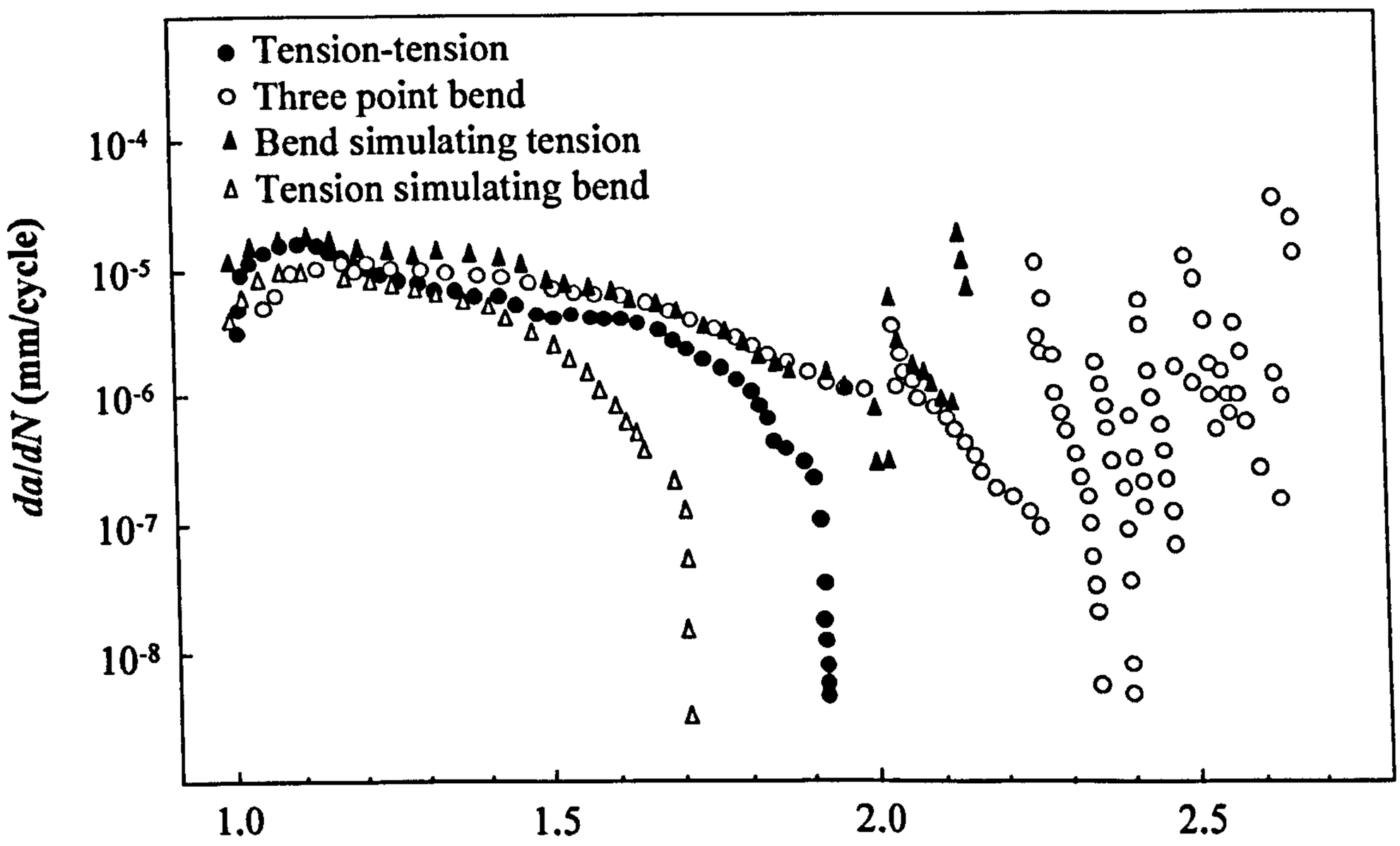

(b)

Figure 2.37 *(a) Fatigue crack growth rates da/dN measured in tension-tension and three point bending in SCS6/Ti-15-3 composite at 25 °C: initial stress intensity range $\Delta K = 16\ MNm^{-3/2}$, and (b) with compliance simulation test superimposed [67]*

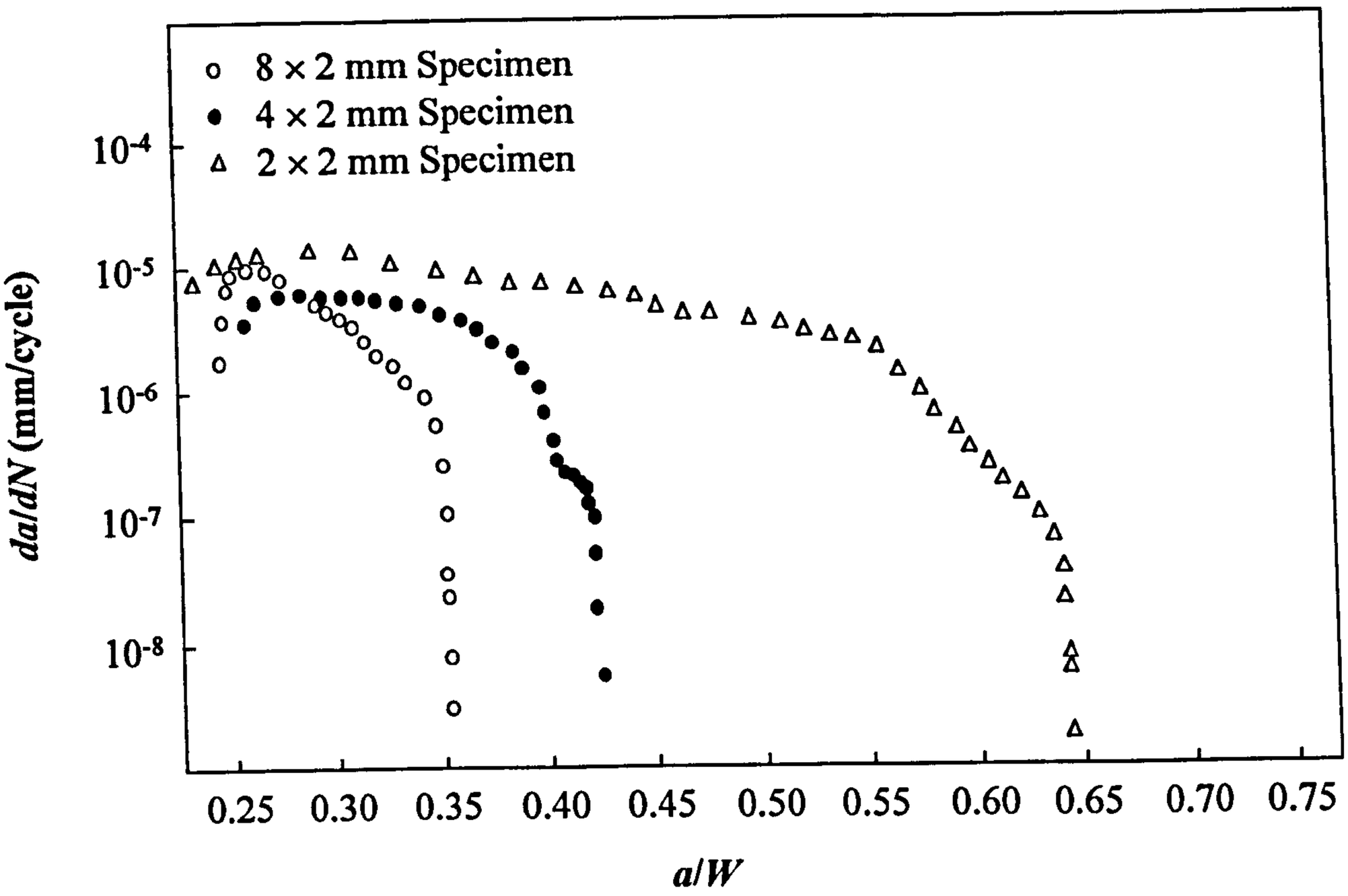

(a)

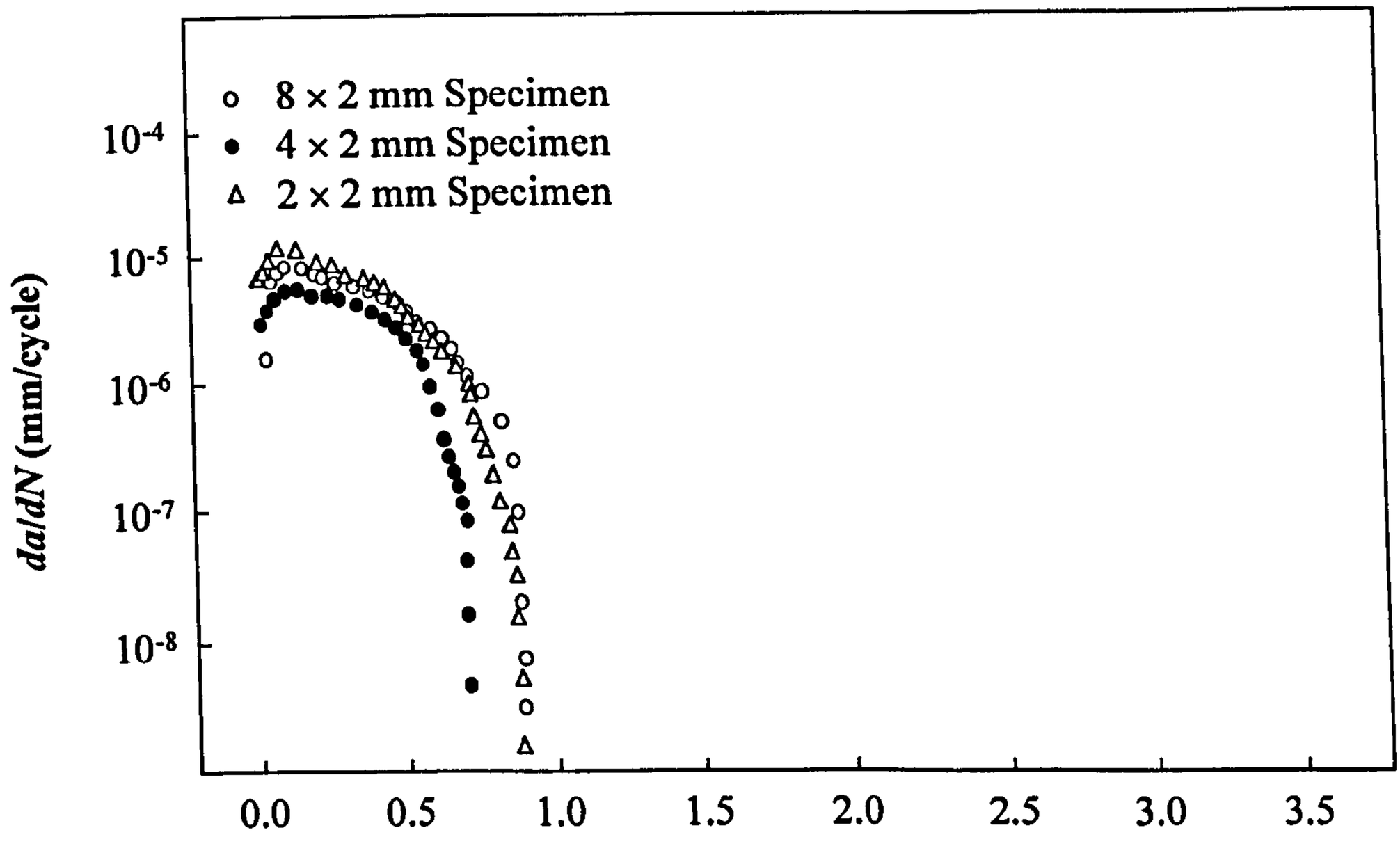

(b)

Figure 2.38 *Fatigue crack growth rates da/dN measured in test pieces of different dimensions versus (a) crack length/specimen width a/W, and (b) extension in crack length beyond the notch, Δa, in SCS6/Ti-15-3 composite at 25 °C: initial ΔK = 13.3 $MNm^{-3/2}$ [67]*

specimen would have little effect on crack growth rates, if they were compared at the same values of applied ΔK. On comparing crack growth rates for specimens of width 8.0, 4.0 and 2.0 mm it was apparent (Figure 2.38) that crack growth rate was more strongly dependent on the distance that the crack had grown away from the notch Δa than a/W (and hence nominal ΔK). There was a very close correlation between da/dN and Δa in the early stages of crack growth, where a specimen failed. For those specimens where the crack arrested, the absolute crack lengths were very similar, the crack having grown past three rows of fibres in each case. The lack of relationship between da/dN and a/W (Figure 2.38 (a)) was a reflection on the importance of the rôle of fibre bridging in resisting crack propagation. The crack growth rates up until either arrest or the incidence of the first fibre failure, were determined by how far the crack had propagated from the initial notch and hence the number of bridged fibres, regardless of the nominal applied ΔK (different at arrest for each specimen size).

The size of the specimen thus determined the fatigue crack growth resistance, with the smaller test pieces having lower crack growth resistance.

2.11 Effects of Seawater Absorption on Fatigue Crack Growth in MMCs

Table 2.2 *Comparison of material properties [68]*

Material	SG	Fibre volume fraction (%)	Young's modulus (GPa)	Compressive yield stress (GPa)	Specific Young's modulus (GPa)	Specific compressive strength (GPa)
Steel HY80	7.8	-	207	550	27 (1)	71
Steel HY130	7.8	-	207	890	27 (1)	114
Aluminium[1]	2.8	-	70	390	25 (0.9)	139
Titanium[2]	4.5	-	110	830	24 (0.9)	184
GRP[3]	2.1	67	50	1000	24 (0.9)	476
CFRP[4]	1.7	67	170	1000	100 (3.7)	588
MMC[5]	3.2	50	230	3000	72 (2.7)	937

Values in paranthesis are normalised with respect to HY80

[1]L65 alloy
[2]6-4 STOA alloy
[3]Glass fibre reinforced plastic (filament wound S glass epoxy)
[4]Carbon fibre reinforced plastic (filamen wound HS carbon epoxy
[5]UD alumina/6061 aluminium

Although MMCs have been predominantly used for the aeronautical industries, they continue to find new uses. Recently, there has been growing interest in the use of both short and continuous fibre metal matrix composites (Al_2O_3/Al6061) in marine applications [68]. Because of their exceptionally high specific strength (see Table 2.2) MMCs have considerable advantages over the traditional steels used in both surface and sub-surface craft. For instance, MMCs can be used in submarines, for the primary pressure hull and also in secondary structures such as casings, fins, control surfaces, internal decks and bulkheads. As an example, a weight reduction of greater than 50% could be achieved by substituting MMCs for steel in a submarine pressure hull, which in naval vehicles could mean extra stealth and survivability. Also, MMCs allow for an increase in diving depth, in some instances up to six times that of a steel pressure hull (see Figure 2.39).

Clearly, the effects of immersion in seawater, on the fatigue crack behaviour of MMCs is an important characteristic to be studied.

Sloan and Seymour [69] studied the effects of seawater exposure on the mechanics of

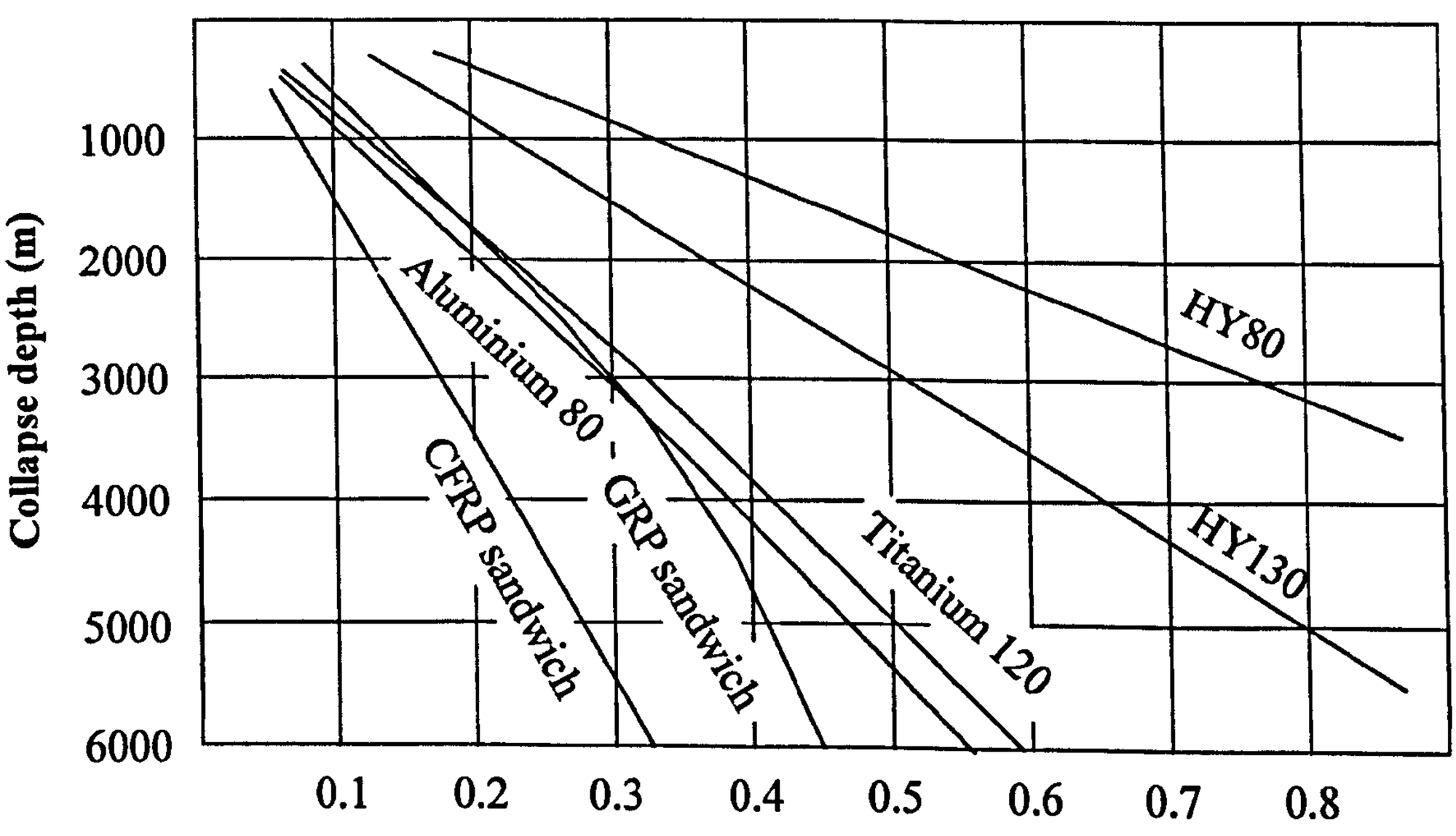

Figure 2.39 *Collapse depth vs pressure hull weight/displacement ratio for materials in Table 2.2 [68]*

mode I fracture and crack growth in a unidirectional AS-4/3501 graphite epoxy composite using a compliant load frame technique (Figure 2.40). Specimens were conditioned in either seawater or air by being loaded in crack-opening mode I, statically for 60 days or in fatigue for 30 days. In the static load conditioning, specimens were loaded in a fixed-displacement load-frame until audible and visible crack extension occurred. The specimens were then loaded in the compliant load frame and fatigued at 0.5 Hz with a load ratio (min. load/max. load) of 0.5. The crack length and applied load were periodically monitored, with crack length being measured relative to reference marks on the specimens using a 7 × optical loupe.

It was found that the primary effect of seawater was to weaken the fibre-to-matrix bond in the composite. The mechanisms that caused this weakening was suggested to be micro-scale fibre debonding resulting from a moisture-weakened fibre-to-matrix bond; moisture proceeded the advancing crack tip by "wicking" along the fibre/matrix interface, rather than by diffusion through the matrix. Fibre debonding and bridging would begin just ahead or behind the crack tip region, and during crack growth bridged fibres could extend well

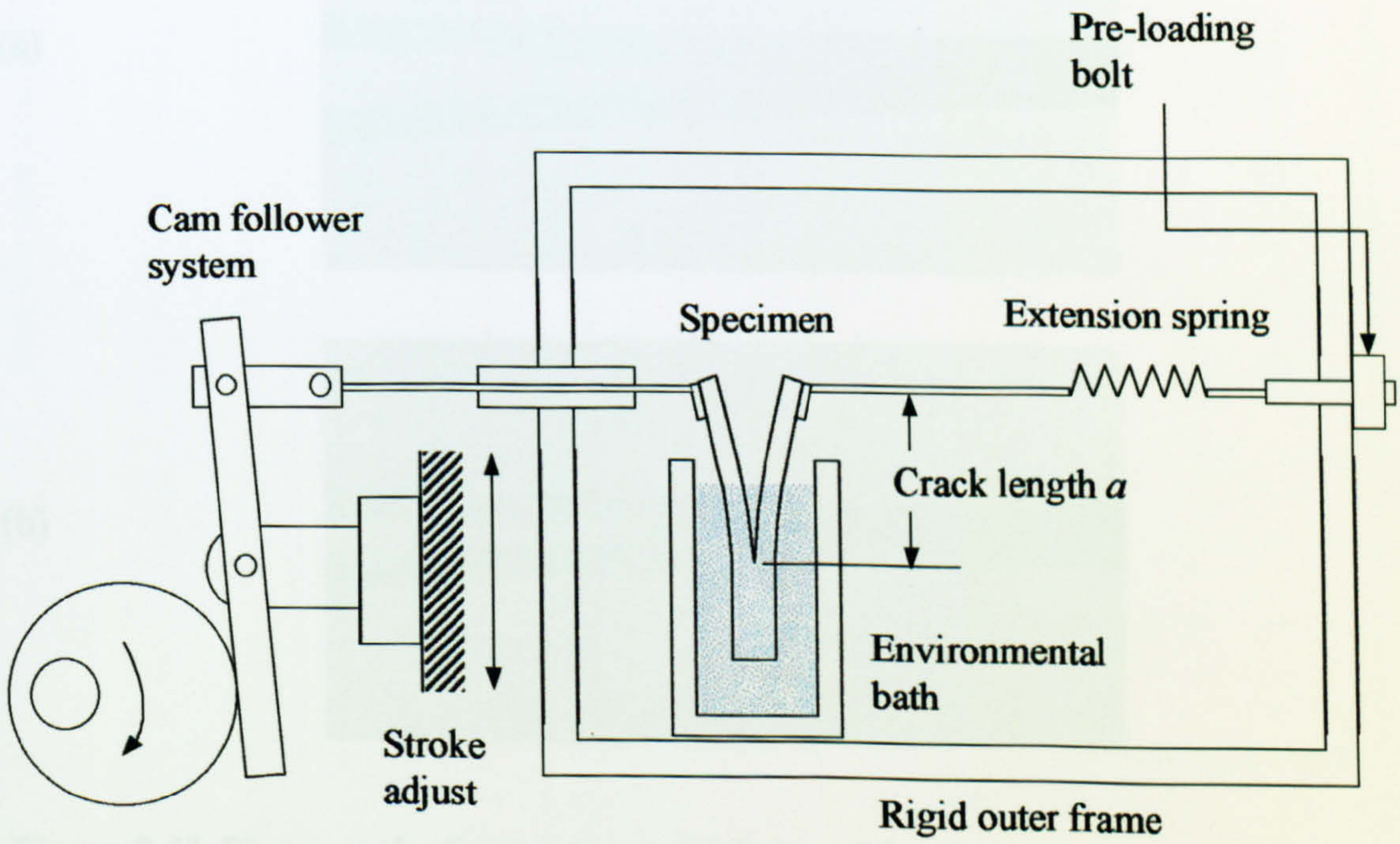

Figure 2.40 *Compliant load-frame used with a cam-follower system for fatigue crack growth [69]*

behind the crack tip in the immersed portion of the specimen (Figure 2.41).

The fibre bridging increased the fracture resistance of the specimens and reduced the rate of crack growth to near zero (Figure 2.42). There was no indication, however, that any components of the seawater, other than the water itself, played a part in the experimental results.

There is, to date, little published data on fatigue behaviour of the continuous reinforced Al_2O_3/Al6061 composites MMCs subject to seawater immersion.

In conclusion, failure mechanisms in composite materials, whether under static or fatigue loading, are difficult to predict. Models which do attempt to predict failure mechanisms tend to be over-simplistic, if attempted analytically, and/or tend also to concentrate on one particular failure mechanism to the exclusion of all others. What is required is an investigation into a comprehensive way of modelling composite materials which can incorporate multiple failure mechanisms in both static and fatigue loading situations.

The data from such models should then be compared to composites failed in monotonic

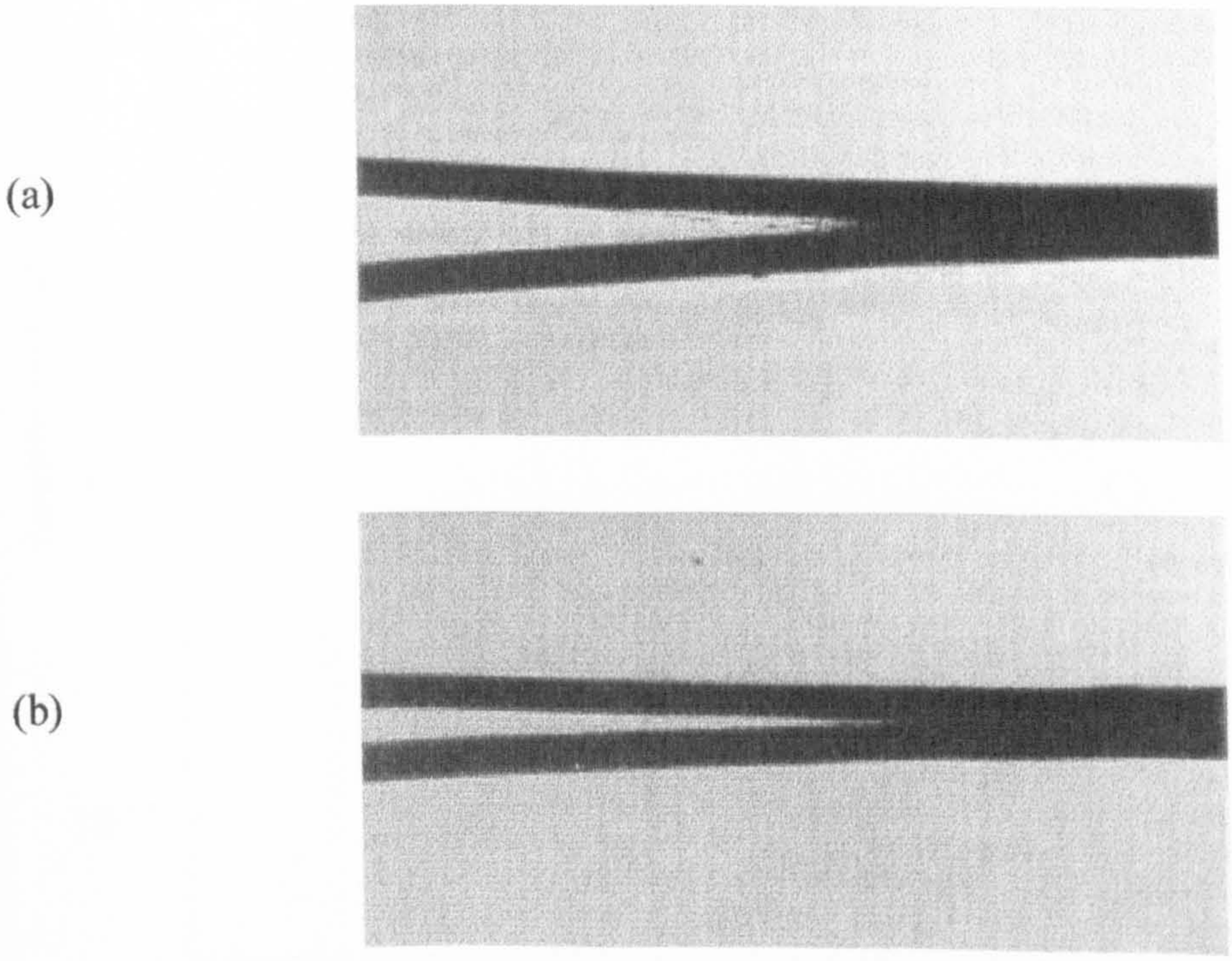

Figure 2.41 *Photograph of a specimen, (a) fatigued for 6 months in seawater. A control specimen (b) (static fracture in air) is also shown. The photographs were taken just prior to fracture and show extensive fibre bridging having occured during the seawater fatigue experiment. There is much greater deflection in the seawater specimen illustrating the increase in fracture resistance accompanying fibre bridging [69]*

loading for verification purposes.

On the experimental side, fatigue properties of composites such as Al_2O_3/6061 should be investigated in air and environmental conditions such as seawater exposure, and in the long-term, models of the environmental behaviour of these composites should be constructed, using simulation techniques, in order to optimise the composite's suitability for a given task.

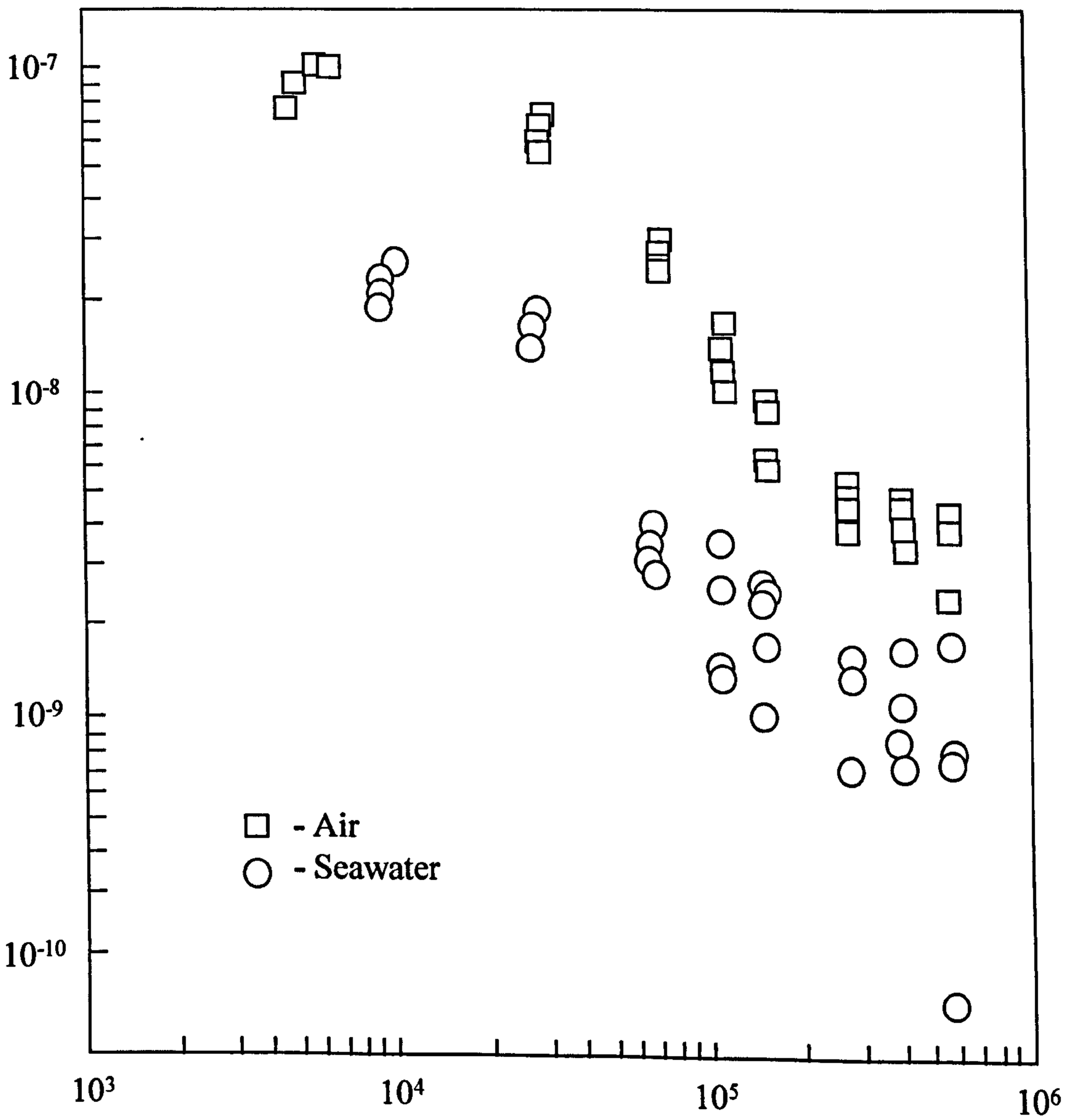

Figure 2.42 *Crack growth rate versus number of cycles for samples fatigued in air and seawater [69]*

3 Introduction to Theoretical and Experimental Work

The literature review presented in Chapter 2, Sections 2.2 to Section 2.8 pertaining to the current status of the ability to model failure mechanisms in MMCs has highlighted the complex nature of the mechanical interactions between the reinforcing fibres and the matrix in which they are situated. The main shortcomings of modelling failure mechanisms include:

i. Studies based purely on analytic closed-form models tend to be over-simplistic, due to geometrical constraints, and do not address the micromechnical behaviour of the composite well enough to predict, in a satisfactory manner, the macroscopic behaviour.

ii. Models which do address the composite micromechanical behaviour, but which involve deriving the governing equations to suit individual model composite geometries and load cases, using numerical solutions, e.g. finite difference methods, tend to be time consuming to construct, difficult to alter due to their complexity, and can usually only predict one type of failure mechanism.

iii. By far the most popular method of modelling composite behaviour, the finite element method, is usually also limited to predicting one specified failure mechanism and is more suited to predicting the behaviour of homogeneous materials, where typically one mode of failure dominates; unlike composites, which frequently fail in several modes simultaneously.

The current situation can be summarised by stating that it is relatively easy to incorporate one type of failure mechanism into a model, but real materials do not generally fail soley in one mode, but suffer failure through several interacting mechanisms, e.g. mode I crack propagation, delamination and fibre bridging. Much research has been carried out investigating individual failure mechanisms, but a more realistic approach to predicting failure in these materials is to incorporate multiple failure mechanisms occurring simultaneously, and interactively on the composite.

Limitations in predicting failure mechanisms in MMCs are such that only approximation to failure in actual use can be determined. A manufacturer of composites wishing to construct a new material has, at present, to work largely from the properties of the constituent materials and previous experience. A model which is capable of predicting macroscopic behaviour

from the constituent materials and working at the micromechanical level, will give a manufacturer an invaluable tool to test new material combinations before any expensive manufacturing processes are involved.

Considering these problems and limitations, the present programme of modelling and experimental work has been designed to use the concept of simulation, in particular, the simulation of composite materials failing in several modes. Before simulation can begin however, the way stress distributions surround an embedded defect in a single fibre model of a MMC have to be investigated. The first stage of the programme compares the differing methods of introducing an embedded defect into the reaction zone of a fibre/matrix composite and the best ways of determining the stress intensity factors at the crack tips.

Section 2.4 considered a method of incorporating cracks into a finite element composite model by element removal, this relatively simple method of introducing embedded defects will be tried and compared to the more sophisticated method in Sections 2.5 to 2.7 where the local stress distribution around a crack tip using a "quarter point" method was derived. Section 2.8 introduced the concept of multiple phase modelling in FEA and this form of modelling will be used to study stress distributions around an embedded defect in the fibre/ matrix interphase, using both conventional and modified finite elements.

The second stage of the programme is to build a simulation of a fibre/matrix composite system which incorporates several fibres, in order to judge how the differing failure mechanisms interact. Methods described in Section 2.9 will be modified and used with a commercial finite element programme to create the simulation. Data gathered from the first stage of the programme can be incorporated at this stage.

Experimental work, involving composites failing under cyclic loading will be carried out, as described in Sections 2.10 and 2.11. Environmental tests with Al_2O_3/6061 composite materials being fatigued in seawater will be conducted and the experimental data compared to the same materials fatigued in air under identical loading conditions.

Data from the fatigue crack growth experiments could be used to aid the construction of models which simulate fatigue crack growth.

4 Modelling and Experimental Methods

4.1 Introduction

This chapter describes the experimental methods used in this programme of studies. The chapter is presented in seven sections. After the introduction, Section 4.2.1 deals with finite element analysis of MMCs, while Section 4.2.2 considers finite element analysis simulation. Section 4.3.1 deals with MMC sample preparation. Sections 4.3.2 concerns fatigue crack growth of the specimens. Finally, fractographic analysis of MMC specimens are dealt with in Section 4.3.3.

A network analysis diagram (Figure 4.1) shows the structure of the current work programme together with possible future work.

4.2 Modelling

4.2.1 Finite Element Analysis of MMCs

Using an HP 9000 model 712/80 workstation, finite element analysis was carried out on unidirectional short fibre metal-matrix composites. The composite's mechanical properties are given in Table 4.1 Two FEA packages were utilised for the modelling. First the Engineering and Mechanical Research Corporation software *Display 3* (version 92) was used for mesh creation and post-processing, *Nisa 2* was used for solving, and stress intensity calculations were performed using *Endure*.

The second package, the Rasna Corporation *Applied Structure* (version 11), was used for meshing, solving and post-processing. Stress intensity factor calculations were included

Table 4.1 *Material properties of short fibre composite*

	Young's modulus (GPa)	**Poisson's ratio**
Fibre	400	0.25
Interface	360	0.34
Matrix	68.9	0.36

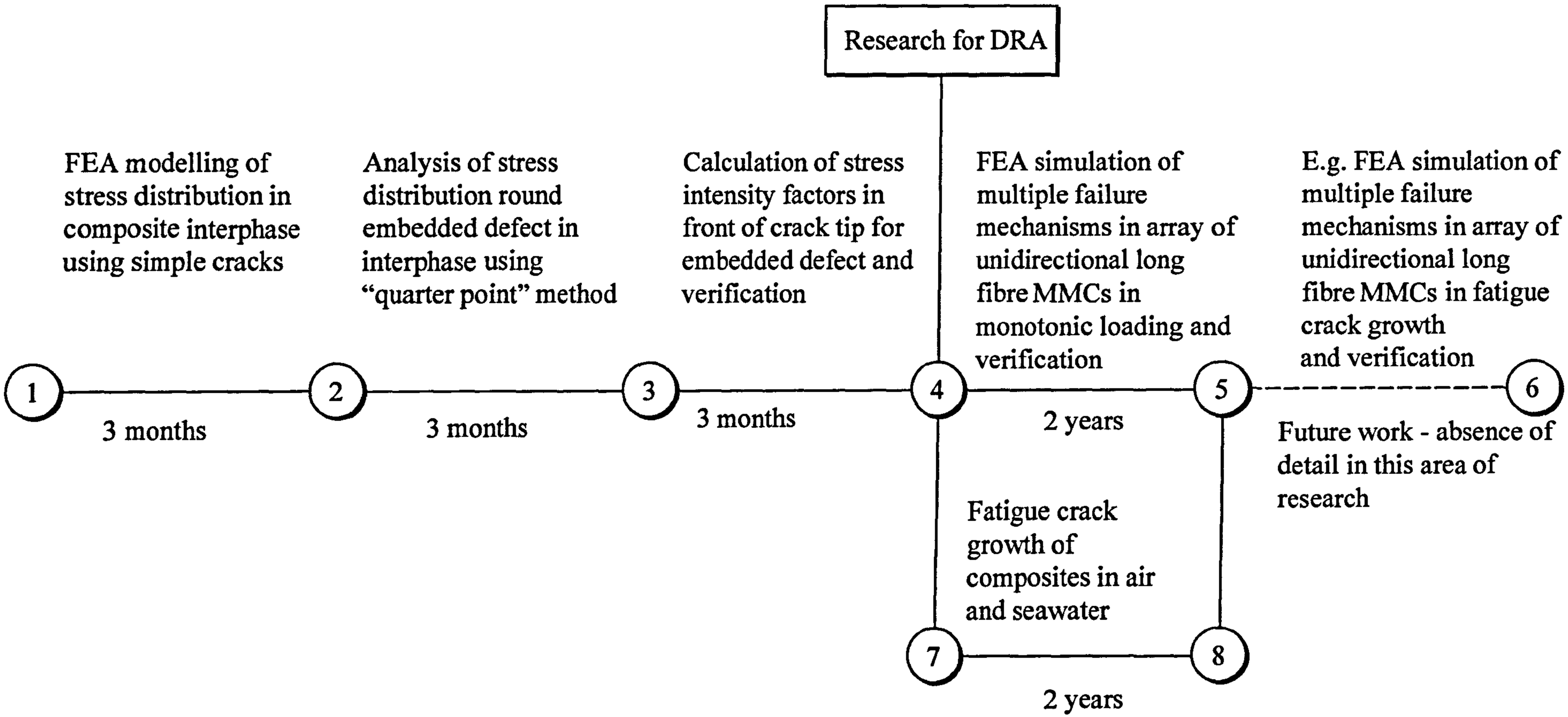

Figure 4.1 *Network analysis of current and future work*

Table 4.2 *Material properties of MMCs*

Material		Young's modulus (GPa)	Poisson's ratio
Fibre	Al_2O_3	210.0	0.3
Matrix	CPAl	68.9	0.33
	6061	68.0	0.33

in the model run by use of "Design Variables" to model an embedded defect in the fibre/ matrix reaction zone.

4.2.2 Finite Element Analysis Simulation

To simulate mode I crack propagation, debonding and fibre bridging, in long fibre unidirectional MMCs, simultaneously and in real time, the Hibbit Carlson & Sorensen FEA package *ABAQUS* (version 5.6) was used, again using the HP 9000 workstation. Fibre/ matrix interface bonding was modelled using contact surfaces. Two differing MMC specimens were modelled – their material properties are listed in Table 4.2.

4.3 Experimental

4.3.1 Sample Preparation

Samples of Al_2O_3/CPAl and Al_2O_3/6061 of size 110 × 7 × 7 mm were prepared from 110 × 80 × 8 mm thick plates, supplied by DRA, using the Buehler KrautKramer Isomet 2000

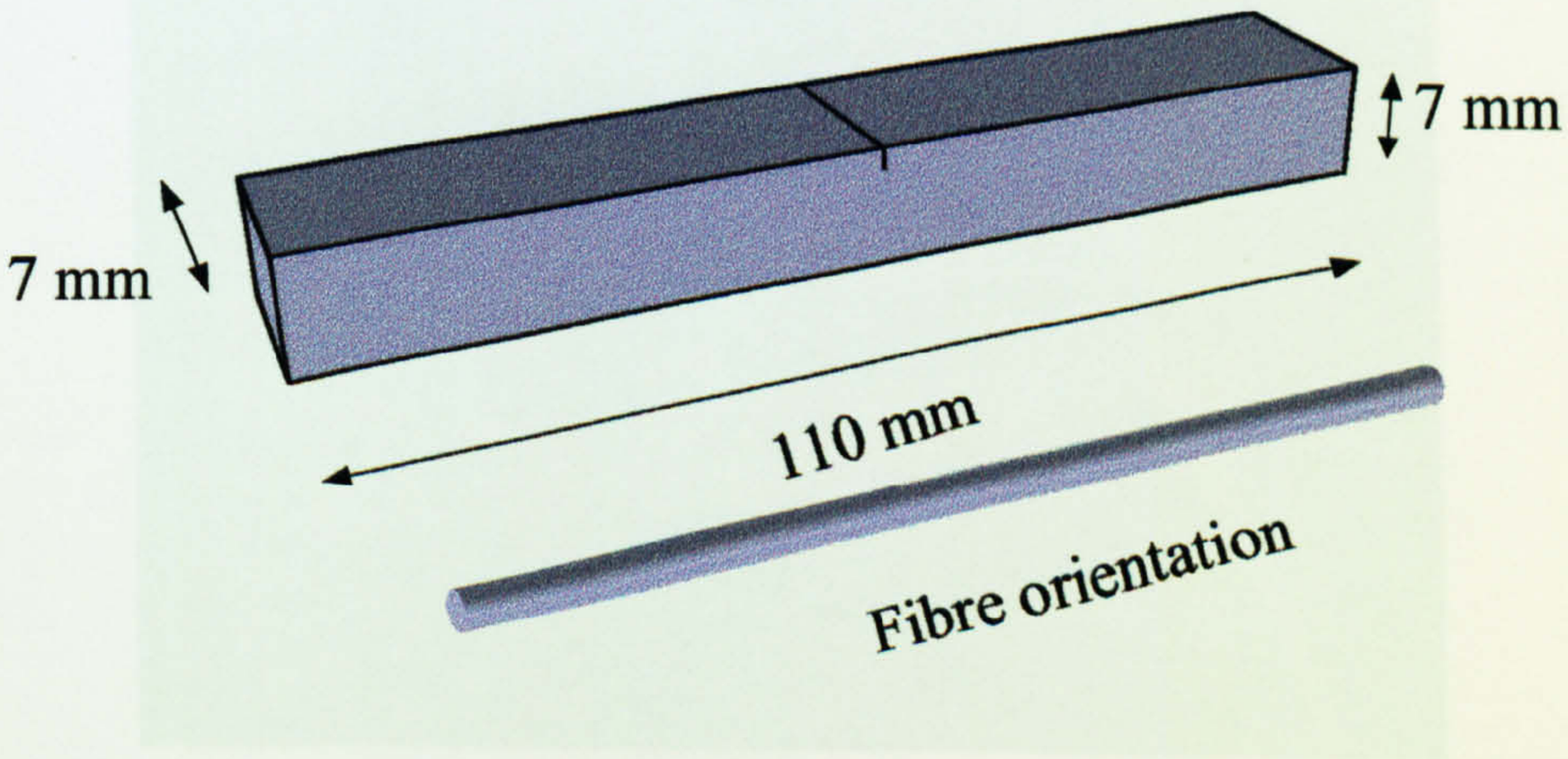

Figure 4.2 *Prepared notched sample with fibre orientation as shown*

saw. A size of 110 × 7 × 7 mm was chosen for the samples as this maximised the number of samples obtainable from the plates. All the samples were ground to the above uniform size using a Buehler KrautKramer Metaserv grinder-polisher. The Isomet 2000 saw was used to cut single-edge notches to a depth of 2 mm (Figure 4.1). The material properties of the specimens as supplied by the manufacturer are given in Table 4.3.

4.3.2 Fatigue Crack Growth

Crack growth data in air and in sea water, was obtained using notched specimens, subject to three point bending crack growth, using a Mayes-servo-electric fatigue rig (Figure 4.3).

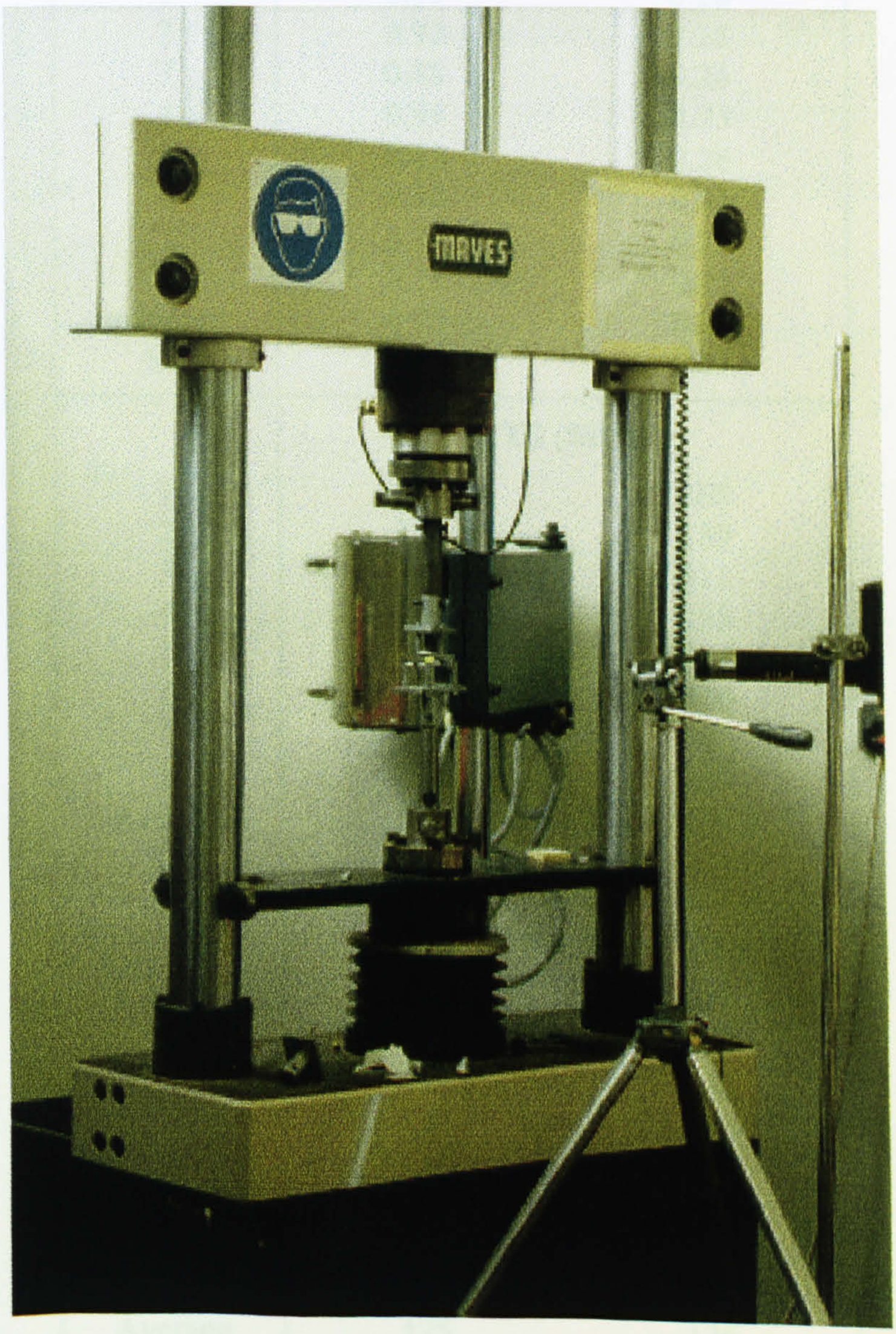

Figure 4.3 *Mayes servo-electric fatigue rig*

Table 4.3 *Material properties of specimens (supplied by DRA)*

Sample No	CPAl/Sumitomo	6061/Sumitomo
	Fibre volume fraction (%)	
1	32.0	37.9
2	41.4	46.0
3	43.8	50.6
4	40.5	48.1
5	43.7	47.0
6	39.8	40.2
7	43.3	46.3
8	36.3	46.8
Average	40.1	46.5
SD	4.1	3.8
	Strain to failure (%)	
1	0.87	0.28
2	0.92	0.28
3	0.88	0.26
4	0.94	0.25
5	0.85	0.26
6	0.80	0.24
7	0.77	0.25
8	0.79	0.25
Average	0.85	0.26
SD	0.06	0.01
	UTS (MPa)	
1	642	268
2	819	139
3	791	311
4	823	298
5	804	314
6	733	300
7	752	303
8	728	297
Average	761.5	301.3
SD	61.0	15.6
	Young's modulus (GPa)	
1	111	117
2	119	135
3	137	140
4	125	136
5	131	143
6	127	137
7	130	137
8	119	139
Average	125	136
SD	8	8

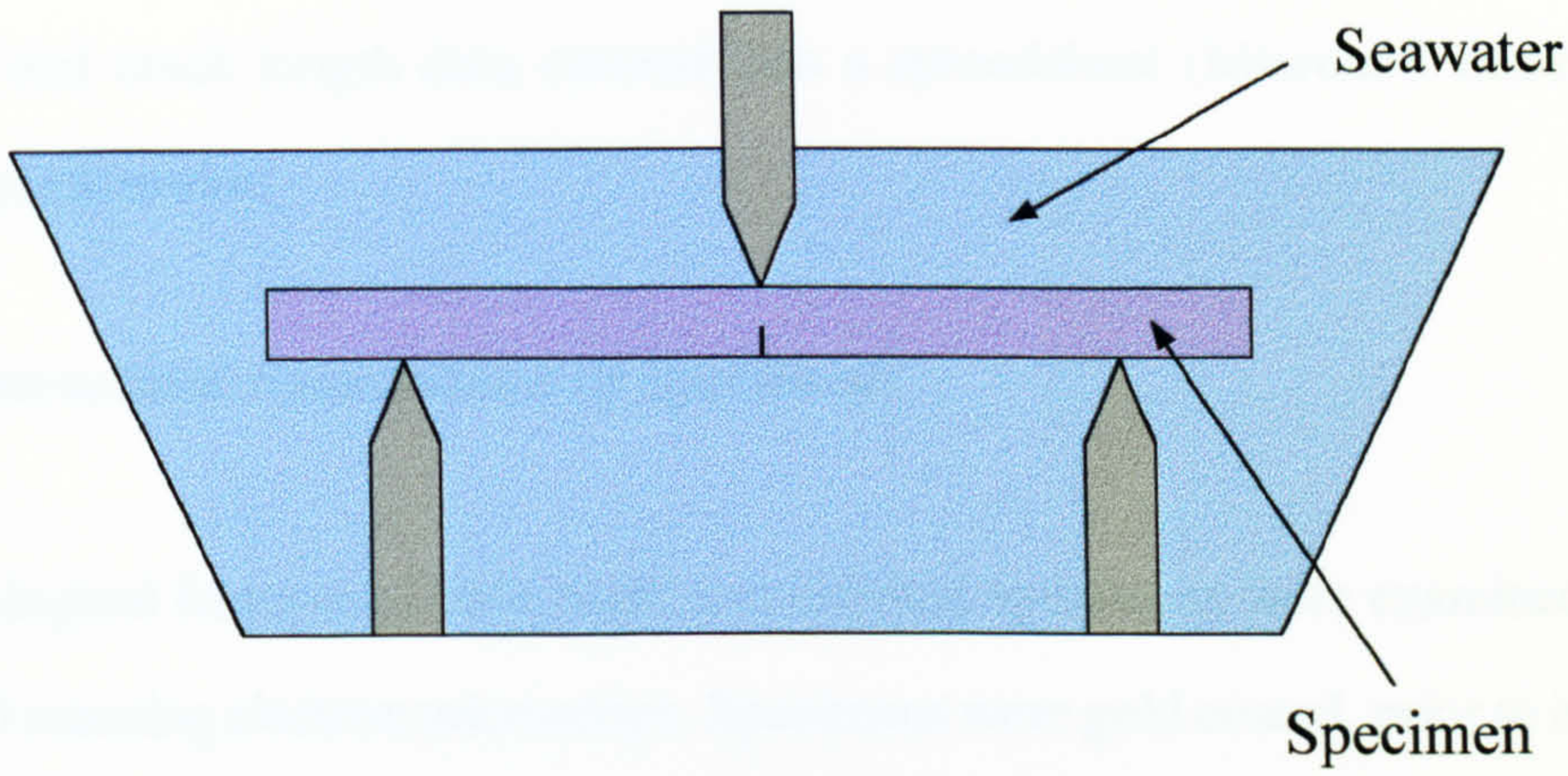

Figure 4.4 *Schematic of test rig with seawater bath fitted*

All samples were sinusoidally cycled at 1Hz in three point bending using the Mayes fatigue rig for differing applied stresses. The environmental fatigue tests were carried out on the Mayes rig fitted with a bath in which the sample and sample holder were submerged in sea water – Figure 4.4 shows a schematic of the setup. Figure 4.5 represents a typical nominal stress cycle for the specimen. A minimum force, F_{min}, was applied in order to keep the specimen from sliding in its holder. The failure stress F_o was determined by applying a monotonic load on a sample specimen until failure, this load was then used as the failure load for all other fatigue specimens. F_{max} was set at 75-90% of F_o. Crack growth was monitored by periodically taking photographs of the crack using a Tamron SP 90 macro lens mounted on a Canon AV1 35mm SLR camera. From the photographs crack growth

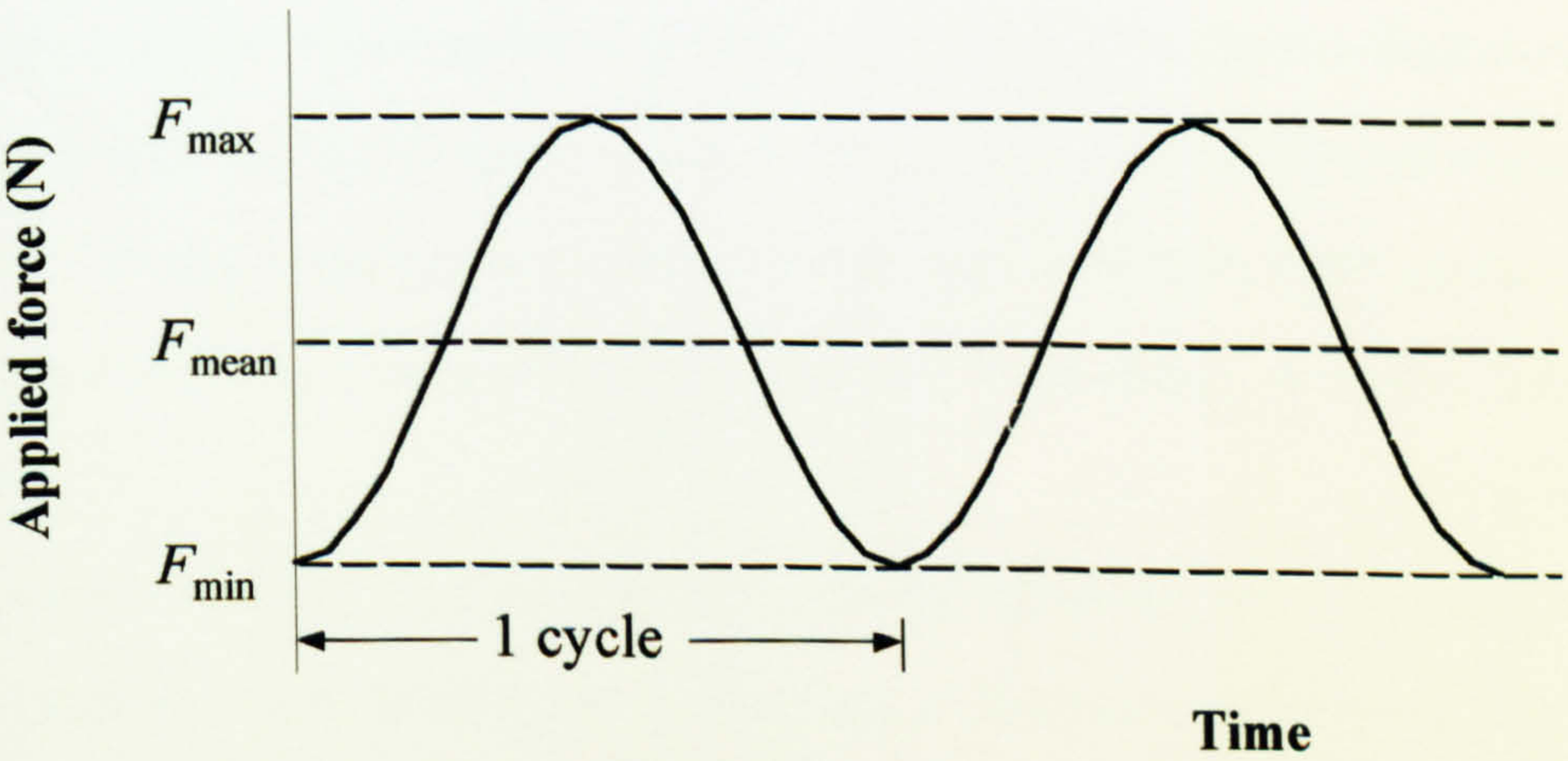

Figure 4.5 *Stress cycle applied to three point bend specimens*

was studied and crack length data entered into a spreadsheet (Microsoft Excel 5.0) for graphical representation.

4.3.3 Microstructural Examination of Specimens

The morphological features of both failed and unfailed specimens were examined using an Hitachi 2400 scanning electron microscope. Specimens were gold coated, prior to installation in the microscope, to avoid any build-up of charge, thus giving higher resolution in the microscope. The specimens were mounted at tilt angle of 45°.

5 Results

5.1 Introduction

The results of the experimental programme are presented here in ten main subsections. After the introduction, Section 5.1, the tensile and shear stress distribution around an embedded defect in the reaction zone of a short fibre metal-matrix composite are investigated in Section 5.2. In Section 5.3, the effects of varying the fibre/matrix moduli for an embedded defect in the reaction zone is considered. The calculation of stress intensity factors for a crack tip inside the reaction zone using two radically different FEA software packages, together with the evaluation of results to see which, if either, is more suited to model crack propagation in MMCs is dealt with in Sections 5.4–5.7. The effects of fibre/matrix bond strength on failure mechanisms are investigated in Section 5.8, time-matching finite element simulation; the failure modes include mode I, crack propagation, debonding and fibre bridging. Comparisons between the results obtained by modelling and those derived by applying loads to sample specimens are made in Section 5.9. The results from fatigue crack growth tests of MMCs in air and a saline solution using three-point bending is presented in Section 5.10.

5.2 Tensile and Shear Stress Distributions in the Interphase

To calculate the tensile and shear stress distributions over the entire interphase of a fibre-reinforced composite, a two-dimensional axisymmetric quarter model of a SiC/Ti metal-matrix composite was constructed in the *Engineering and Mechanics Research Corporation* finite element package *Display 3* [70]. A discontinuous carbon fibre of length 900 μm and radius 12.5 μm embedded in a titanium metal-matrix of length 1000 μm and radius 90 μm was modelled. An homogeneous interphase of 5 μm radius extended from fibre to the matrix.

A tensile stress of 20 MPa was applied to the composite end whilst the left and base of the composite were constrained in the r and y directions respectively (Figure 5.1). The constituent material properties of the composite used are listed in Table 5.1. Figure 5.1 also

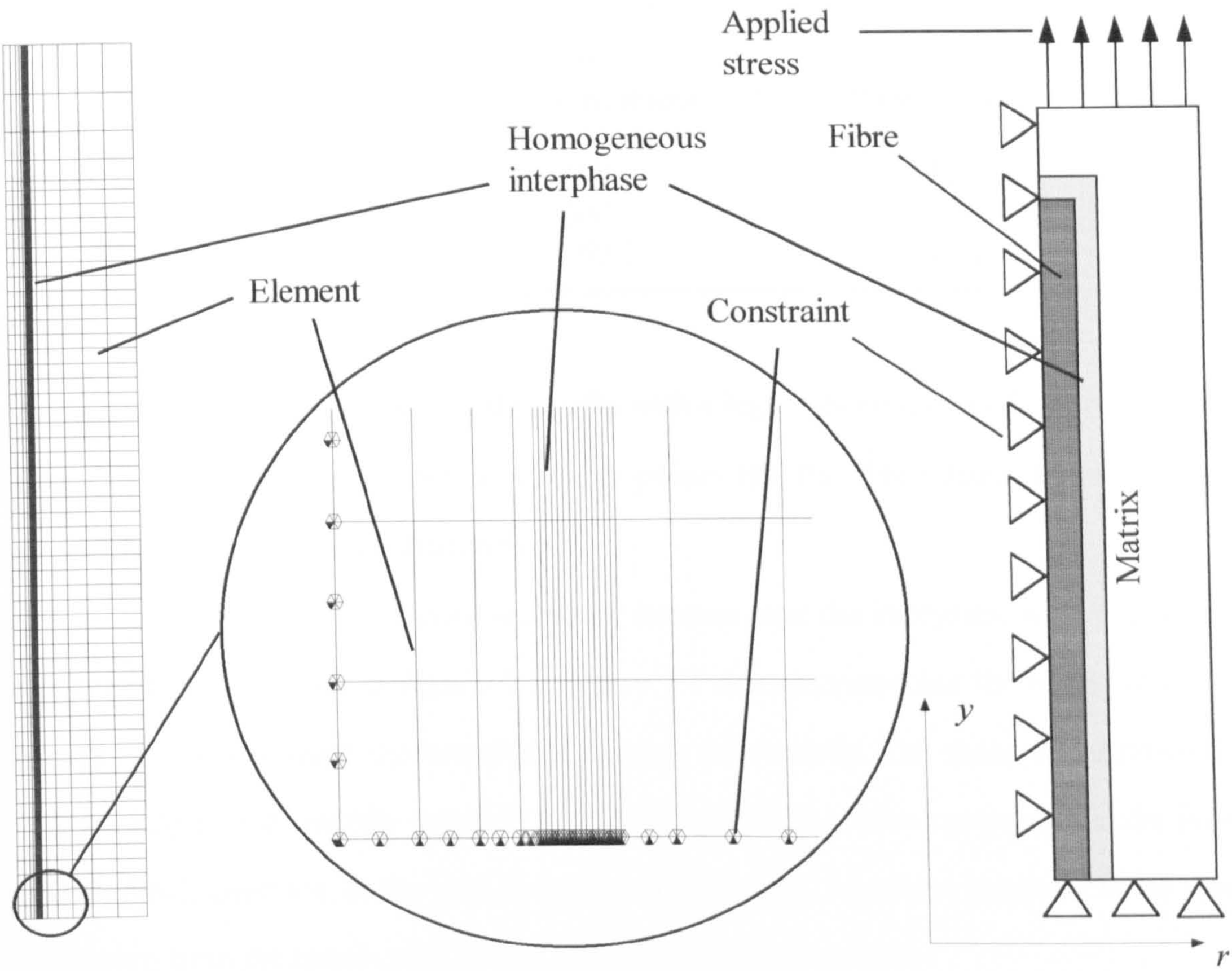

Figure 5.1 *Two-dimensional half mesh with close-up of interphase. Right, schematic representation of model*

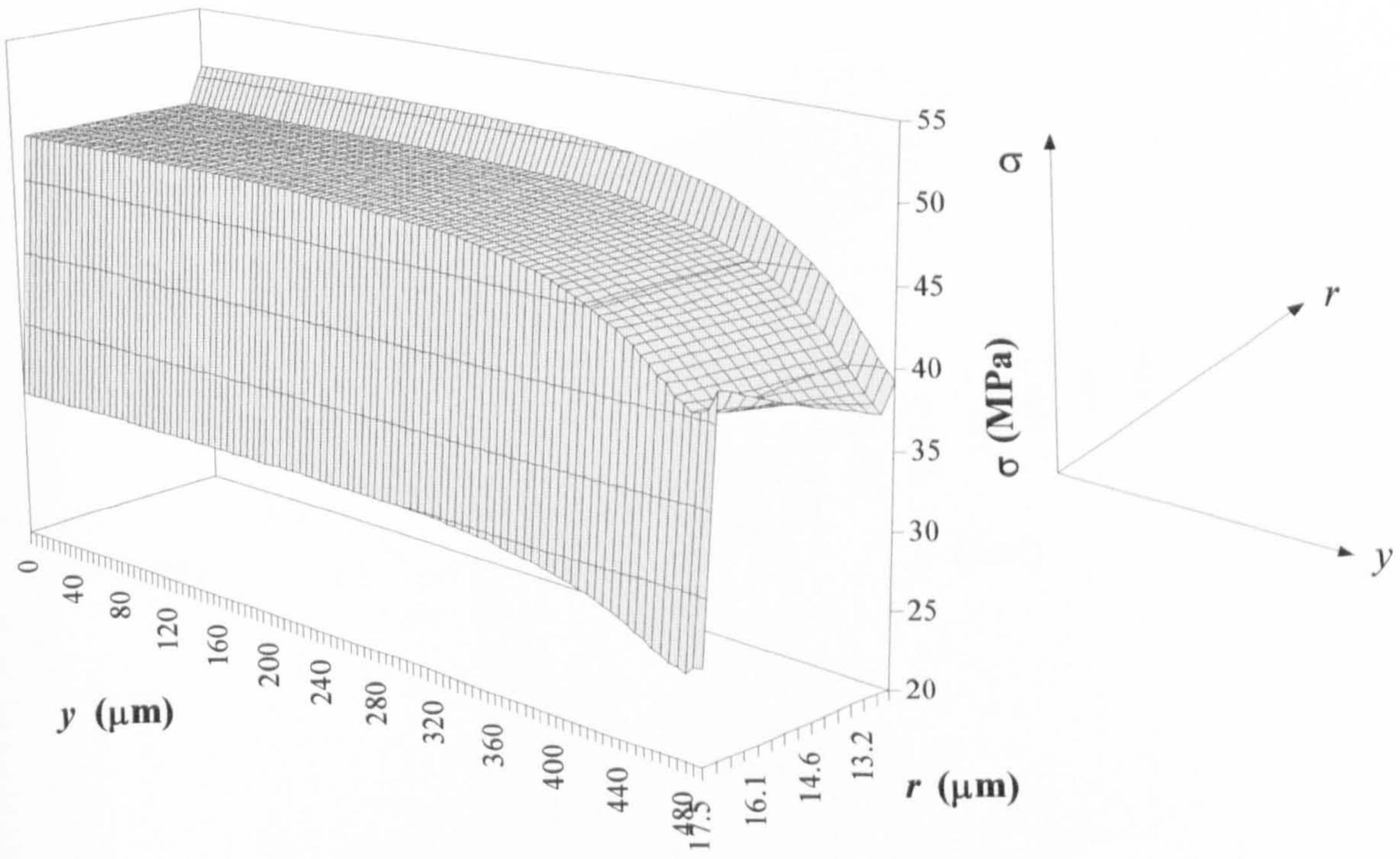

Figure 5.2 *Tensile stress distribution over interphase*

Table 5.1 *Constituent material properties of composite [61]*

	Young's modulus (GPa)	Poisson's ratio
Fibre	400	0.25
Interphase	360	0.34
Matrix	92.3	0.36

illustrates the actual mesh used for the model with a high concentration of elements in the interphase, necessary to generate enough points for the three-dimensional surface representations of the stress distributions.

The distributions of both tensile and shear stresses over the interphase were calculated using the model outlined in Figure 5.1. Figure 5.2 demonstrates that the tensile stress is constant radially through the interphase, varying only axially. The shear stress however (Figure 5.3) is only radially constant towards the middle of the composite in the fibre (longitudinal) direction; as the peak shear stress is reached, a positive gradient can be seen to develop from the matrix side, to the fibre side of the interphase.

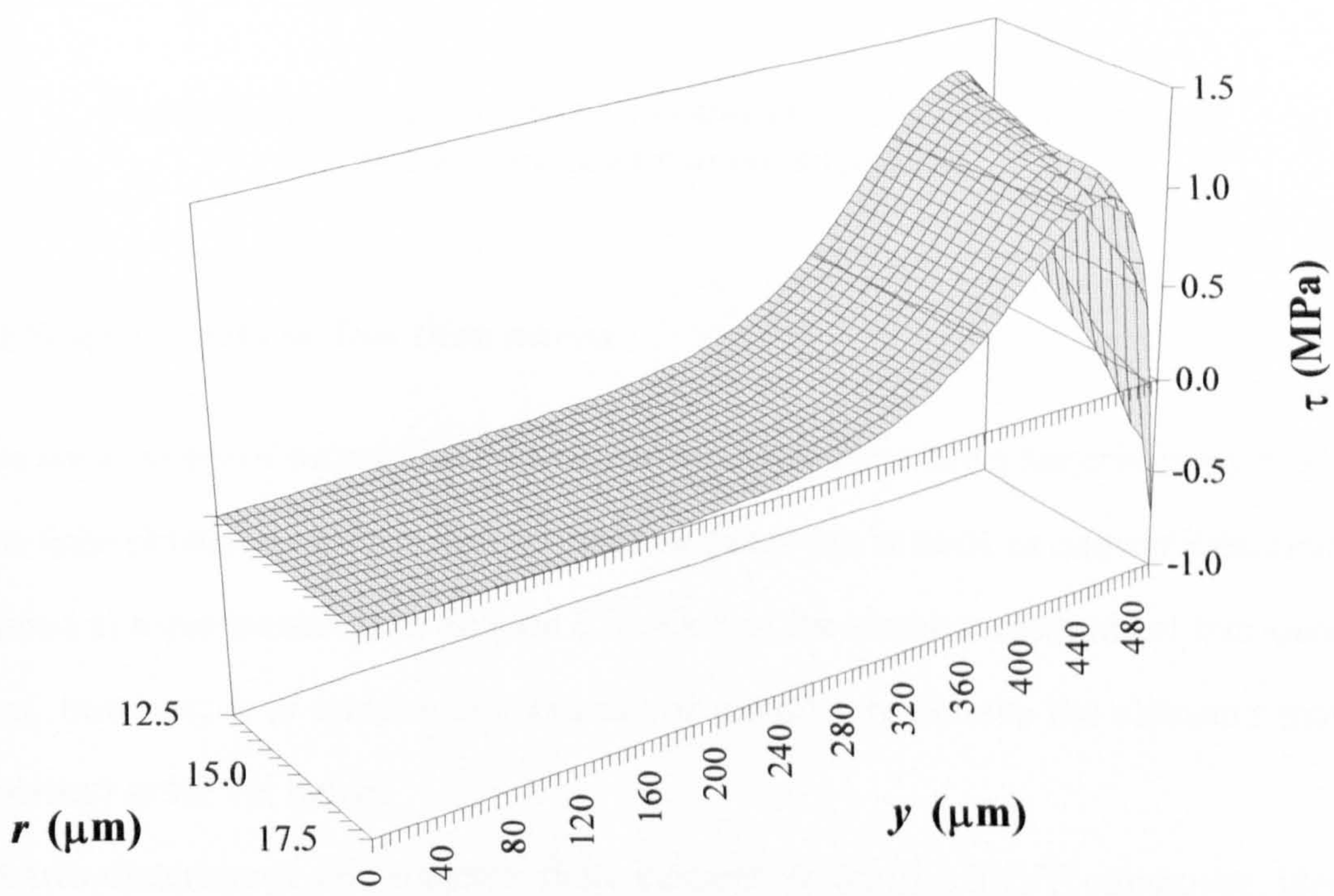

Figure 5.3 *Shear stress distribution over interphase*

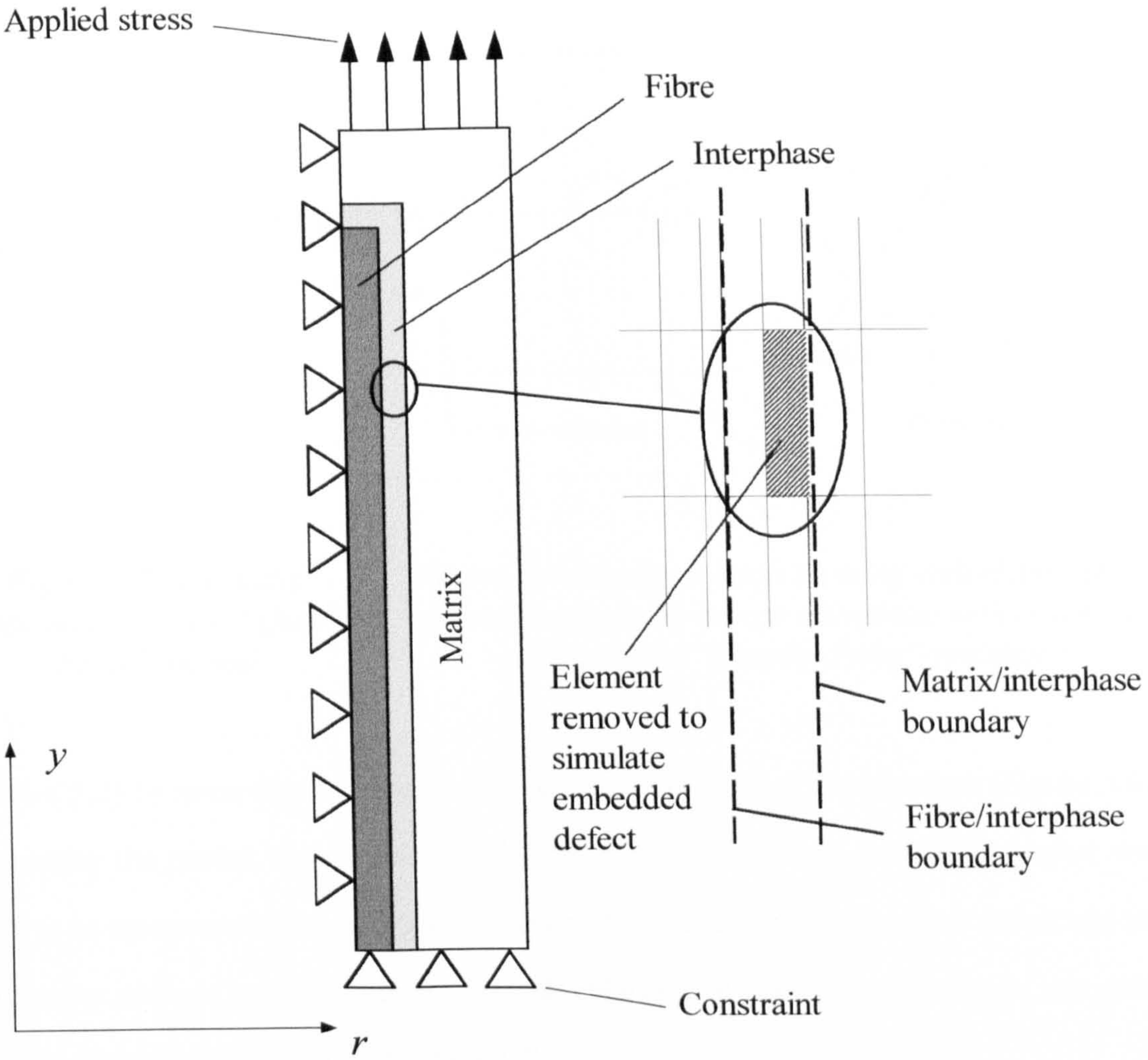

Figure 5.4 *Schematic showing a simple crack (by element removal) being introduced into the interphase*

5.2.1 Simple Cracks in Two Dimensions

There are a variety of ways of introducing embedded defects into a material being modelled by the finite element technique. Special crack elements can be used, or conventional elements modified in some manner (see Section 5.3). One of the simplest methods of introducing a defect, however, is to remove an element (or completely remove the element's material properties) in the FE model.

A two-dimensional axisymmetric finite element model of a SiC/Ti composite, identical to that in Section 5.1, but differing in the number of elements in the interfacial region, was generated in *Display3* (Figure 5.4). The interfacial region was constructed so as to be two elements wide. An embedded defect was introduced at the point of maximum shear stress

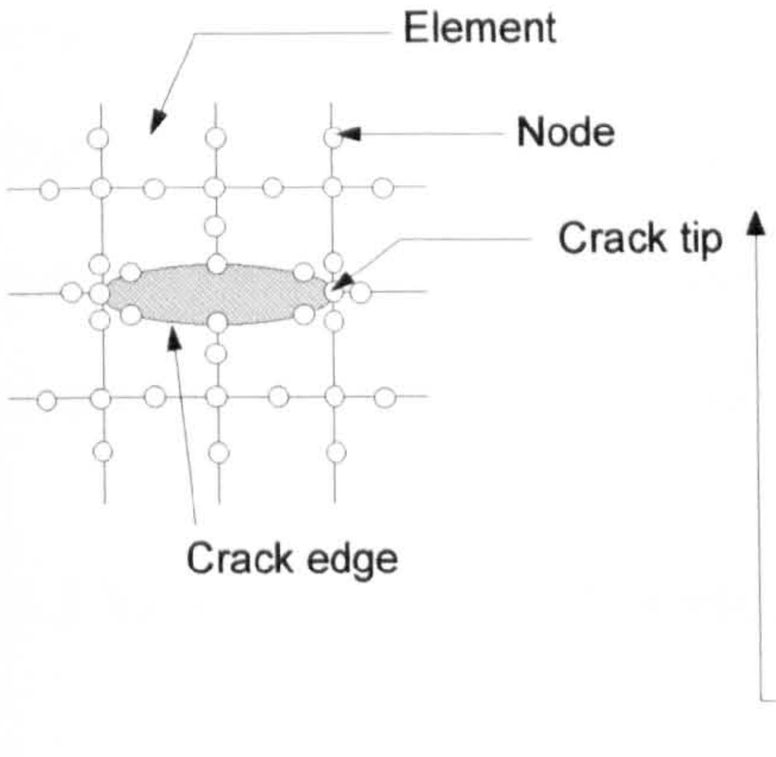

Figure 5.5 *Schematic representation of the "Quarter Point" method*

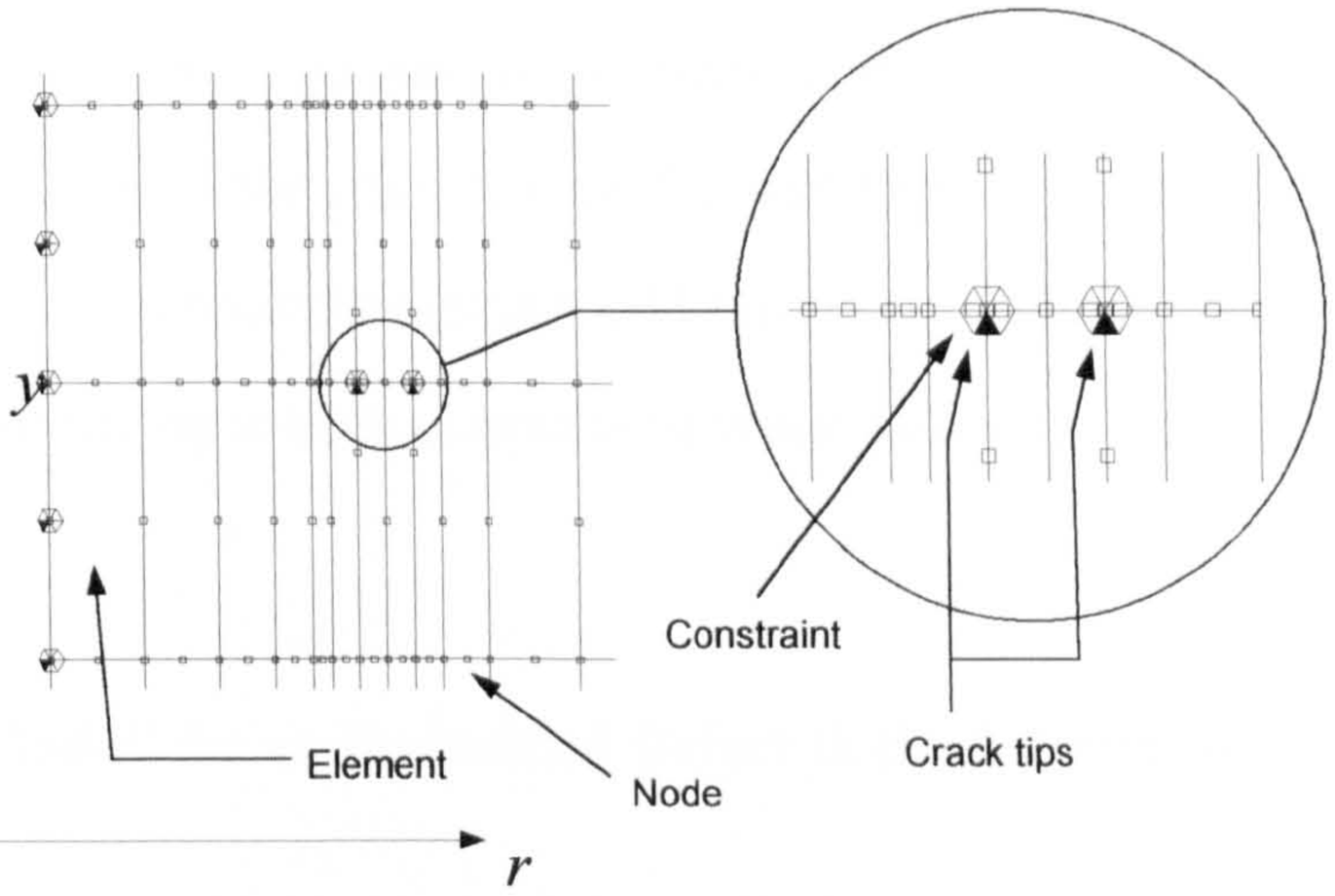

Figure 5.6 *Display 3 mesh showing embedded defect placed horizontally across interphase with crack-tip nodes at the "Quarter Point" position*

(Section 5.2) by removing an element on the right hand side of the interface (Figure 5.4). On running the model, the maximum principal stress distribution around the defect was found to be unrepresentative of a true defect due to both the geometry of the defect and the fact that no account had been taken of the singularity that occurs at a crack tip; this point has been considered in detail in Section 5.3.

5.2.2 The "Quarter Point" Method

The finite element method is an established standard tool for the determination of stresses in engineering structures and components. The method is usually based upon assumptions for displacement and/or stresses, which are defined in terms of polynomial functions over elements of finite size. It is not possible, therefore, to obtain exact representations of the behaviour in the region of a singularity. To overcome this difficulty, a finite element mesh can be constructed with very substantial mesh refinement around the crack tip. However, such refinement can be very expensive in computer time and extremely time consuming in preparation. There are also special elements which can be used in the region of the crack tip which contain a singularity which may even be the exact *Westergaard* solution [54, 55]. However, a good approximate to the *Westergaard* solution can be obtained by the use of standard eight-noded, isoparametric elements with their mid-side nodes displaced from

their nominal position to a position which is one quarter the element length, nearer to the crack tip. Nodes in front and to the rear of the crack (Figure 5.5 and 5.6) are displaced in this manner thus simulating the $r^{-1/2}$ *Westergaard singularity*. The use of the "quarter point" method thus leads to a considerable saving in both computer time and data preparation, as described in Section 5.3 below.

5.3 Variation of Fibre/Matrix Moduli for an Embedded Defect in the Interphase

In the axisymmetric, two-dimensional finite element model described in this section a *type I* crack of semi length 1.25 μm was introduced halfway, axially, along the interfacial region, mid-way between fibre and matrix, with major axis parallel to the radial axis . The "quarter point" method was used for the elements at the crack tip.

The maximum principal stress distributions in front of the crack tip along the boundary line between fibre/interphase and interphase/matrix were obtained for varying values of fibre and matrix Young's moduli (E_f and E_m): E_f was increased from 360 GPa to 400 GPa, while simultaneously E_m was decreased from 360 GPa to 92.3 GPa. Figures 5.7 and 5.8

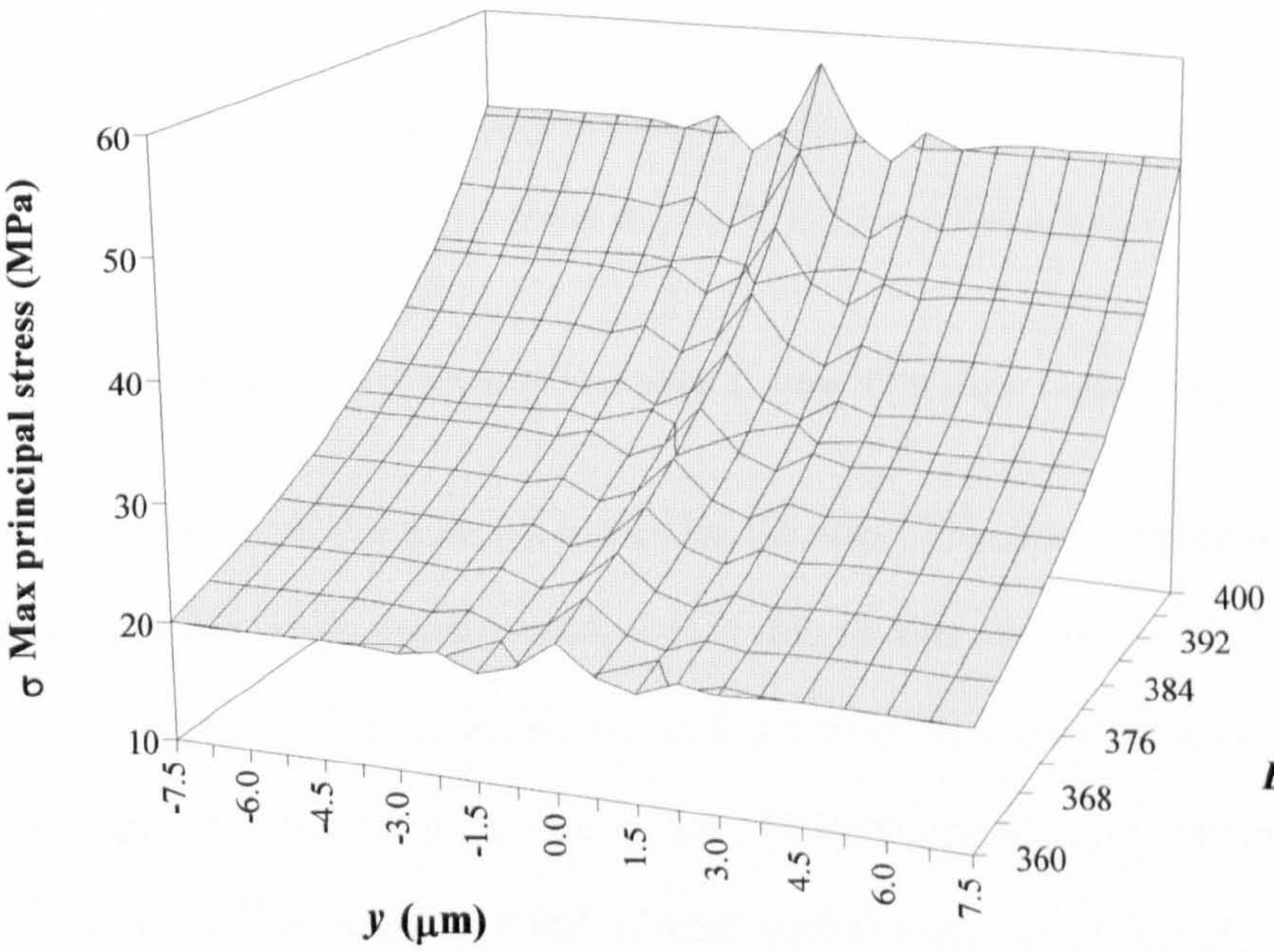

Figure 5.7 *Three-dimensional plot showing how the maximum principal stress distribution for a line, 7.5 microns either side of the right hand side crack tip, placed in the interphase, varies with increasing fibre and decreasing matrix Young's modulus*

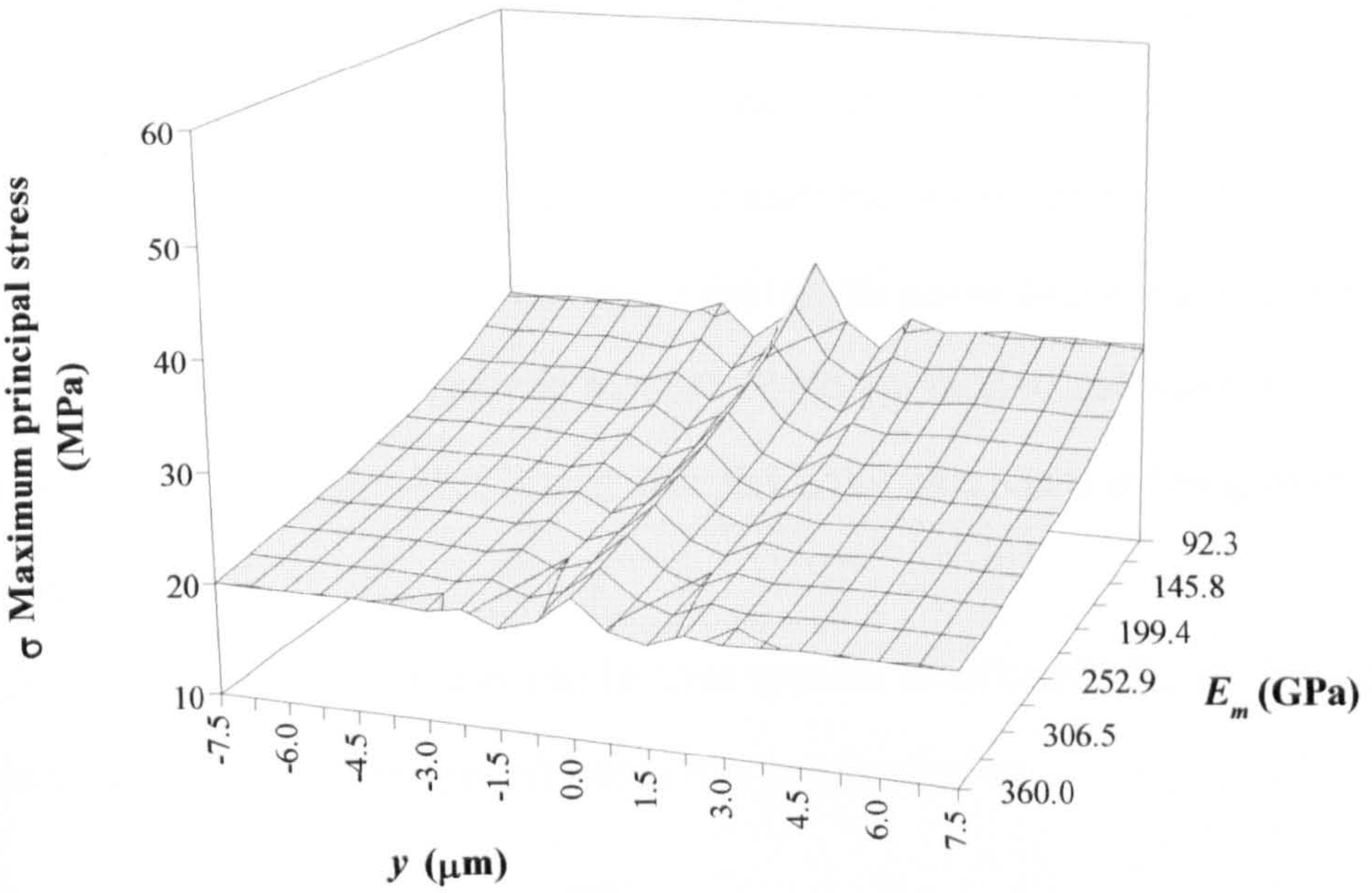

Figure 5.8 *Three-dimensional plot showing how the maximum principal stress distribution for a line, 7.5 microns either side of the left hand side crack tip, placed in the interphase, varies with increasing fibre and decreasing matrix Young's modulus*

demonstrate what effect varying the moduli has on the stress distributions in front of the craclk tips. It can be quite clearly seen that the overall stress distribution on the fibre side increases with increasing fibre modulus, but also the concentration of maximum stress at $y = 0$ increases at a greater rate. On the matrix side, despite the matrix modulus falling, there is a steady increase in the overall stress distribution along the interphase/matrix boundary, and again, the point of maximum stress at $y = 0$, increases at a greater rate.

5.4 Calculation of Stress Intensity Factors Using *Display 3* and *Endure*

For stress intensity factor calculation using the *Display 3/Endure* combination, a half model of the composite has to be constructed; this is due to the way in which *Endure* calculates stress intensity factors. The model shown in Figure 5.9 was constructed with a horizontal crack located in the interface at the mid-point of the composite and starting from the vertical mid-point of the interphase. A total of nine models were constructed, with the crack tip being extended outwards from the centre to the next adjacent element for each model. Each crack tip used elements incorporating nodes shifted to the "*quarter point*" position to

simulate the $r^{-1/2}$ singularity as required by the *Westergaard* solution. After the stress distributions had been obtained for all model runs, the output from these runs was fed into *Endure* and the stress intensity factors for each run were determined.

In Section 5.2 it was found that since the tensile stress distribution across the interphase was constant radially, an analytic method could be used to calculate K_I in the interphase. However, this constant value is only true since the interphase is being modelled as entirely homogeneous.

A centre crack plate theory can be thus applied to calculate K_I, i.e. for a crack length of semi length a and for an applied stress σ it can be shown:

$$K_I = \sigma\sqrt{\pi a} \qquad \{5.1\}$$

for an infinitely large plate. For a plate with finite width, the formula has a shape factor and becomes:

$$K_I = \sigma\sqrt{\pi a}\left(\frac{W}{\pi a}\tan\frac{\pi a}{W}\right)^{1/2} \qquad \{5.2\}$$

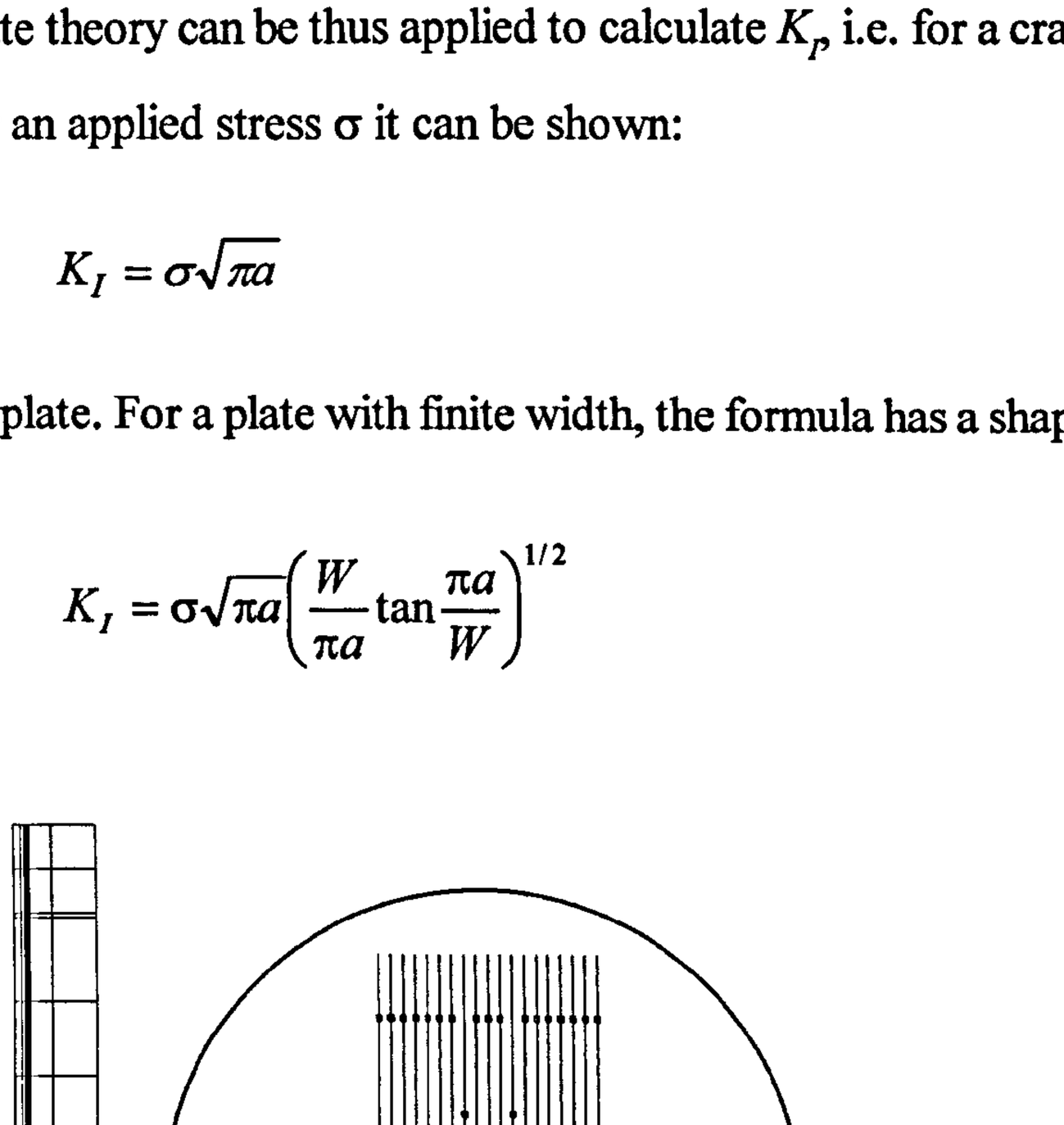

Figure 5.9 *Two-dimensional half model mesh constructed in Display 3 showing high concentration of elements in the interphase*

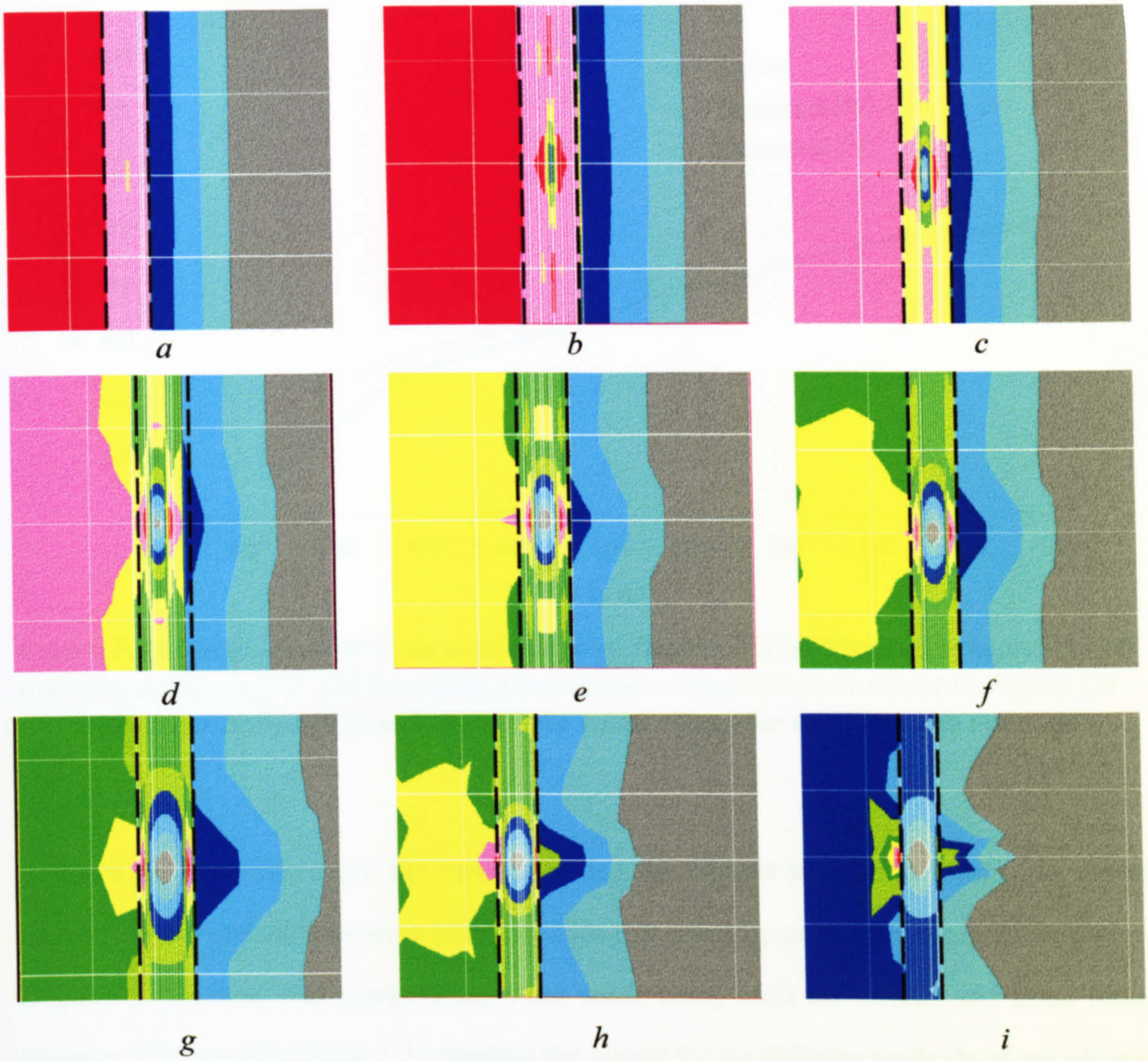

Figure 5.10 *Diagrams (a)–(i) (produced from the mesh in Figure 5.9) show the maximum principal stress distribution around a growing centre crack in the interphase (between dotted lines) – the fibre is on the left hand side and the matrix is on the right*

where W is the width of the interphase.

Figure 5.10 (a)–(i) shows maximum principal stress distributions around the crack tips as the crack increases in size in the interphase: initially the crack is very small and it has little or no effect on the principal stress distribution in the fibre. However, by the time the crack has reached a semi length of just over a micron – Figure 5.10 (d) – the distribution of stresses in the fibre has been greatly influenced by the stress distribution in front of the fibre side crack tip, with a lesser influence on the stress distribution in the matrix from the matrix side crack tip. At $a = 2$ μm – Figure 5.10 (g) – the stress distribution from the fibre-side crack tip has extended well into the fibre; the distribution of stresses in front of the matrix-side crack tip are relatively smooth inside the matrix.

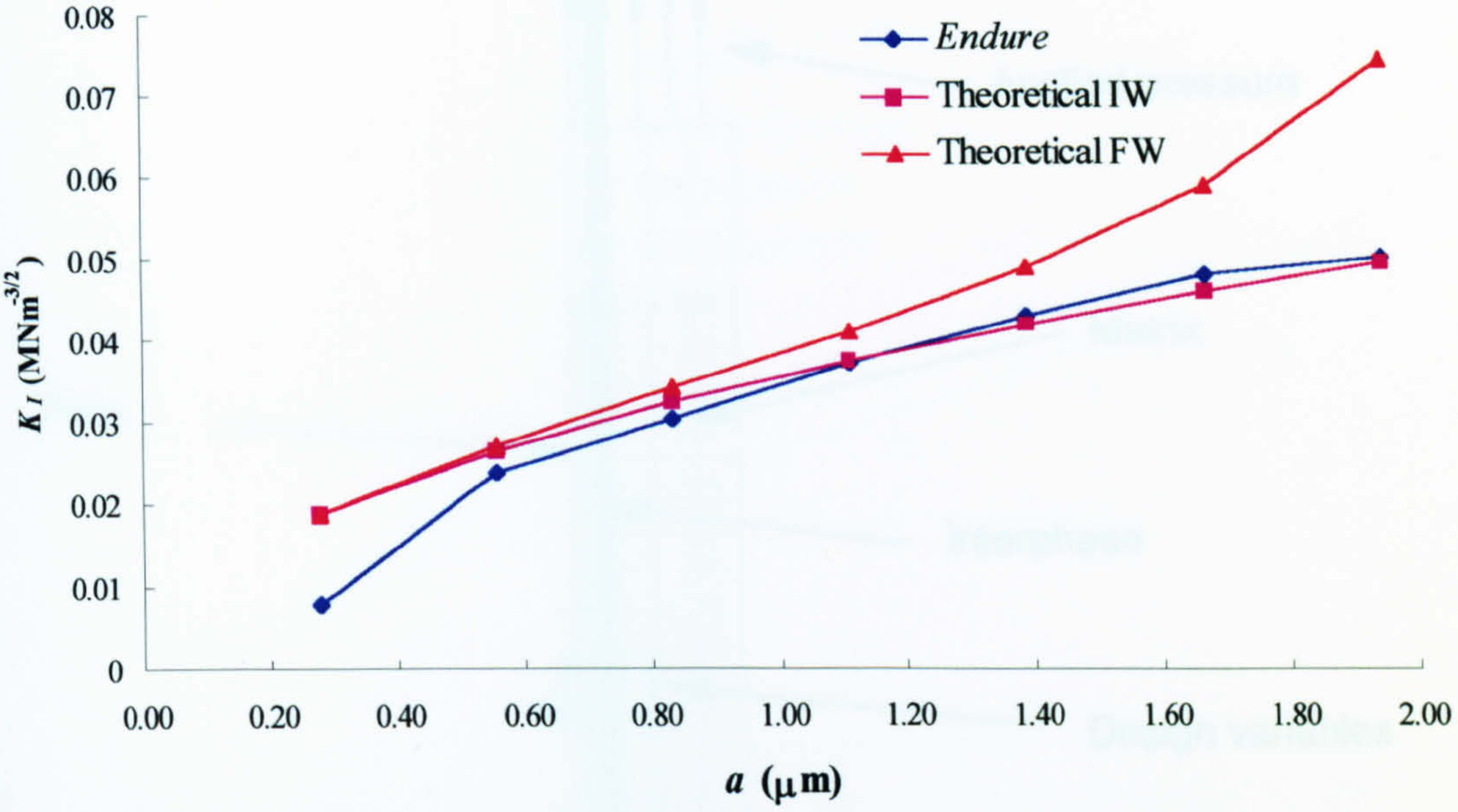

Figure 5.11 *Comparison of K_I as obtained from Display3/Nisa/Endure vs theoretical IW (infinite width) and FW (finite width) predictions – obtained from model in Figure 5.9 – with closer correlation with the infinite width values for the fibre-side crack tip*

Since the fibre-side crack tip was generating the highest stresses in front of it, stress intensity factor calculations were performed for this crack tip using numerical techniques in *Display 3* (*Endure*) and comparisons were made using both the infinite and finite plate theories. The graph in Figure 5.11 displays the results for the differing methods of calculating K_I. Apart from the initial crack length, there is a good correlation between the output from *Endure* and the theoretically predicted infinite width values, but poor correlation between the finite width values. This correlation was augmented by verification which will be covered in Section 5.7. As the crack tip approached the fibre the stress intensity calculations became unstable and *Endure* was unable to calculate K_I at interphase/fibre boundary. Hence the semi crack length was limited to $a = 2$ μm.

5.5 Calculation of Stress Intensity Factors Using *Applied Structure*

A two-dimensional, axisymmetric quarter model of the fibre/interphase/matrix depicted in Figure 5.1 was constructed in *Applied Structure* (Figure 5.12). As in previous models, constraints were placed on the left hand side in the *r*-direction and on the mesh base in the *y*-direction. Again, as in previous models the fibre/interphase/matrix regions were given

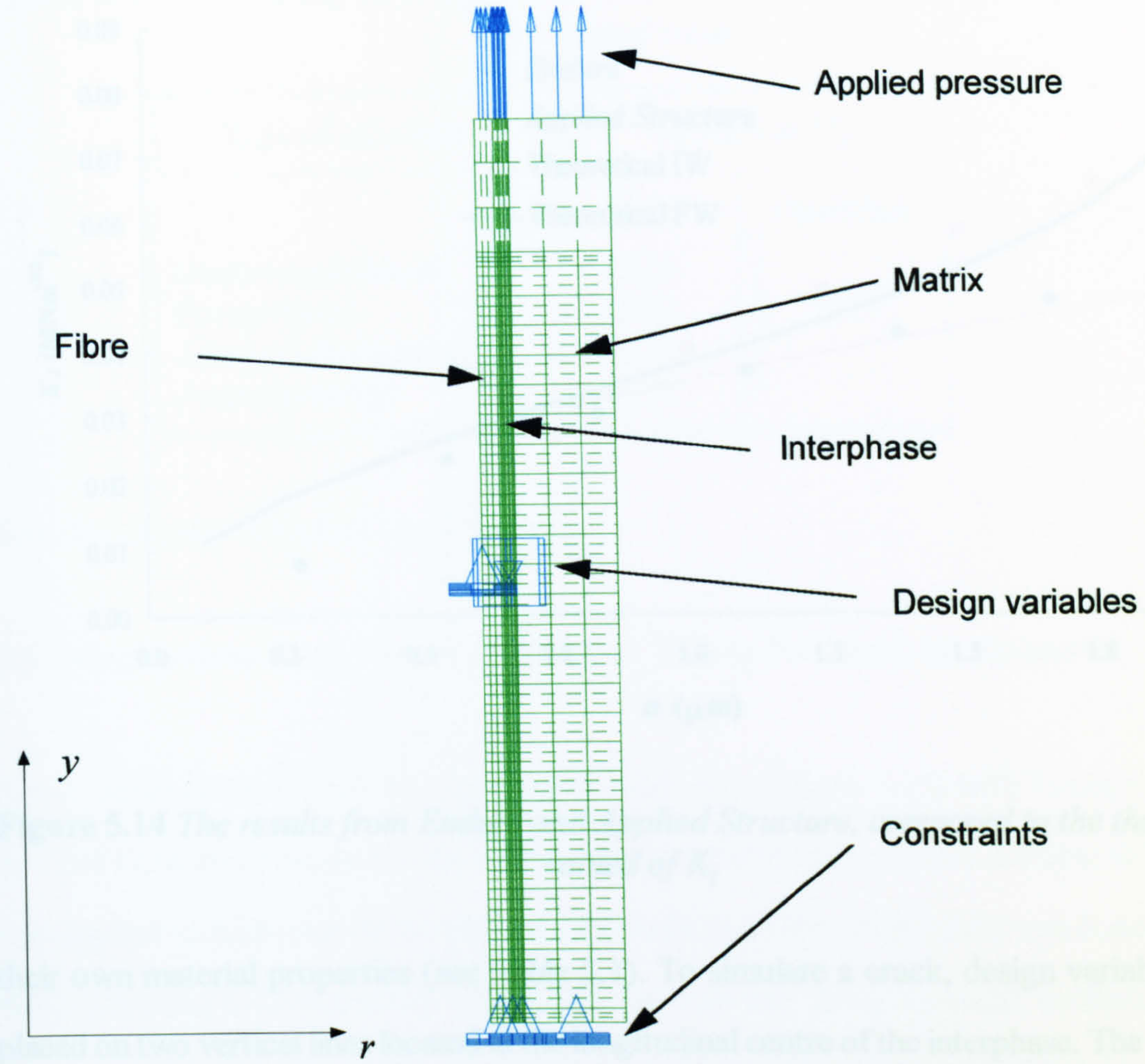

Figure 5.12 *Applied Structure mesh showing the unique "design vaiables" which enable a crack to be "grown" to a specified length*

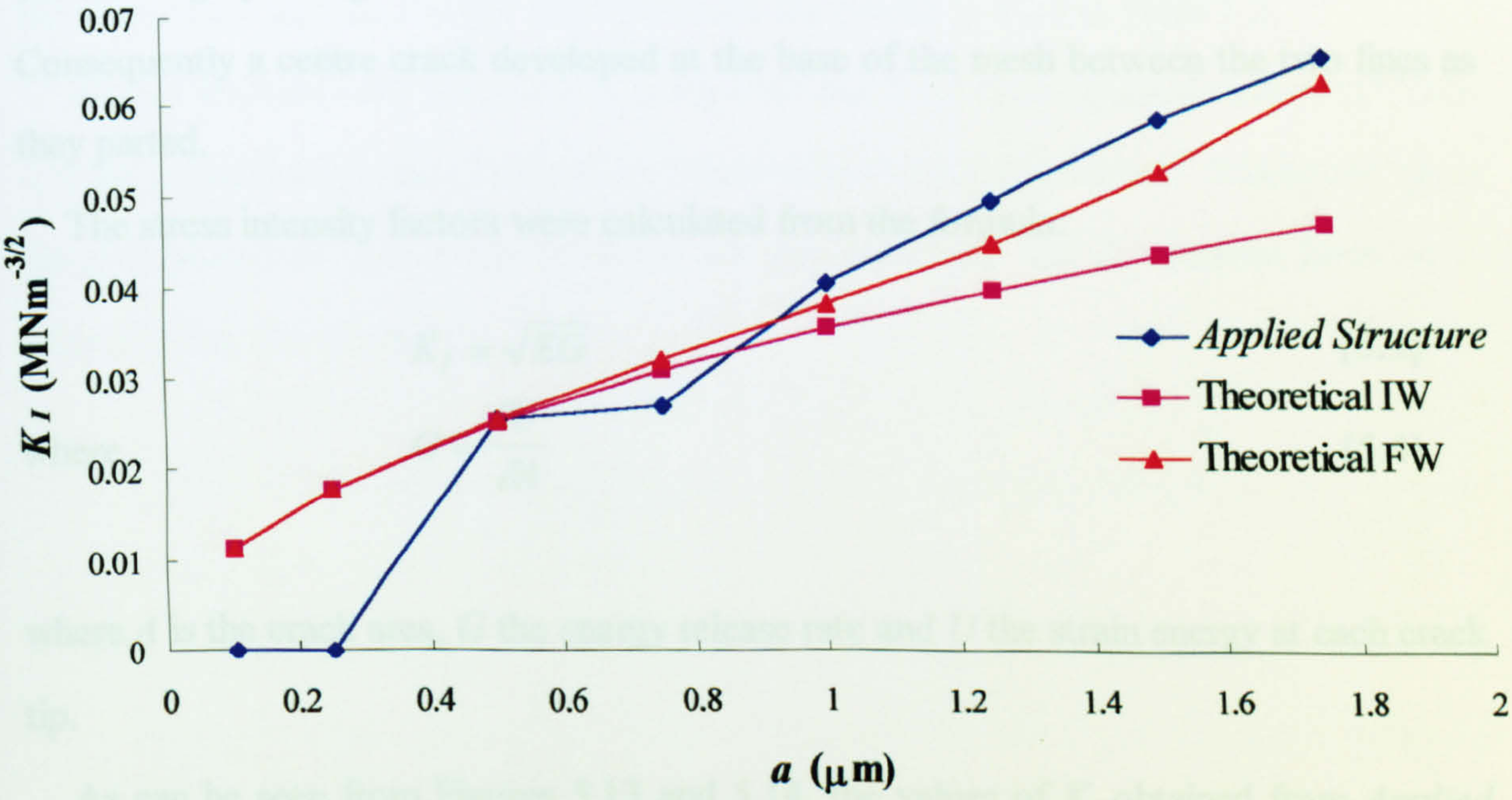

Figure 5.13 *The results from Applied Structure are in closer agreement with the theoretical FW (finite width) values compared to Display 3*

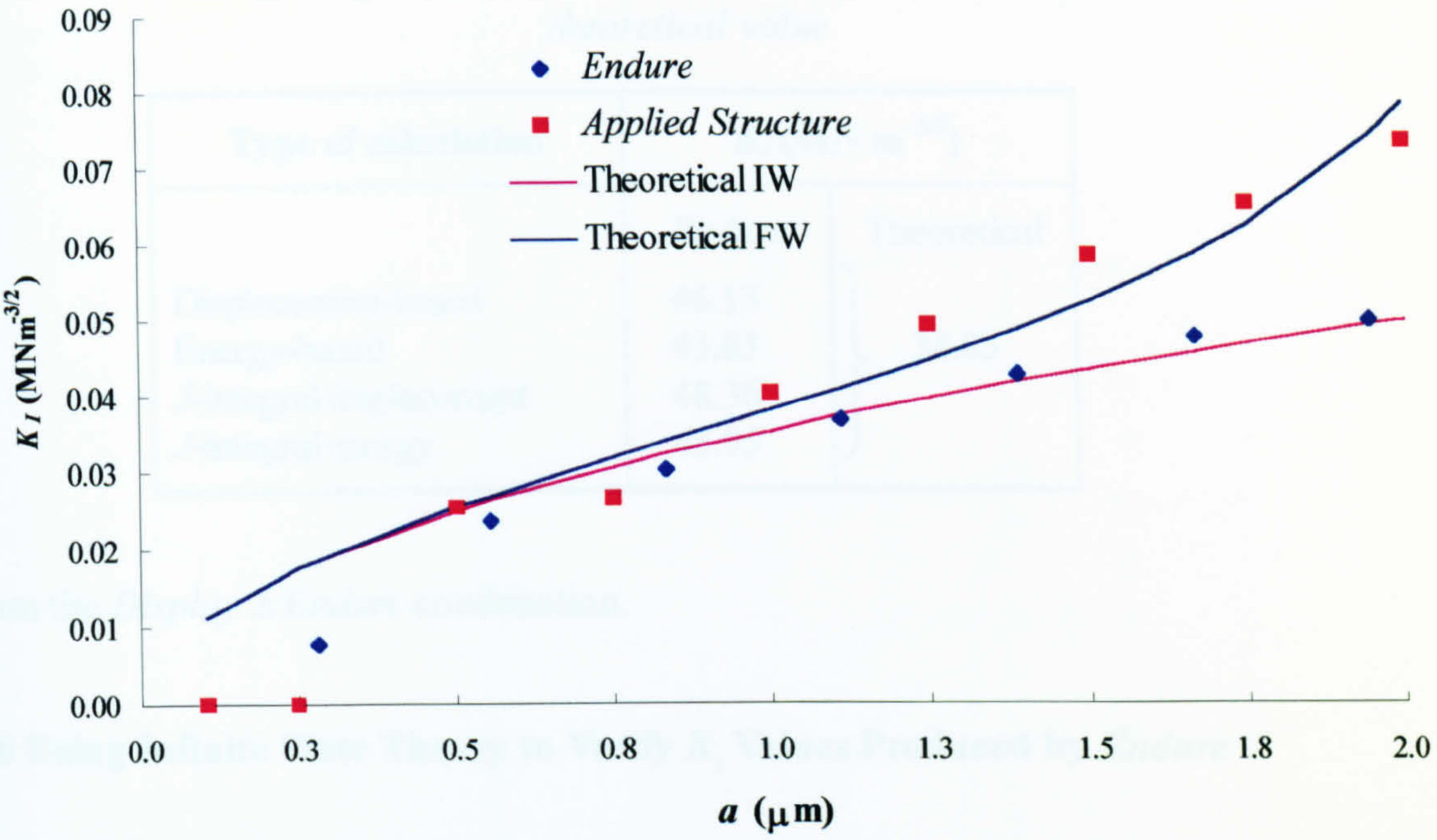

Figure 5.14 *The results from Endure and Applied Structure, compared to the theoretical valued of* K_I

their own material properties (see Table 5.1). To simulate a crack, design variables were placed on two vertical lines located at the longitudinal centre of the interphase. The variables had the effect that the two lines parted, moving towards fibre and matrix respectively – this of course meant that the elements on either side of the two lines in the interphase would become highly elongated; the area between these lines had no constraints attached. Consequently a centre crack developed at the base of the mesh between the two lines as they parted.

The stress intensity factors were calculated from the formula:

$$K_I = \sqrt{EG} \qquad \{5.3\}$$

where

$$G = \frac{\partial U}{\partial A} \qquad \{5.4\}$$

where A is the crack area, G the energy release rate and U the strain energy at each crack tip.

As can be seen from Figures 5.13 and 5.14, the values of K_I obtained from *Applied Structure* agree more closely with the finite width theoretical values compared those obtained

Table 5.2 *The differing ways Endure calculates K_I for a reference plate compared to theoretical value*

Type of calculation	K_I (MN m$^{-3/2}$)	
	Endure	Theoretical
Displacement-based	46.13	38.83
Energy-based	43.83	
J-integral displacement	48.36	
J-integral energy	45.95	

from the *Display 3/Endure* combination.

5.6 Using Infinite Plate Theory to Verify K_I Values Produced by *Endure*

A two-dimensional full model of an infinite steel plate (Figure 5.15) with Young's modulus $E = 200$ GPa, and Poisson's ratio $\nu = 0.3$, was produced in *Display 3*. A stress of 200 MPa was applied to both ends of the plate and the right hand side of the plate was constrained in the x-direction; a 12 mm crack was introduced mid-way along the plate, by disconnecting element nodes along the crack. The crack tip itself, was modelled using elements with their nodes at the quarter point position (see close up in Figure 5.15) to simulate the $r^{-1/2}$ singularity as required by the *Westergaard solutions*. The resultant stress output from running the model was fed into *Endure* and produced the results as seen in Table 5.2.

Endure automatically calculates K_I using both *crack tip opening displacement* (CTOD) calculation and energy-based *virtual crack extension* (VCE) approaches*. *J*-integrals, again using displacement and energy methods are also calculated and K_I obtained from the J_I integral using the formula:

$$K_I = \sqrt{\frac{2\mu J_I}{1-\nu}} \qquad \{5.5\}$$

where

$$\mu = \frac{E}{1+\nu} \qquad \{5.6\}$$

*See Appendix 3

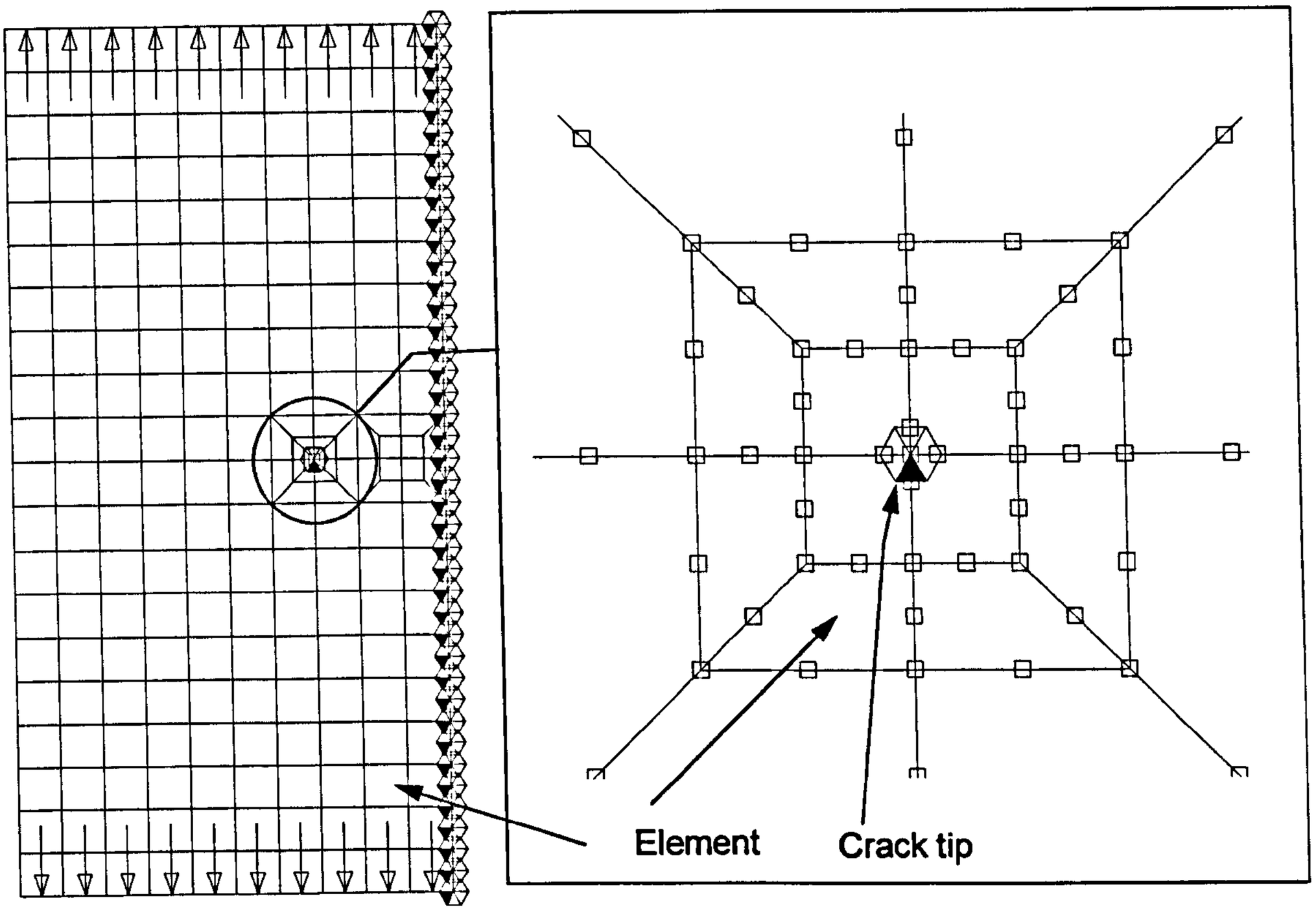

Figure 5.15 *Mesh used to verify K_I values from Display 3 with close-up of crack tip*

The theoretical values of K_I were obtained from the infinite plate formula:

$$K_I = \sigma\sqrt{\pi a} \qquad \{5.1\}$$

where s is the applied stress and a the crack length.

The output from *Endure* is in the units in which the *Display 3* mesh is constructed, in this case mm, so in order that K_I is in the correct form, i.e. $MNm^{-3/2}$, a multiplying factor of $10^{-3/2}$ must be used.

The best numerical estimate for K_I came from the energy-based VCE approach with an agreement of +12.8% over the analytic value, the next best value came from the J-integral energy approach with an agreement of +18.3%.

Although a refined mesh was used for the crack work for verification purposes, it was found that quite large, but regular, elements could be used for the crack tips without any significant deterioration in the predicted K_I values.

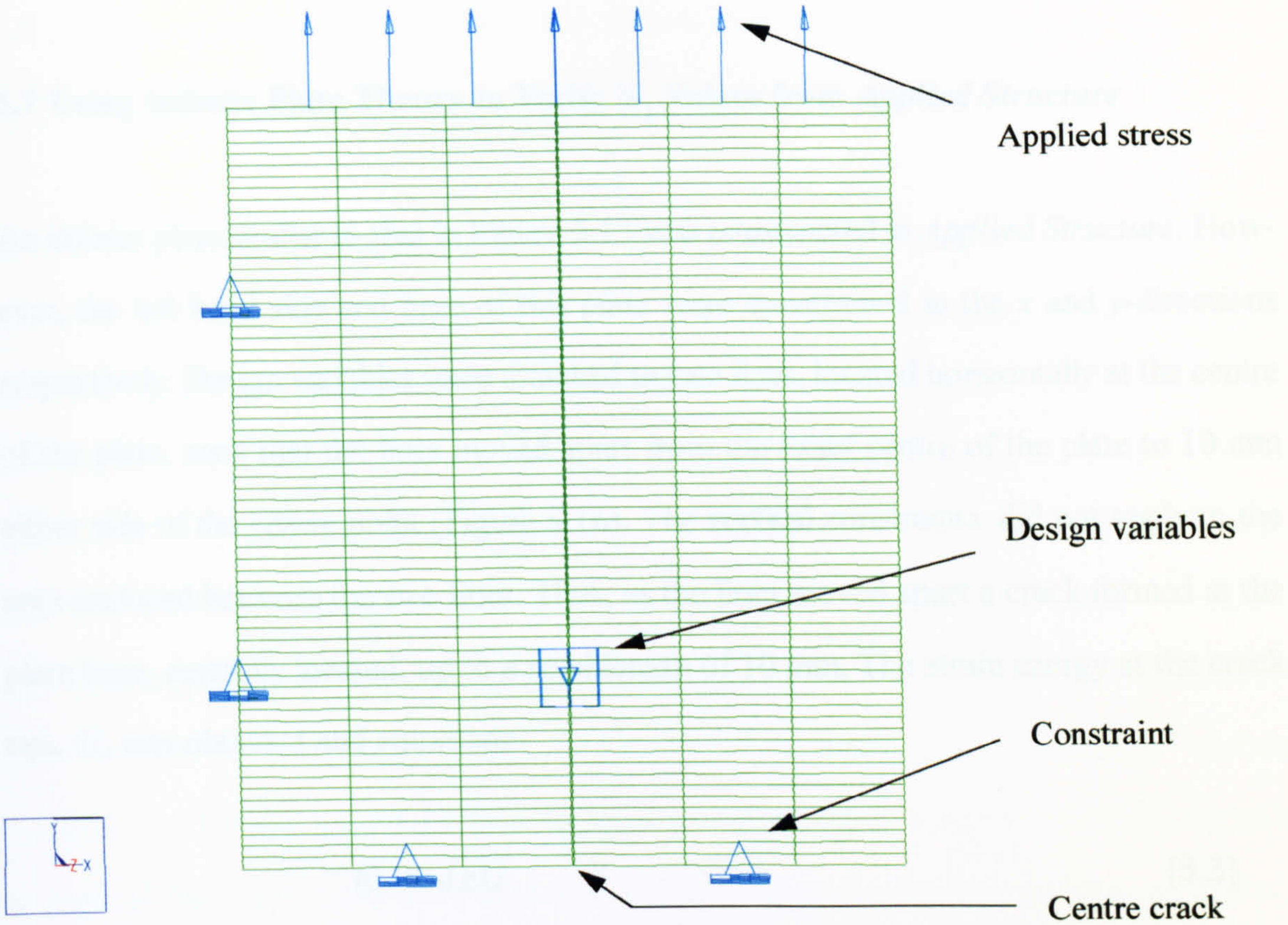

Figure 5.16 *Applied Structure mesh of reference plate, again showing design variables*

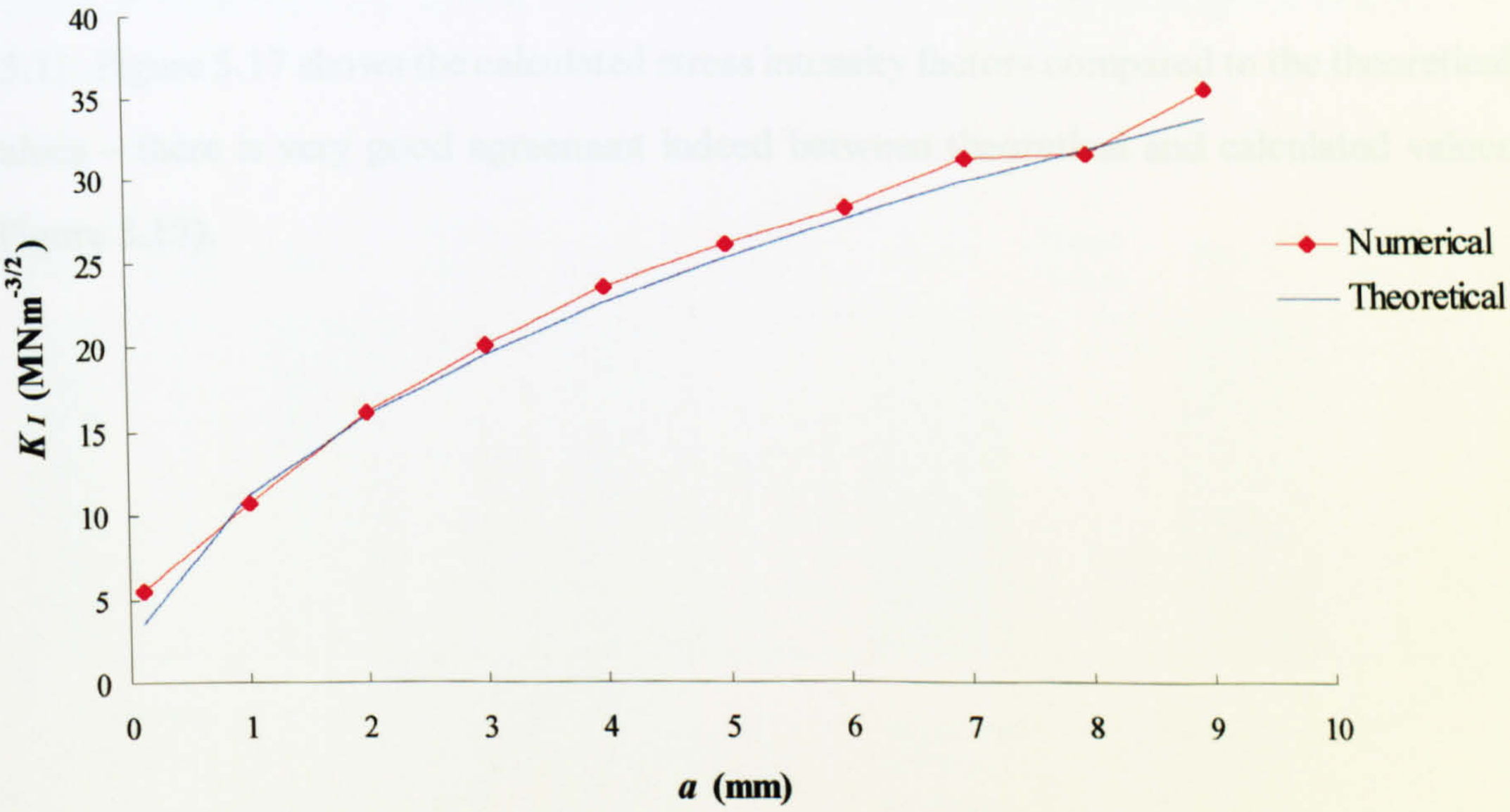

Figure 5.17 *The results from Applied Structure show very good agreement to the theoretically predicted results – due in this case to a "regular" mesh*

5.7 Using Infinite Plate Theory to Verify K_I Values from *Applied Structure*

An infinite plate similar to that in Figure 5.15 was constructed in *Applied Structure*. However, the left hand side and base of this plate were constrained in the x and y-directions respectively. Design variables were attached to two lines, located horizontally at the centre of the plate, such that the lines moved apart from the exact centre of the plate to 10 mm either side of the centre point (Figure 5.16). The vertical constraints did not apply to the area enclosed between the two lines. Thus, as the lines moved apart a crack formed at the plate base, centrally located, up to a semi length of 10 mm. The strain energy at the crack tips, U, was obtained and equations:

$$K_I = \sqrt{EG} \qquad \{5.3\}$$

and

$$G = \frac{\partial U}{\partial A} \qquad \{5.4\}$$

used to calculate K_I

The theoretical values for K_I were obtained from the infinite plate formula in Equation {5.1}. Figure 5.17 shows the calculated stress intensity factors compared to the theoretical values – there is very good agreement indeed between theoretical and calculated values (Figure 5.17).

5.8 Real time failure mechanisms – simulation

5.8.1 The use of contact surfaces in ABAQUS

A two-dimensional, axisymetric quarter model of a continuous fibre Al_2O_3/Al MMC was constructed in *ABAQUS*. From fractographic analysis and from manufacturer's data, the fibre diameter and volume fraction were determined to be 10 μm and 0.45 respectively. The composite modelled was 50 μm in length and 78 μm in width and consisted of nine fibres in ten matrix bays, which when constructed as a symmetrical quarter model reduced to the four and a half fibres situated in five matrix bays as shown in Figure 5.18. Table 5.3 shows the material properties applied to the fibres and matrix bays. The differing failure mechanisms incorporated into the model used the "contact surface", "bond surface" and "debond" options available in *ABAQUS* together with a "fracture criterion" sub-option. Critical nodal stresses in front of the crack tip(s) were used to determine the particular time and type of failure. Mode I cracking for both fibre and matrix, fibre bridging and fibre/matrix debonding were all incorporated into the model.

The *ABAQUS* debond options, all use a master/slave surface concept. In the models discussed here, element faces making up the fibre side of the fibre/matrix interface were chosen to constitute the master surfaces, and element faces comprising the matrix side

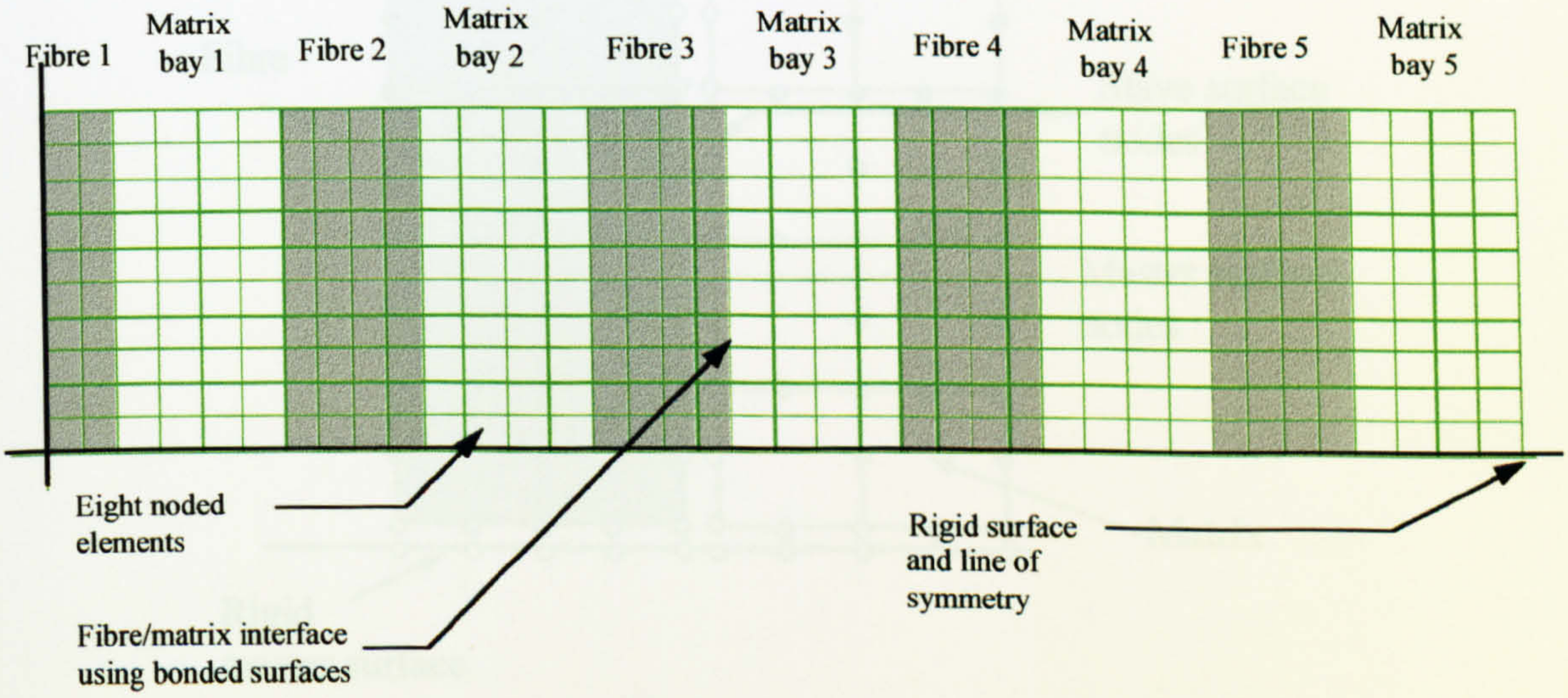

Figure 5.18 *Finite element mesh showing four and a half fibres situated in five matrix bays*

Table 5.3 *Material properties of Al_2O_3/Al composite*

Property	E (GPa)	v
Al_2O_3 fibre	210	68.9
Al matrix	0.3	0.33

were selected as the slave surfaces (Figure 5.19). For the fibre/matrix interface, the fibre-side surface was chosen as the master and the matrix side surface as the slave – i.e. the surface comprised of the stiffer element set was selected as the master [4]. A rigid surface defined the *r*-axis and the composite was bonded to this surface in the normal direction only, thus allowing for mode I failure, but also allowing for Poisson contraction of the composite (Figure 5.19). Of the three debond options available in *ABAQUS* (*finite sliding*, *small sliding* and *infinitesimal sliding*), the *small sliding* option was chosen for computational efficiency and because this method of contact modelling was well suited to the problem of composite failure. Figure 5.20 is a schematic of how the small sliding algorithm works: using initial nodal coordinates, unit normal vectors are first computed for all nodes on the master surface, e.g. $\mathbf{N}_a$ and $\mathbf{N}_b$. These unit normal vectors are used to define a smooth varying normal vector $\mathbf{N}(x)$, at any point, x, on the master surface. The algorithm then determines which master nodes will interact with slave node c for the entire analysis.

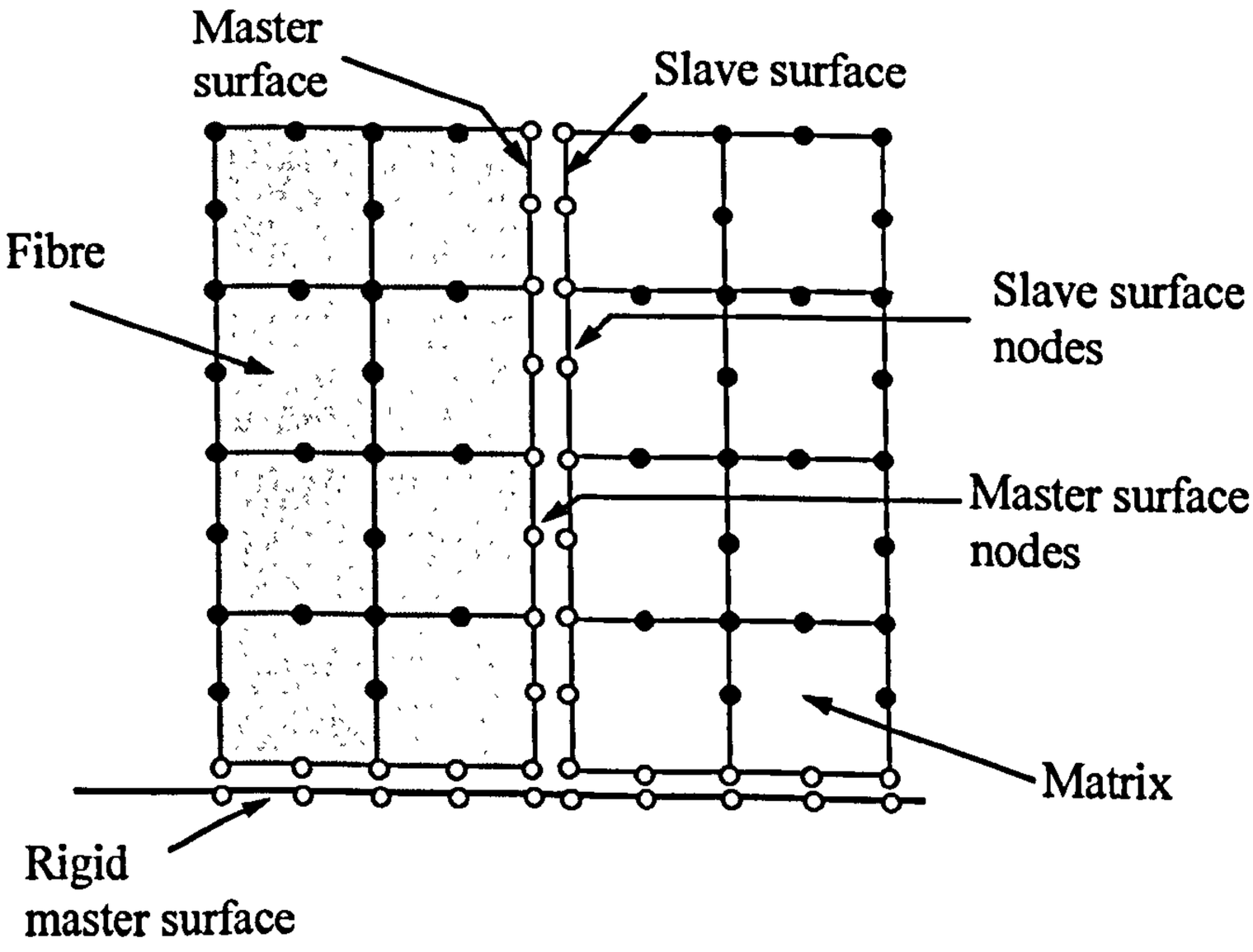

Figure 5.19 *Elements and nodes making up the master/slave surfaces for the fibre/ matrix interface and the r-axis, composite bonding*

Table 5.4 *Failure properties of composite*

	First run 1 UTS		Second run UTS	
	σ_c (MPa)	τ_c (MPa)	σ_c (MPa)	τ_c (MPa)
Fibre	1775	887.5	1775	887.5
Matrix	190	95	190	95
Interface	190	95	903.25	451.63

A point on the surface, x_0, is computed for slave node *c* such that the vector formed by the slave node and x_0 coincide with $N(x_0)$. The example in Figure 5.20 assumes that x_0 is on the element face with end nodes *a* and *b*. A potential contact condition between node *c* and the line perpendicular to $N(x_0)$ will be enforced. At any time $t > 0$, node *c* is constrained not to penetrate this line. The load transfer always occurs between node *c* and nodes *a* and *b*.

Mode I failure of the fibre was set at the UTS of the fibre and similarly mode I failure of the matrix was set at the matrix UTS [See Bill F for book].

To determine interfacial bond strength, initially, data from monotonic loading of specimens in three-point bending were used via the short-beam bend test. Using the equations:

$$\tau = \frac{3}{4}\frac{F}{bd} \qquad \{5.7\}$$

and

$$\sigma = \frac{2l\tau}{d} \qquad \{5.8\}$$

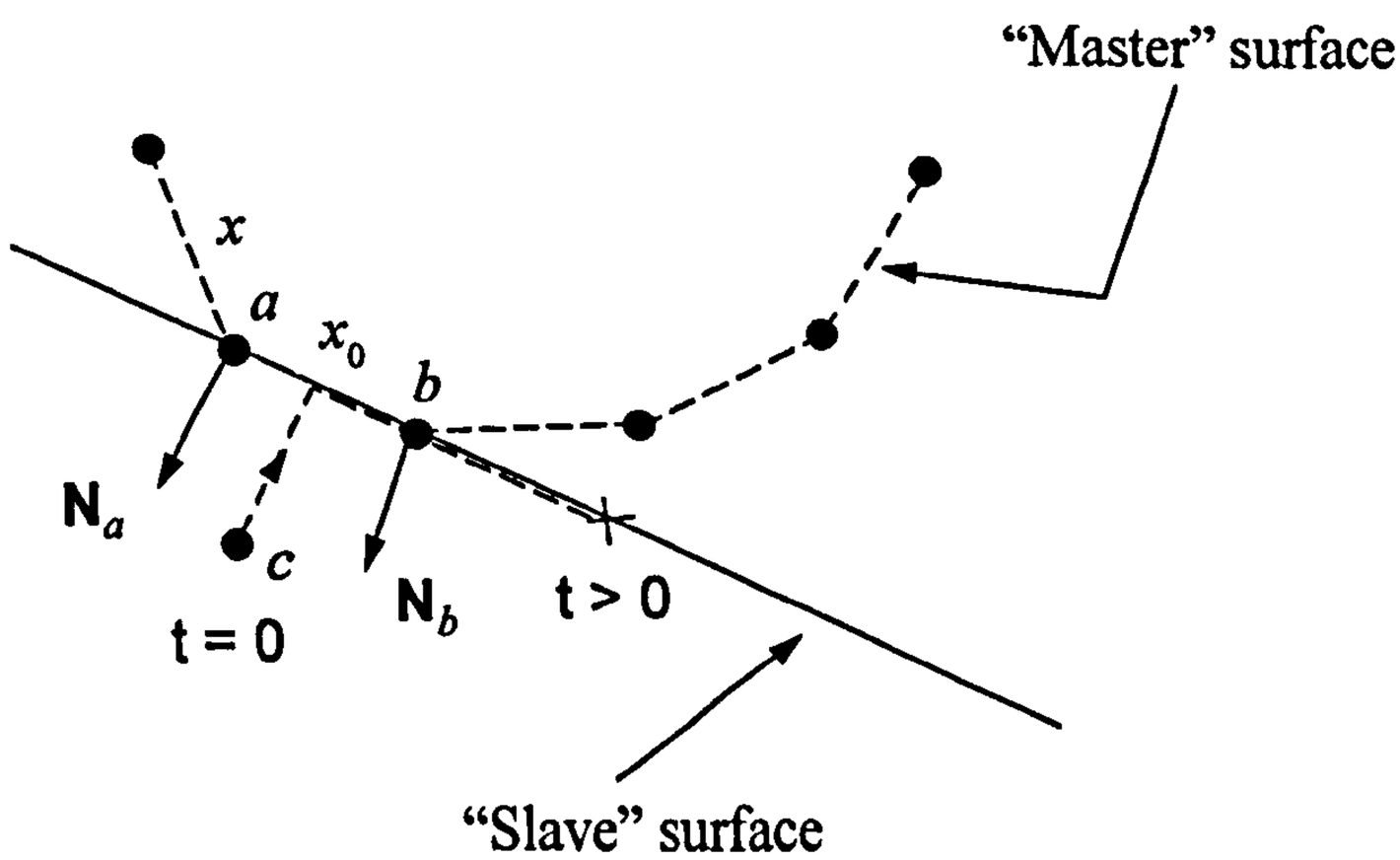

Figure 5.20 *Schematic showing debonding algorithm in ABAQUS*

where F was the applied fracture force, b the sample width, d, the sample breadth, l the distance between the outer loading points. The values obtained for σ and τ were: from {5.7} $\tau = 31.7$ MPa leading to $\sigma = 589$ MPa from {5.8}. Compared to the UTS values of the individual constituents σ seemed high compared to the UTS of aluminium and τ seemed too low (see Table 5.4). Given that the short-beam bend test was known to be highly sensitive to composite volume fraction, it was felt that the above figures were inaccurate. The nodal failure stresses for the fibre/matrix interface were therefore set at the UTS values of the matrix [4]. The failure criterion was set as follows:

$$\sqrt{\left(\frac{\hat{\sigma}_n}{\sigma^f}\right)^2 + \left(\frac{\tau_1}{\tau_1^f}\right)^2 + \left(\frac{\tau_2}{\tau_2^f}\right)^2} = f\,,\ \hat{\sigma}_n = \max(\sigma_n, 0) \qquad \{5.9\}$$

where σ_n is the normal component of stress carried across the interface, τ_1 and τ_2 are the shear stress components in the interface, and σ^f, τ_1^f, τ_2^f are the normal and shear failure stresses. A crack tip node debonds when the fracture criterion, f, reaches the value 1.0 within a given tolerance: $1 - f_{tol} \leq f \leq 1 + f_{tol}$. f_{tol} was set at 0.05 for the duration of the modelling [4]. Also the shear stresses τ_1^f and τ_2^f were set at 50% σ^f.

The model was run twice, once with the fibre/matrix interface set at the matrix UTS, the second time with the interface bonding set at the UTS obtained by a rule of mixtures (RoM) formula (Table 5.4): 0.45 UTS_{fibre} + 0.55 UTS_{matrix}.

A tensile total strain of 1% was applied to the composite. The left hand side of the model was constrained radially. A crack was seeded in the right hand side matrix bay, by excluding the end node from the node list making up the bonded surfaces (Figure 5.21). The strain was applied incrementally and the type and progress of the failure mechanisms observed for each increment. The model run was complete at either 1% applied strain or total composite failure.

5.8.2 Running the simulation

Crack propagation started along the matrix as soon as the critical nodal stress reached the

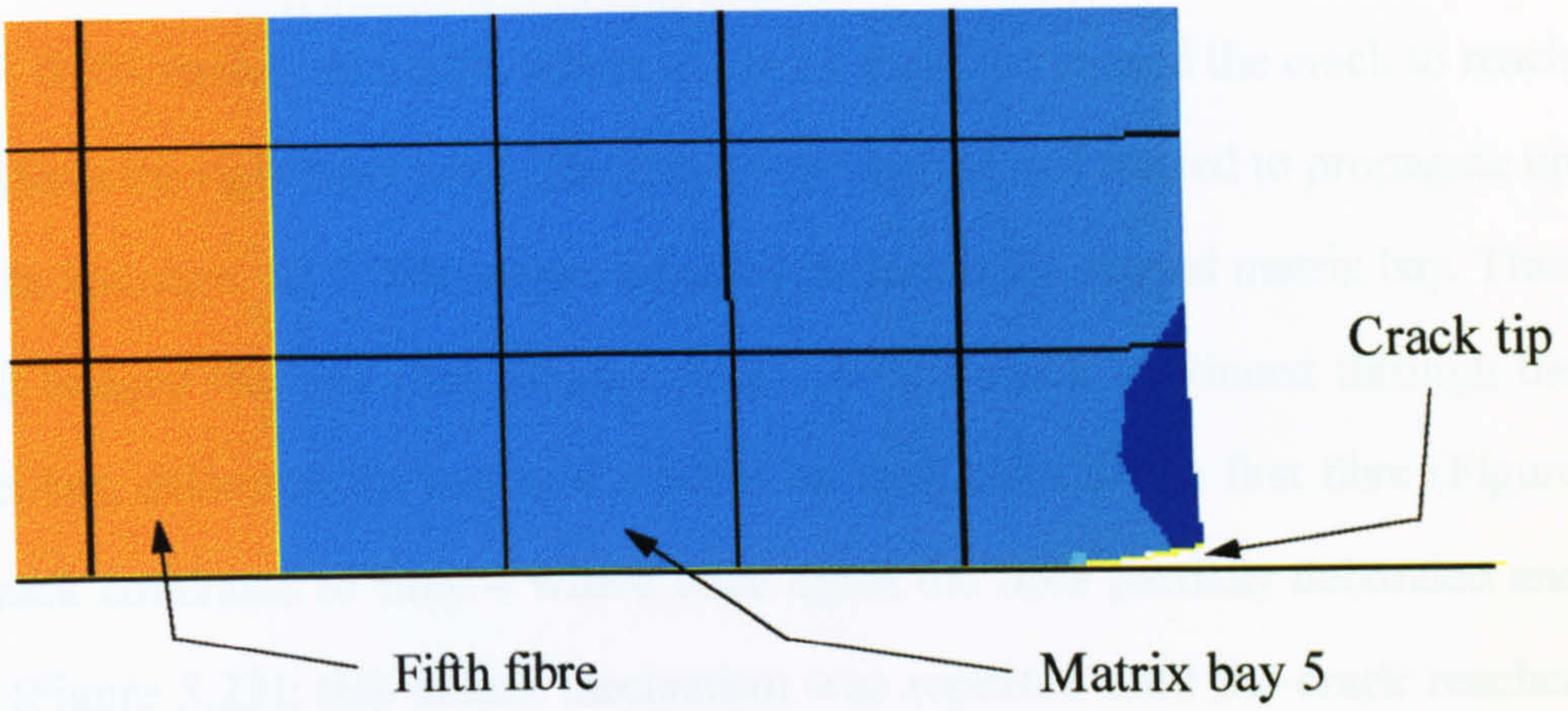

Figure 5.21 *Seed edge crack on right hand side of matrix bay*

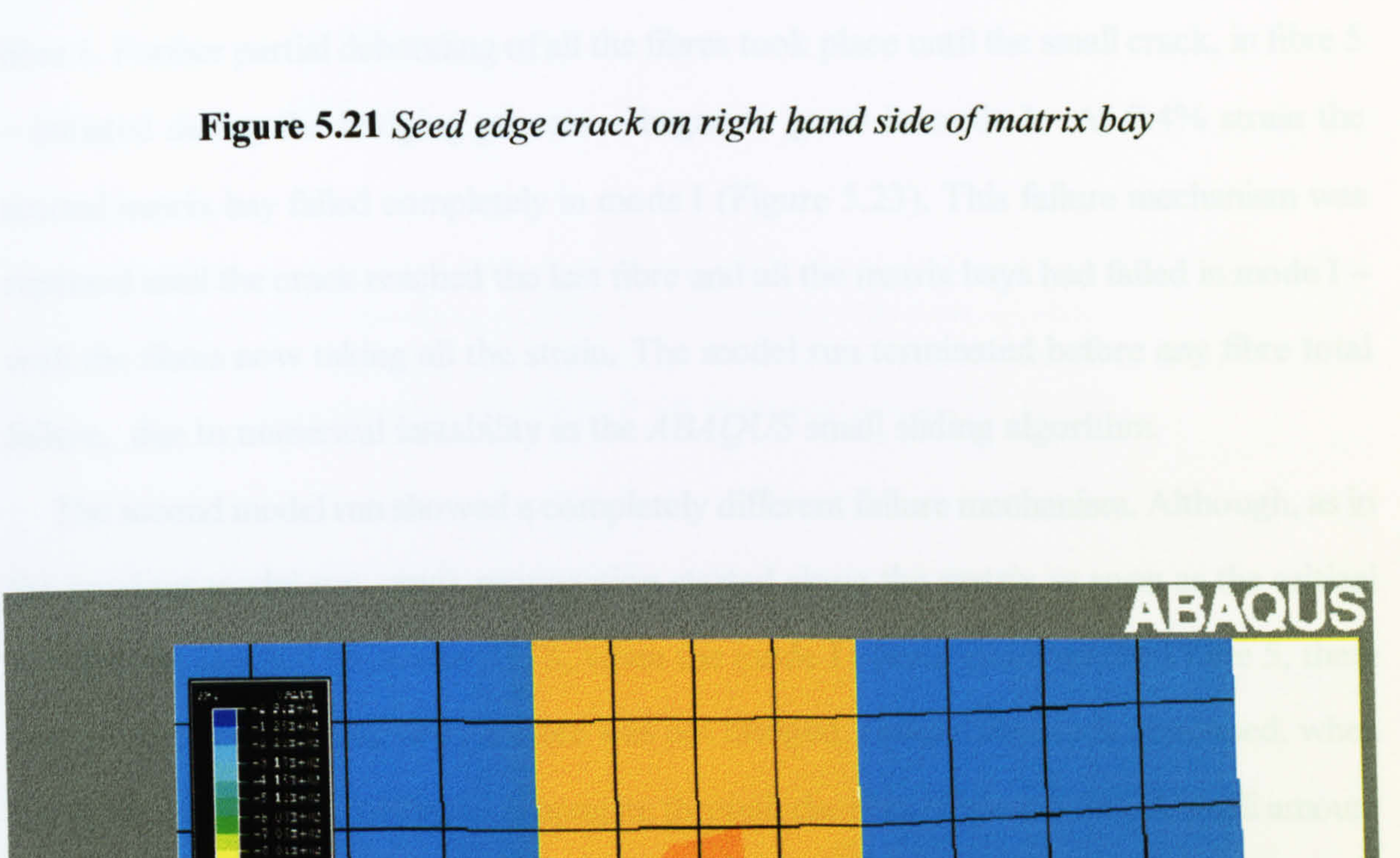

Figure 5.22 *Fibre bridging and partial fibre/matrix debonding*

matrix UTS (~ 0.2% strain). At 0.25% strain, mode I failure had caused the crack to reach the first fibre (from the right hand side). The crack was blunted, but started to propagate up the fibre/matrix interface. At 0.28% strain, cracking began in the second matrix bay. Thus the crack had bridged the first fibre (Figure 5.22). As the crack continued through the second matrix bay, delamination was now evident on both sides of the first fibre (Figure 5.23). The crack continued to fibre 4 where once again the fibre partially debonded and was bridged (Figure 5.23); this failure mechanism was repeated until the crack reached fibre 1. Further partial debonding of all the fibres took place until the small crack, in fibre 5 – initiated during the bridging process – began to grow in mode I. At 0.4% strain the second matrix bay failed completely in mode I (Figure 5.23). This failure mechanism was repeated until the crack reached the last fibre and all the matrix bays had failed in mode I – with the fibres now taking all the strain. The model run terminated before any fibre total failure, due to numerical instability in the *ABAQUS* small sliding algorithm.

The second model run showed a completely different failure mechanism. Although, as in the previous model run, crack propagation started along the matrix as soon as the critical nodal stress reached the matrix UTS, when the mode I matrix crack reached fibre 5, there was no partial debonding and the fibre was not bridged. Instead the crack continued, when the applied strain was 0.48%, to propagate through the fibre (Figure 5.24). A small amount of fibre matrix delamination was also apparent at the fibre matrix interface, where the mode I crack had entered the fibre. Again, due to the instability of the small sliding algorithm in *ABAQUS*, the model run terminated before the fibre completely failed.

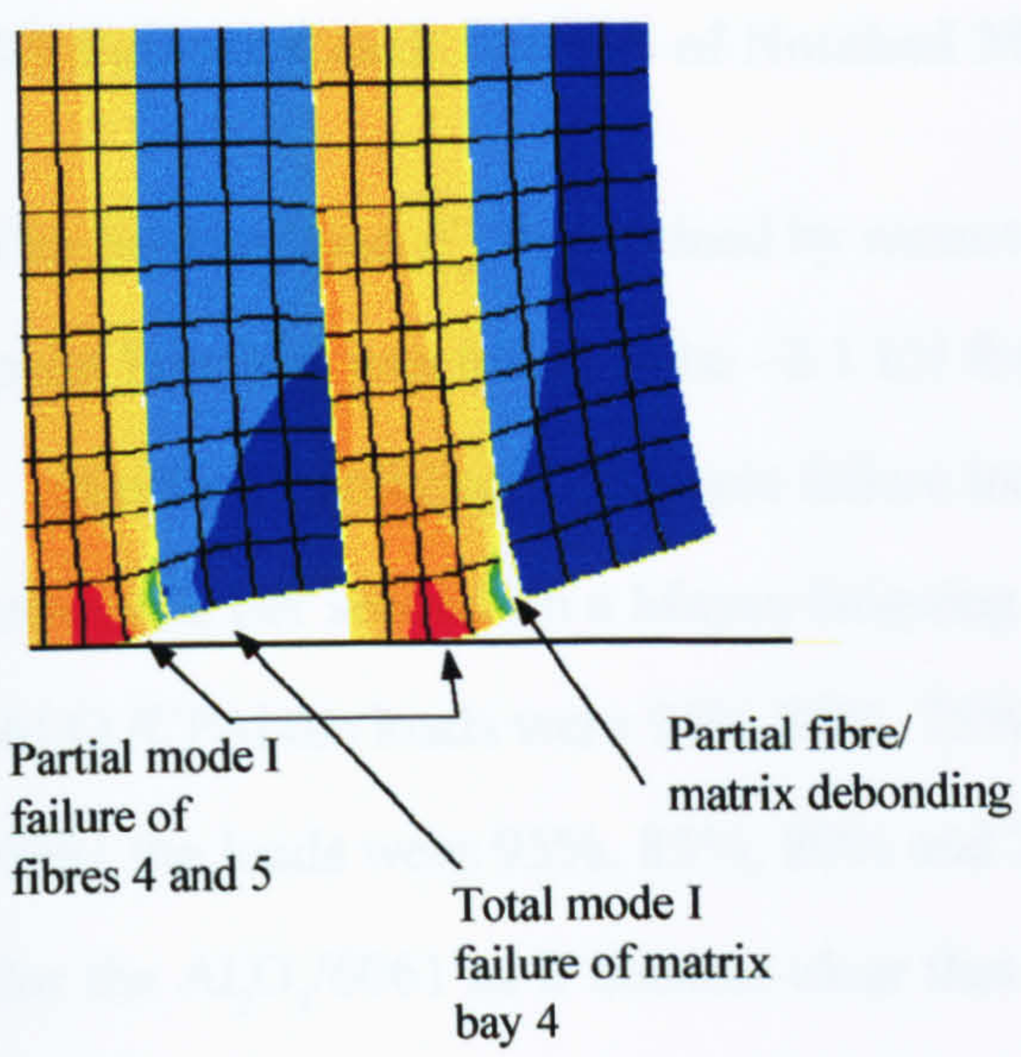

Figure 5.23 *(a) Total mode I failure of matrix bays 4 and 5 together with partial mode I failure and partial debonding of fibre 5 – this model has been distorted by a factor of 10 to highlight the differing types of failure mechanism; (b) schematic diagram of (a) showing how the fibres have been bridged by the matrix*

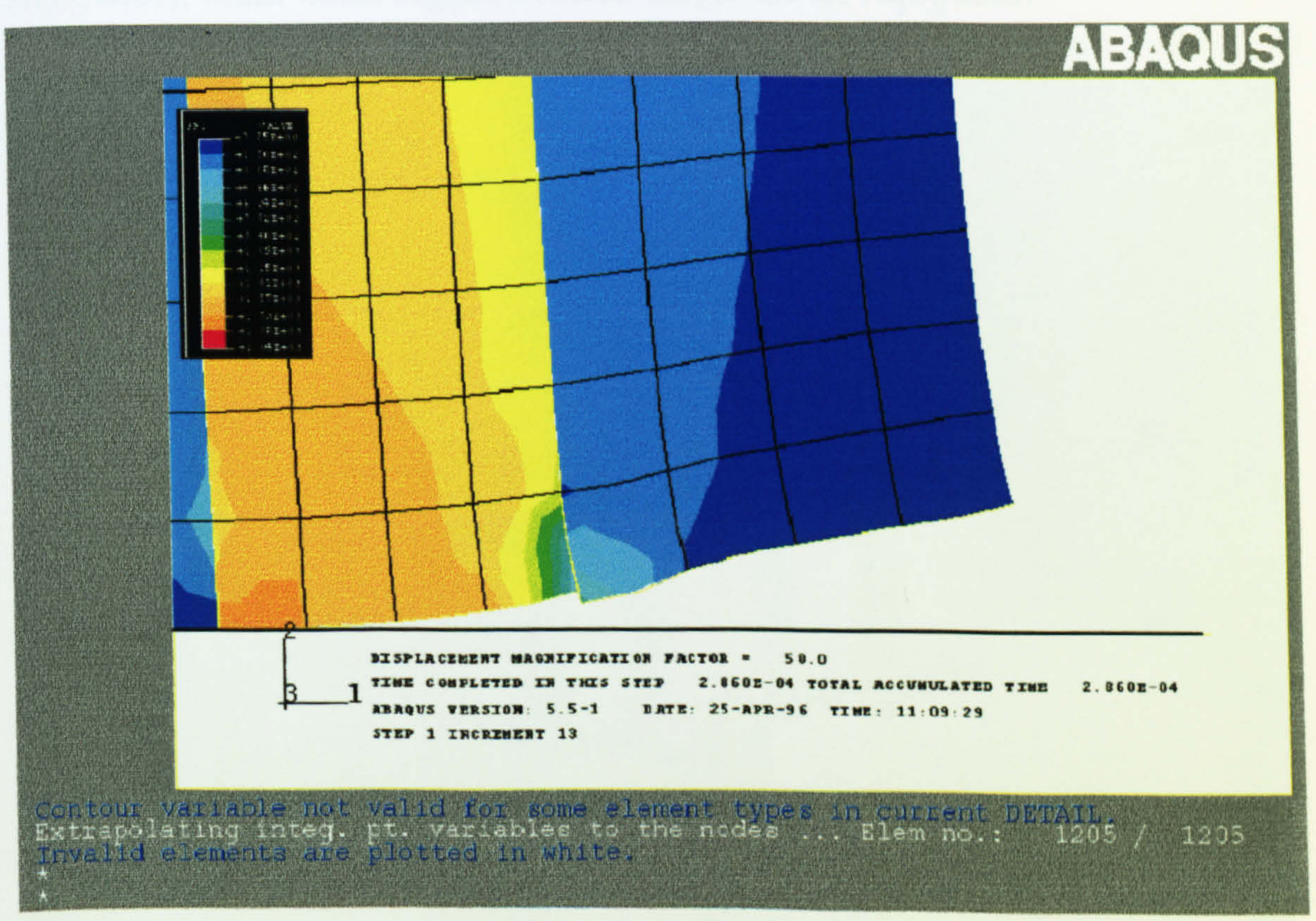

Figure 5.24 *Mode I crack is not arrested at fibre/matrix interface, but continues into the fibre*

5.9 Fatigue Crack Growth of Notched MMC Specimens

The fracture load F_o, determined by monotonically breaking a notched specimen in three-point bending, was found to be ~2.1 kN for both types of specimen.

Having established the sample failure load, the samples were fatigued at a frequency of one cycle per second on a Mayes fatiguing rig (Figure 5.25). Four loads were chosen: for Al_2O_3/CPAl the loads were 95%,80%, 75% and 70% of fracture load (2.1 kN). For Al_2O_3/6061 the loads were 95%, 85%, 80% and 70% of fracture load (higher loads were chosen for the Al_2O_3/6061 as it became clear that this composite had a much greater fatigue life than the Al_2O_3/CPAl and it became clear that at the lower loads, Al_2O_3/CPAl would not fail in a reasonable time period for the chosen frequency).

The results for both Al_2O_3/CPAl and Al_2O_3/6061 are summarised in Table 5.5. It is quite clear from Table 5.5 that Al_2O_3/6061, whilst having an identical failure stress has a fatigue life in the order of 10-100 times that of Al_2O_3/CPAL; this would seem to contradict the UTS figures for both types of material (761.5 GPa for Al_2O_3/CPAl and 301.3 GPa for Al_2O_3/6061), which would suggest a shorter fatigue life for Al_2O_3/6061.

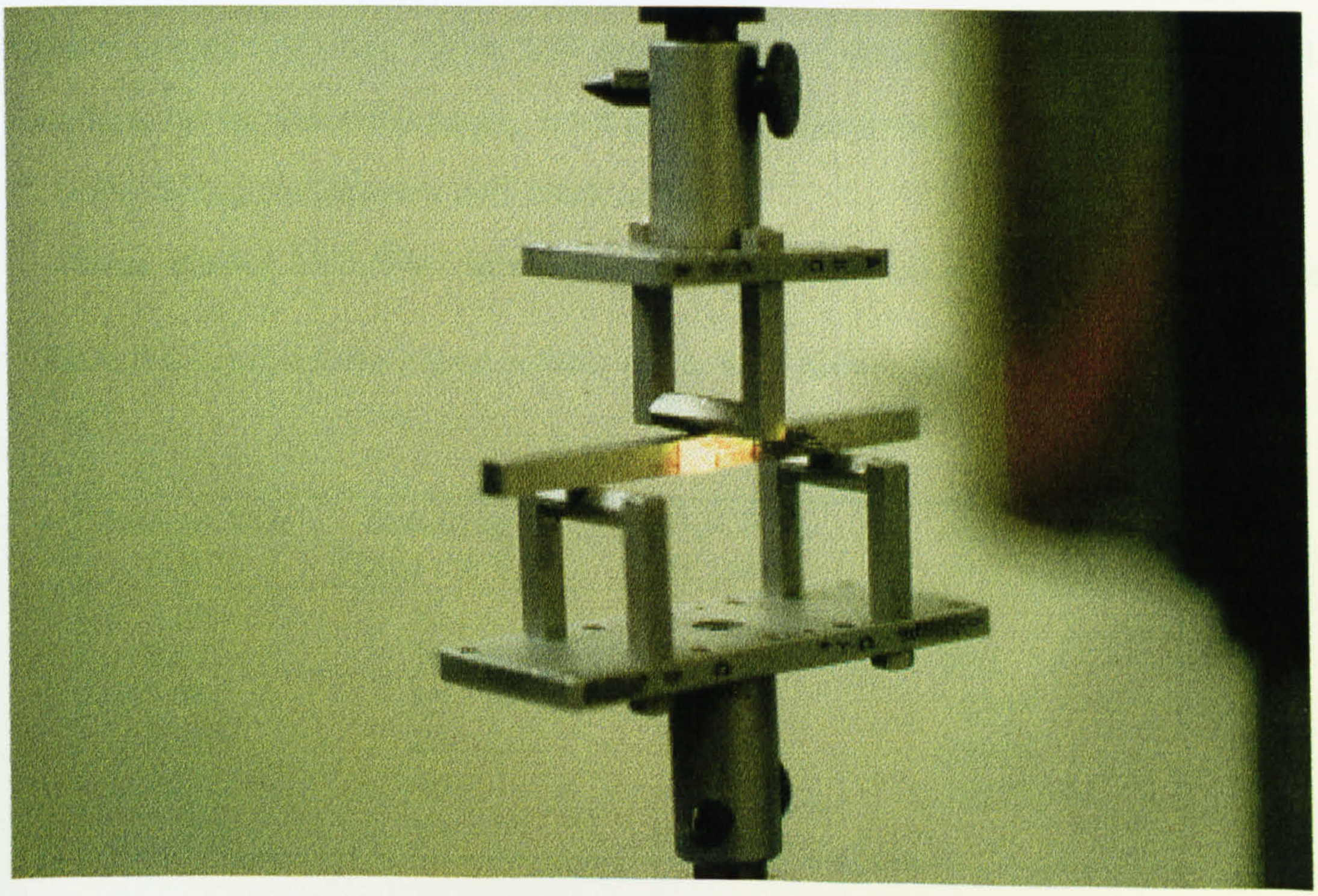

Figure 5.25 *Three point bend specimen in sample holder*

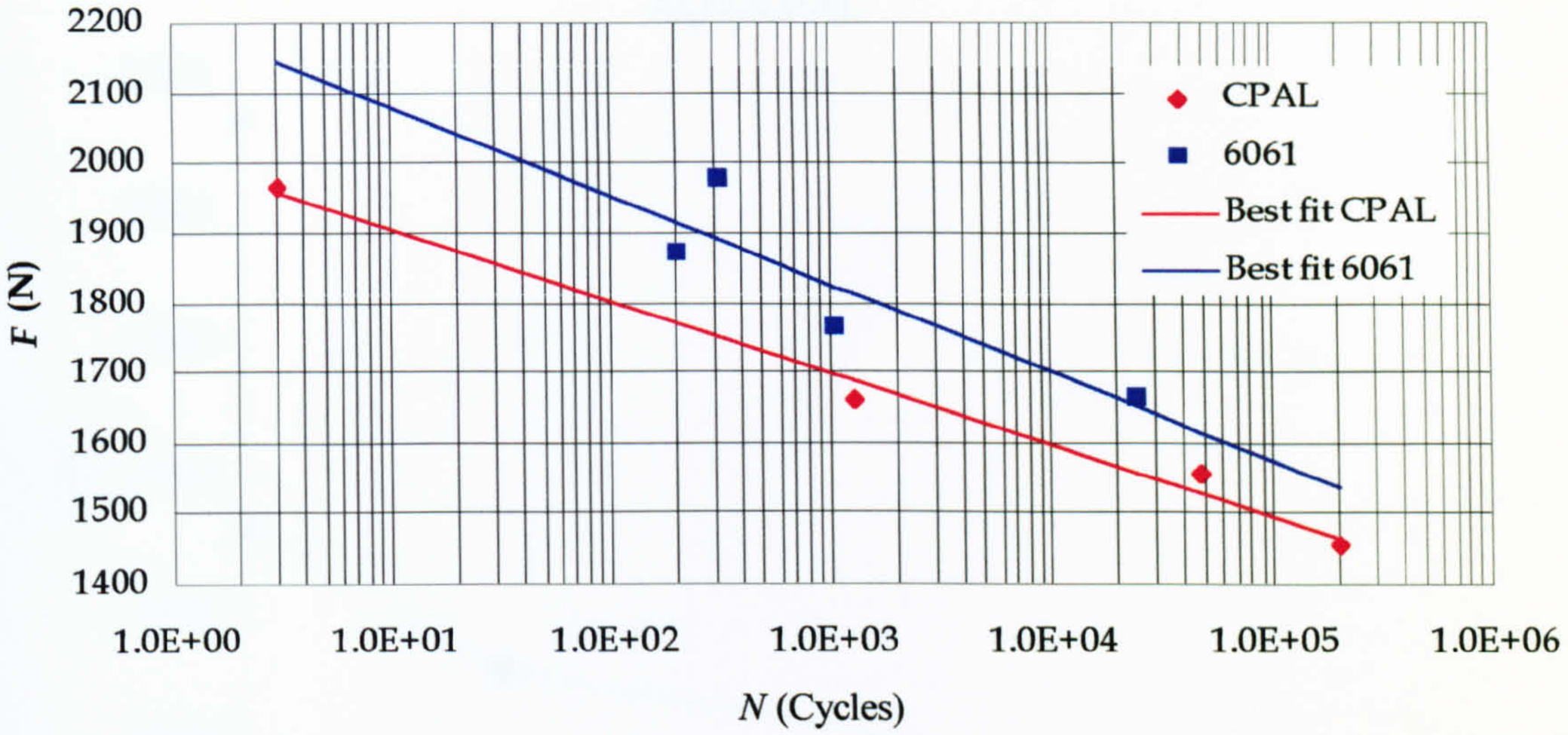

Figure 5.26 *Log-linear graph of Al_2O_3/CPAl and Al_2O_3/6061, together with their respective lines of best fit*

A detailed log-linear graph of the samples' fatigue life, complete with lines of best fit, is shown in Figure 5.26, while linear S/N graphs for Al_2O_3/CPAl and Al_2O_3/6061 samples are shown in Figures 5.27 and 5.28 respectively.

For an applied 75% breaking force, Figure 5.29 illustrates a plot of crack length a vs number of cycles N, while Figure 5.30 shows a plot of da/dN vs ΔK for an Al_2O_3/6061 sample; as can be seen in this figure, crack growth reaches a maximum at $\Delta K = 19.1$ $MNm^{-3/2}$, before falling continuously until crack arrest.

For an unfailed Al_2O_3/6061 bend specimen, Figure 5.31 (a) shows a crack leaving the

Table 5.5 *Applied force v total number of cycles to failure for Al_2O_3/CPAl and Al_2O_3/6061*

Fatigue load F (kN)	Breaking Force (% F_o)	Al_2O_3/CPAL *N* (Cycles)	Al_2O_3/6061 *N* (Cycles)
1.968	95	3	312
1.872	90	-	200
1.768	85	-	1057
1.661	80	1264	23953
1.560	75	47056	748739 *
1.453	70	196482	-

* Indicates material did not fail

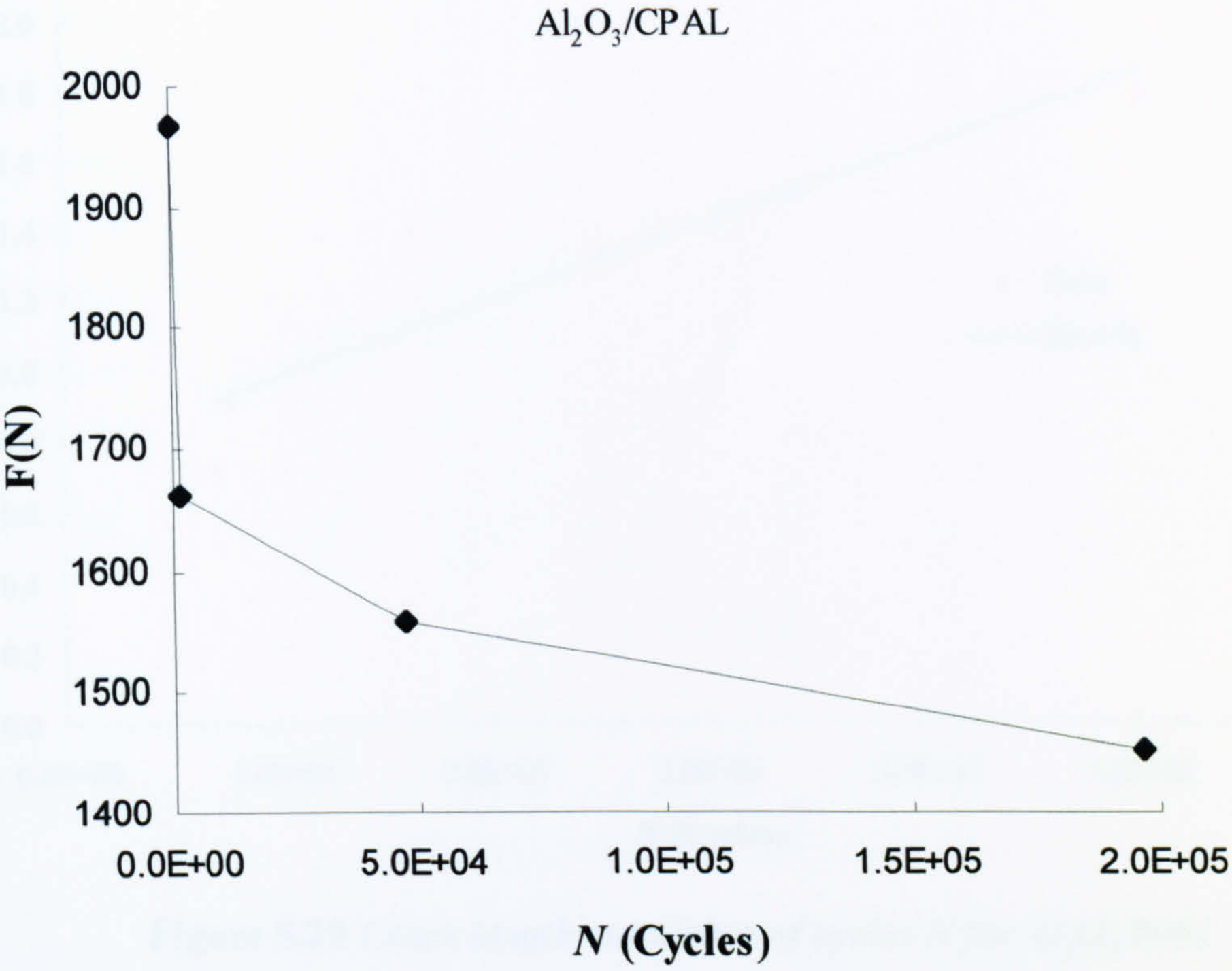

Figure 5.27 *Linear S/N curves of Al_2O_3/CPAl*

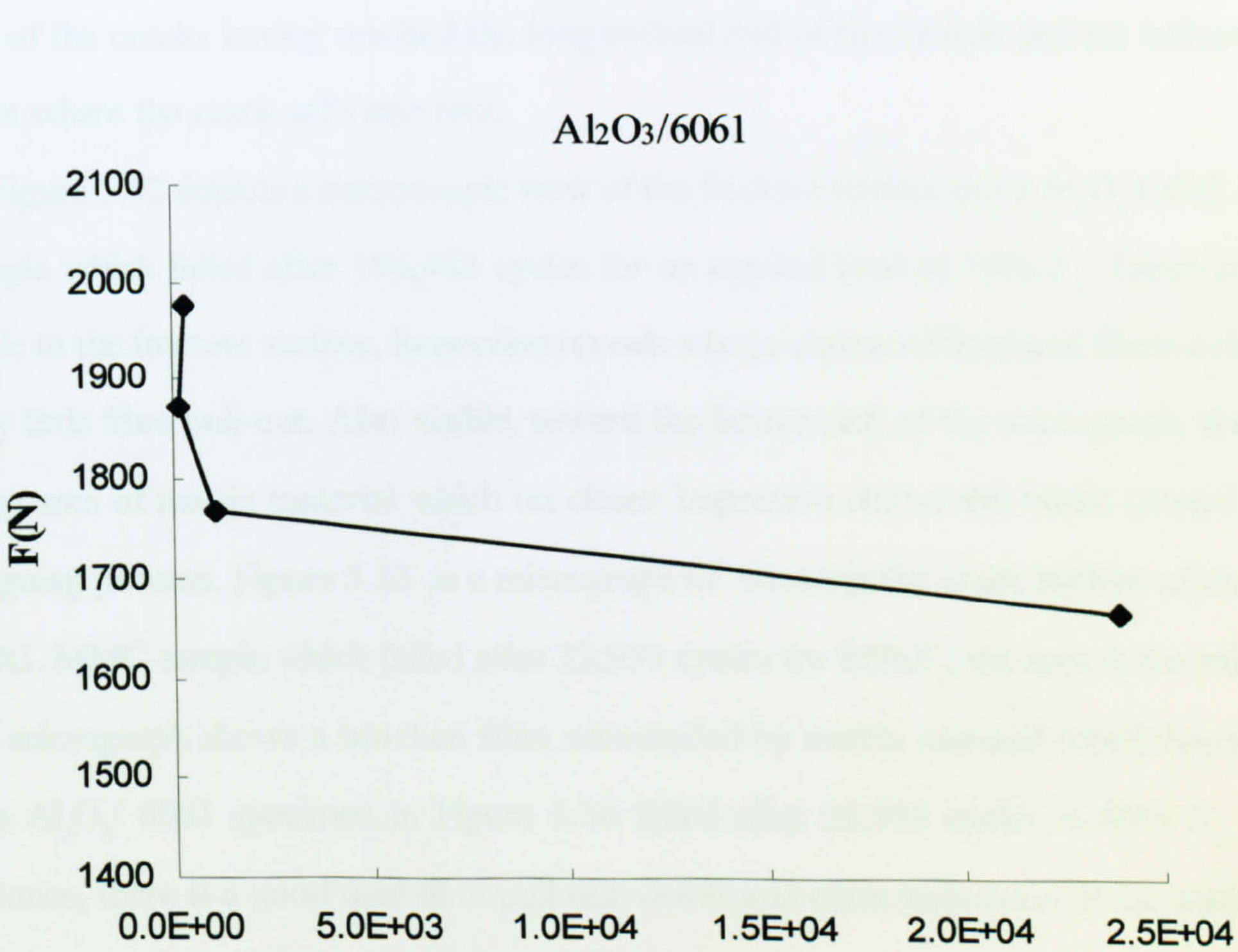

Figure 5.28 *Linear S/N curves of Al_2O_3/6061*

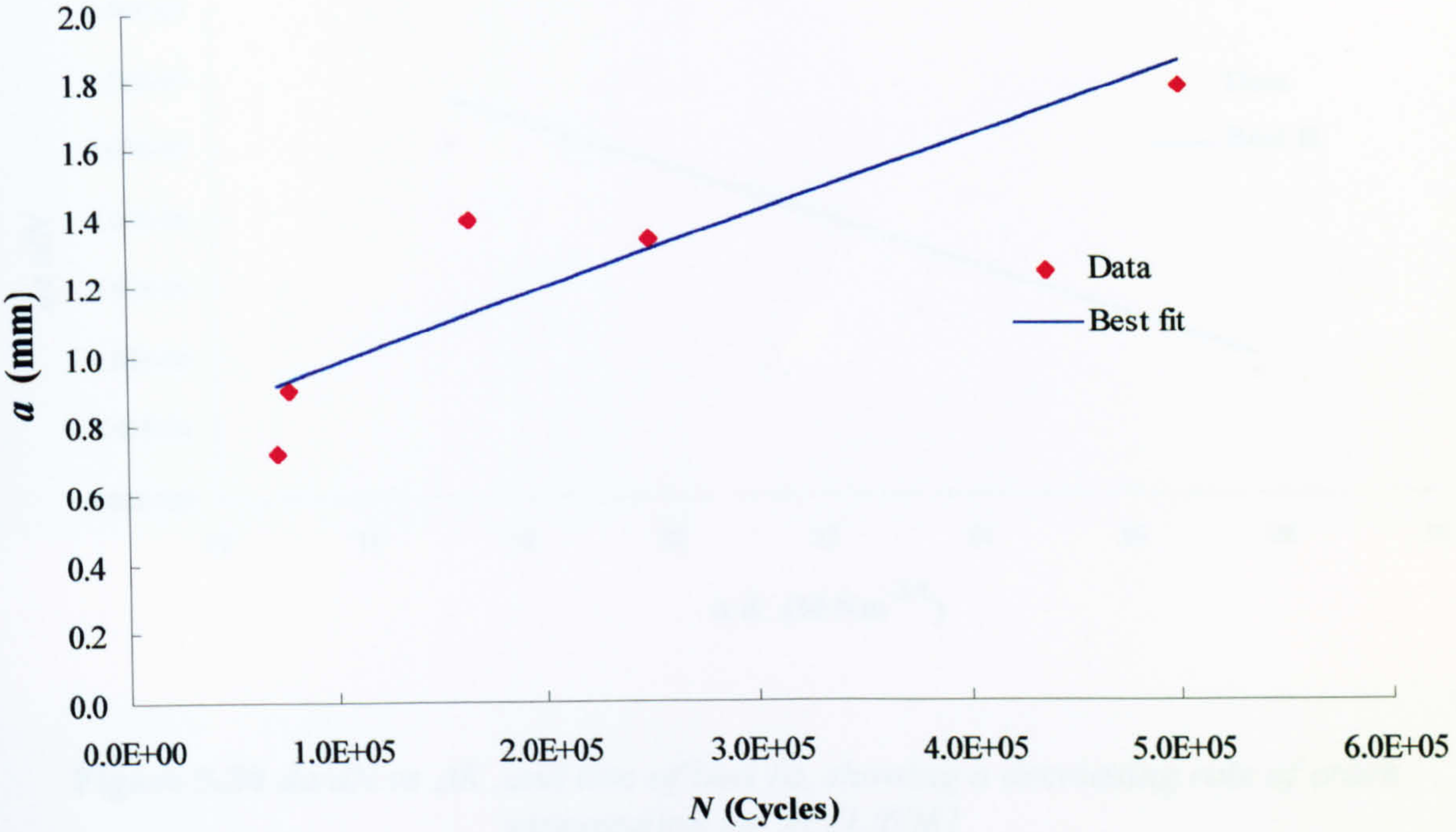

Figure 5.29 *Crack length vs number of cycles N for Al_2O_3/6061*

notch tip at an angle and splitting into two further cracks. Figure 5.31 (b) depicts the same view, but as seen from directly above, (c) shows the site of the crack initiation, (d) shows one of the cracks having reached the longitudinal end of the sample and (e) indicates the point where the crack split into two.

Figure 5.32 depicts a microscopic view of the fracture surface of an Al_2O_3/CPAL MMC sample which failed after 196,482 cycles for an applied load of 70% F_o. Taken at a 45° angle to the fracture surface, inspection reveals a large cluster of fractured fibres exhibiting very little fibre pull-out. Also visible, toward the bottom left of the micrograph, there is a large area of matrix material which on closer inspection shows slip bands caused by the fatiguing process. Figure 5.33 is a micrograph of showing the crack surface of an Al_2O_3/ CPAL MMC sample which failed after 23,953 cycles for 80%F_0; the area in the middle of the micrograph shows a brocken fibre surrounded by matrix material which has yielded. The Al_3O_3/ 6061 specimen in Figure 5.34 failed after 23,953 cycles at 80% F_o. In this instance, there is a good deal fibre pull-out visible and close inspection of the micrograph shows some of the fibres displaying multiple fracture sites along their longitudinal axis. Figure 5.35 is a close up of the above specimen showing an embedded fibre which has

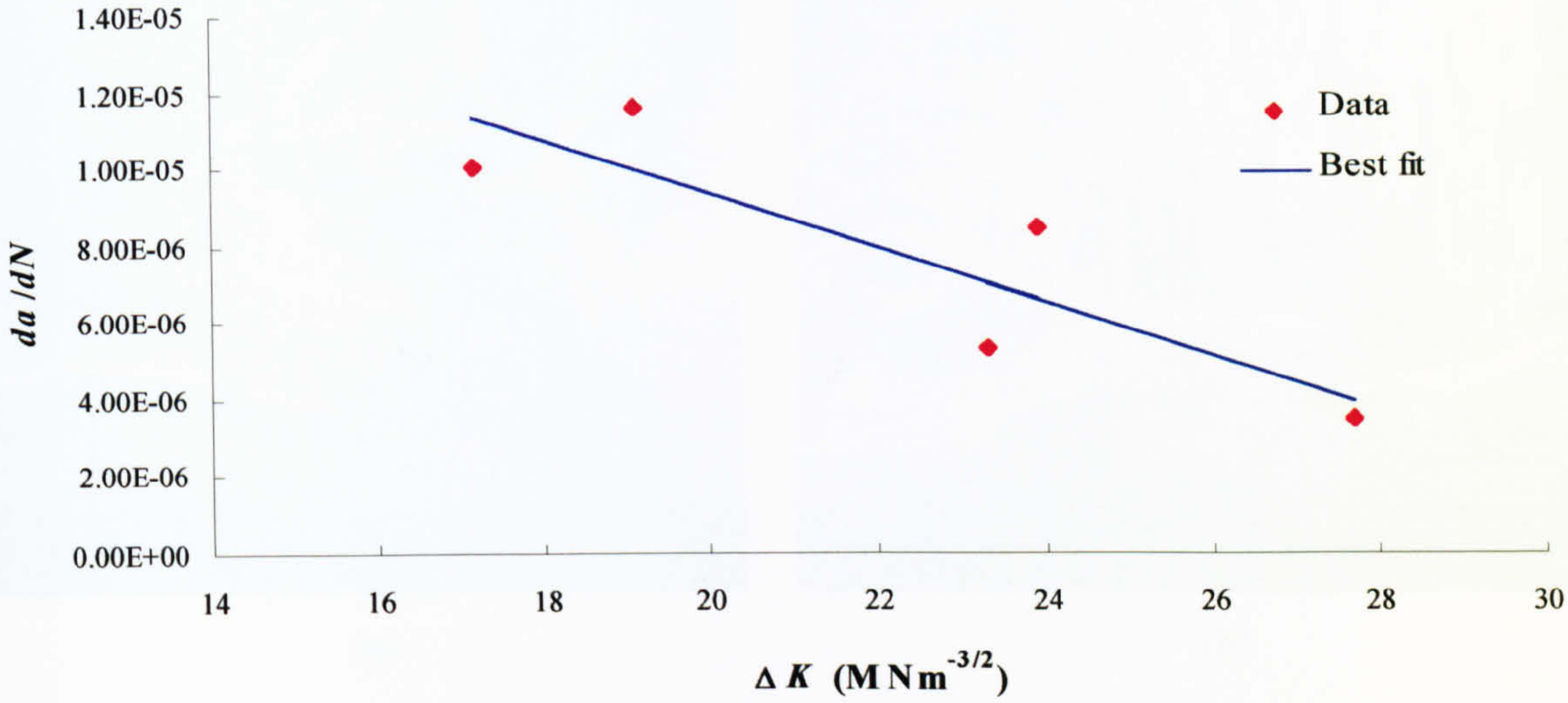

Figure 5.30 *da/dN vs ΔK ,and line of best fit, showing a decreasing rate of crack propagation for Al_2O_3/6061*

completely fractured into two sections the upper section having completely pulled out of the matrix; Figure 5.36 shows a fibre debonding from the matrix material.

5.10 Fatigue Crack Growth of Notched MMC Specimens in Sea Water

The fatigue life data obtained by testing Al_2O_3/6061 specimens at 1 Hz in sea water, along with the air test results, is shown in Figure 5.37. The best fit results for sea water show a reduction in fatigue life per given cycle. The gradients of the lines of best fit are –118.701 for air fatiguing and –111.726 for sea fatiguing which are very similar, which translates into a ratio of lines of best fit for the two sets of data having an average of 96% (of air fatiguing) with standard deviation 0.13% .

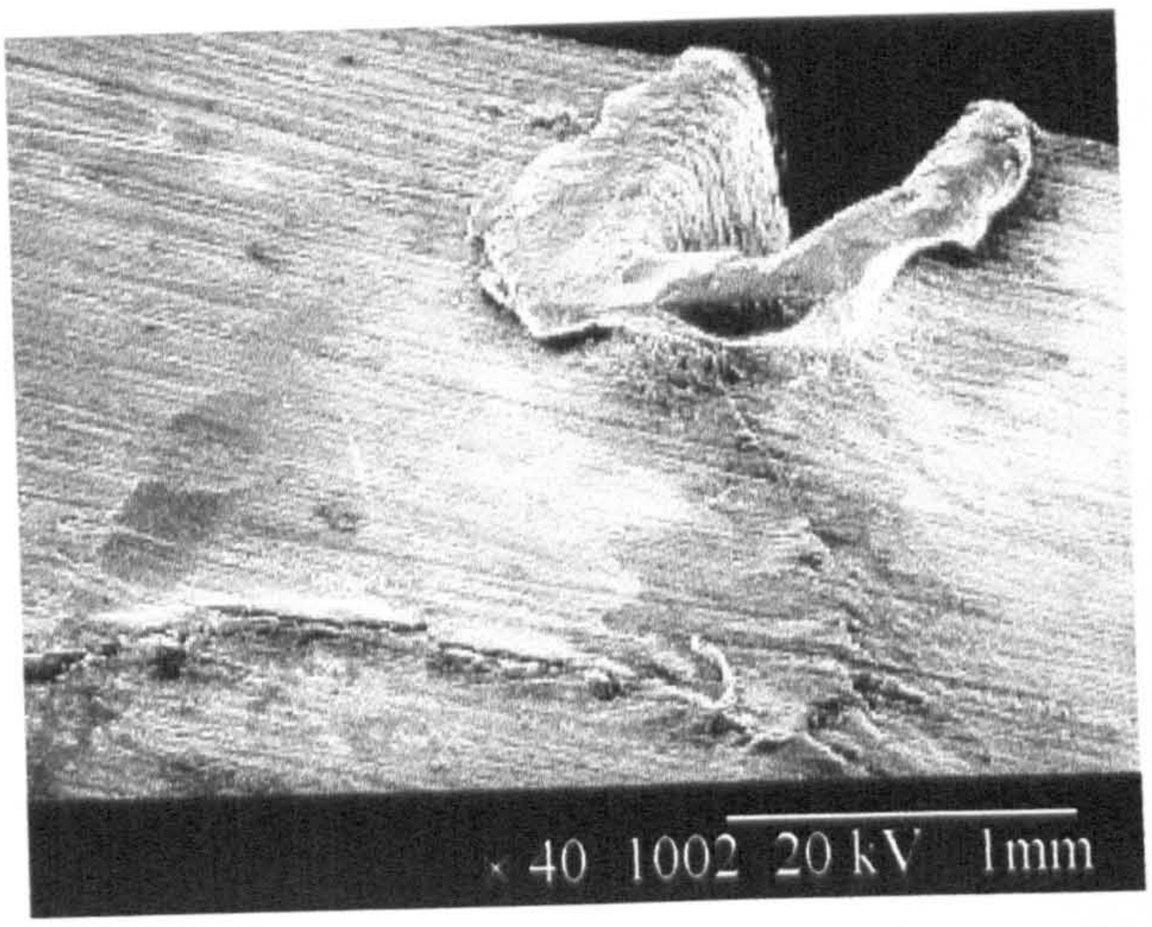

(a)

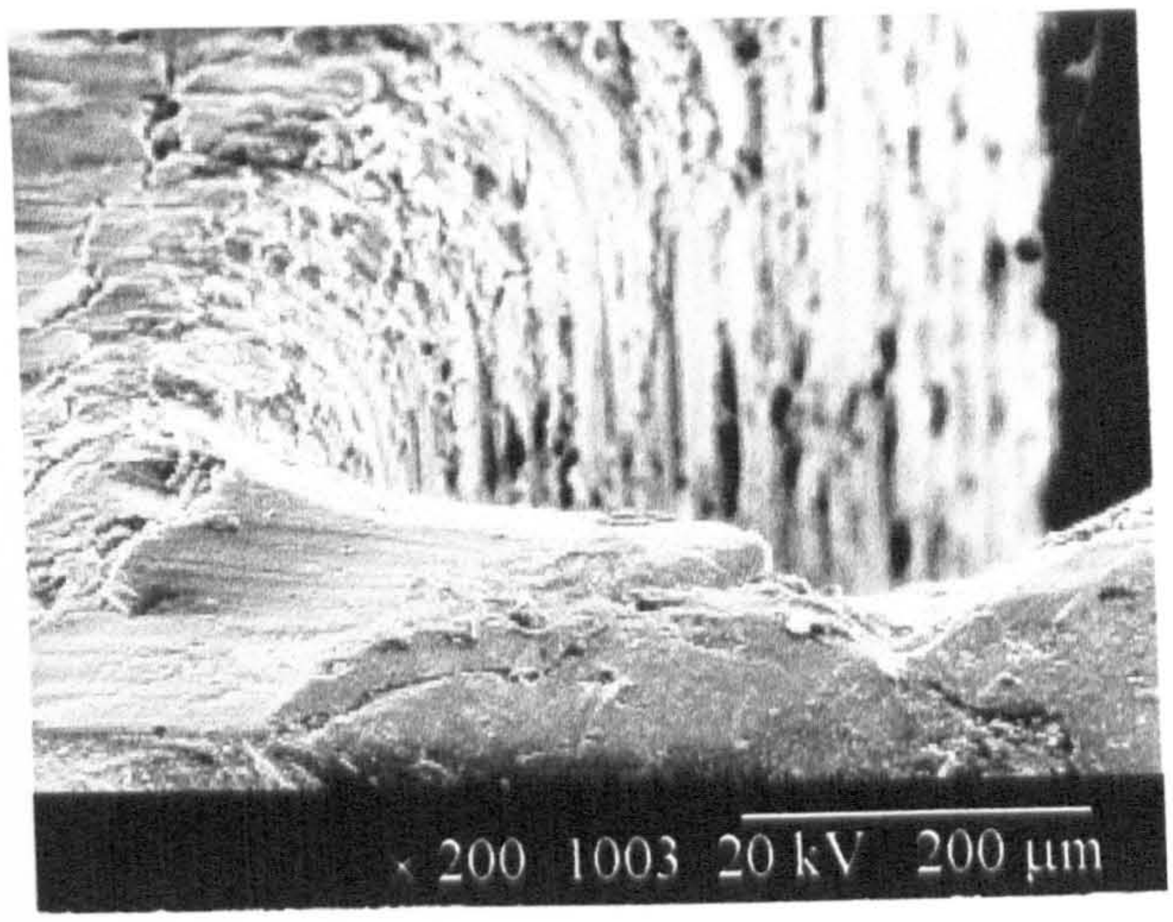

(b)

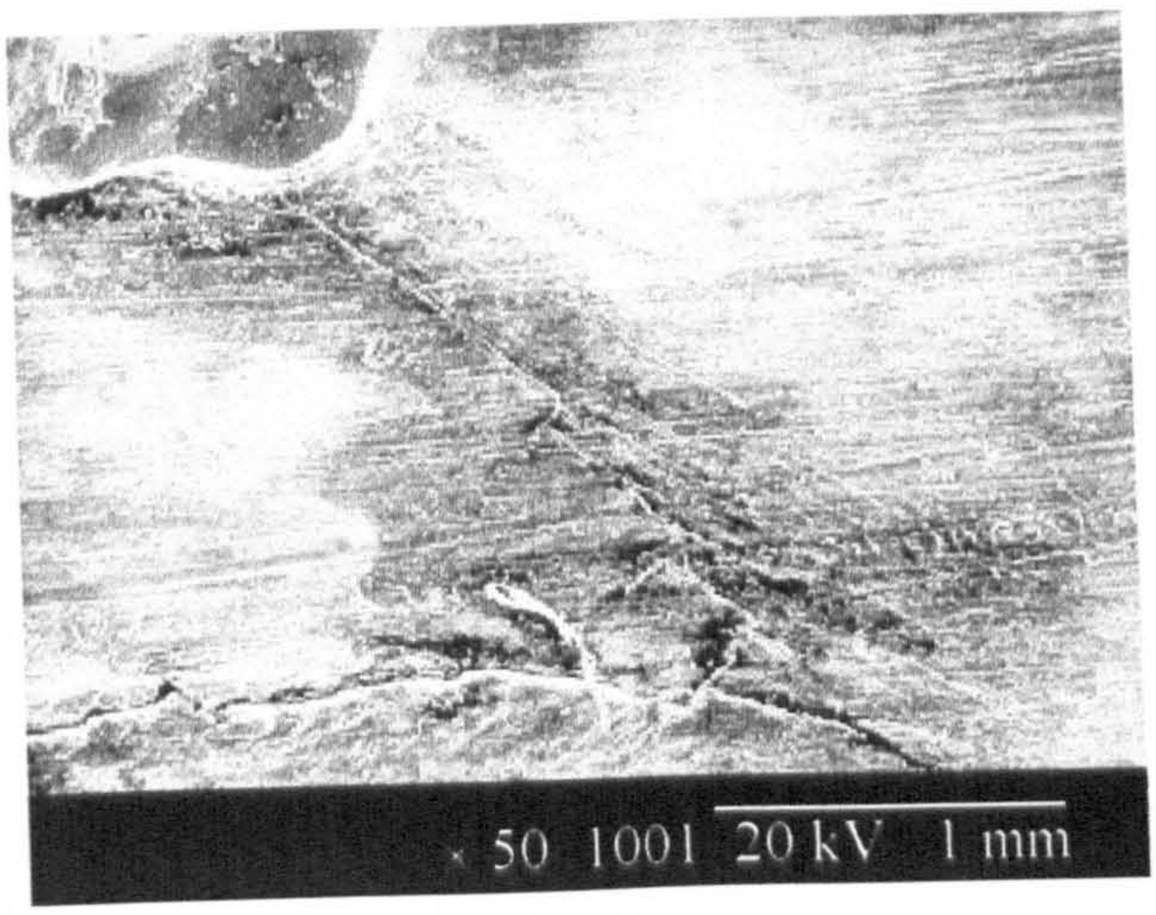

(c)

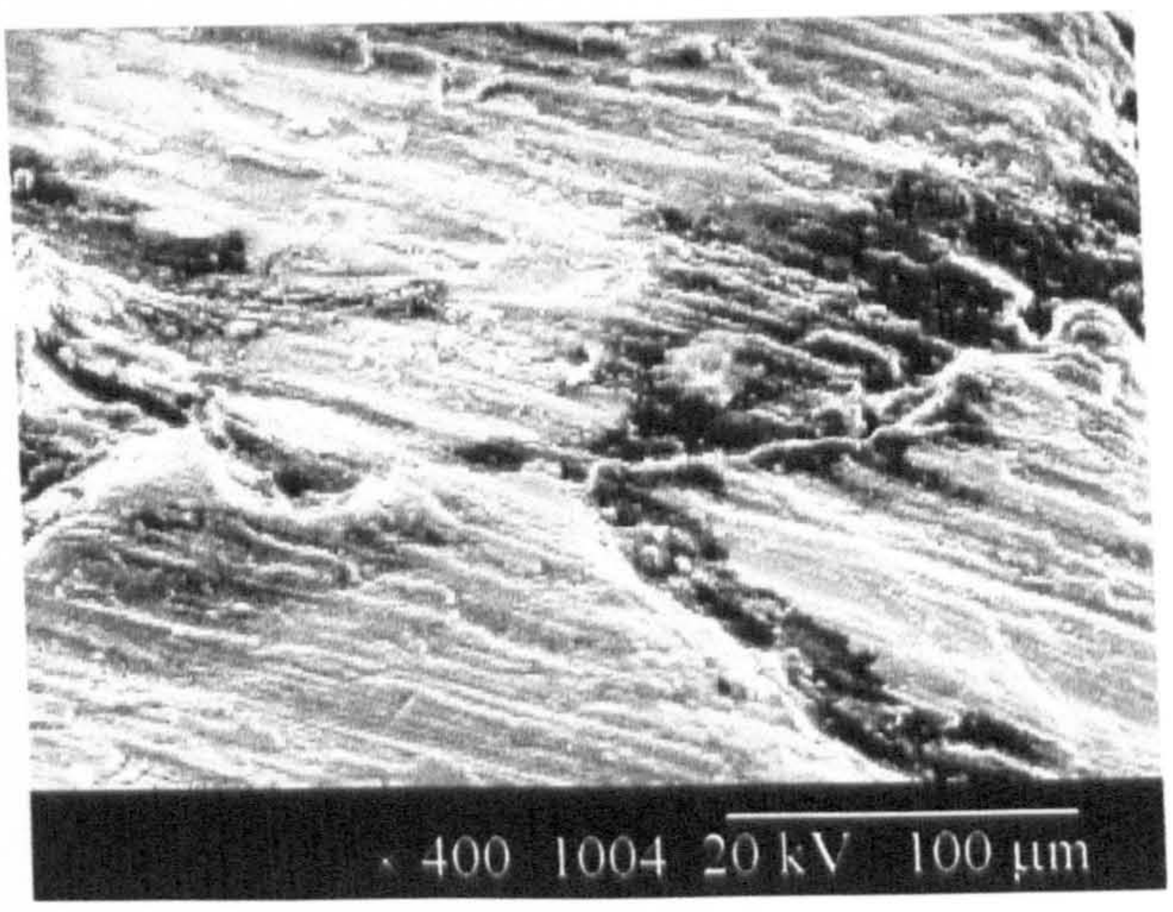

(d)

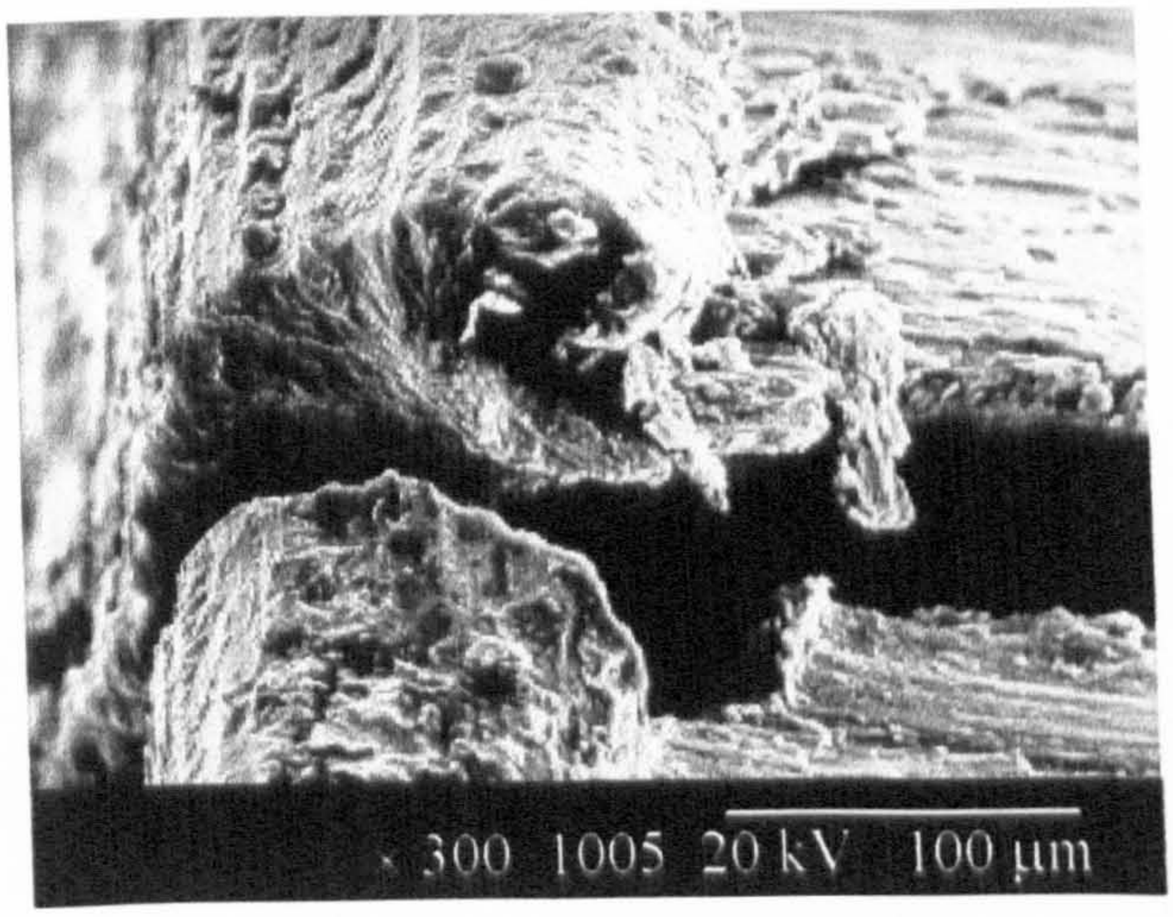

(e)

Figure 5.31 *Micrographs of an Al_2O_3/6061 bend specimen showing (a) notch tip, (b) crack initiation site, (c) crack growth from site of initiation and splitting into two main crack faces, (d) an enlargement of the region of crack splitting shown in (c) and (e) the end of one of the cracks at the sample edge*

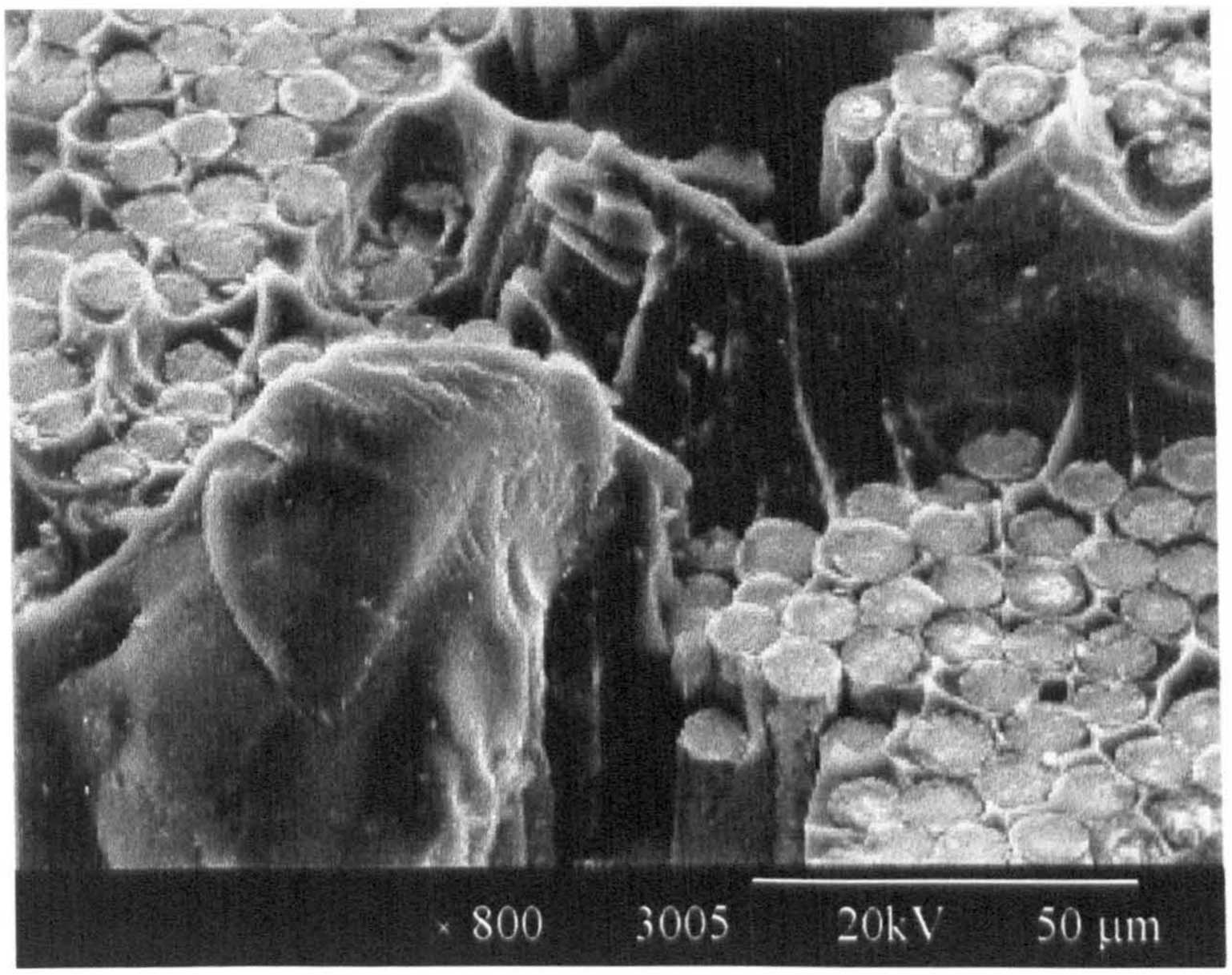

Figure 5.32 *Al_2O_3/CPAL composite fatigued at 70% F_0 for 196,482 cycles, the large quantity of matrix material seen to the mid-left of the picture shows slip bands*

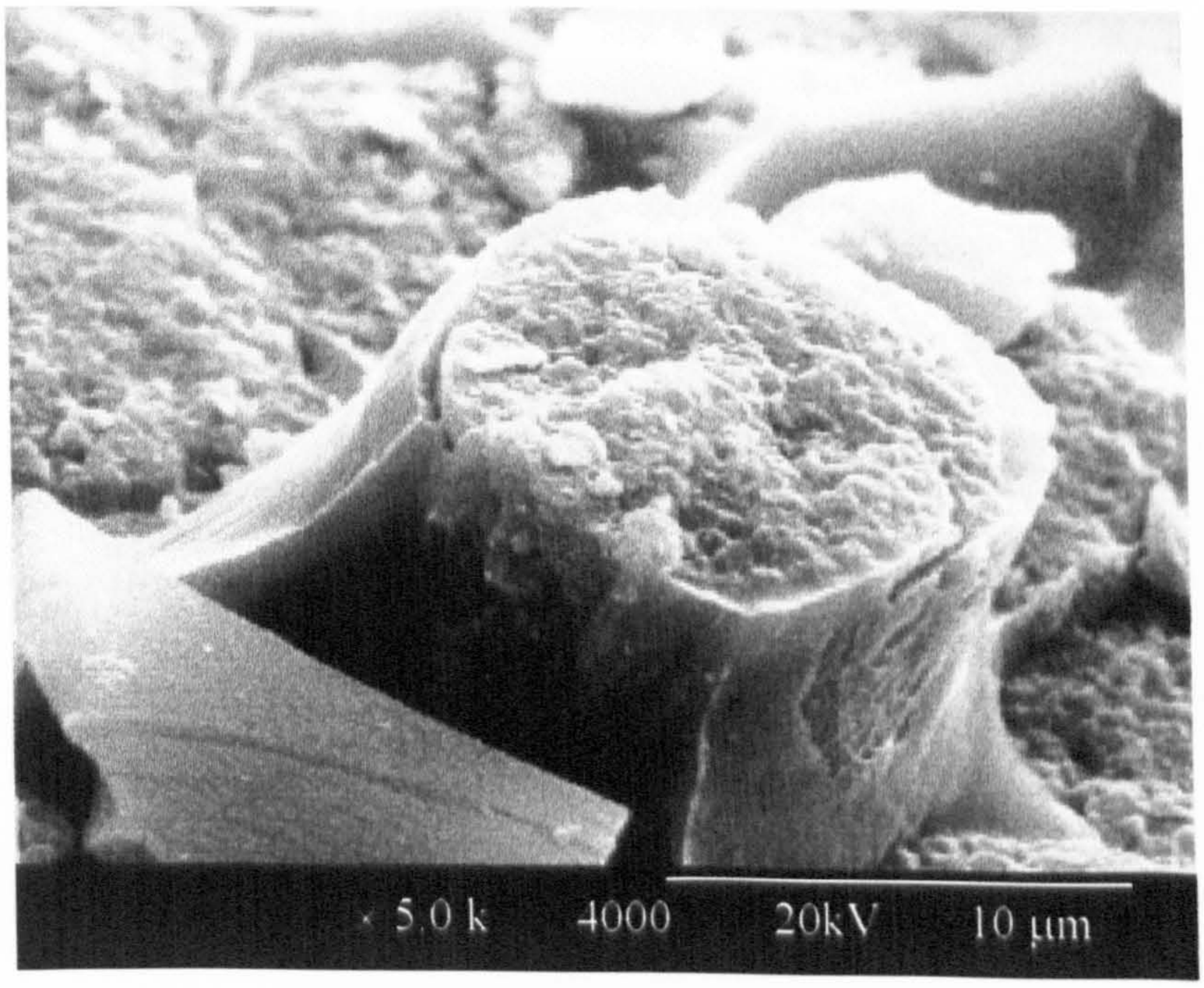

Figure 5.33 *Al_2O_3/CPAL composite fatigued at 70% F_0 for 196,482 cycles, the area in the middle of the picture shows broken fibre surrounded by matrix material which has yielded*

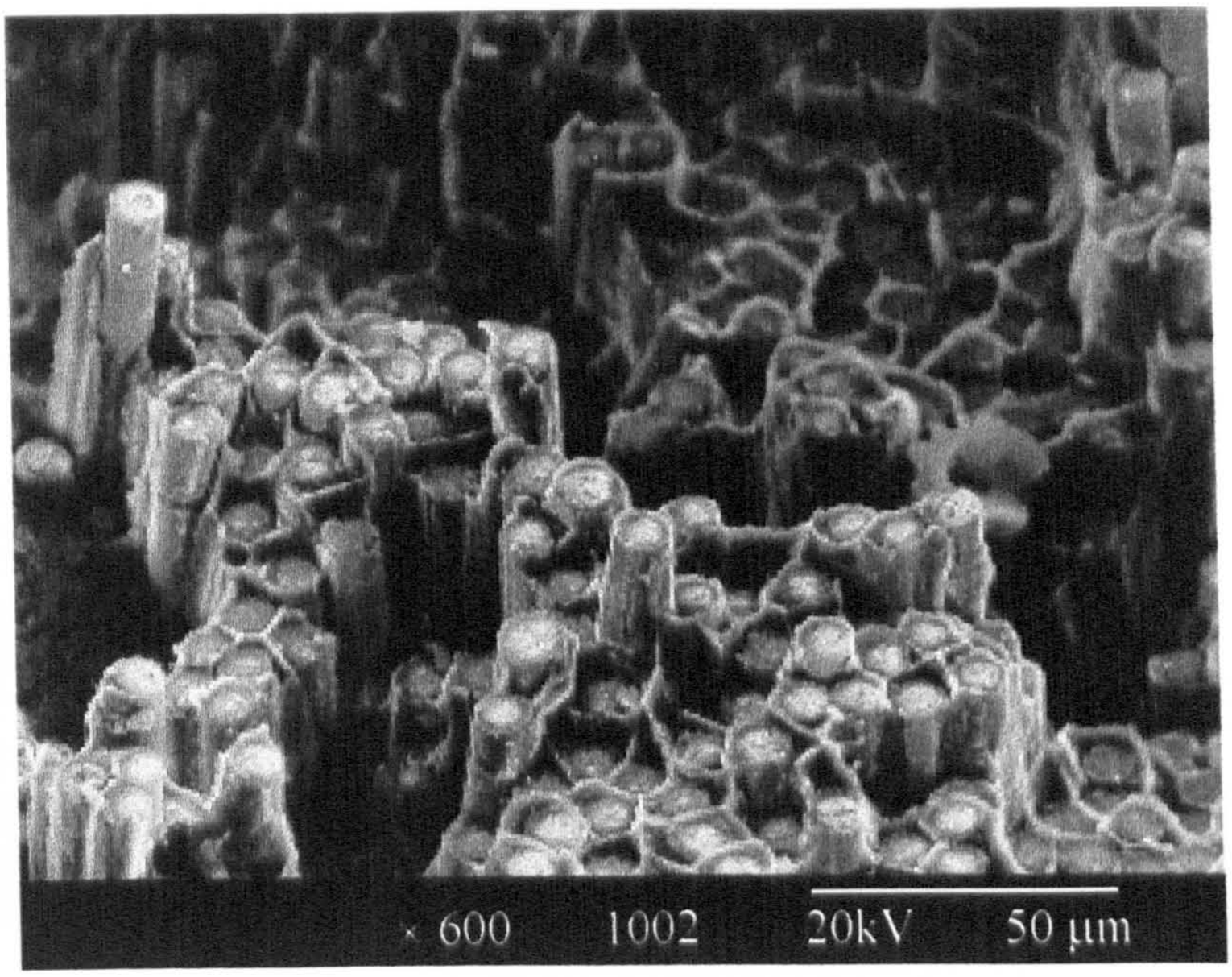

Figure 5.34 *Al_2O_3/6061 composite fatigued at 80% F_0 which failed after 23,953 cycles showing a large amount of fibre pull-out*

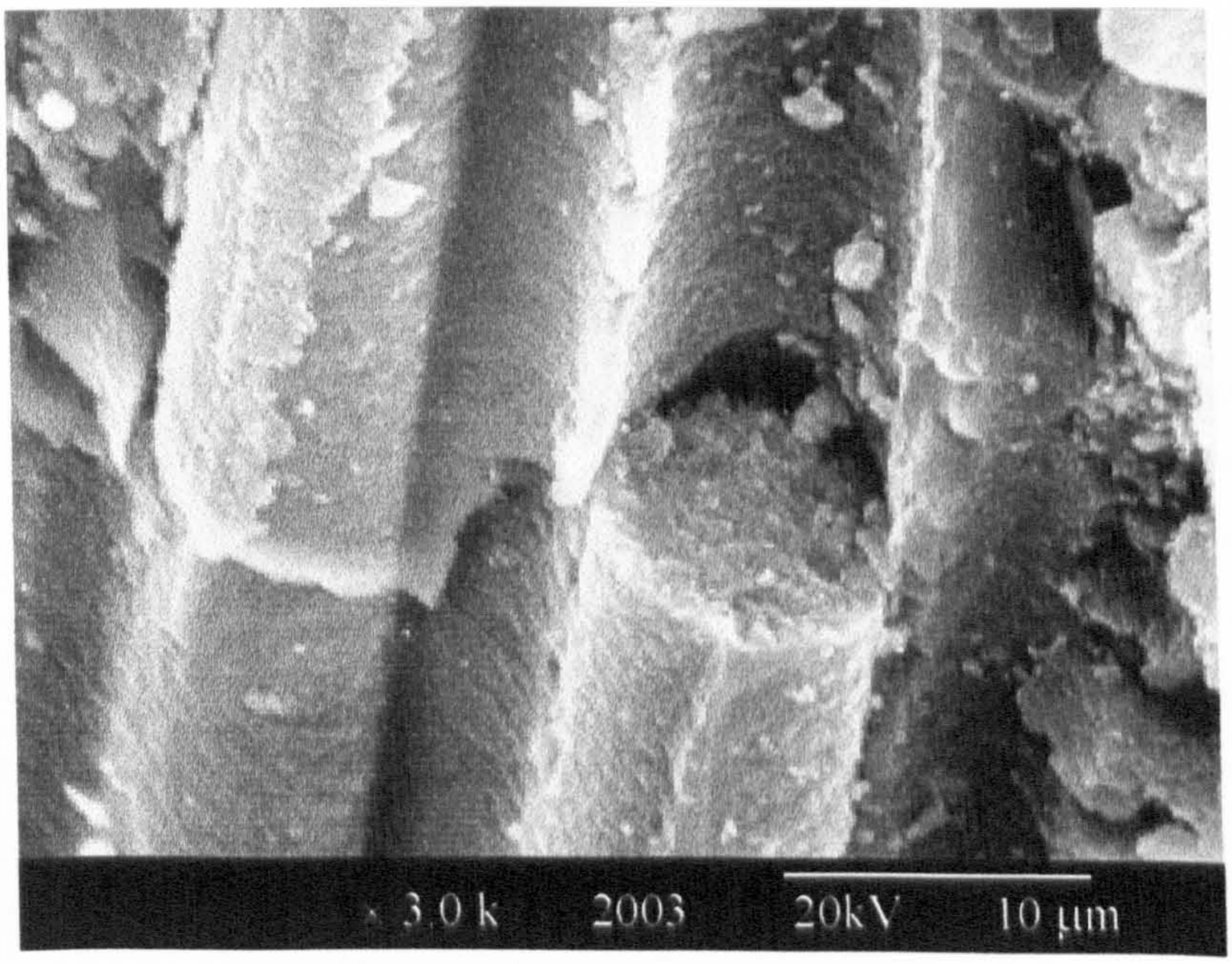

Figure 5.35 *Close-up of Al_2O_3/6061 composite fatigued at F = 1.661 kN (80% F_0) which failed after 23,953 cycles showing an embedded fibre which has broken into two parts, the second part having pulled out of the surrounding matrix*

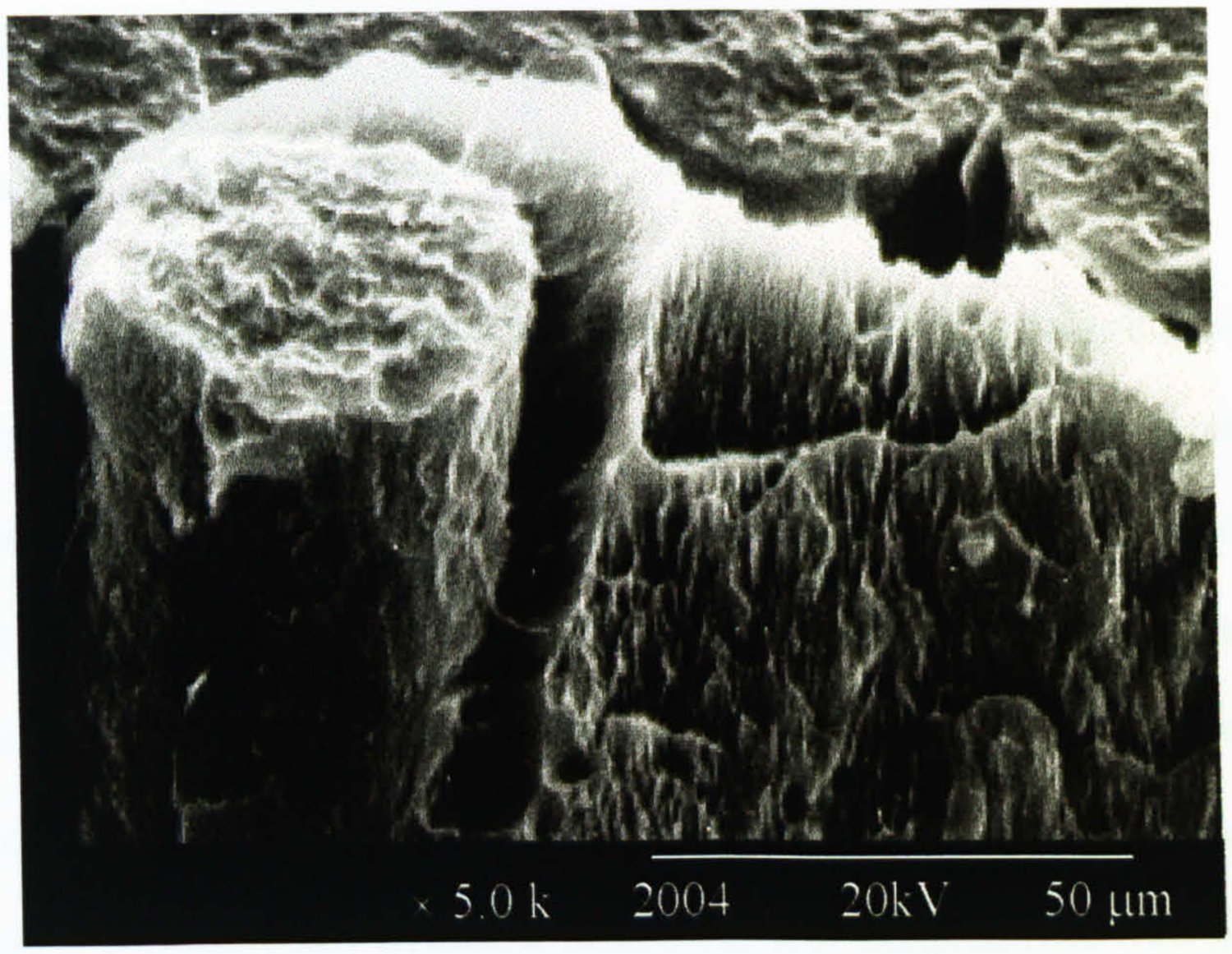

Figure 5.36 *A single fibre in Al_2O_3/6061 composite fatigued at 80% F_0 which failed after 23,953 cycles showing a broken fibre debonding from the surrounding matrix*

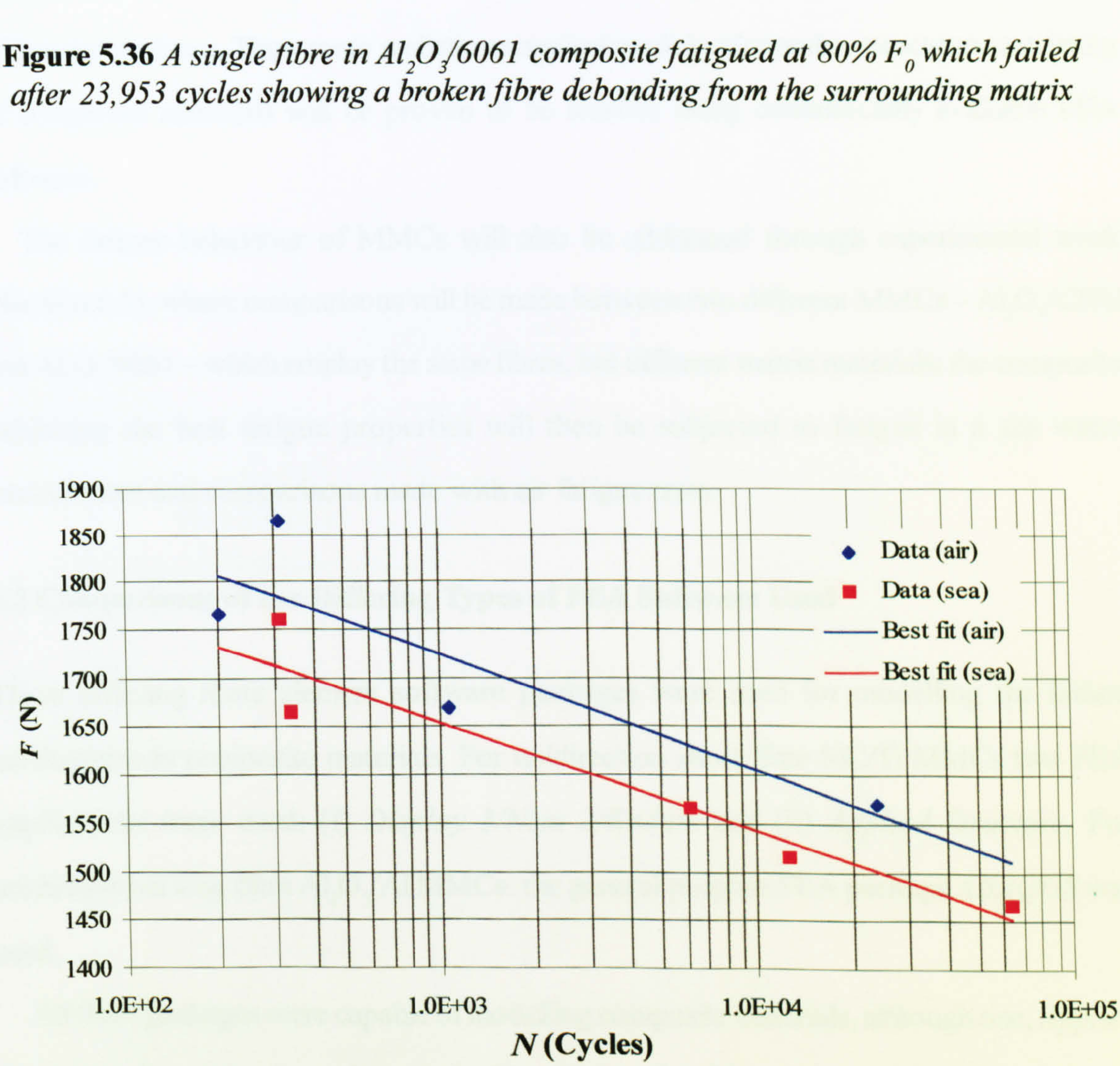

Figure 5.37 *Log-linear graph comparing Al_2O_3/6061 samples fatigued in air and seawater*

6 Discussion

6.1 Introduction

In this chapter, a computational method for realistically predicting failure in MMCs, will be sought, with the different types of finite element software used for the work study being discussed in Section 6.2. In Section 6.3, the implications the use of these differing packages will have on the results will be considered. Using a traditional stress intensity factor approach to FEA composite modelling, the limitations of conventional FEA micromechanic models will be demonstrated in Section 6.4. A more novel method of modelling (also discussed in Section 6.4) using commercially available software, will demonstrate that multiple failure mechanisms can be incorporated into a single FEA model, running in real time, by the use of *bonded surfaces*. Thus, more realistic numerical models of complex structures consisting of composite materials will be proven to be feasible using commercially available FEA software.

The fatigue behaviour of MMCs will also be addressed through experimental work (Section 6.5), where comparisons will be made between two different MMCs – Al_2O_3/CPAl and Al_2O_3/6061 – which employ the same fibres, but different matrix materials; the composite exhibiting the best fatigue properties will then be subjected to fatigue in a sea water environment and comparisons made with air fatigue tests.

6.2 Comparisons of the Differing Types of FEA Software Used

Three differing finite element software packages were used for modelling the failure mechanisms in composite materials. For unidirection short fibre SiC/Ti MMCs two FEA applications were used: (i) *Display 3/Nisa 2/Endure* and (ii) *Applied Structure*. For unidirectional long fibre Al_2O_3/Al MMCs: the general purpose FEA package *ABAQUS* was used.

All three packages were capable of modelling composite materials, although one, *Applied Structure*, due to the dynamic nature of its solving algorithms was perhaps less suitable.

Before further discussion of the results, a description of the relative strengths and

weaknesses of each package should be outlined since all three, perhaps with the exception of *ABAQUS*, were designed with specific purposes in mind.

6.2.1Display 3/Nisa 2/Endure

Of the three finite element packages here, *Display3/Nisa 2/Endure* follows a classical design of FEA application. The underlying geometry for the finite element model is constructed in the *Display 3* pre-processor, this geometry then has a finite element mesh placed on it, with associated material and element properties being then added. Finally the boundary conditions are applied and the model is ready to solve. The actual elements themselves employ an "h-method" (or aspect ratio-method) [72] solution, whereby each element has a fixed assumed displacement shape function, e.g. quadratic eight-noded isoparametric, to calculate displacements and hence stresses. A text file, incorporating all the model details, is then

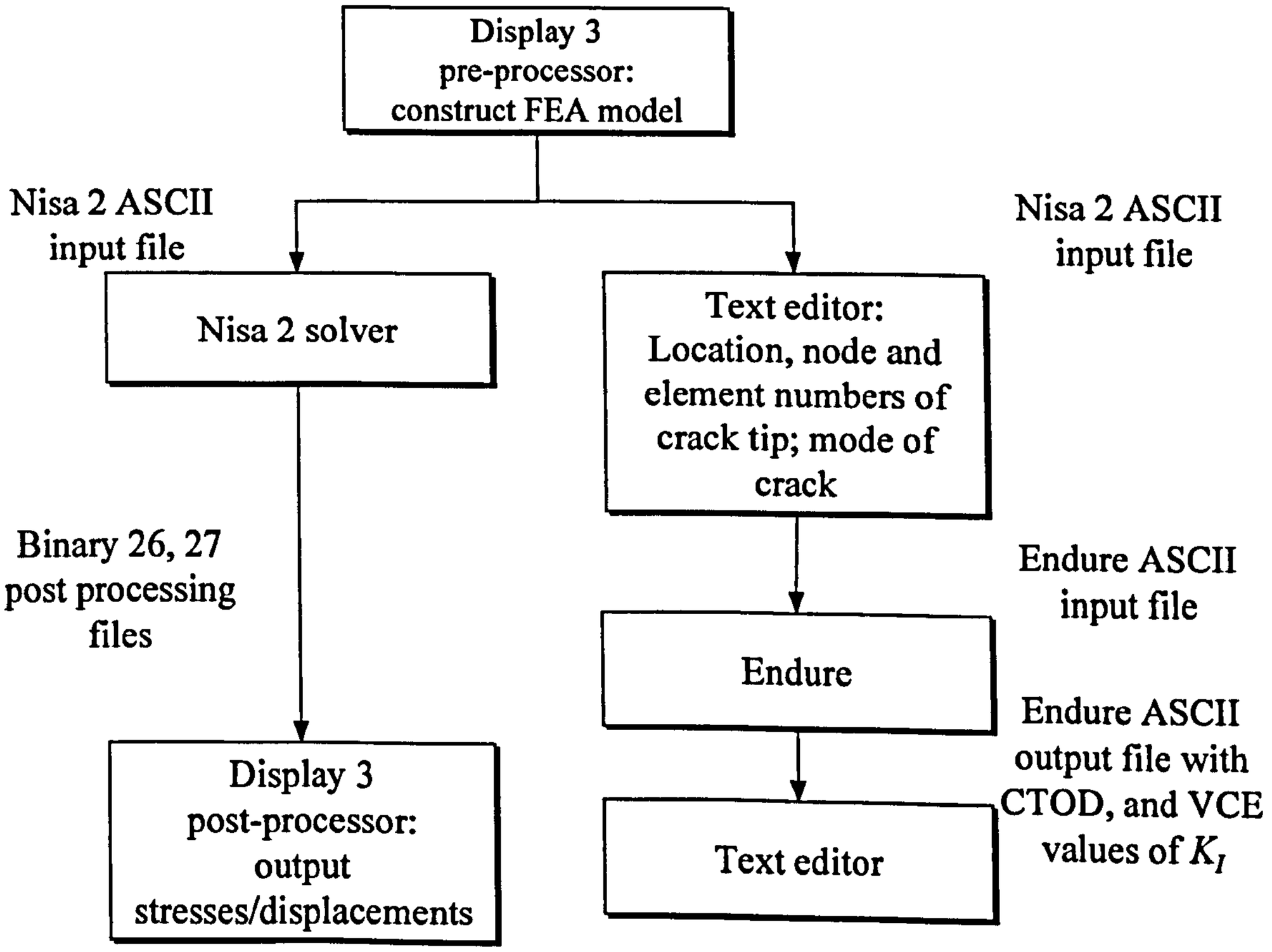

Figure 6.1 *Schematic diagram of procedure for obtaining stresses/displacements/K_I values from the Display 3/Nisa 2/Endure FEA software*

saved in *Display 3*, and then *Nisa 2* uses the information in this file to solve the model. For a successful model run, further files are created which are then read back into the post-processing module of *Display 3*.

For the crack analysis used in Section 5.4, the crack in the interphase was grown by starting with a small defect, saving the model, calculating the stress intensity factor at the crack tip, extending the crack, saving the model under a different name, and so on until the crack length was almost the entire width of the interphase.

Stress intensity factors were calculated using *Endure*, which like *Nisa 2*, required a separate file to be saved in *Display 3*. In fact *Endure* used the same file that *Nisa 2* used, with additional information about the element and node numbers constituting the crack tip supplied into a special *Endure* file, by the user (Figure 6.1). Stress intensity calculations for the crack were then output to a file for analysis. *Endure* used both CTOD methods and energy based methods as well as *J*-integral methods based on CTOD and energy, to calculate K_I.

The results shown in Figure 6.2 are for the CTOD calculations of K_I which showed good agreement with the theoretical values obtained from using equation {5.1} $K_I = \sigma\sqrt{\pi a}$

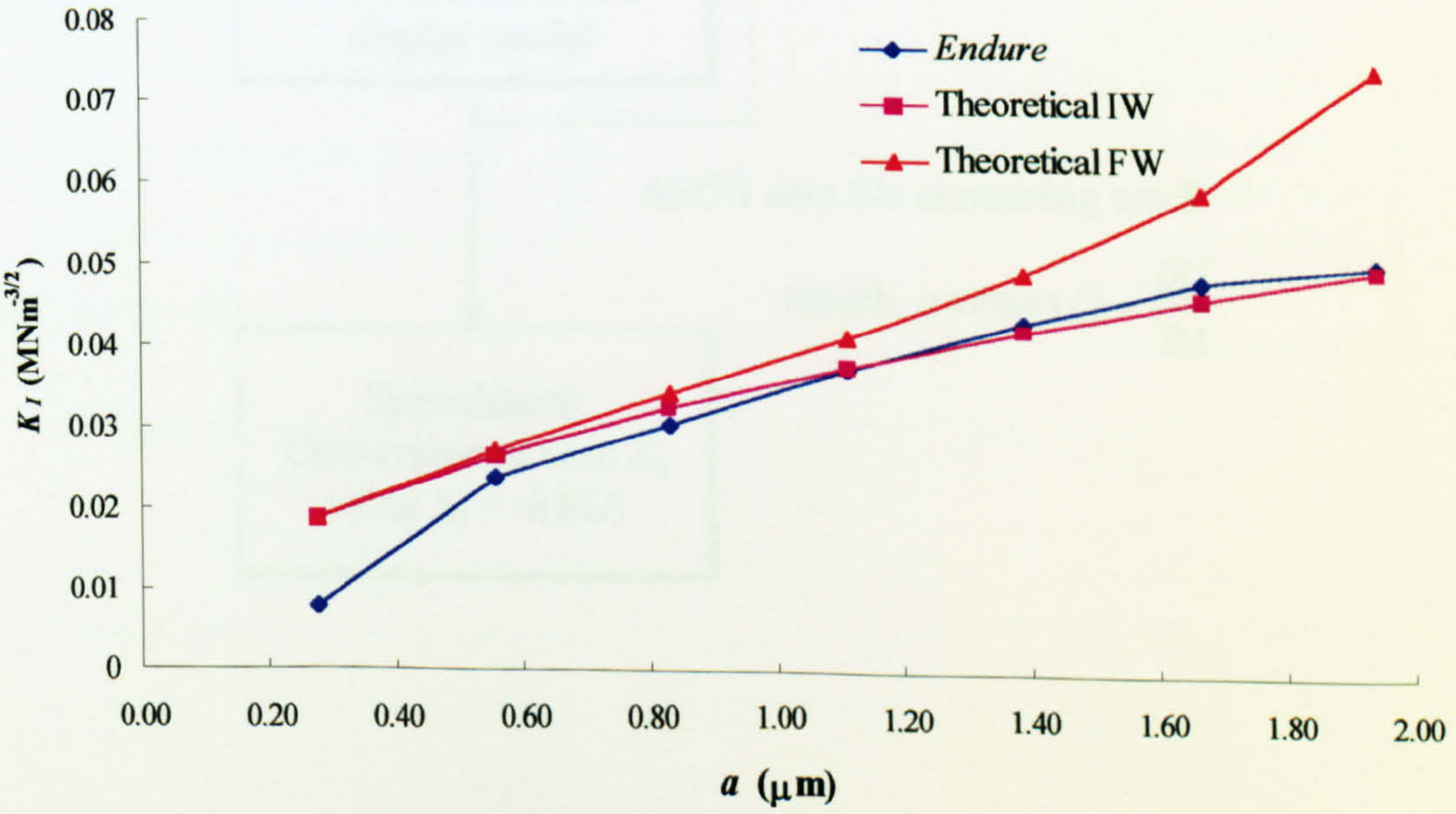

Figure 6.2 *Comparison of K_I as obtained from Endure vs theoretical predictions – obtained from model in Figure 5.9*

(infinitely wide plate) and {5.2} $K_I = \sigma\sqrt{\pi a}\left(\frac{W}{\pi a}\tan\frac{\pi a}{W}\right)^{1/2}$ (finite width plate) with σ being the applied stress, a the crack length and W the plate or specimen width. On the verification model run, ironically, the K_I values were not as in close agreement with theoretical values, despite the use of more symmetrical and uniform elements in the FE mesh.

For modelling failure mechanisms in composites *Display 3/Nisa 2/Endure* is limited, as many other "classic" FE packages are, in that to be able to perform crack propagation with stress intensity factor calculations, a separate model for each crack increment must be built and the crack tip stress intensity factor then calculated – a laborious process.

6.2.2 Applied Structure

The most unusual of the three finite element packages used in the work programme, *Applied Structure*, is primarily designed with optimization in mind. For an example of this, consider two holes in a square plate, subject to a tensile applied strain; by moving the holes on a

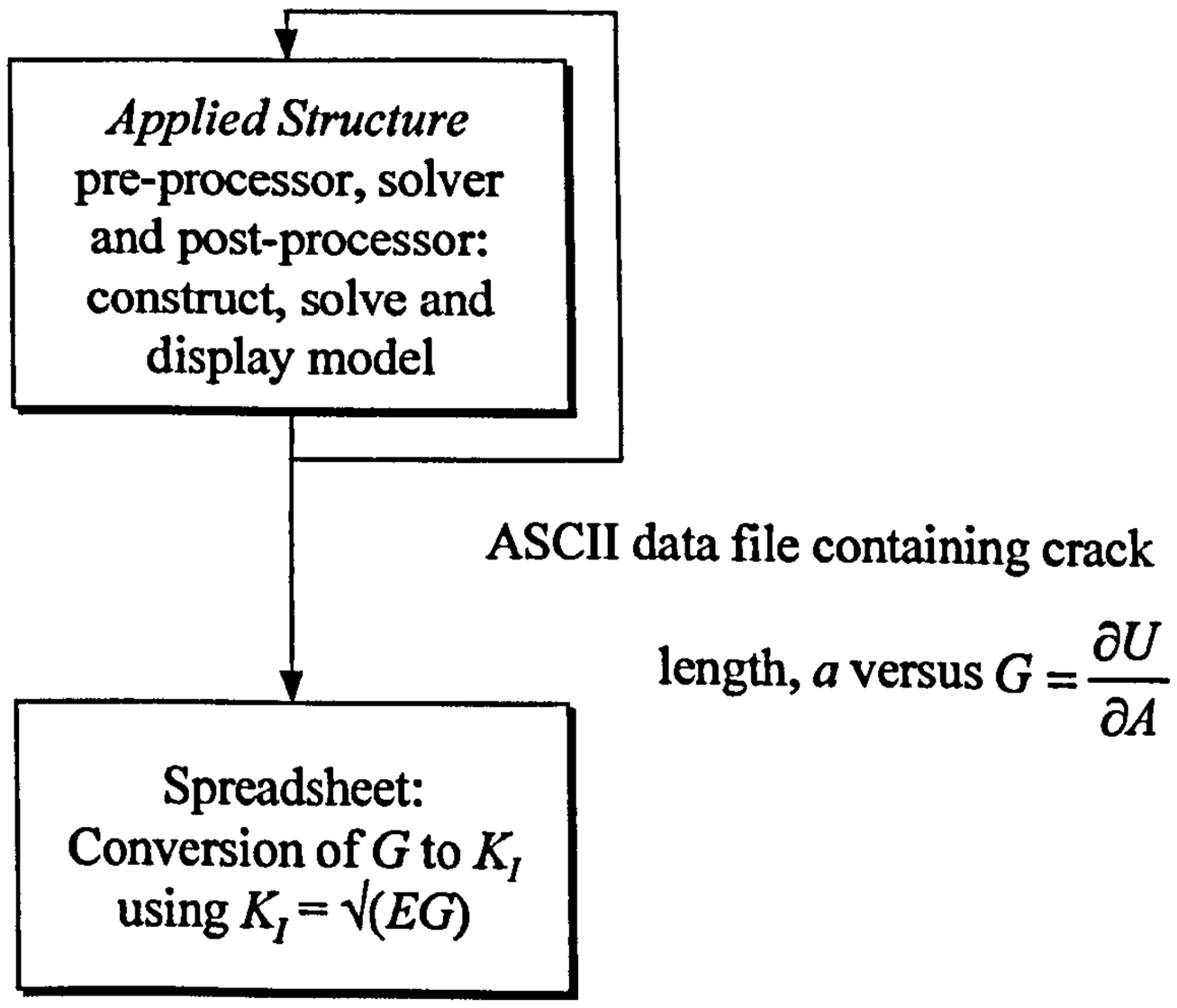

Figure 6.3 *Schematic diagram of procedure for obtaining stresses/displacements/K_I values from Applied Structure*

user-prescribed path, *Applied Structure* can find the optimum position for each hole that gives the minimum distribution of stress interaction between the two holes.

Applied Structure is used via one interface (Figure 6.3), which controls model geometry, meshing and execution. Unlike classic finite element packages which use the "h-method" of solution, such as *Display 3* or *ABQUS*, *Applied Structure* uses a polynomial method of solution or "p-method"; here, the element boundaries are fixed, but the order of the assumed displacement function is varied for each element. Starting at polynomial order 1, the displacement function along each element boundary is then increased until convergence between successive solutions is obtained, or until the polynomial order reaches a maximum of 9. The convergence criteria can be related to a single node or element, or the entire model and can be based on parameters such as local displacement, local strain energy, global root mean square (RMS) stress or a user-defined parameter such a nodal or element stress values. The model is thus optimized for the correct number of nodes per element and

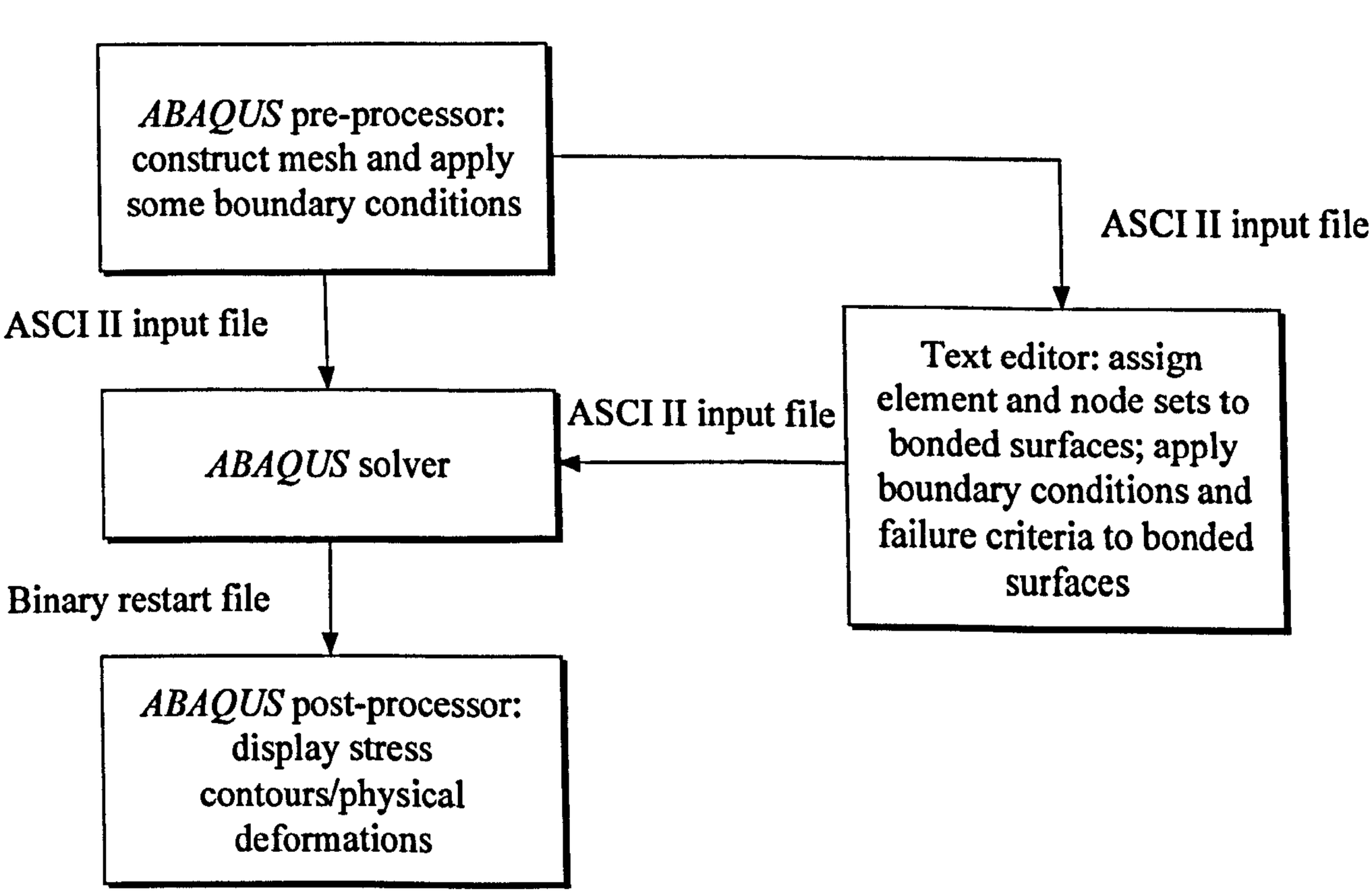

Figure 6.4 *Schematic diagram of model construction process in ABAQUS*

has them where they are required – in areas of high stress, for instance – in theory taking out much of the "guesswork" needed in classic finite element analysis, to decide were to concentrate the mesh.

By using what are described as design variables, the geometry of a model can be changed in a strain-free manner during a model run, although this change in geometry, of course, changes the element topology which can, despite the "p-method " of solution, lead to numerical instability in some instances.

6.2.3 ABAQUS

Although described as a general purpose finite element package, *ABAQUS* has several variants, depending on the nature of the analysis. For the work outlined here, *ABAQUS Standard* was used. *ABAQUS* is superficially similar to *Display 3/Nisa 2/Endure* in that it comprises a pre-processor/solver/post-processor and uses the "h-method" of assigning element toplogy (Figure 6.4). However, unlike *Display 3*, many of the algorithms available to the solver can not be implemented in the pre-processor, due to the fact that Hibbit Karlson and Sorenson [41] who make and distribute this package, have concentrated primarily on the Solver and post-processor, leaving the user to obtain his or her of-the-shelf pre-processor. Only within the last three years, has *ABAQUS* designed its own pre-processor, which as yet is still not up to the standard of the solver and post-processor.

The algorithms used in the present study – the contact surface family – can not be implemented in the pre-processor and must be added in the form of text in a text editor. This form of modelling is not unlike computer programming, with a typical model being many thousands of lines long due to the assignment of master/slave bond properties to each of the hundreds of nodes lying along the master/slave surface interfaces.

6.3 Comments on the Expected Results

In Sections 5.4–5.7 *Display 3/Nisa 2/Endure* and *Applied Structure* were used to calculate K_I for an embedded defect in the homogeneous interphase of a SiC/Ti unidirectional short fibre composite. *Display 3* could only model crack propagation, if each crack length

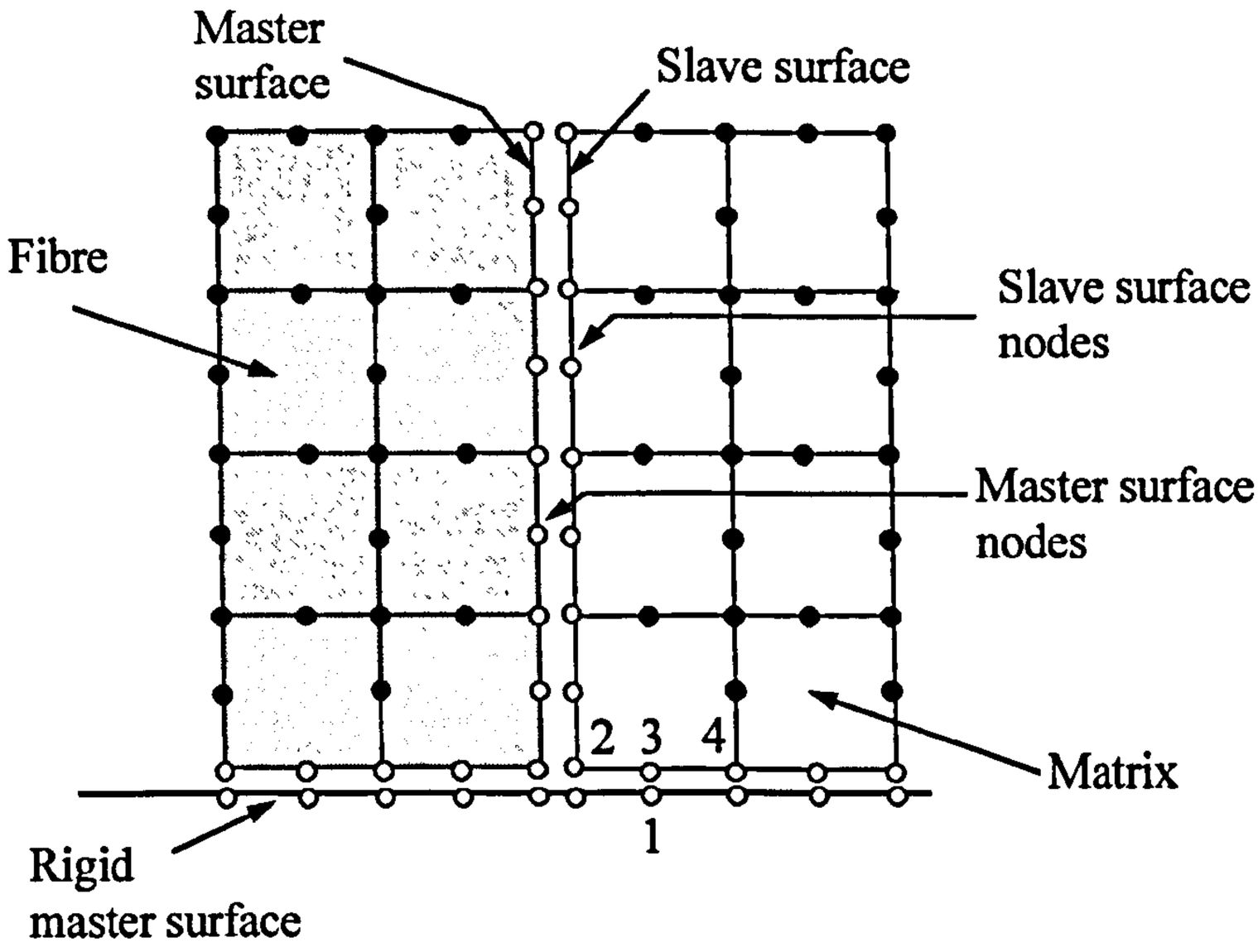

Figure 6.5 *Elements and nodes making up the master/slave surfaces for the fibre/matrix interface and the r-axis, composite bonding. Master node 1 can interact with slave nodes 2,3 and 4*

increment were a new model. *Applied Structure* was able to propagate a crack during the model run. However, the changing element geometry as the crack progressed led to inaccuracies in the K_I values. Also, *Applied Structure* could not propagate a crack too far, as this would result in the elements at each side of the design variable lines collapsing to zero width.

For modelling multiple failure mechanisms, the fibres had to simulate being embedded in the matrix – as in the real composite – which could only be achieved by use of special contact elements, or in the case of *ABAQUS*, the creation of contact surfaces. *Display 3* did have a contact element capability, but this was for compressive stresses only, the contact element did not have any bonding capabilities. *Applied Structure* had no bonded surface capabilities.

ABAQUS was chosen to build simulations of multiple failure mechanisms in composite materials, primarily because of the bonded surface algorithms incorporated into the package, which could, in two dimensions, be used to model the way fibres are embedded into a matrix. The bonded surface options in *ABAQUS* use a master/slave concept, Figure 6.4, whereby a single node in the master surface can interact with a small node set (comprising 2–4 nodes say) in the slave surface; of course two adjacent nodes in the master surface can

share the same slave node(s) in the slave node subset (see Figure 5.20). *ABAQUS* recommend that the stiffer element set comprise the master surface, which for the composites being modelled meant that nodes on the fibre interfaces would be masters and those on the matrix interface, slaves. There were three types of algorithm available to the user, finite sliding, small sliding and infinitesimal sliding. The finite sliding formulation allowed two interacting surfaces to slide and rotate a finite distance. In the small sliding case, nodes between master and slave surface elements (Figure 6.5) could not slide more than one element length and the rotation and deformation of the master surface should not cause the local tangent planes to become a poor representation of the master surface. The infinitesimal sliding algorithm was much the same as that of the small sliding and in addition ignored non-linear geometric effects.

All three of the bonded surface algorithms were incorporated into test models to determine which was the most appropriate and reliable:

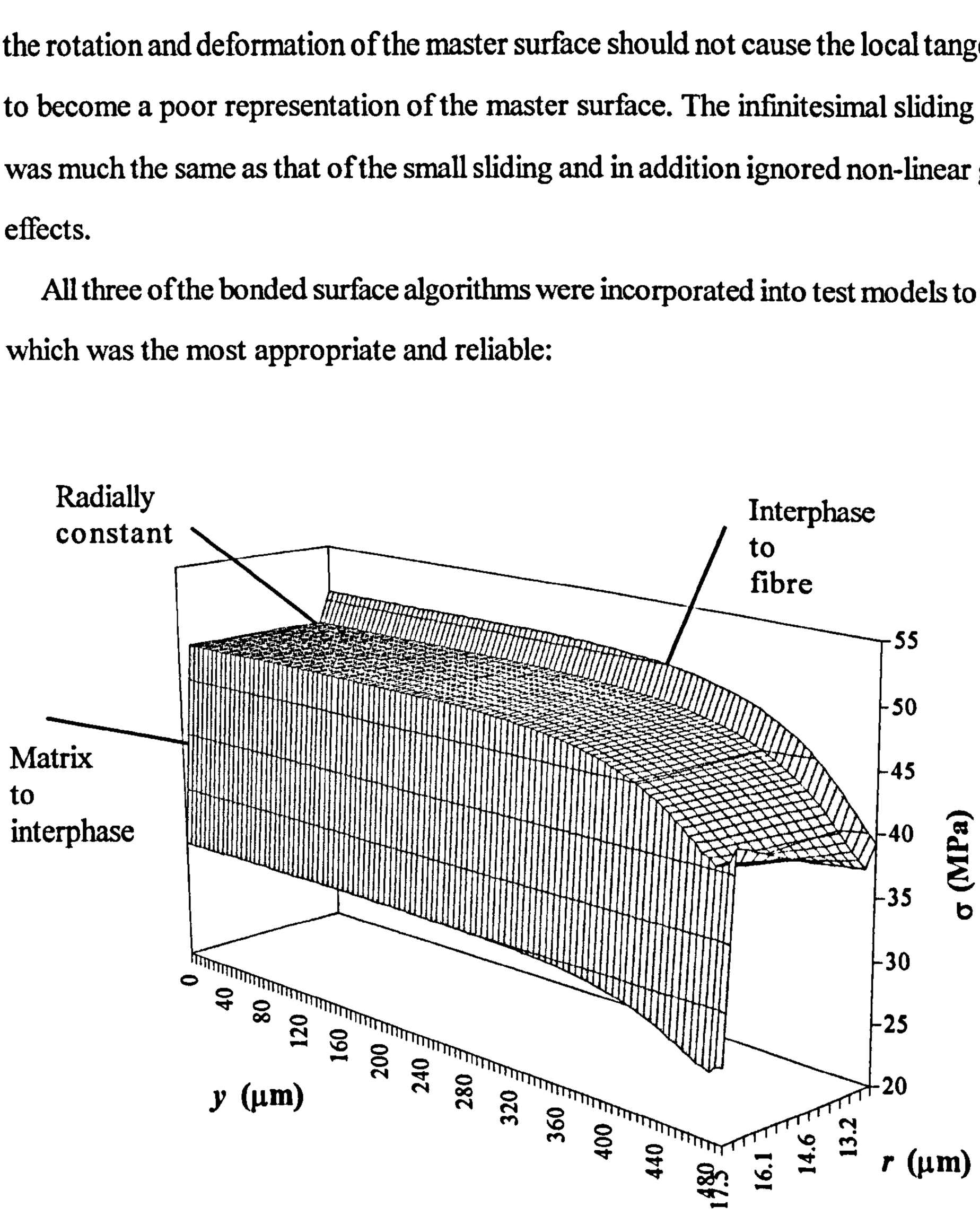

Figure 6.6 *Tensile stress distribution, σ, over the entire interphase, showing the instanteneous jump between* σ_{matrix} *and* $\sigma_{interphase}$, $\sigma_{interphase}$ *and* σ_{fibre}

i. *Finite sliding algorithm*. Because of the way the finite sliding algorithm works, *ABAQUS* changes the geometry of the model, in a strain-free manner, to correctly place nodes along the contact surfaces. Although no undesirable effects should be introduced by these changes in geometry, in practice, for *all* the test models, the algorithm was found to be unstable and gave unreliable stress distribution results compared to the results from the small- and infinitesimal sliding algorithm models. This algorithm was also extremely expensive in computational terms and the model runs were very lengthy.

ii. *Small sliding algorithm*. This algorithm proved much more stable than the finite sliding algorithm. When compared to identical conventional models of composites, i.e. containing no bonded surfaces, the stress distributions in both types of model were the same, indicating that the bonding algorithms were behaving correctly.

iii. Infinitesimal sliding algorithm. The infinitesimal sliding algorithm gave the best results overall, with the algorithm staying stable to near total failure of the composite – none of the algorithms

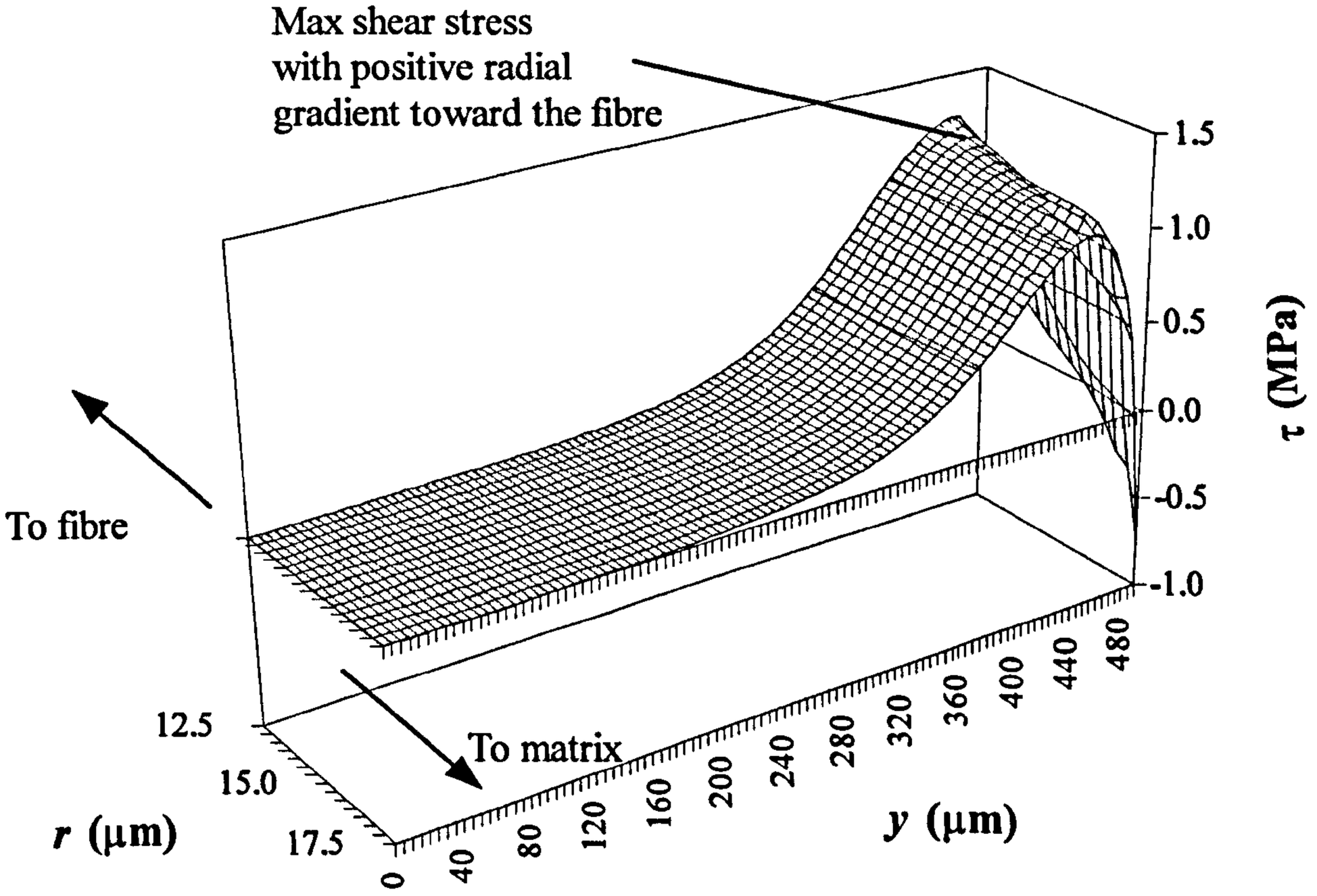

Figure 6.7 *Showing a radial tensile stress, τ, gradient at the peak tensile stress only – toward the middle of the fibre the shear stress distribution is the same in the fibe, interphase and matrix*

allowed the composite to completely fail, but became unstable and terminated as the simulation approached total composite failure. This algorithm also had the most economic computational run time.

The infinitesimal sliding algorithm was chosen to carry on the rest of the simulation investigations, since this was the most reliable and had the most economic computational run time.

6.4 Comparison of Results

6.4.1 Tensile and Shear Stress Distributions Over the Interphase

The results for the tensile stress distribution over the entire interphase, as detailed in Chapter 5.2, are shown in Figure 6.6. Although the phases are perfectly bonded to each other, the transition in tensile stress distribution from one phase to the next is near instantaneous (approximately one element wide) at the fibre/interphase and interphase/matrix boundaries. The difference in the size of the step in tensile stress distribution between the phases is reflected in the difference in Young's modulus between matrix and interphase (267.7 GPa) and interphase and fibre (40 GPa). Across the interphase, the tensile stress is constant, except at the fibre end where there are very high stress concentrations due to the square nature of the modelled fibre tip. This constant behaviour can be explained by the fact that the interphase is materially homogeneous, the effect of the perfect bonding has an effect on the shear stress distribution only (Figure 6.7) where a gradient can be seen radially across the interphase at the peak stress. Toward the middle of the fibre the tensile stress is the same across the fibre, through the interphase and into the matrix (Figure 6.7).

The implications of the above stress distributions in the interphase are twofold: firstly if an embedded defect is placed in the longitudinal centre of the interphase, due to the constant value of both tensile and shear stress distributions, an analytical formula – such as the infinite and finite width plate formulas for calculating stress intensity factors at a crack tip – can be used in finite element modelling for comparative purposes with numerically generated values. Secondly, the shear stress gradient at the maximum peak shear stress implies that the maximum shear stress at the fibre/interphase boundary is greater than at the interphase/

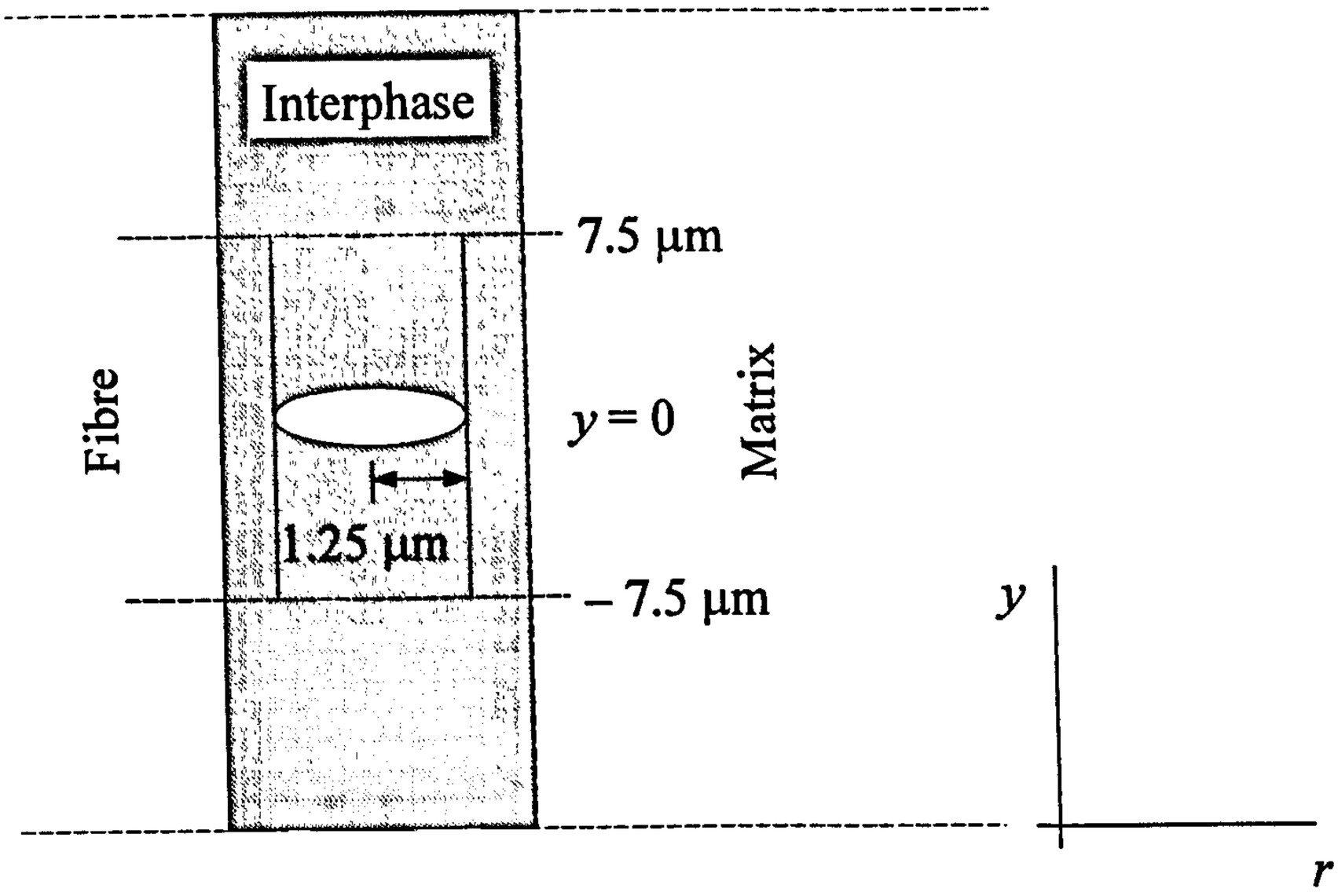

Figure 6.8 *Schematic diagram showing position within the interphase of the embedded defect*

matrix border, which emphasises the importance of the fibre/interphase bond strength, for possible sites of fibre interphase debonding.

6.4.2 Embedded Defects Consisting of Simple Cracks

In Section 5.2.1 a simple crack, consisting of a removed element, was placed at the point of maximum shear stress in the interphase, next to the fibre/interphase boundary. The model run showed that the stress distributions around the defect were unrepresentative of a true embedded defect; this was due entirely to the geometry of the modelled defect which was square-edged and thus unrepresentative of a real crack's geometry.

A much more refined mesh around the crack region would have given a more realistic stress distribution. However, for detailed analysis of fracture behaviour the simple crack method of element removal was totally unsatisfactory and for calculation of stress intensity factors a considerably more sophisticated method, such as the "*quarter point*" node placement [53] method was necessary.

6.4.3 Embedded Defects Using "Quarter Point" Eight-noded Isoparametric Elements

The results described in Section 5.3 showed that for an embedded defect, made up of elements utilising the "*quarter point*" method, placed in the interphase as illustrated in Figure 6.8, it can be seen (Figures 5.7 and 5.8) that the overall stress distribution on the fibre side increases with increasing fibre modulus, but also the concentration of maximum stress at $y = 0$ increases at a greater rate. On the matrix side, despite the matrix modulus falling, there is a steady increase in the overall stress distribution along the interphase/ matrix boundary, and again, the point of maximum stress at $y = 0$, increases at a greater rate.

Clearly the fibre modulus dominates the distribution of stresses in the interphase, and the chance of crack propagation into the fibre increases with increasing fibre modulus.

Of course the above results are for a perfectly bonded fibre/interphase/matrix. For a more weakly bonded system, the high stress distributions around the crack may initiate debonding and/or fibre bridging (see Sections 5.9 and 6.4.4).

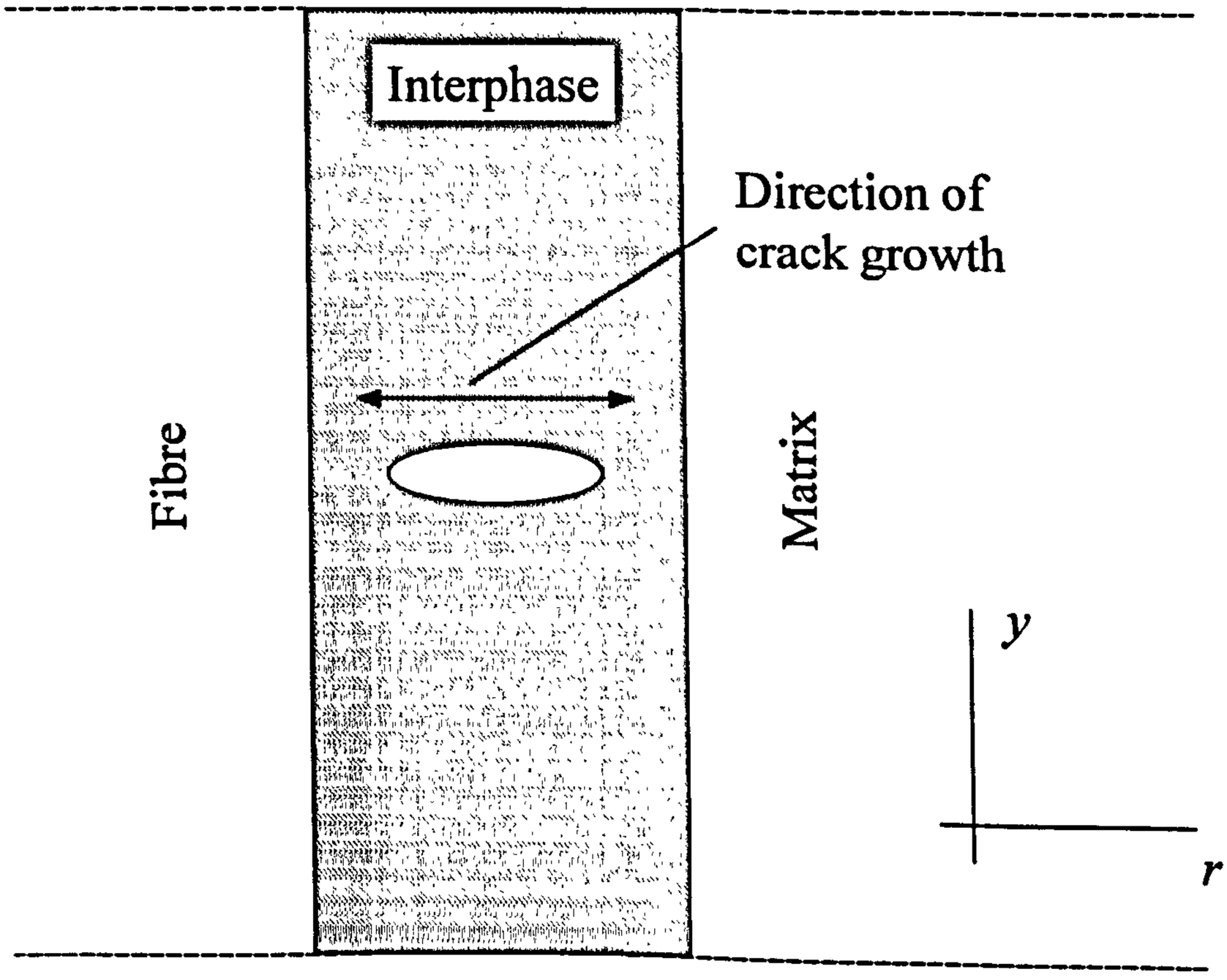

Figure 6.9 *Schematic showing position and direction of mode I crack propagation for an embedded defect in the interphase*

6.4.4 The Calculation of Stress Intensity Factors for a Mode I Crack Embedded in the Interphase

Figure 6.9 is a schematic diagram of the model used in Section 5.4 to calculate the maximum principal stress distribution around, and mode I stress intensity factors for, the crack tips of an embedded defect placed in the longitudinal and radial centre of the interphase.

Figure 5.10 demonstrated that the greatest stress distribution is around the fibre-side crack tip – due, as mentioned in the previous section, to the high fibre modulus compared to that of the matrix – and as the composite is subject to an increasing tensile stress, this implies that the crack will be more likely to propagate toward the fibre. What happens when the crack reaches the fibre will depend on type of fibre/interphase bond. However, Sections 5.9 and 6.4.5 will show that for a unidirectional long fibre reinforced composite, the fibre/matrix bond plays a crucial rôle in determining the dominant mode of crack propagation in the composite as a whole.

By comparing the stress intensity calculations generated in both *Display 3*/*Endure* and *Applied Structure* with the theoretical values it is clear that the theoretical finite width and

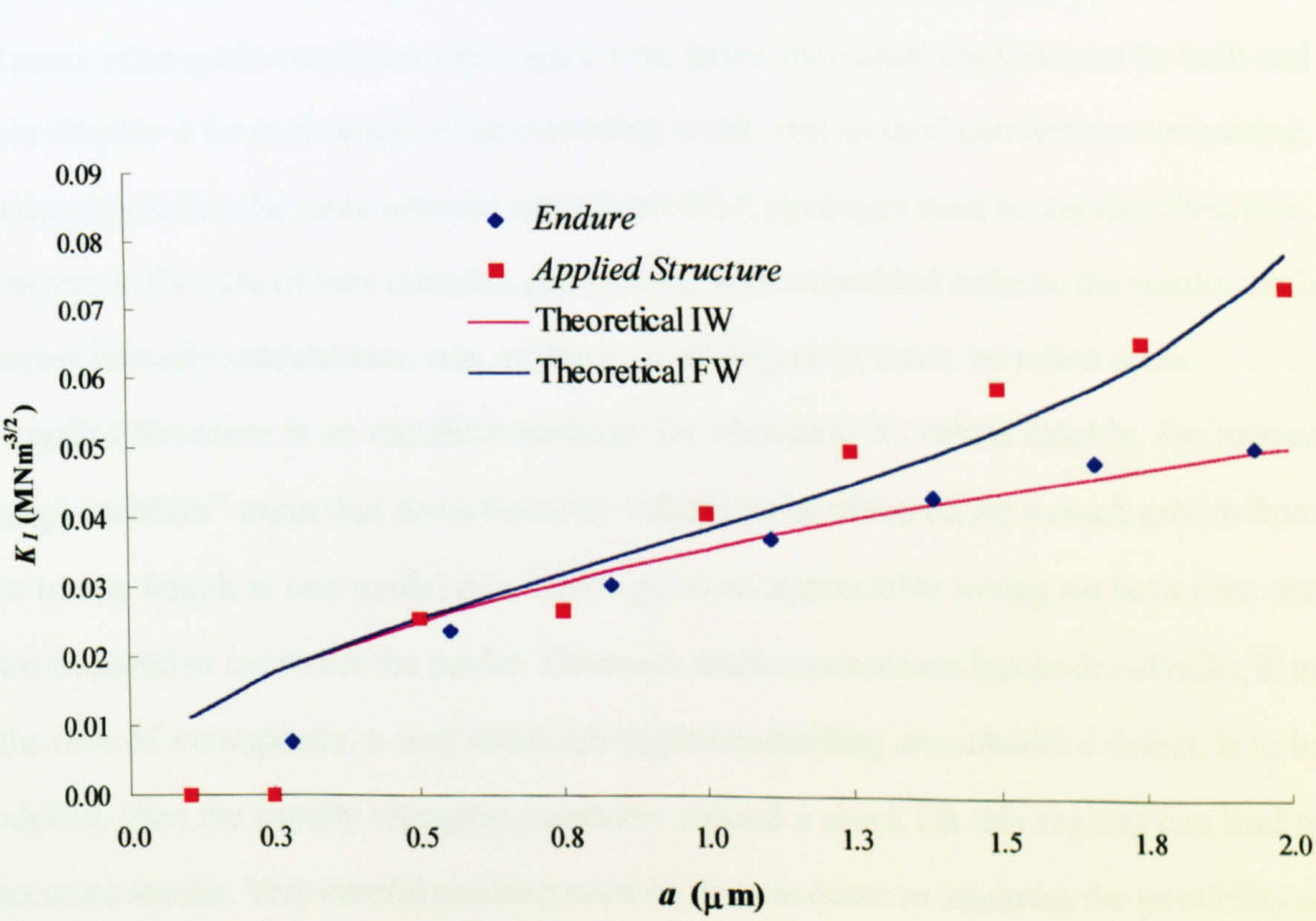

Figure 6.10 *Reproduction of Figure 5.14, the results from Endure and Applied Structure, compared to the theoretical valued of* K_I

infinite width calculations are upper and lower bounds respectively for the values generated in the two finite element packages. The values from *Endure* tend to follow the infinite width formula more closely, while the K_I calculations using *Applied Structure* follow the finite width formula more nearly – Figure 6.10. However, it can also be seen from Figure 6.10 that the first two K_I values generated in *Applied Structure* follow an erratic path and this is due to numerical instability in the calculations caused both by the width of the interphase and the constantly changing aspect ratios of the elements in the interphase (the elongation described in Section 5.5).

The verification procedures performed in Section 5.6, using a large steel plate as a test model, confirmed that *Applied Structure* was more suited to modelling objects on the macroscopic scale, where the geometry allowed reasonably regular elements.

Display 3, in conjunction with *Endure*, is a competent all-round package for modelling fracture behaviour and calculating stress intensity factors in both traditional and composite materials.

The *Display 3/Nisa 2/Endure* combination of packages is more suited to stress distribution and crack propagation analyses, although for the latter, individual models must be built and run in *Display 3* for each length of an extending crack; this method can be time consuming, when compared to the more unusual non-classic FEA packages such as *Applied Structure*. However, in the case of very complex geometries, with embedded defects, the results, such as stress intensity calculations, can, within a small degree of error, be relied upon.

Applied Structure is an excellent package for obtaining K_I values quickly, the unique "design variables" mean that stress intensity values can be obtained for a crack grown from zero to any length in one model run, which gives an appreciable saving on both time and effort required to construct the model. However, such convenience has its drawbacks; if, as in the case of a composite, a very small sub-region containing an embedded defect, is to be modelled, then the rapidly changing geometry around a crack (in this region) can lead to inaccurate results. Very careful meshing must be done in order to minimise the possibility of numerical errors.

6.4.5 The Use of Simulation to Predict Failure Mechanisms in Composites

In Section 5.8 *ABAQUS* was used to simulate multiple failure mechanisms in a unidirectional long fibre composite. The main effects of varying fibre/matrix bond strength on failure mechanisms manifested themselves on the way in which mode I cracks crossed from matrix to fibre, and vice versa. Figure 5.23 showed that for a weakly bonded fibre/matrix, the matrix around the fibres fail in mode I, the crack bridging the fibres. The bridging process can be explained thus – as Figure 5.23 indicates – for an increasing strain, the crack (initiated on the right hand side of the picture) starts to propagate as the matrix reaches its UTS (without first yielding plastically, since this was not incorporated in the model) and fails in mode I. When the matrix crack reaches the fibre it is arrested and blunted due to the weak fibre/matrix bond. It is this crack blunting and fibre/matrix slippage, which eventually absorbs energy. However, as the strain increases, a stress concentration builds up within the fibre and passes through it until it reaches the next matrix bay. Although the stress is insufficient to cause fibre fracture it is still great enough to initiate mode I failure in the next matrix bay. As the strain increases the weakly bonded fibre matrix begins to fail in shear, causing fibre matrix debonding.

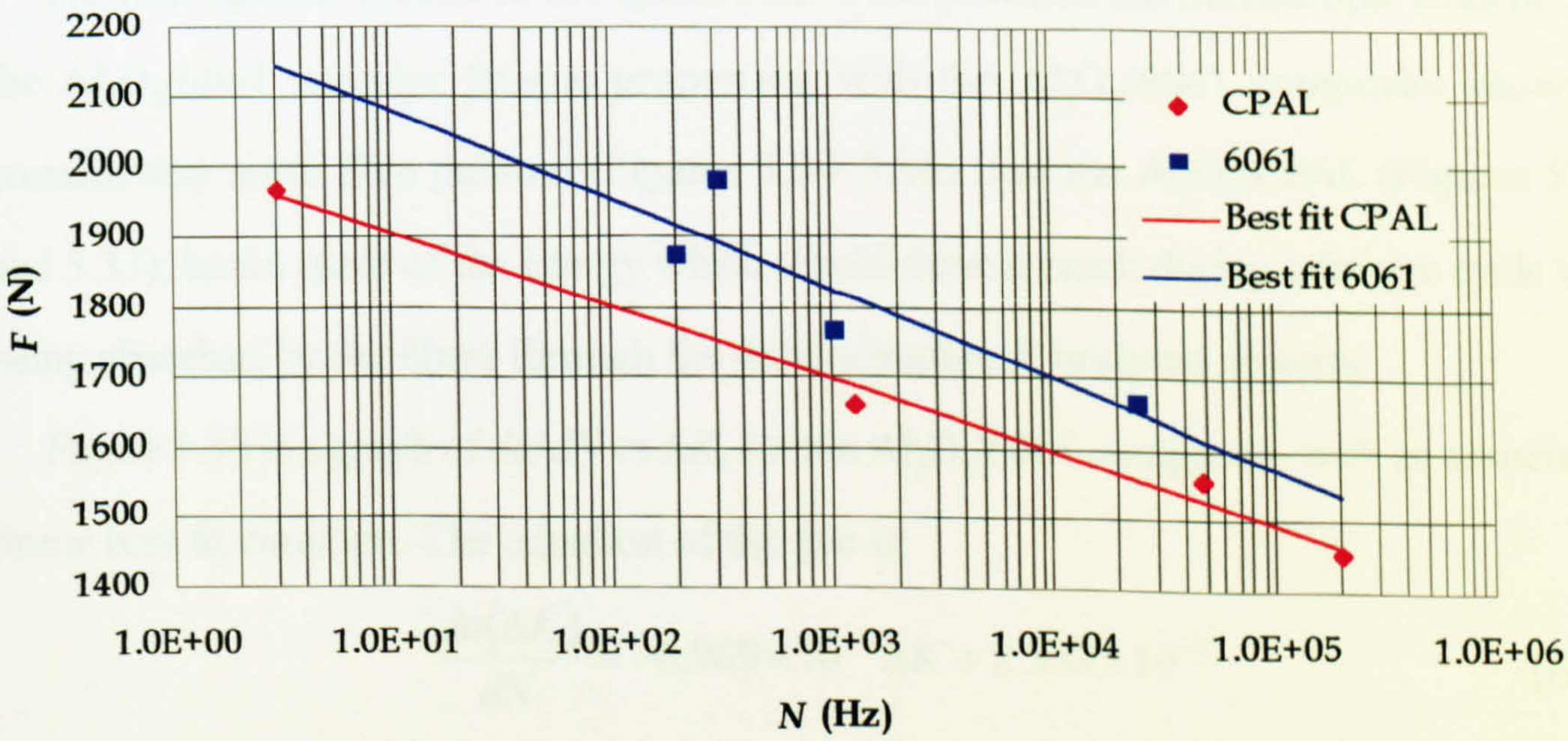

Figure 6.11 *Reproduction of Figure 5.26, log-linear graph of Al_2O_3/CPAl and Al_2O_3/ 6061, together with their respective lines of best fit*

For a strongly bonded fibre/matrix differing mechanisms come into play. When the crack reaches the fibre (Figure 5.24), because of the strong fibre matrix bond, there is little or no crack blunting, the stresses in front of the crack are thus sufficiently high to cause the crack to proceed directly into the fibre and composite experiences little or no fibre bridging. This does seem to confirmed by the first fibre/matrix interface in Figure 5.24 which show only a very small amount of fibre/matrix interfacial slippage.

6.5 Fatigue Crack Growth of MMCs

The fatigue results for Al_2O_3/CPAl and Al_2O_3/6061 given in Section 5.9 showed that although identically prepared samples had the same approximate monotonic fracture load (2.1 kN) the Al_2O_3/6061 appeared to have superior fatigue properties. The lines of best fit for the log-linear plot of applied force, F, against the number of cycles to failure, N, is shown in Figure 6.11. The equations of the lines are

$$F_{CPAL}(N) = -102.82N + 2007.84 \qquad \{6.1\}$$

and

$$F_{6061}(N) = -125.746N + 2203.48 \qquad \{6.2\}$$

respectively.

The micrographs presented in Figures 5.32–5.36 provided the microscopic evidence of the Al_2O_3/6061 superior fatigue properties, with the Al_2O_3/6061 composite showing considerably more fibre pull-out (Figures 5.34–5.36) than the Al_2O_3/CPAL (Figures 5.32 and 5.33); hence more of the energy which would drive a crack during a fatigue cycle was being absorbed by the fibres through the debonding/crack bridging process.

Figure 5.30 is a graph of da/dN vs ΔK, for the Al_2O_3/6061 composite, with an associated linear best fit equation. The equation of the line is:

$$\frac{da(\Delta K)}{dN} = -6.969\times10^{-7}\,\Delta K + 2.332\times10^{-5} \qquad \{6.3\}$$

For zero crack propagation, i.e. $da/dN = 0$, $\Delta K = 33.46$ MNm$^{-3/2}$.

6.6 Seawater Fatigue

When identical samples of Al_2O_3/6061 were fatigued in both air and water, the graph in Figure 5.31 was produced. The gradients of the best fit lines produced from the data are –118.701 for fatiguing in air and –111.726 for fatiguing in sea water. Since these lines are virtually parallel, the implications are that the results in air are consistently better than the sea water results, independently of the number of cycles. If the Al_2O_3/6061 material were to be used in a seawater environment then a 4% drop in fatigue life should be expected.

6.7 Summary

This chapter has sought to determine a computational method for realistically predicting failure in MMCs. The limitations of conventional FEA composite modelling have been demonstrated, and a *bonded surface* method of modelling, using commercially available software, offering multiple failure mechanisms has been incorporated into a single model running in real time. This type of modelling has very good commercial potential. Although at the time of writing, the text-based method necessary to implement the bonded surface algorithm requires a good deal of time and patience if a complex model is to be constructed.

The fatigue behaviour of MMCs has also been addressed through experimental work, where comparisons have been made between two different MMCs employing the same fibres, but having differing matrix materials; the composite exhibiting the best fatigue properties, then being subject to fatigue in a seawater environment and comparisons made with the air fatigue tests.

7 Main Conclusions and Future Work

7.1 Conclusions

Finite element analysis of both long and short fibre composites was performed using three differing finite element packages.

1. A model of the interphase of a Ti/SiC composite material was constructed using the finite element software *Display 3/Nisa/Endure*, the distributions of both tensile and shear stresses in the interphase were obtained in the form of three dimensional surfaces. From the surfaces it was apparent that the tensile stress distribution was constant radially across the interphase, varying only axially; this constant radial stress was due to the material homogeneity of the phase. The shear stress distribution, was only radially constant at longitudinal centre of the composite; as the peak shear stress was reached a positive gradient was seen to develop from the matrix/interphase interface to the fibre/interphase interface. Because of this peak shear stress gradient at the fibre interphase boundary , there was a greater possibility of fibre interface debonding at this point. However, if an embedded defect was placed in the longitudinal centre of the interphase, because of the constant value of both tensile and shear stresses at this geometric position, an analytical formula could be used to calculate the mode I stress intensity factor (K_I) at the crack tip and compared to the K_I values generated using FEA.

2. A simple crack consisting of one element removed from the FEA mesh was placed in the interphase. A model run showed that the stress distributions around the crack were not representative of a true defect since the geometry of the element meant that the defect was rectangular in shape and the crack tip was therefore square-edged. A more sophisticated model incorporating an embedded defect made up of elements utilising the "*quarter point method*" – to more accurately represent the distribution of stresses in front of the crack tip – was built into an axisymetric half model using the finite element package *Display3*. The stress distributions were obtained for differing values of both fibre and matrix Young's moduli, and it was found that the increasing fibre moduli increased the stress distribution in

an exponential manner along the fibre/interphase boundary and the interphase/matrix border, with by far the greatest increase being on the fibre side. It was found that the exponential distribution was even more pronounced directly in front of the crack tips. Thus, crack propagation was highly influenced by the fibre moduli, with the embedded centre crack being more likely to travel in the fibre direction if the matrix modulus was significantly lower than that of the fibre. The above results were for a perfectly bonded fibre/interphase/ matrix. A more weakly bonded system may have undergone fibre bridging or debonding.

3. For the half model described above, stress intensity factors in front of the fibre side crack tip, were calculated using two differing finite element packages – *Display 3/Nisa/ Endure* and *Applied Structure* – for comparative purposes, and to evaluate which package was more suitable for modelling composite failure mechanisms. The *Display 3* family of software used the classical approach to modelling crack propagation, in which crack was incorporated into a model, the stress intensity factor in front of the crack tip calculated and the model rebuilt with the crack extended. *Applied structure* was capable of extending the crack manually by the use of "design variables" which changed the geometry of the mesh, while the model was running, in a strain-free manner.

The values from one FEA package *Display* 3/*Nisa/Endure* were in agreement with values, calculated using an infinitely wide plate formula; however the *Display 3* family could not propagate a crack without prior knowledge of the crack path. Values from *Applied Structure* were also in agreement with the theoretical values predicted using a finite width plate formula. Unfortunately, *Applied Structure* suffered from numerical instability, caused by high element aspect ratios, caused by the changing mesh geometry during a model run and, because of this, the first and last few K_I values calculated were somewhat inaccurate. Verification procedures using a large steel plate as a test model confirmed that *Applied Structure* was better suited to modelling on the macroscopic scale, where the element geometry was more regular.

4. A simulation algorithm to model composites failing in several modes, simultaneously, and running in real time was developed in the finite element computer package *ABAQUS*. A small specimen of Al_2O_3/6061 composite was modelled in which four and a half fibres situated in five matrix bays were subject to a uniform strain in the longitudinal direction. By comparing two differing fibre/matrix bond strengths, one set at the matrix UTS, the other set at a value determined by a rule of mixtures combination of fibre and matrix UTS. It was found that the weakly bonded fibre/matrix interface led to fibre bridging and fibre/ matrix debonding, while the strongly bonded interface led to the composite failing almost completely in mode I with little fibre bridging. From this model run it became apparent that the fibre/matrix interface should be relatively weakly bonded e.g. set at the matrix UTS in order that fibre bridging/debonding be encouraged leading to material more resistant to mode I crack growth.

5. Edge notched Al_2O_3/CPAl and Al_2O_3/6061 unidirectional long fibre reinforced metal matrix composite specimens were fatigued in air at 1Hz. Although both MMCs had approximately the same monotonic fracture load, it transpired that the Al_2O_3/6061 composite had a greater fatigue life in the order of 10–100 times that of the Al_2O_3/CPAL. It was also found that applying forces of 75% (or less) of the monotonic failure force F_o (for the Al_2O_3/6061) resulted in crack arrest.

The Al_2O_3/6061 composite was also subject to fatigue crack growth in seawater. It was found that immersion in seawater, reduced the fatigue life of the sample by an average of 4%.

7.2 Future work

There is a great deal of work which could yet be carried out in simulating failure mechanisms of metal matrix composites under monotonic loading. For instance, there was insufficient time during the project to incorporate matrix plasticity into the model, but this would be the logical next step. Nor was there time to incorporate frictional effects at the fibre matrix interface – all of which could readily be incorporated into the existing models. Other work

could incorporate the effects of a separate homogeneous/heterogeneous interphase between fibre and matrix. Thermal changes such as heat treatment or thermal cycling could also be incorporated to observe their effects on the failure mechanisms.

After simulation failure mechanisms in Al_2O_3 MMCs under monotonic loading, the next step would be to simulate failure mechanisms under fatigue loading. At present it can take up to one hour of CPU time to run a five fibre composite failure simulation under monotonic loading. Clearly, for fatigue loading, the simulation would have to be able to complete one cycle within the space of a few minutes. An investigation in how to reduce run times would therefore have to be undertaken. For example, the use of simpler models containing a maximum of four fibres and four matrix bays, with larger elements and run on a multi processor computer would certainly bring the run times down.

References

1. R. Mitra and Y. R. Mahajan, Interfaces in discontinuously reinforced metal matrix composites; An overview, *Bull. Mater. Sci.*, **18**, 4, 405–434, 1995.

2. Z. Hashin and B. W. Rosen, "The Elastic Moduli of Reinforced Materials", *J. Appl. Mech.*, 1964, **31**, 223.

3. N. Melantis, C. Galiotis, C. Tetlow and P. L. Davies, Interfacial shear stress distribution in model composites: the effect of fibre modulus, *Composites*, **24**, 459–466, 1993.

4. R. M. Christensen, *Mechanics of Composite Materials*, John Wiley and Sons, 1979.

5. Chun-Hway and P. F. Betcher, Thermal Expansion Coefficients of Unideirectional Fibre-Reinforced Ceramics, *J. Am Ceram. Soc.*, 1988, **71**, 10, 438–441.

6. W. J. Baxter, The strength of metal matrix composites reinforced with randomly oriented discontinuous fibres, *Metallurgical Transactions A*, 1992, **23 A**, 3045.

7. C-H. Hsueh and P. F. Becher, Thermal Expansion Coefficients of Unidirectional Fibre-Reinforced Ceramics, *J. Am. Ceram. Soc.*, 1988, **71**, 10, 438–441.

8. W. Schneider, "Thermal Stresses and Coefficients of Thermal Expansion of Glass Fibre Plastic Laminates, Measured in Unidirectional Layers", (in Ger.), *Kunstsoffe*, 1971, **61**, 4, 273–277.

9. V. M. Levin, "On the Coefficients of Thermal Expansion of Heterogeneous Materials" (in Russ.), *Mekh. Tverd. Tela.*, 1967, **1**, 88–94.

10. N. Laws, " The overall Thermoelastic Moduli of Transversly Isotropic Composites According to the Self-Consistent Method",*Int. J. Eng. Sci.*, 1974, **12**, 79–87

11. G. J. Dvorak and Bahei-El-Din, Plasticity analysis of fibrous composites, *Journal of Applied Mechanics*, **49**, 327–335, 1982.

12. G. J. Dvorak and M. S. M. Rau, *International Journal of Engineering Science*, **14**, 36–373, 1976.

13. G. J. Dvorak and Bahei-El-Din, Elastic-plastic behaviour of fibrous composites, *Journal of the Mechanics and Physics of Solids*, **27**, 51–72, 1978.

14. J. Q. Tarn, J. G. Dvorak and M. S. M. Rao, Shakedown of unidirectional composites. *International Journal of Solids and Structures*, **11**, 751–764, 1975.

15. B. K. Min and F. W. Crossman, History-dependent thermochemical properties of graphite/aluminium unidirectional composites. Composite Materials: Testing and Design (6th conference), ASTM STP 787, ed I M Daniel. American Society for Testing and Materials, p371–392, 1982.

16. B. K. Min, A plane stress formulation for elastic plastic deformation of unidirectional composites, *Journal of Mechanics Physics and Solids*, **29**, 327–352, 1981.

17. J. Aboudi, A continuum theory for fibre-reinforced elastic-viscoplastic composites. *International Journal of Engineering Science*, **20**, 605–621, 1982.

18. J. Aboudi, Micromechanical analysis of the strength of unidirectional fibre composites, *Computational Science and Technology*, **33**, 79–86, 1988.

19. J. Aboudi, The effective thermomechanical behaviour of inelastic fibre-reinforced materials, *Int. J. Eng. Sci.*, **23**, 773–787, 1985.

20. W. Becker, M. J. Pindera and C. T. Herakovich, Mechanical response of unidirectional boron/aluminium under combined loading, CCMS-87-06, VPI-E-87-17, Virgin Polytechnic Institute and State University, 1987.

21. C. T. Sun and J. L. Chen, A micromechanical model for plastic behaviour of fibrous composites, *Computational Science and Technology*, **40**, 115–129, 1991.

22. Sun C T, Chen J L, Sha G T and Koop W E, Mechanical characterization of SCS-6/Ti-6-4 metal matrix composite *J. Comp. Mat.*, **24**, 1029–1059, 1990.

23. C. H. Chen and S. Cheng, Mechanical properties of anisotropic fibre-reinforced composites, *Journal of Applied Mechanics*, **37**, 186–189, 1970.

24. M. R. Begley and R. M. McMeeking, Numerical analysis of fibre bridging and fatigue crack growth in metal matrix composite materials, *Journal of Materials Science and Engineering*, **A200**, 12–20, 1995.

25. L. N. McCartney, *Proc. Royal Soc. Lond.*, **A409**, 329, 1987.

26. J. W. Hutchinson and H. M. Jensen, *Mech. Mater.*, **9**, 139, 1991.

27. R. N. McMeeking and A. G. Evans, *Mech. Mater.*, **9**, 217, 1990.

28. M. R. Begley and R. M. McMeeking, Fatigue crack growth with fibre failure, *Comp. Sci. Technol.*, 1995, **53**, 365–382.

29. H. Tada, P. C. Paris and G. R. Irwin, The stress analysis of cracks handbook, *Del Research*, St Louis, 1985.

30. D. F. Adams, and D. R. Doner, Transverse normal loading of a unidirectional composite *J. Comp. Mat.*, **1**, 152–164, 1967.

31. D. F. Adams, Inelastic analysis of a unidirectional composite subjected to transverse normal loading. *J. Comp. Mat.*, **4**, 310–328, 1970.

32. D. F. Adams, A micromechanical analysis of crack propagation in an elastoplastic composite material. *Fibre Sci. Technol.*, **7**, 237–256, 1974.

33. D. F. Adams, Analytical/experimental correlations of failure modes in composites. SEM Spring Conference on Experimental Mechanics, Las Vegas, 272–277, June 1985.

34. D. F. Adams, and A. K. Miller, Hygrothermal microstresses in a unidirectional composite exhibiting inelastic material behaviour, *J. Comp. Mat.*, **11**, 285–299, 1977.

35. D. F. Adams, and D. A. Crane, Finite element micromechanical analysis of a unidirectional composite including longditudinal shear loading. *J. Computers and Structures*, **18**, 1153–1165, 1984.

36. D. F. Adams, and D. A. Crane, Combined loading micromechanical analysis of a unidirectional composite, *Composites*, **15**, 181–192, 1984.

37. G. J. Dvorak and J. L. Teply, Periodic hexagonal array model for plasticity analysis of composite materials. Placticity Today: Modelling, Methods and Application, W Olszak Memorial Volume, ed. A Sawxzuk and B Bianchi. Elsever Science Publishers, Amsterdam, the Netherlands, p623–642, 1985

38. J. L. Teply and G. J. Dvorak, Bounds on overall instantaneous properties of elastic plastic composites. *J. Mech. Phys. Solids*, **36**, 29–58, 1988.

39. Y. A. Bahi-El-Din and J. G. Dvorak, A review of Plasticity theory of fibrous composite materials, metal matrix composites: Testing, analysis and failure modes, ASTM STP 1032, ed. W S Johnson, American Society for Testing and Materials, Philadelphia, PA, p103–129, 1989.

40. J. F. Wu, Shephard M S, J. G. Dvorak and Y. A. Bahei-El-Din, A material model for the finite element analysis of metal matrix composites, *Comp. Sci. Technol.*, **35**, 347–366, 1989.

41. *ABAQUS*, Hibbit, Karlson and Sorensen Inc., 100 Medway St., Providence Rhode Island, 02906, USA.

42. M. R. Wisnom, Factors affecting the transverse tensile strength of unidirectional continuous silicon carbide fibre reinforced 6061 aluminium, *Journal of Composite Materials*, **24**, 707–726, 1990.

43. M. R. Wisnom, Micromechanical modelling of the transverse tensile ductility of unidirectional SiC/6061 aluminium. *J. Composite Technol. and Research*, **14**, 61–69, 1992.

44. D. S. Li and M. R. Wisnom, non-linear stress–strain behaviour of unidirectional SiC fibre-reinforced aluminium alloy. *Jou. Strain Anal.*, **27**, 137–144, 1992.

45. D. S. Li, M. R. Wisnom, and D. J. Dingley, The mechanical properties of the matrix in continous fibre 6061 aluminium metal matrix composites. *Comp. Sci. Technol.*, **42**, 413–427, 1991

46. P. Martineou, R. Pailler, M. Lahaye and R. Naslain, SiC filament/titanium matrix composites – Part 2. *J. Mat. Sci.*, **19**, 2749–2770, 1984.

47. C. Rhodes and R. A. Spurling, Fibre-matrix reaction zone growth kinetics in SiC reinforced Ti-6Al-4v as studied by transmission electron microscopy. Recent Advances in Composites in the United States and Japan ASTM STP 864, ed. J R Vinson and M Taya. American Society for Testing and Materials, Philadelphia, PA p585-599, 1985.

48. C. J. Yang, S. M. Jeng and J. M. Yang, Interfacial properties measurements for SiC fibre-reinforced titanium alloy composites. *Scr. Metall. Mater.*, **24**, 469–474, 1990.

49. J. M. Yang, S. M. Jeng and C. J. Yang, Fracture mechanisms of fibre-reinforced titanium alloy matrix composites, Part I: interfacial behaviour. *Mat. Sci. Eng.*, **A138**, 155–167, 1991.

50. J. M. Yang, S. M. Jeng and C. J. Yang, Fracture mechanisms of fibre-reinforced titanium alloy matrix composites, Part I: interfacial behaviour, *Mat. Sci. Eng.*, **A138**, 155–167, 1991.

51. C. A. Bigelow and R. A. Naik, A macro-micro-mechanics analysis of a notched metal matrix composite. Composite materials: Testing and Design (10th Volume), ASTM STP1120, ed. G C Grimes. American Society for testing and Materials, Philadelphia, PA, 222–233, 1992.

52. R. S. Barsoum. On the use of isoparametric finite elements in linear fracture mechanics, *International Journal for Numerical Methods in Engineering*, **10**, 25–37, 1976.

53. R. D. Henshell and K. G. Shaw, Crack tip finite elements are unnecessary, *International Journal for Numerical Methods in Engineering*, **9**, 495–507, 1975.

54. A. A. Griffith, The phenomena of rupture and flow in solids, *Transactions, Royal Society of London*, **A-221**, 203–205, 1920.

55. L. B. Valla Jr., Stress intensity factor evaluation using singular finite elements, *Engineering Fracture Mechanics*, **16**, 557–568, 1982.

56. T. K. Hellen,On the method of virtual crack extensions, *International Journal for Numerical Methods in Engineering*, 9, 187–207, 1975.

57. M. R. Wisnom, Modelling fibre-matrix interface failure in unidirectional metal-matrix composites, Paper presented at 2nd International *ABAQUS* User conference, 1989.

58. D. S. Li and M. R. Wisnom , Micromechanical modelling of SCS-6 fibre-reinforced Ti-6Al-4V under transverse tension – Effect of fibre coating, *J. Comp. Mat.*,

59. M. R. Nedele and M. R. Wisnom, Stress concentration factors around a broken fibre in a unidirectional carbon fibre-reinforced epoxy, *Composites*, **25**, 549–557, 1994.

60. D. D. Robertson and S. Mall, Fibre-matrix interphase effects upon transverse behaviour in metal matrix composites, *J. Comp. Technol. and Research.* JCTRER, **14**, 3–11, 1992

61. A. Daadbin, A. J. Gamble and N. D. Sumner, The effect of the interphase and material properties on load transfer in fibre composites, *Composites*, 1992, **23**, 4, 210

62. J. G. Bakuckas Jr, A. C. W. Lau, T-M Tan and J. Awerbuch, A numerical model for predicting crack path and modes of damage in unidirectional composites, Technical Conference Proceedings of the American Society for Composites. Sixth Technical Conference, 502–512, 1991.

63. P. J. Cotteril and P. Bowen, Fatigue crack propagation in a SiC fibre-reinforced Ti-base metal matrix composite, *Proc. Conf. Fatigue 90*, 1990, Vol IV, 2551.

64. P. J. Cotteril P. Bowen, and A. R. Ibbitson, Fatigue crack growth in continuous fibre reinforced metal matrix composites, *Proc. Conf. on Test Techniques for Metal Matrix Composites*, ed. N. D. R. Goddard (Institute of Physics, London, 1990), 82.

65. P. P. Benham, R. J. Crawford and C. G. Armstrong, Mechanics of Engineering Materials, Longman Group Ltd., 1996.

66. P. J. Cotteril and P. Bowen, Fatigue crack growth in a fibre reinforced titanium MMC at ambient and elevated temperatures, *Composites*, 1993, **24**, 3, 214.

67. P. J. Cotterill and P. Bowen, Fatigue crack growth in Ti-15-3 matrix SCS-6 fibre metal matrix composit under tension tension loading, *Material Science and Technology*, **12**, 523, 1996.

68. R. S. Dow and J. Bird, The use for composites in marine environments, *Ironmaking and Steelmaking*, 1994, **21**, 6, 431.

69. F. E. Sloan and R. J. Seymour, The effect of seawater exposure on mode I interlaminar fracture and crack growth in graphite/epoxy, *Journal of Composite Materials*, **26**, 18, 2655, 1992.

70. Display III Users Manual, Engineering Mechanics Research Corporation, P. O . Box 696, Troy, Michigan 48099, USA.

71. H. L. Ewalds and R. J. H Wanhill, Fracture Mechanics, Edward Arnold, 1984.

72. T. J. Bond, Some considerations of the finite element method in stress analysis, PhD Thesis, University of Nottingham, 1972.

Appendix 1

Nomenclature for Begley and McMeeking [24]

a	Matrix crack length
a_0	Initial notch size
D	Diameter of fibres
$E_L = fE_f + (1-f)E_m$	Young's modulus of composite – rule of mixtures
$\overline{E}$	Effective Young's modulus for orthotropic materials
E_f, E_m	Young's modulus of fibre and matrix respectively
f	Volume fraction of fibre
$\kappa = \frac{K_{tip}}{K_a}$	Normalised stress intensity factor at the matrix crack tip
F(a/w)	Finite width effect correction to stress intensity factors
τ	Shear sliding stress at the fibre/matrix interface
n	Number of discretised grid points
N	Paris law exponent
S	Fibre strength
w	Specimen width
$\lambda = \frac{D(1-f)^2 E_m^2}{4\tau f^2 E_l^2 E_f}$	Bridging law coefficient
$\sigma_b, \Delta\sigma_b$	Bridging stress during load cycle, change in bridging stress
$\delta t, \Delta\delta t$	Total crack opening, total change in crack opening
δ_a	Matrix crack opening due to the applied load
δ_b	Matrix crack opening due to the bridging effects of the fibres
K_P	Stress intensity factor due to a point force on the crack face
K_a	Stress intensity factor due to applied loading
$\Sigma = \frac{4\lambda\overline{E}\sigma_b}{w}$	Normalised bridging stress
$\Sigma_a = \frac{4\lambda\overline{E}\sigma_a}{w}$	Normalised applied load
Σ_j	Normalised bridging stress at discretised locations

$\overline{b}_j$	Normalised crack opening due to the applied load at discretised locations

Appendix 2

Definition of Stress Intensity Factors

There are three modes of crack tip deformation [65,71]:

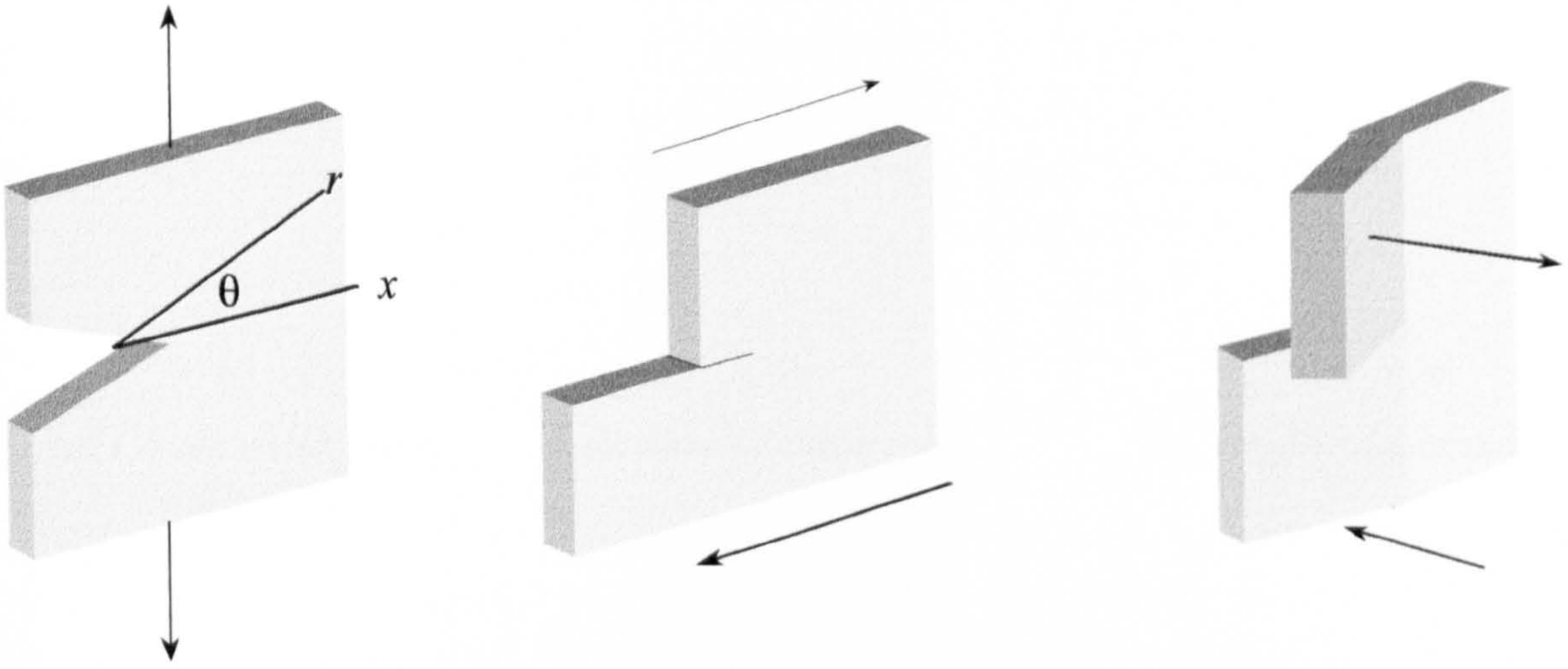

(i) Opening mode I *(ii) Shearing mode II* *(iii) Tearing mode III*

Figure A1 *Crack tip nomenclature*

The singularity in the stress field along any radial line from the tip of the crack are all proportional to $Kr^{-1/2}$, where K is known as the stress intensity factor. There is a value of K corresponding to each of the characteristic loading modes:

K_I – crack opening mode

K_{II} – shearing mode

K_{III} – twisting mode

To date most of the fracture mechanics work reported in the literature has been centred upon the first of these cases.

Figure A2 shows some typical crack configurations found in fracture mechanics and the expressions for K_I are as follows:

(a) Centre crack of length 2a in a sheet of finite width

$$K_I = \sigma\sqrt{\pi a}\left(\frac{w}{\pi a}\tan\frac{\pi a}{w}\right)$$

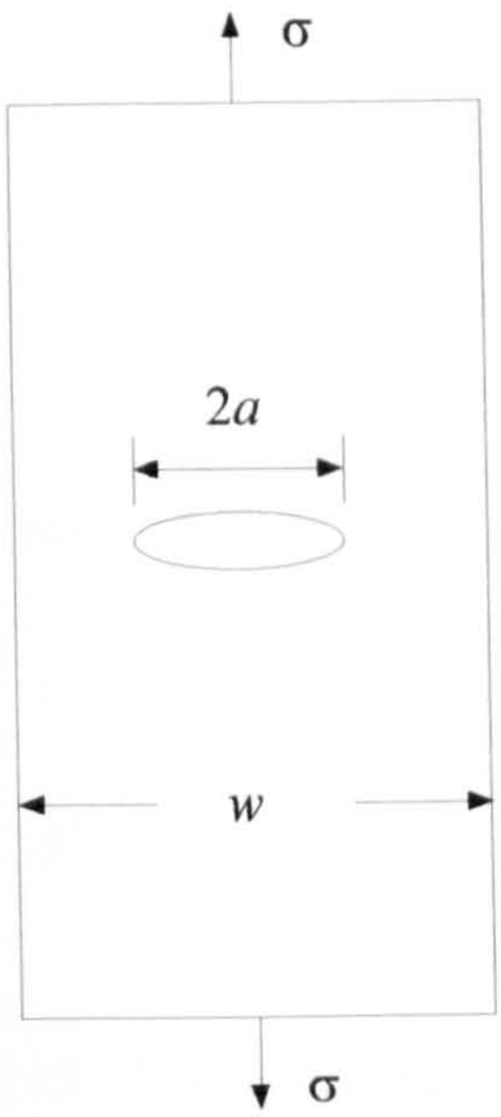

(a) Centre crack finite width plate

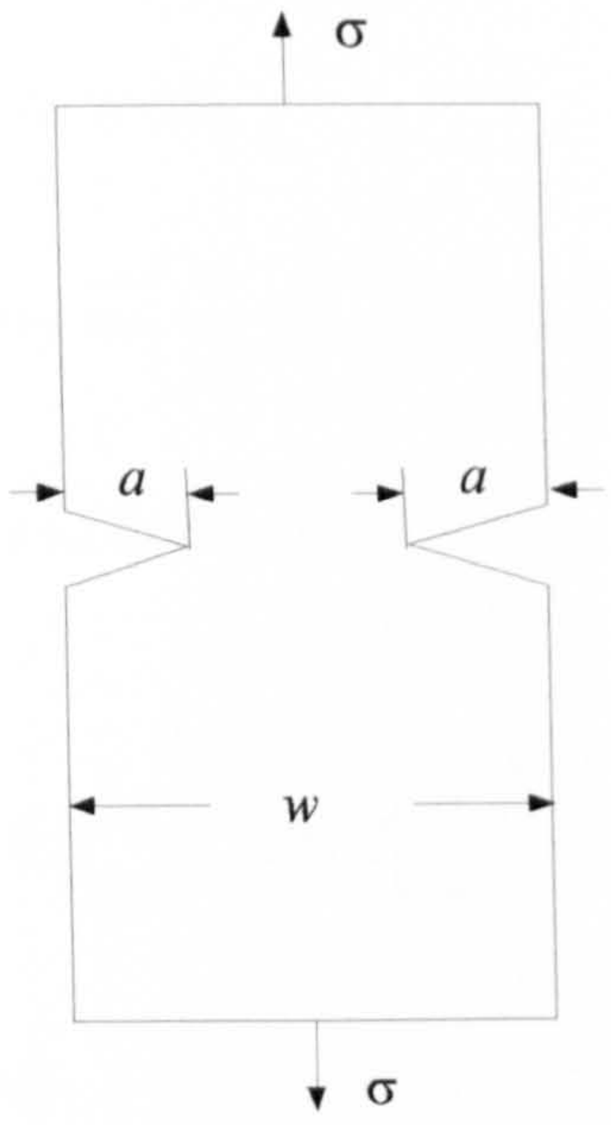

(b) Double edge crack

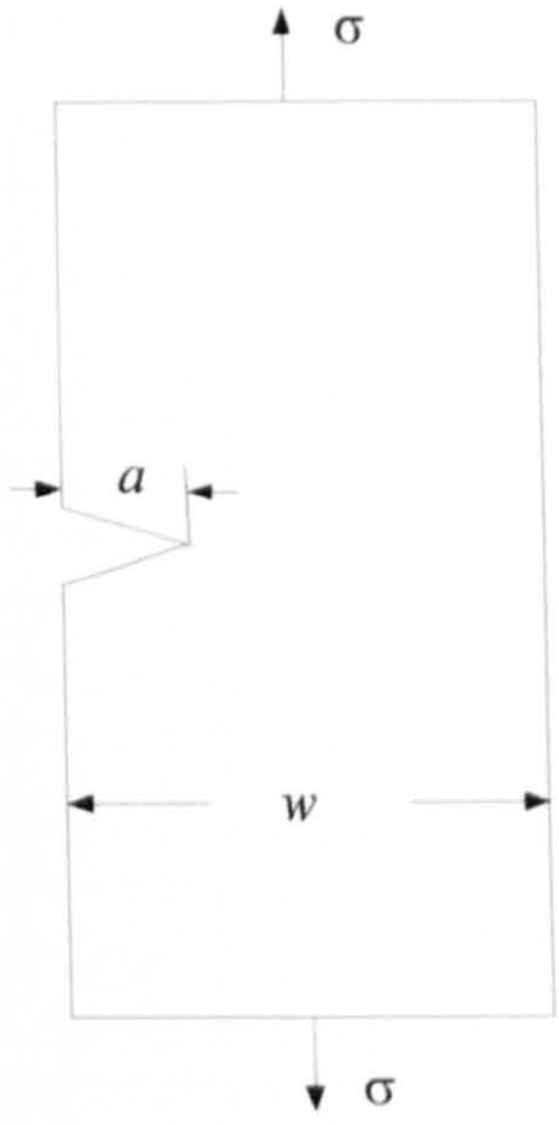

(c) Single-edge crack

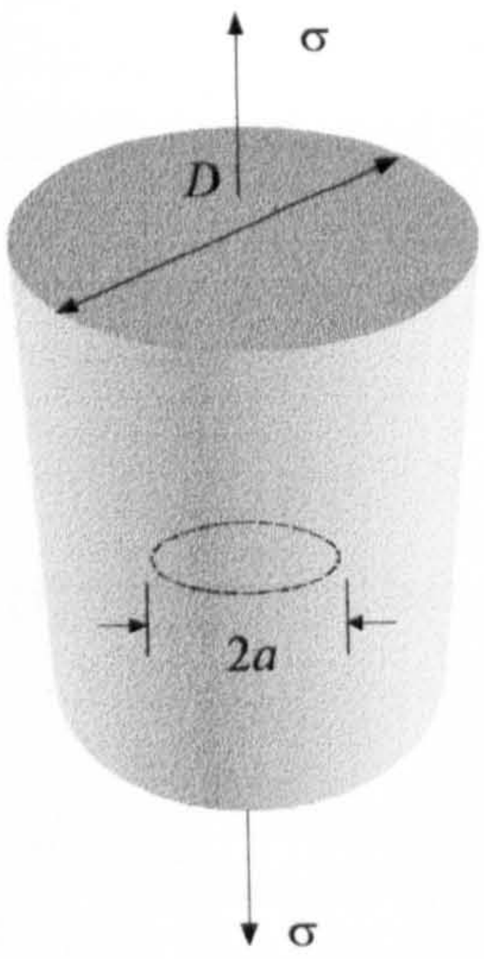

(d) Internal penny crack

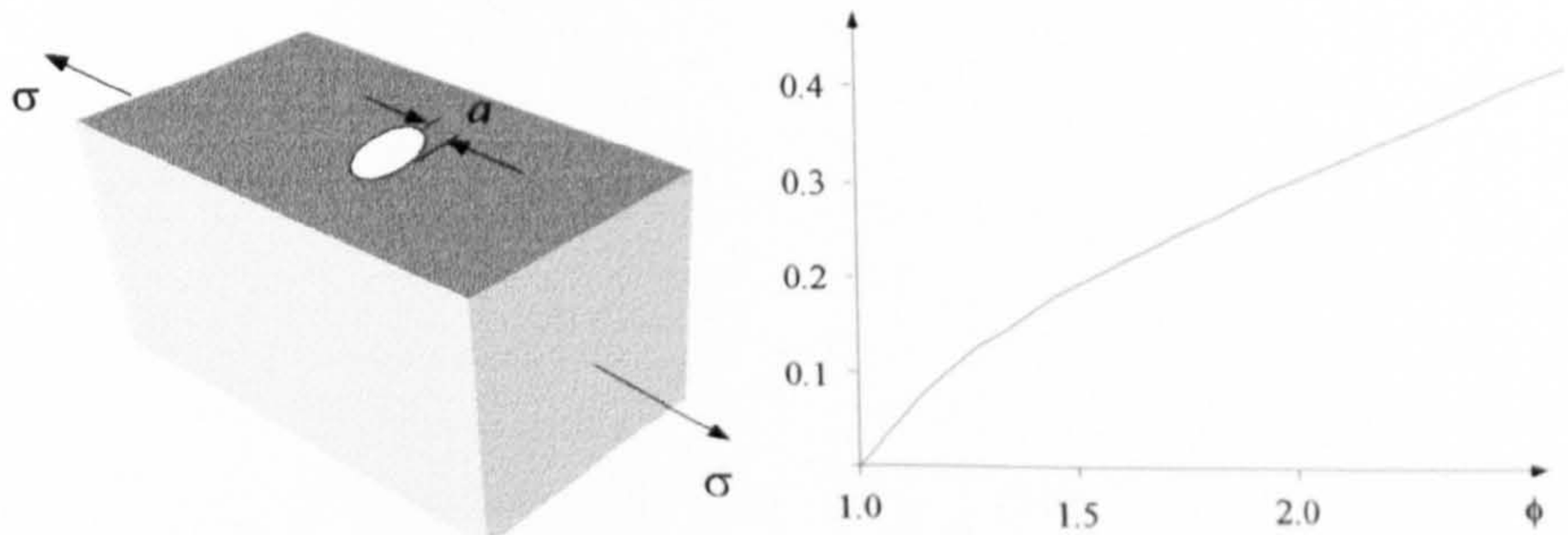

(e) Elliptical surface crack

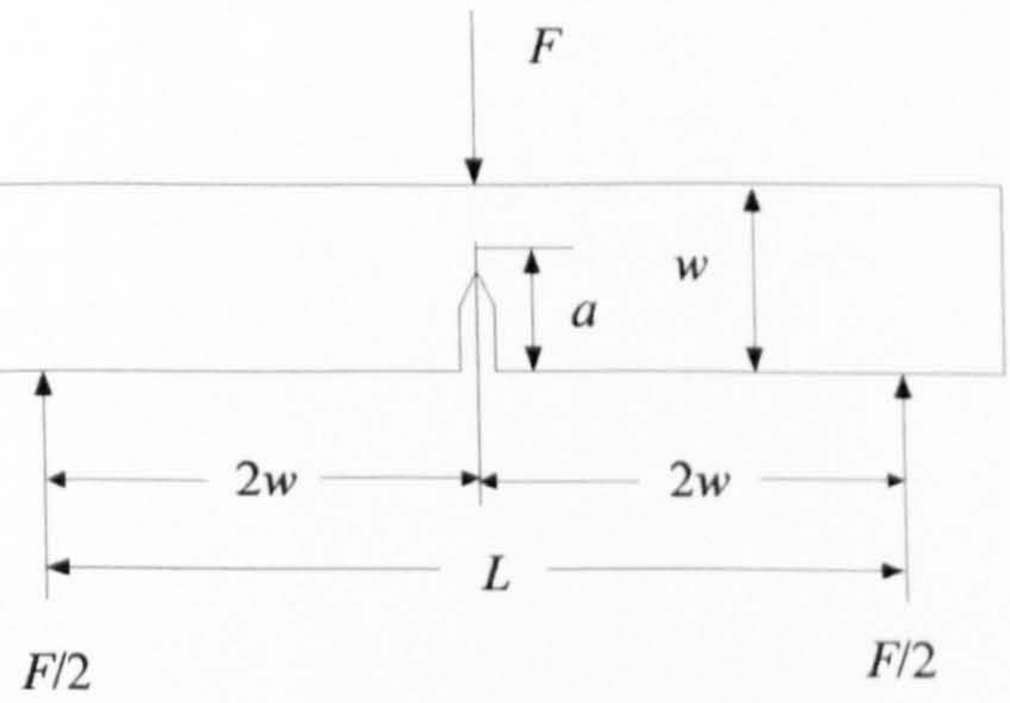

(f) Three-point bending

Figure A2 *typical crack configurations found in classic fracture mechanics*

(b) Edge crack in a plate of finite width

$$K_I = \sigma\sqrt{\pi a}\left(\frac{w}{\pi a}\tan\frac{\pi a}{w} + 0.2\frac{w}{\pi a}\sin\frac{\pi a}{w}\right)$$

(c) Single edge crack in a plate of finite width

$$K_I = \sigma\sqrt{\pi a}\left[1.12 - 0.23\frac{a}{w} + 10.6\left(\frac{a}{w}\right)^2 - 21.7\left(\frac{a}{w}\right)^3 + 30.4\left(\frac{a}{w}\right)^4\right]$$

(d) Penny-shaped internal crack

$$K_I = \sigma\sqrt{\pi a}\left(\frac{2}{\pi}\right)$$

(e) Semi-elliptical surface flaw

$$K_I = \sigma\sqrt{\pi a}\left(\frac{1.12}{\sqrt{\phi}}\right)$$

(f) Three-point bending

$$K_I = \frac{3FL}{2Bw}\left[1.93\left(\frac{a}{w}\right)^{1/2} - 3.07\left(\frac{a}{w}\right)^{3/2} + 14.53\left(\frac{a}{w}\right)^{5/2} - 25.11\left(\frac{a}{w}\right)^{7/2} + 25.8\left(\frac{a}{w}\right)^{9/2}\right]$$

Appendix 3

CTOD vs VCE approach

The CTOD approach

Consider the point *p* a distance *r* in front of the crack tip at an angle θ to the horizontal (Figure A3). The expressions for elastic stress, suggested by Irwin et al. [65,72], are:

$$\sigma_x = \frac{K_I}{\sqrt{2\pi r}}\cos\left(\frac{\theta}{2}\right)\left[1-\sin\left(\frac{\theta}{2}\right)\sin\left(\frac{3\theta}{2}\right)\right]$$

$$\sigma_y = \frac{K_I}{\sqrt{2\pi r}}\cos\left(\frac{\theta}{2}\right)\left[1+\sin\left(\frac{\theta}{2}\right)\sin\left(\frac{3\theta}{2}\right)\right]$$

$$\tau_{xy} = \frac{K_I}{\sqrt{2\pi r}}\sin\left(\frac{\theta}{2}\right)\cos\left(\frac{\theta}{2}\right)\cos\left(\frac{3\theta}{2}\right)$$

and $\sigma_z = \nu(\sigma_x + \sigma_y)$ (plane strain)

$\sigma_z = 0$ (plane stress)

where K_I is the mode I stress intensity factor and ν the poisson ratio.

It can be seen from the above equations that σ_{ij} is a function of both *r* and θ. For fixed θ, (θ = 0 for a point diectly in front of the crack tip along the *x*-axis) a plot of σ_{ij} against $r^{-1/2}$ is approximately linear and so the equation:

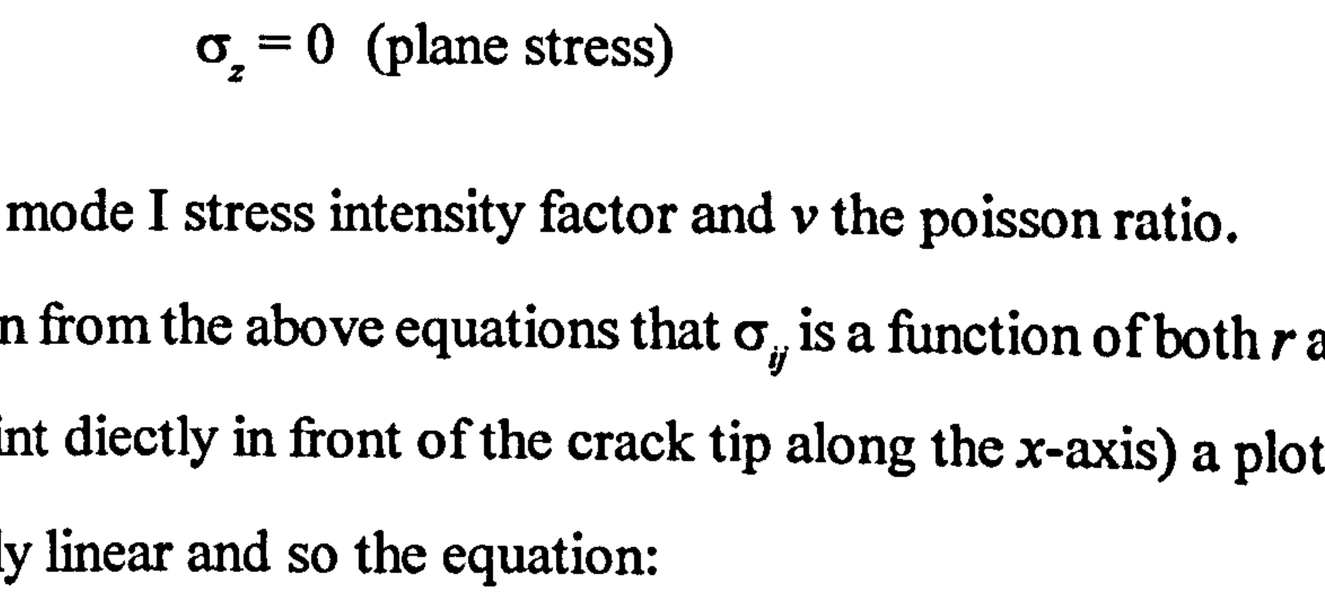

Figure A3 *Crack with point p at a distance r in front of the crack tip*

$$\sigma_y = \frac{K_I}{\sqrt{2\pi}} \frac{1}{\sqrt{r}}$$

will have gradient $\frac{K_I}{\sqrt{2\pi}}$ and K_I can be thus calculated.

The VCE approach

The solution of a static finite element displacement problem requires that a set of equations relating to stiffness, displacement and nodal loads be developed and solved. The equations take the form [56]:

$$\mathbf{K}\underline{\mathbf{u}} = \underline{\mathbf{b}} \qquad \{A1\}$$

where $\underline{\mathbf{u}}$ is the displacement vector, $\underline{\mathbf{b}}$ is the nodal load vector and **K** the stiffnes matrix. Most of the displacemenst in $\underline{\mathbf{u}}$ are unknown, however all of $\underline{\mathbf{b}}$ is known. The strain energy V is given in terms of the stiffness matrix and displacement vector by:

$$V = \frac{1}{2}\underline{\mathbf{u}}^{\mathrm{T}}\mathbf{K}\underline{\mathbf{u}} \qquad \{A2\}$$

The Endure user's manual suggests, that Endure uses a direct Gaussian elimination scheme for solving equation {A1} using forward elimination together with back substitution represented by equations {A3} and {A4}:

$$\mathbf{U}\underline{\mathbf{u}} = \mathbf{L}^{-1}\underline{\mathbf{b}} \qquad \{A3\}$$

for the forward elimination where **U** is an upper triangular matrix, **L** a lower triangular matrix and $\mathbf{L}^{-1}$ the inverse of the lower triangular matrix. For the back substitution:

$$\underline{\mathbf{u}} = \mathbf{U}^{-1}\mathbf{L}^{-1}\underline{\mathbf{b}} \qquad \{A4\}$$

with $\mathbf{L}^{-1}$ being the inverse of the lower triangular matrix. Hence, from {A2}:

$$V = \frac{1}{2}\underline{\mathbf{b}}^{\mathrm{T}}\mathbf{L}^{-1\mathrm{T}}\mathbf{U}^{-1\mathrm{T}}\mathbf{L}\,\mathbf{U}\,\mathbf{U}^{-1}\mathbf{L}^{-1}\underline{\mathbf{b}} \qquad \{A5\}$$

writing $\underline{\mathbf{b}}' = \mathbf{L}^{-1}\underline{\mathbf{b}}$, then:

$$V = \frac{1}{2}\,\underline{\mathbf{b}}'^{\mathrm{T}}\mathbf{U}^{-1\mathrm{T}}\mathbf{L}\,\underline{\mathbf{b}}' \qquad \{A6\}$$

Since $\mathbf{U}^{-1\mathrm{T}}$ is lower triangular, with main diagonal coefficients equal to the corresponding coefficients in **U**, which in turn are pivots a_{ii}^{*} for each equation i at its elimination stage, $\mathbf{U}^{-1\mathrm{T}}\mathbf{L}$ is a multiplication of two lower trangular matrices resulting in the diagonal matrix **D**:

$$\mathbf{D} = \begin{bmatrix} a_{11}^{*-1} & & 0 \\ & a_{22}^{*-1} & \\ 0 & & a_{nn}^{*-1} \end{bmatrix} \qquad \{A7\}$$

hence: $$V = \frac{1}{2}\underline{\mathbf{b}}'^{\mathrm{T}}\mathbf{D}\,\underline{\mathbf{b}}'$$

or $$\sum_i \underline{\mathbf{b}}'^2/a_{ii}^{*} \qquad \{A8\}$$

being the summation over all the degrees of freedom in the structure. The above result holds for any structure, any mechanical loading and zero prescribed displacements.

Energy release rates

For a small virtual increase in crack length Δa, with no change in external or mechanical loads, the total potential energy is given by:

$$\pi = \frac{1}{2}\underline{\mathbf{u}}^{\mathrm{T}}\mathbf{K}\,\underline{\mathbf{u}} - \underline{\mathbf{u}}^{\mathrm{T}}\underline{\mathbf{b}} \qquad \{A9\}$$

The energy release rate G is obtained from the variation of p wrt a constant load, i.e.

$$\delta\pi = \frac{1}{2}\underline{\mathbf{u}}^{\mathrm{T}}\{\delta\mathbf{K}\}\underline{\mathbf{u}} + \{\delta\underline{\mathbf{u}}\}^{\mathrm{T}}\mathbf{K}\,\underline{\mathbf{u}} - \{\delta\underline{\mathbf{u}}\}^{\mathrm{T}}\underline{\mathbf{b}} - \underline{\mathbf{u}}^{\mathrm{T}}\{\delta\underline{\mathbf{b}}\}$$

using {A1} this becomes:

$$\delta\pi = \frac{1}{2}\underline{\mathbf{u}}^{\mathrm{T}}\{\delta\mathbf{K}\}\underline{\mathbf{u}} - \underline{\mathbf{u}}^{\mathrm{T}}\{\delta\underline{\mathbf{b}}\}$$

If the loading is due to forces outside the crack tip element, then vector $\delta\underline{\mathbf{b}} = \underline{\mathbf{0}}$, and the final term can thus be dropped.

$$\therefore \qquad \delta\pi = \frac{1}{2}\underline{\mathbf{u}}^{T}\{\delta\mathbf{K}\}\underline{\mathbf{u}} - \underline{\mathbf{u}}^{T}\{\delta\underline{\mathbf{b}}\}$$

hence:
$$G = -\frac{d\pi}{da} = -\frac{1}{2}\underline{\mathbf{u}}^{T}\frac{\partial\mathbf{K}}{\partial\mathbf{a}}\,\underline{\mathbf{u}} \qquad \{A10\}$$

and
$$G = \frac{1-\nu^2}{E}\left(K_I^2 - K_{II}^2\right) + \frac{1+\nu}{E} \text{ (plane strain)} \qquad \{A11\}$$

$$G = \frac{1}{E}\left(K_I^2 - K_{II}^2 + K_{III}^2\right) \text{ (plane stress)} \qquad \{A12\}$$

Thus G can be calculated and for mode I cracks:

$$K_I = \sqrt{EG}$$

Where E is the Young's modulus of the material and ν, the poisson ratio.

Appendix 4

Partial *ABAQUS* restart file for soft bonded Al_2O_3/6061 simulation

HEADING
ABAQUS job created on 04-Apr-96 at 12:52:14
**
Node numbers and their respective cartesian coordinates within the mesh

*NODE
1, 0., 0.
2, 0.00125001, 0.
3, 0.00250002, 0.
....

1425, 0.1035, 0.025
1426, 0.105, 0.025
**
**
Elements making up the element set fibre; this element set will then have the fibre material properties assigned to it. The first digit is the element number, the remaining eight digits are the nodes making up the element.

*ELEMENT, TYPE=CPS8, ELSET=FIBRE
1, 1, 3, 11, 9, 2, 7,
10, 6

e.g. the line above indicates that element 1 consists of nodes 1, 3, 11, 9, 2, 7, 10 and 6

2, 3, 5, 13, 11, 4, 8,
12, 7
....

340, 1261, 1263, 1277, 1275, 1262, 1268,
1276, 1267

Elements and node numbers making up the matrix

*ELEMENT, TYPE=CPS8, ELSET=MATRIX
21, 86, 88, 102, 100, 87, 96,
101, 95
22, 88, 90, 104, 102, 89, 97,
103, 96
....

379, 1408, 1410, 1424, 1422, 1409, 1416,
1423, 1415
380, 1410, 1412, 1426, 1424, 1411, 1417,
1425, 1416

**
** Matrix
**
The material properties assigned to AL are applied to the element set MATRIX

*SOLID SECTION, ELSET=MATRIX, MATERIAL=AL
1.,
**
** Fibre
**
The material properties assigned to AL2O3 are applied to the element set FIBRE

*SOLID SECTION, ELSET=FIBRE, MATERIAL=AL2O3
1.,
**
** Al2O3
** Date: 04-Apr-96 Time: 12:41:41
**
The material properties of AL2O3 are defined

*MATERIAL, NAME=AL2O3
**
*ELASTIC, TYPE=ISO
210000., 0.3
**
** Al
** Date: 04-Apr-96 Time: 12:41:41
**
The material properties of Al are defined

*MATERIAL, NAME=AL
**
*ELASTIC, TYPE=ISO
68900., 0.33
**
Definition of the axisymmetric rigid surface

*rigid surface,type=segments,name=asurf,ref node=5000
start,-0.001,0.0
line,0.106,0.0

Definition of the elements forming the outside periphery of the fibres – these elements will be used to define the contact surfaces

*elset,elset=fib1b
1,2

....

Definition of the elements forming the outside periphery of the matrix – these elements will be used to define the contact surfaces

*elset,elset=mat1b
21,22,23,24

....

*elset,elset=fib1r
2,4,6,8,10,12,14,16,
18,20
*elset,elset=fib2l
61,65,69,73,77,81,85,89,
93,97

....

Assign the nodes along the bonded surface of the fibre (master surface) node set - allowing any of the nodes along this surface to act as a crack initiator if so desired

*nset,nset=bondf1b
1,2,3,4
**5
*nset,nset=bondf2b
235,236,237,238,239,240,241,242
**243
....

Define the surfaces using the element sets previously assigned to their respective element sets

*surface definition,name=fib1bs
fib1b,s1
*surface definition,name=fib2bs
fib2b,s1
....

Specify a uniform surface interaction which can be applied to all the contact surfaces

*surface interaction,name=both
1.0

Define the contact surfaces. The first surface given in the definition will be assigned as a "slave", the second as a "master". The "small sliding" variable assigned to the contact pair indicates that the small sliding algorithm should be used

*contact pair,interaction=both,small sliding
fib1bs,asurf
fib2bs,asurf

fib3bs,asurf

....

Apply the initial conditions to each of the surfaces and the node sets constututing the master surface. The "type =contact,normal" indicates that contact modelling in the normal direction only will be used. If "type =contact" is used, then the surface is bonded in all directions

*initial conditions,type=contact,normal
fib1bs,asurf,bondf1b
*initial conditions,type=contact,normal
fib2bs,asurf,bondf2b
....

**

*RESTART, WRITE, FREQUENCY=1
**
** step 1,Boundary conditions
**
Maximum number of increments that the model should attemt before termination

*STEP,inc=100
**
Boundary conditions

*STATIC
8.0E-04,0.00287
**
** U(0,y)=0
**
*BOUNDARY, OP=NEW
1, 1,, 0.
6, 1,, 0.
....
73, 1,, 0.
78, 1,, 0.
5000,1,2
5000, 6
**
** U(0,50)=(0,0.001)
**
*BOUNDARY, OP=NEW
81, 1,, 0.
81, 2,, 0.001
**
** U(r,50)=0.001
**

```
*BOUNDARY, OP=NEW
     82, 2,,      0.001
     83, 2,,      0.001
     84, 2,,      0.001
....

   1424, 2,,      0.001
   1425, 2,,      0.001
   1426, 2,,      0.001
**
```

Debond criteria to be applied to the slave surface "mat1ls" and the master surface "fib1rs" with the normal, shear stress and maximum tolerance values given in the fracture criterion sub-option

```
*DEBOND,SLAVE=mat1ls,MASTER=fib1rs,TIME INC=0.0002,
FREQUENCY=1,OUTPUT=BOTH
0.,1.
0.0002,0.,
*FRACTURE CRITERION,TYPE=CRITICAL
STRESS,TOLERANCE=0.05,DISTANCE=0.0
1.9E+2,9.5E+1,9.5E+1

*DEBOND,SLAVE=mat1rs,MASTER=fib2ls,TIME INC=0.0002,
FREQUENCY=1,OUTPUT=BOTH
0.,1.
0.0002,0.,
*FRACTURE CRITERION,TYPE=CRITICAL
STRESS,TOLERANCE=0.05,DISTANCE=0.0
1.9E+2,9.5E+1,9.5E+1
....
```

Output all relevant data to postprocessing file

```
*CLOAD, OP=NEW
*DLOAD, OP=NEW
*TEMPERATURE, OP=NEW
**
*NODE PRINT, FREQ=1
U
*NODE FILE, FREQ=1
U
**
*EL PRINT, POSITION=INTEGRATION POINT, FREQ=1
S
E
*EL FILE, POSITION=INTEGRATION POINT, FREQ=1
S
E
```

```
**
*EL PRINT, POSITION=NODES, FREQ=0
**
*EL FILE, POSITION=NODES, FREQ=0
**
*EL PRINT, POSITION=CENTROIDAL, FREQ=0
**
*EL FILE, POSITION=CENTROIDAL, FREQ=0
**
*EL PRINT, POSITION=AVERAGED AT NODES, FREQ=0
**
*EL FILE, POSITION=AVERAGED AT NODES, FREQ=0
**
*MODAL PRINT, FREQ=99999
**
*MODAL FILE, FREQ=99999
**
*ENERGY PRINT, FREQ=0
**
*ENERGY FILE, FREQ=0
**
*PRINT, FREQ=1
**
*END STEP
```

Appendix 5

The Modelling of Crack Propagation Through the Interfacial Region of a SiC/ Titanium Metal Matrix Composite

The modelling of crack propagation through the interfacial region of a SiC/titanium metal matrix composite

D. Griffin, A. Daadbin, P.K. Datta and J.S. Burnell-Gray

Department of Mechanical Engineering and Manufacturing Systems,
University of Northumbria at Newcastle, UK

Keywords: Mathematical model, composite, interface, stress intensity, crack propagation

ABSTRACT

Finite element models of the interfacial region between a silicon carbide fibre and titanium metal matrix have been constructed using the *Engineering Mechanics Research Corporation* finite element package *Display 3* and the *Rasna Corporation* package *Astruct*. The distributions of both tensile and shear stresses across the interface have been obtained and an elliptical crack of semi length 1.5 μm introduced. The Young's moduli of fibre and matrix were varied from a nominal value of 360 GPa to 400 GPa for the fibre and 360 GPa to 92.3 GPa for the matrix; the resultant stress distribution showed that increasing fibre moduli dominated interfacial stress distribution, particularly directly in front of the crack tip, and increased the chance of crack propagation into the fibre. The stress intensity factors for a *type I* crack, in the interfacial region, using the finite element packages *Endure* and *Applied Structure* have been calculated and the results compared with theoretical calculations.

1. INTRODUCTION

Metal matrix fibre reinforced composite materials are becoming increasingly utilised as their high specific strength and stiffness, together with their high temperature capabilities, are realised [1,2]. Materials reinforced with silicon carbide (SiC) fibres, such as titanium metal matrix composites (MMC) combine the light weight and ductility of the matrix material, with the high specific stiffness and strength of the reinforcement; such materials offer significant advantages for use in aerospace and in other safety critical applications; for such applications the primary requirement is resistance to fracture and fatigue.

One of the major problems in analysing the crack propagation behaviour of composite materials is the inability of the *Linear Elastic Fracture Mechanics* (LEFM) to characterise their fracture behaviour. In general for composites:

G_{Ic} composite $\neq G_{Ic}$ matrix $V_m + G_{Ic}$ fibre V_f

where

G_{Ic} = critical strain energy release rate

V_m, V_f = volume fraction of matrix and fibres.

The difficulty stems from the fact that the process of fracture in composite materials is controlled by a series of energy absorbing mechanisms - debonding, delamination, fibre bridging and matrix microcracking. Additional complications arise due to the presence of a fibre/matrix interface.

Commonly, a fibre reinforced composite will have an interfacial layer between matrix and reinforcement caused by chemical interaction during the production stages (Table 1). The type of reaction occurring, and resultant interfacial properties, will depend on the properties of the reinforcing material, and matrix [1], as will the actual degree of inter-diffusion between the two materials. In the case of a silicon carbide/titanium matrix composite, a tungsten core carbon fibre is coated with a layer of silicon in order to control the degree of diffusion between the highly reactive titanium matrix, and the fibre.

Table 1. Possible chemical composition of the interface

W core		Fibre
SiC		
TiO_2 TiO_{2-x} SiO_2 other ?	TiC Ti_xC_{1-x} SiC SiOC other ?	TiSi $TiSi_2$ Ti_xSi_{1-x} other ?
Ti matrix		

The interface between the reinforcing fibre and supporting matrix plays a crucial role in the load transfer characteristics of the composite as a whole [3]. Strengthening by fibre reinforcement depends on the process of load transfer, and is limited by the shear strength of the interface. Thus load transfer across the interface is of prime concern in the control of mechanical properties.

Table 2. Material properties of modelled composite

	Young's modulus (GPa)	Poisson's ratio
Fibre	400	0.25
Interface	360	0.34
Matrix	92.3	0.36

The interfacial region is frequently the site of crack initiation and hence can be responsible for diminishing the mechanical properties of a composite. Depending on interfacial properties, a crack travelling through the interface will either cause debonding of the reinforcement, or will initiate a fracture in the fibre itself; in case of the former happening, globally, the composite will be more ductile (tougher) and in the latter case, brittle.

Clearly, the behaviour of a composite, under working conditions, is difficult to predict, due to the complexity of the material. A great deal of costly material testing has to be utilised to characterise a composite [4]. Theoretical modelling of the interface behaviour, and various fracture and energy absorbing properties, can be used to simplify the situation.

2. MODELLING PROCEDURE

A 1000 μm discontinuous silicon carbide fibre of radius 12.5 mm embedded in a titanium metal matrix of length 1200 μm and radius 90 μm was modelled using the finite element packages *Display 3* and *Astruct*. The interface between fibre and supporting matrix was given its own material properties, which were assumed to be distributed homogeneously [5]. The thickness of the interface was set at 5 mm [5].

For calculation of the stress distribution, both radially and axially across the interface, a two-dimensional, axisymmetric quarter model of the fibre/matrix interface was constructed using eight-noded, parabolic elements with a high concentration of elements in the interface region (Fig 1). Table 2 shows the material properties of the fibre/matrix interface used in the models.

Fig 1. Two-dimensional axisymmetric model

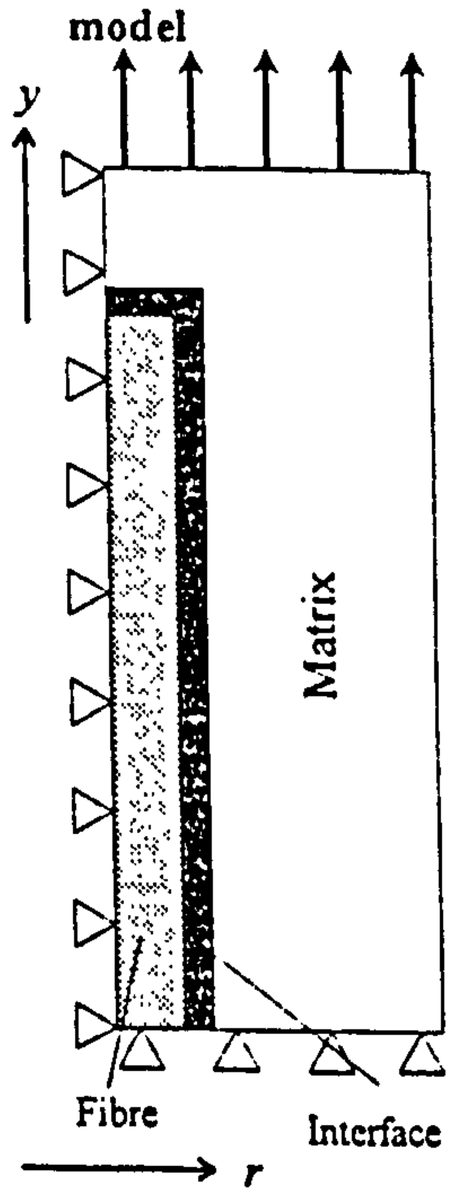

A pressure of 20 MPa was applied to one end of the composite model, the other being restrained in the axial direction. A restraint was also placed radially on the fibre side. The distributions of both tensile and shear stresses along the interface axis and radially outward were calculated and the results, as seen in Fig 2, show clearly that the tensile stress is constant radially across the interface, varying only axially. The shear stress however (Fig 3) only displays a consistency towards the middle of the composite; as the peak shear stress is reached, a positive gradient can be seen to develop from the matrix to the fibre side of the interface.

Fig 2. Tensile stress distribution across fibre/matrix interface

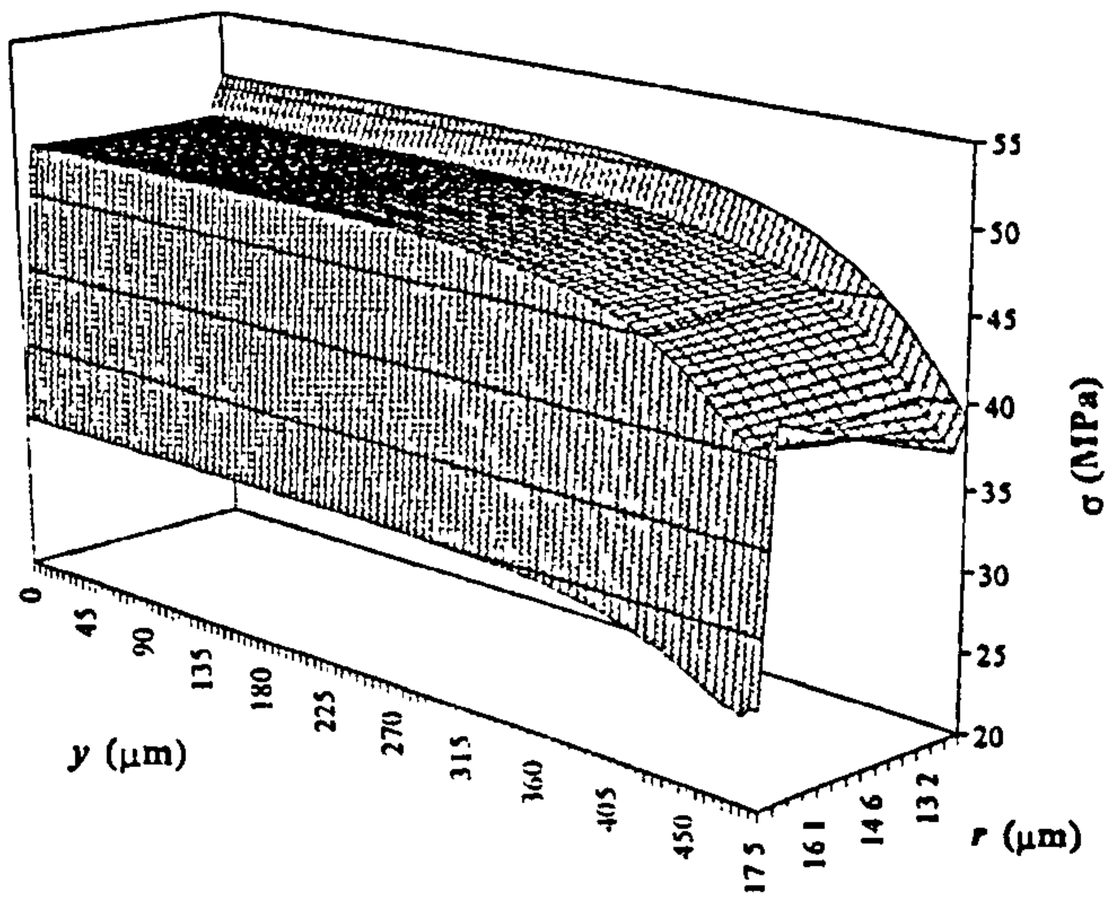

Fig 3. Shear stress distribution across fibre/matrix interface

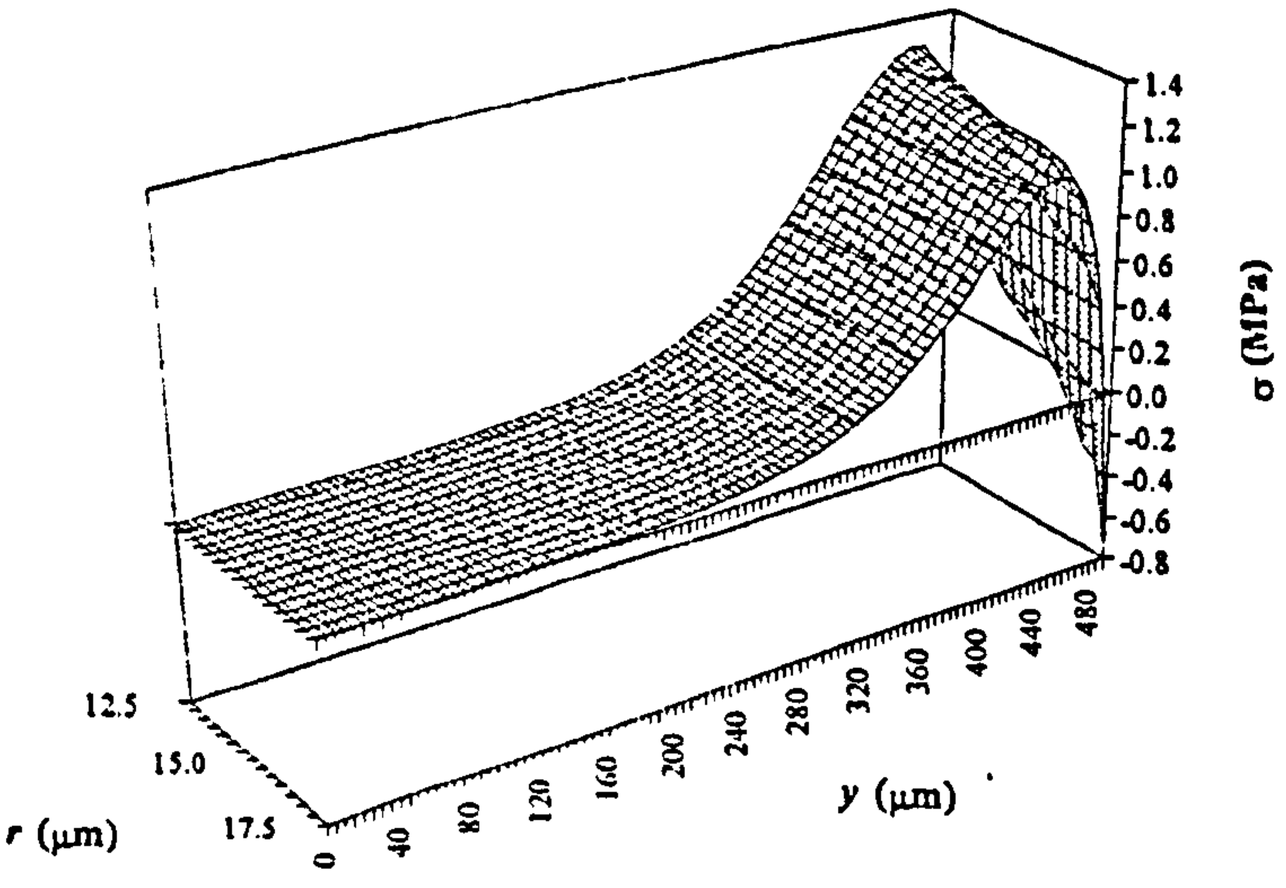

Fig 4. Finite element model of crack with nodes around crack tip moved to "quarter point" position

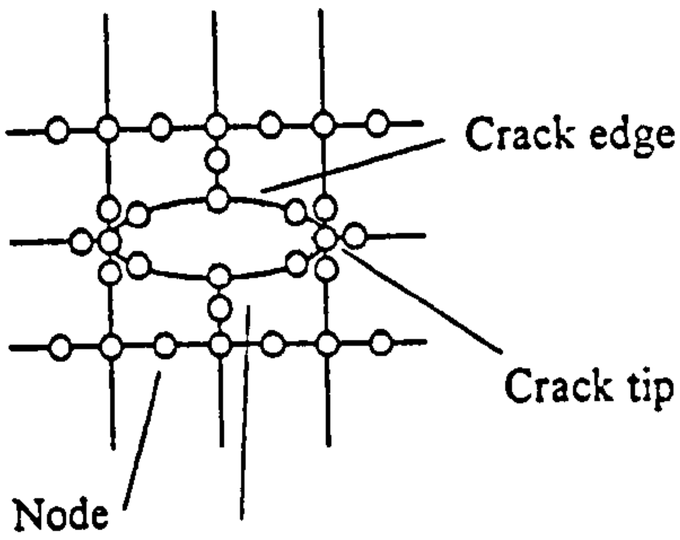

3. RESULTS AND DISCUSSION

3.1 Stress Distribution in front of Crack Tips

An "elliptical" *type I* crack of semi length 1.25 μm was introduced halfway, axially, along the interface, midway between fibre and matrix with major axis parallel to the radial axis. The quarter point method was used on the elements at the crack tip (Fig 4) to simulate the $r^{-1/2}$ singularity as required by the Westergard solutions [6,7].

The stress distributions in front of the crack tip along the boundary line between fibre/interface and in front of the crack tip along the boundary line between interface/matrix were obtained for varying values of fibre and matrix Young's moduli. The fibre and matrix Young's moduli were varied from that of the interface (360 GPa) to 400 GPa and 92.3 GPa respectively. Figs 5 and 6 show the effect on the stress distributions. It can be quite clearly seen that the overall stress distribution on the fibre side increases with increasing fibre modulus, but also the concentration of maximum stress at $y = 0$ increases at a greater rate. On the matrix side, despite the matrix modulus falling, there is a steady increase in the overall stress distribution along the interface/matrix boundary line, and again, the point of maximum stress at $y = 0$, increases at a greater rate. Clearly, the fibre modulus dominates the distribution of stresses in the interface, and the chance of crack propagation into the fibre, increases with increasing fibre modulus.

Fig 5. Stress distribution in front of crack tip (fibre side)

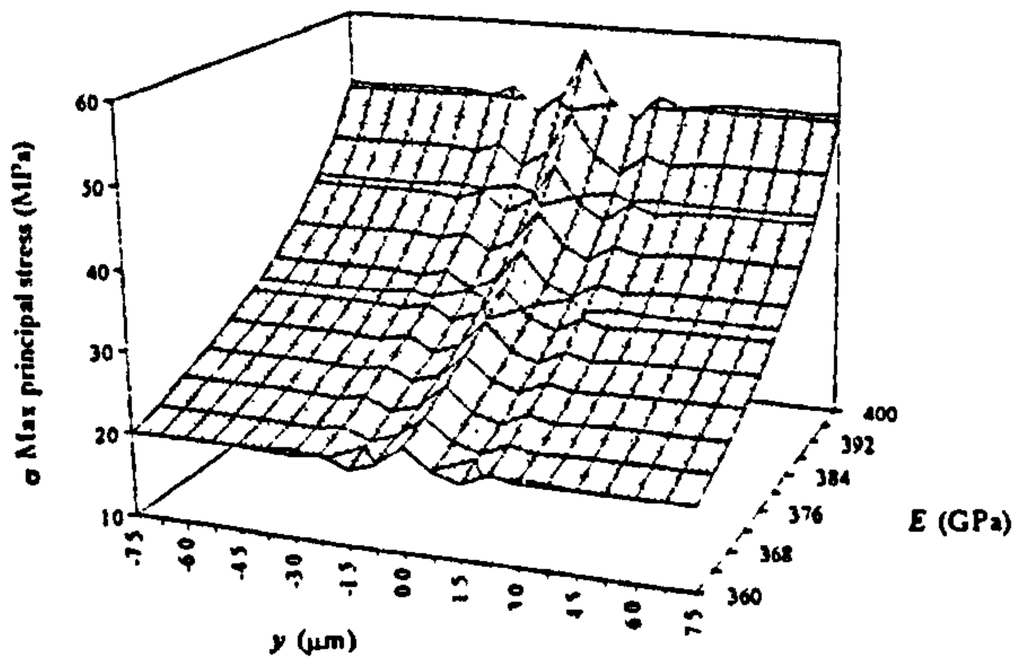

Fig 6. Stress distribution in front of crack tip (matrix side)

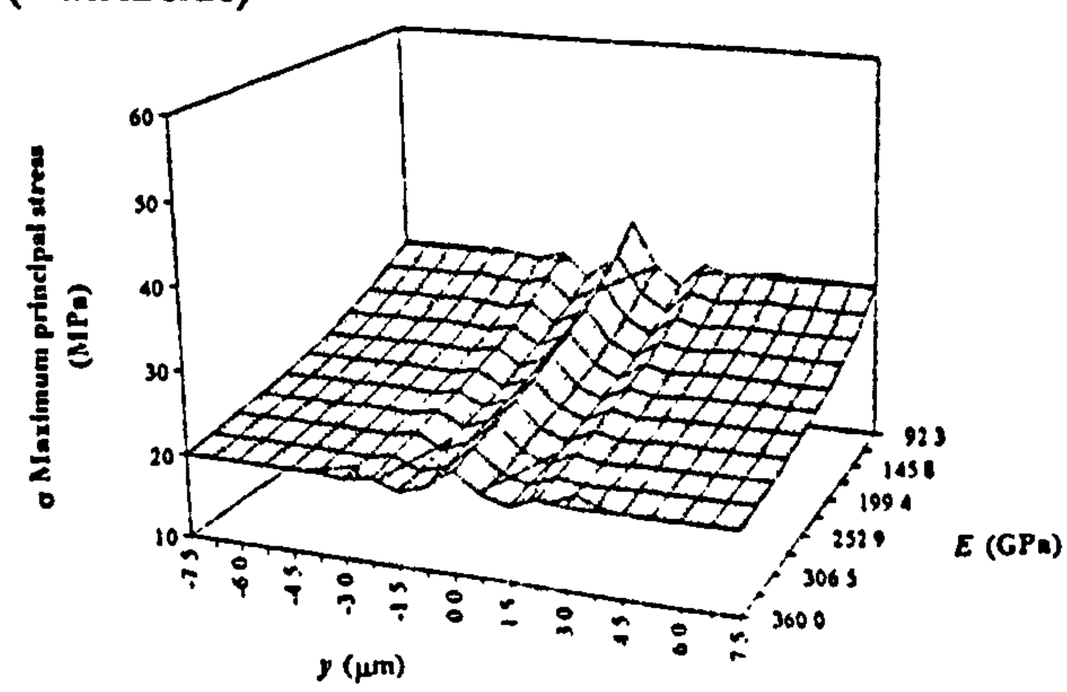

3.2 Stress Intensity Factor Calculation

Two differing finite element packages were used to obtain the stress intensity factors of a crack in the interface region: *Endure* and *Applied Structure*.

Endure

Endure directly calculates stress intensity factors for a given crack length. In use conventional isoparametric elements, with mid-side nodes relocated to the "quarter point" position are used to model the crack tip. The quarter point element simulates the elastic stress singularity of the $\sigma r^{-1/2}$ type, when the mid-side nodes are shifted to the quarter point position as shown in Fig 4. Two methods can be used to calculate K_I, one uses a J integral approach [8], the other displacement. For a two-dimensional crack the J integral approach is:

$$J_I = \oint_C \left(Wn_i - T_i \frac{\partial u_i}{\partial x} \right) \quad \text{so that} \qquad K_I = \sqrt{\frac{2\mu J_I}{1-\nu}}$$

where W is strain energy density, T_i the traction components on the contour C, n_i the components of the unit outward normal vector to C, u_i the displacement components μ the shear modulus and ν the poisson ratio.

For the displacement approach [9]:

$$K_I = \frac{2\mu\sqrt{2\pi}}{k+1}(4V_b - V_c)/\sqrt{L} \qquad \text{where} \qquad V = \frac{4\beta_1(1-\beta_2^2)}{4\beta_1\beta_2 - (1+\beta_2^2)}$$

μ is the shear modulus, $k = (3 - \nu)/(1 + \nu)$ and

$$\beta_1^2 = 1 - \frac{c^2}{c_1^2}$$

$$\beta_2^2 = 1 - \frac{c^2}{c_2^2}$$

c_1, c_2 being the dilational and equivoluminal wave speeds in the material.

Endure was run for a crack extended from an initial length of 0.25 μm to a final length of 2 μm, and the results compared to the theoretical values of K_I (Fig 7).

Fig 7. Stress intensity factor values from *Endure* compared to theoretical values

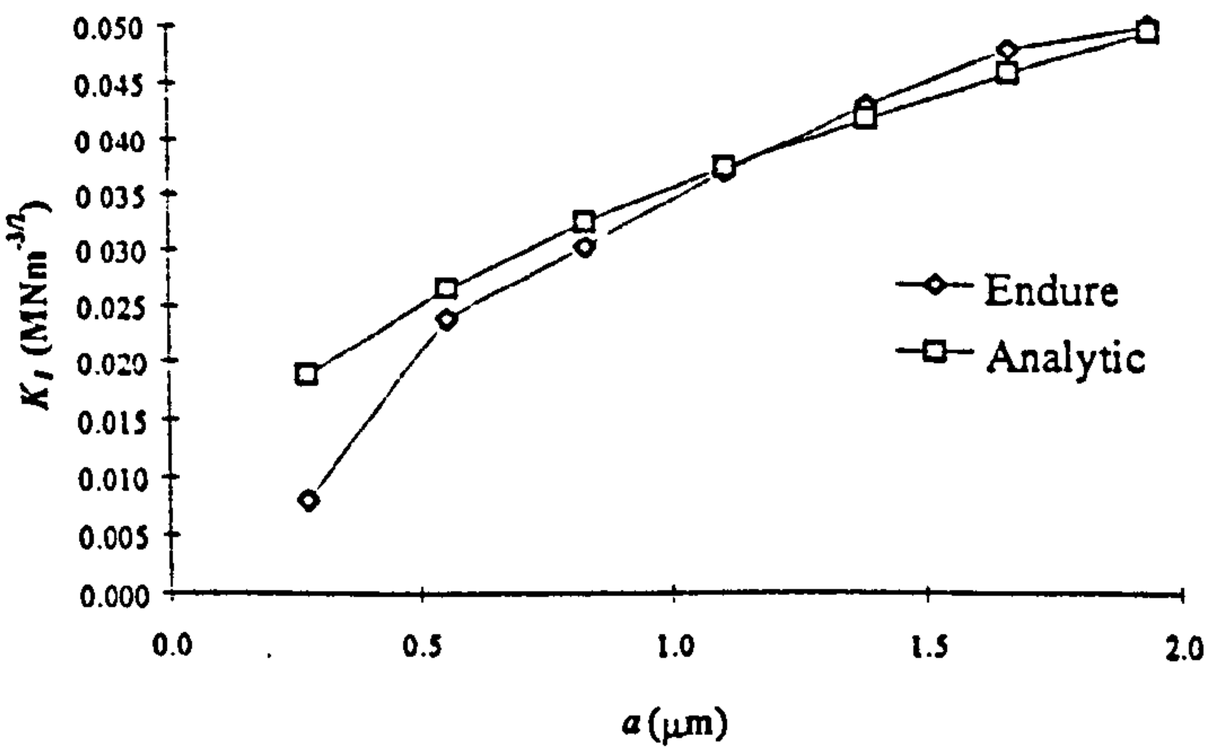

Apart from the initial crack length, there was close agreement between theoretical and calculated values of stress intensity.

Applied Structure

Applied structure is radically different from the classic finite element package, incorporating what are known as *design variables*; with such variables, many differing parameters can be altered in one model run. To calculate the stress intensity factors for a crack in the interface, nodes which constitute the crack tip are allowed to move a set distance while the model is running. Thus, the crack is allowed to propagate while the model is still running. The strain energy at each crack tip, U, is output in graphical form and by obtaining the partial derivative, i.e.:

$$G = \frac{\partial U}{\partial A}$$

Where A is the crack area, the energy release rate, G, is obtained. For the interfacial region, the stress

intensity factor K_I is given by:

$$K_I = \sqrt{EG}$$

E being the Young's modulus of the interface.

Fig 8. Stress intensity factor values from *Astruct*, compared to theoretical values

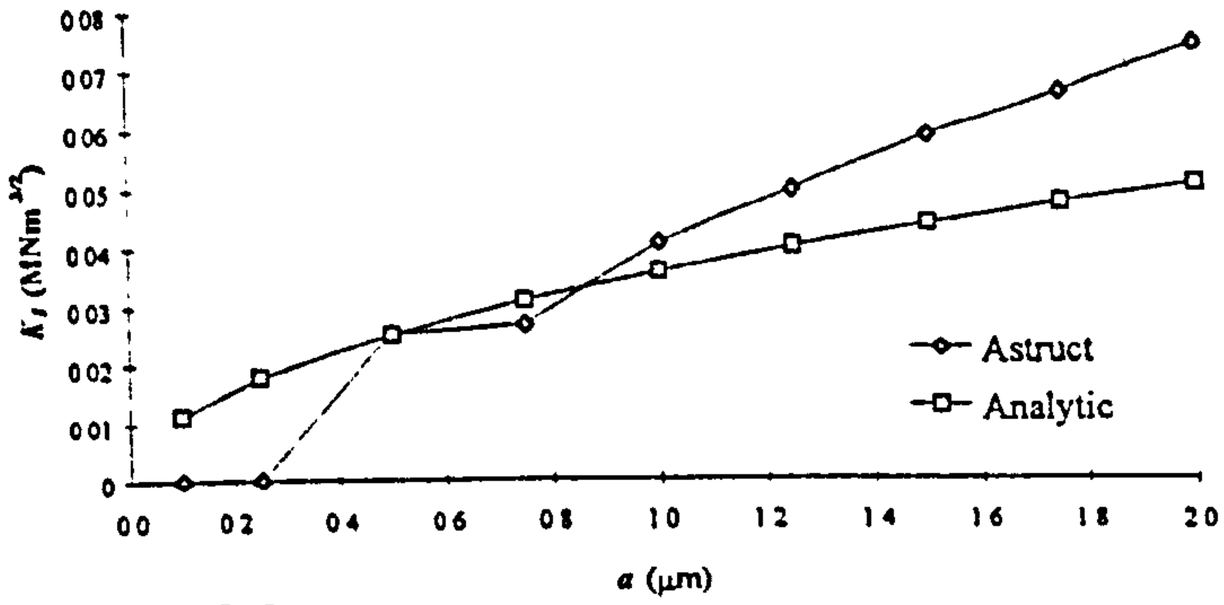

As can be seen from Fig 8, the calculated values of K_I do not correspond as closely to the theoretical values, as those obtained from *Endure*; however, these values were considerably easier to obtain with only one model run being necessary, as opposed to the ten model runs necessary in *Endure*.

CONCLUSION

Models of the interfacial region of a Ti/SiC composite have been constructed using two differing finite element packages, the distribution of both tensile and shear stresses in the interface have been obtained. The stress distribution in front of the tips of an elliptical crack were modelled for differing values of both fibre and matrix Young's moduli, and it was found that the increasing fibre moduli exponentially increased the stress distribution along the border line between fibre/interface and interface/matrix, by far the greatest increase being on the fibre side. Directly in front of each crack ($y = 0$) the stress increased even more sharply. Crack propagation is thus highly influenced by fibre moduli, with the crack more likely to travel in the fibre direction if the matrix modulus is significantly lower than that of the fibre.

Stress intensity factors for both crack tips were calculated at $y = 0$ using two differing finite element packages, *Endure* and *Applied Structure*. The values obtained from *Endure* were in close agreement with the theoretical values. The values of K_I from *Applied Structure* did not agree as closely with the analytical results, but were considerably easier to obtain.

REFERENCES

1) Datta, P. K., Strafford, K. R. and Burnell-Gray, J. S.:Key Paper for Composites 1993.
2) Bender, B. A., Jessen, T. L.: Composites., 1994, 25, 87.
3) Melantis, N., Galiotis, C., Tetlow, P. L., Davies, C. K. L.: Composites., 1993, 24, 459.
4) Feest, A. E.: Composites., 1994, 25, 75.
5) Daadbin, A , Gamble A. J. and Sumner, N. D.: Composites.,1992, 23, 210.
6) Henshell, R. D., Shaw K. G.: Int J for Num Meth in Eng., 1975, 9, 495.
7) Barsoum, R. S.: Int J for Num Meth in Eng., 1976, 10, 25.
8) Parks, D. M.: Num Meth in Frac Mech., 1978, 464
9) Tracey, D. M.: Int J for Num Meth in Eng., 1977, 11, 401.

Appendix 6

SIMULATION OF FAILURE MECHANISMS IN Al_2O_3/Al METAL MATRIX COMPOSITES USING FINITE ELEMENT MODELLING TECHNIQUES

D. Griffin, A. Daadbin, J. S. Burnell-Gray and P. K. Datta
Surface Engineering Research Group, School of Engineering, University of Northumbria at Newcastle, UK

ABSTRACT

This work has been designed to study the failure mechanisms of continuously reinforced metal matrix composites. With this aim in mind, a model with reference to a unidirectional Al_2O_3/Al composite has been constructed incorporating mode I crack propagation, fibre bridging and fibre/matrix debonding.

A two-dimensional axisymmetric quarter model of the composite, consisting of four and a half fibres situated in five matrix bays was built using the general purpose finite element package *ABAQUS*. All the failure mechanisms used the unique "contact surface" options available in *ABAQUS*.

The model was subject to a tensile strain and an edge crack was seeded from the right hand side matrix bay. Two differing fibre/matrix bond strengths were incorporated into the model – the first had an interfacial strength equal to the matrix UTS, the second had a UTS calculated from a rule of mixtures formula – to determine how the failure mechanisms would differ for the different bond strengths.

It transpired that the dominant mode of failure for the relatively weakly bonded interface was fibre bridging, with partial fibre debonding playing a secondary rôle. For the higher fibre/matrix bond strength, mode I cracking was the dominant mode of failure.

INTRODUCTION

Because of their high specific strength and stiffness, together with their high temperature capabilities, fibre reinforced metal matrix composites (MMCs) are becoming increasingly utilised. Well designed MMCs combine the light weight and ductility of the matrix material, with the high specific strength and stiffness of the reinforcement.

One of the main difficulties in analysing the failure mechanisms in composites is the inapplicability of the rule of mixtures in describing the fracture behaviour, i.e.

$$G_{Ic}\ \text{composite} \neq G_{Ic}\ \text{matrix}\ V_m + G_{Ic}\ \text{fibre}\ V_f \qquad (1)$$

where, G_{Ic} = critical strain energy release rate, V_m and V_f = volume fraction of matrix and

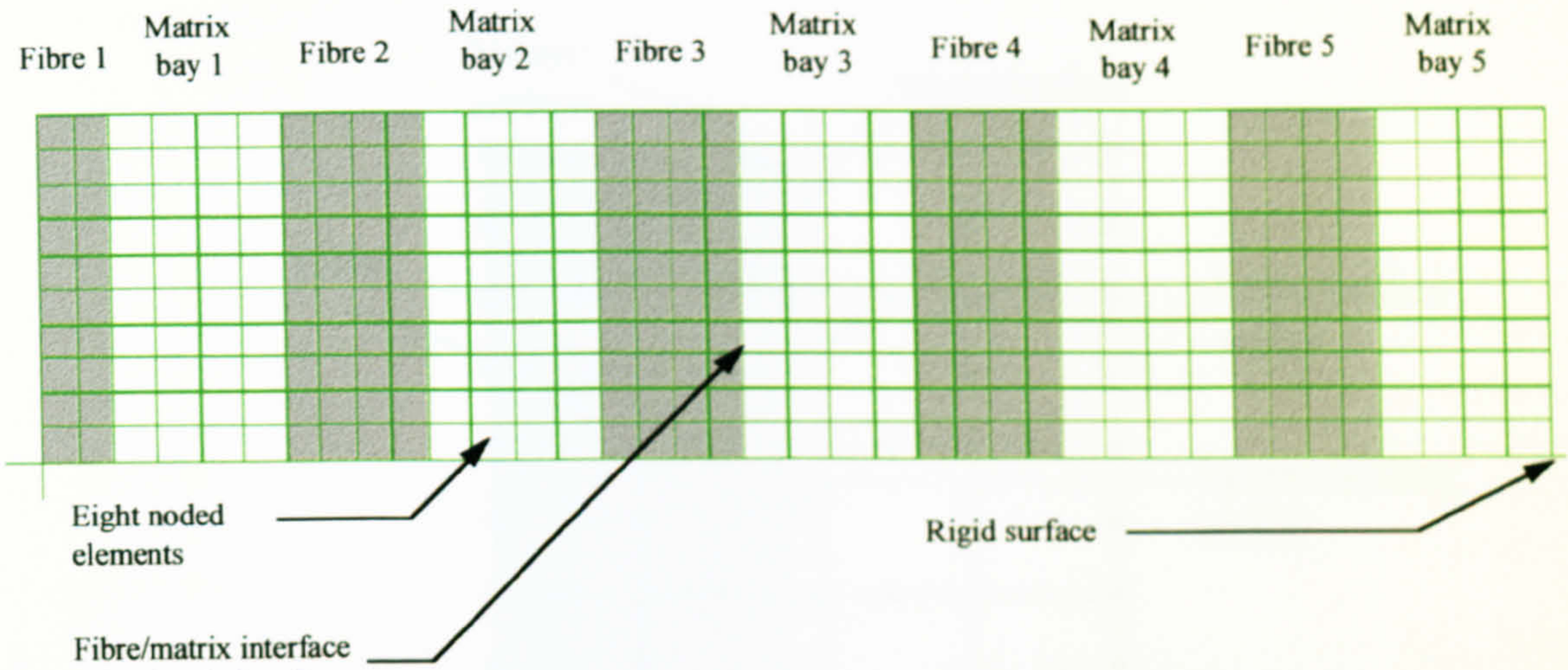

Figure 1: Finite element mesh showing four and a half fibres situated in five matrix bays

fibres respectively. The difficulty is due to the fact that composite failure is made up of a series of energy absorbing mechanisms – debonding, delamination, fibre bridging and matrix microcracking. Additionally, the interface between fibre and matrix plays a crucial rôle in the load transfer characteristics of the composite as a whole. Strengthening by fibre reinforcement depends on the process of load transfer, and is limited by the shear strength of the interface. Greater insight on the failure process of composites can be obtained by adopting the approach of fracture analysis using finite element analysis (FEA).

MODELLING PROCEDURE

A two-dimensional, axisymmetric quarter model of a continuous fibre Al_2O_3/Al MMC was constructed in *ABAQUS*. From fractographic analysis and from manufacturer's data, the fibre diameter and volume fraction were determined to be 10μm and 45% respectively. The composite modelled was 25μm in length and 39μm in width and consisted of four and a half fibres situated in five matrix bays (Figure 1). Table 1 shows the material properties applied to the fibres and matrix bays. The differing failure mechanisms incorporated into the model used the "*contact surface*", "*bond surface*" and "*debond*" options available in *ABAQUS* together with a "*fracture criterion*" suboption. Critical nodal stresses in front of the crack tip(s) were used to determine the particular type, of failure. Mode I cracking for both fibre and matrix, fibre bridging and fibre/matrix debonding were all incorporated into the model.

The *ABAQUS* debond options use a master/slave surface concept – as indicated in Figure 2. In the models discussed here element faces making up the fibre side of the fibre/matrix

Table 1: Material properties of fibre and matrix bays

Property	Al_2O_3	Al
Young's modulus E (GPa)	210	68.9
Poisson's ratio v	0.3	0.33

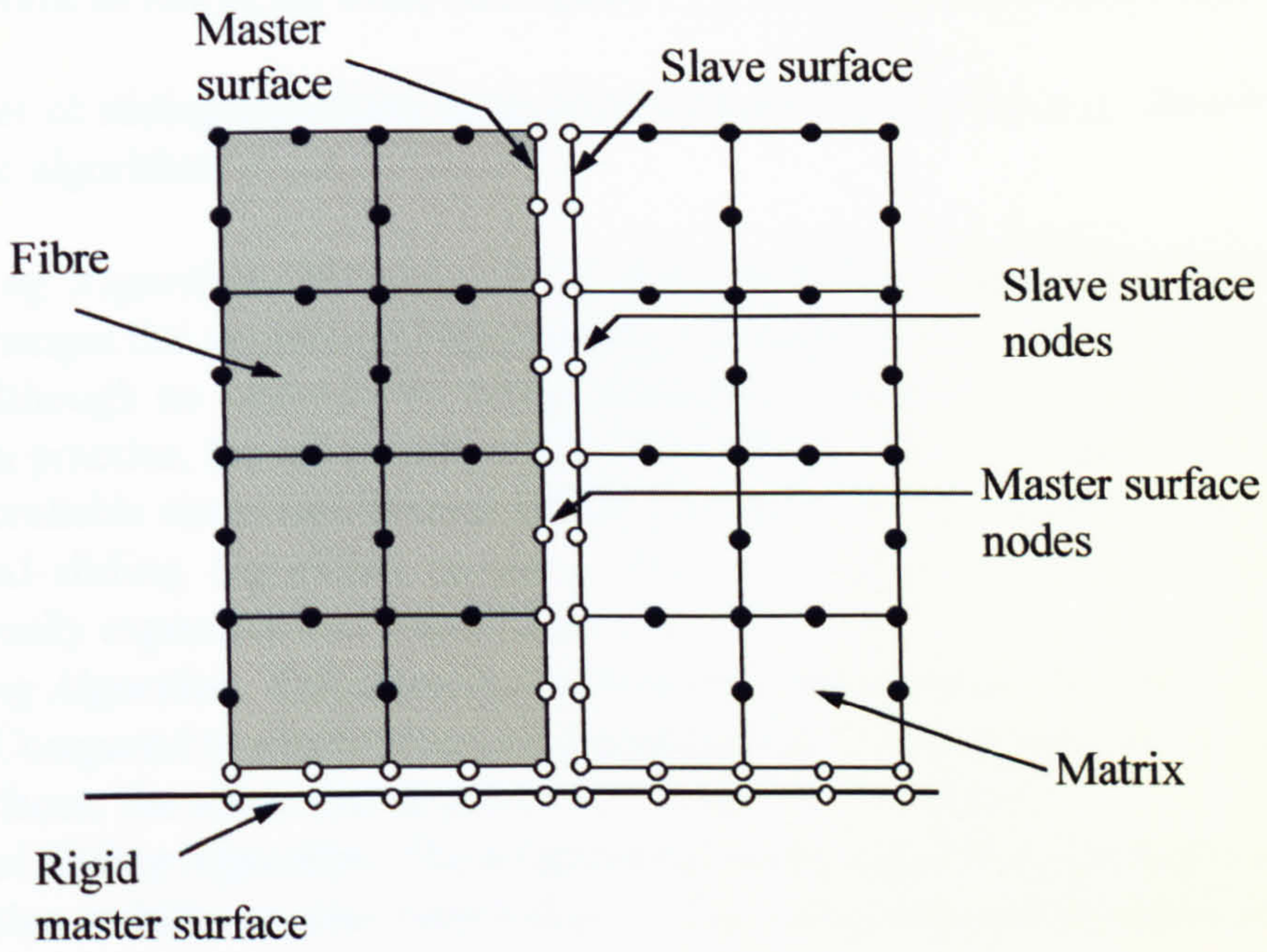

Figure 2: Elements and nodes making up the master/slave surfaces for the fibre/matrix interface and the *r*-axis, composite bonding

interface were chosen to constitute the master surfaces and element faces comprising the matrix side were selected as the slave surfaces. For the fibre/matrix interface, the fibre side surface was chosen as the master and the matrix side surface as the slave – i.e. the stiffer element set forming the surface was chosen as the master. A rigid surface made up the *r*-axis and the composite was bonded to this surface in the normal direction only, thus allowing for mode I failure, but also allowing for Poisson contraction of the composite. Three debond options are available in *ABAQUS – finite sliding*, *small sliding* and *infinitesimal sliding*. The *finite sliding* formulation allows sliding of a finite amplitude, and arbitrary rotation, of the two surfaces in contact. In the *small sliding* formulation, the nodes between the master and slave surface elements should not slide more than one element length and the rotation and deformation of the master surface should not cause the local tangent planes to become a poor representation of the master surface (see Figure 3). Finally the *infinitesimal sliding*

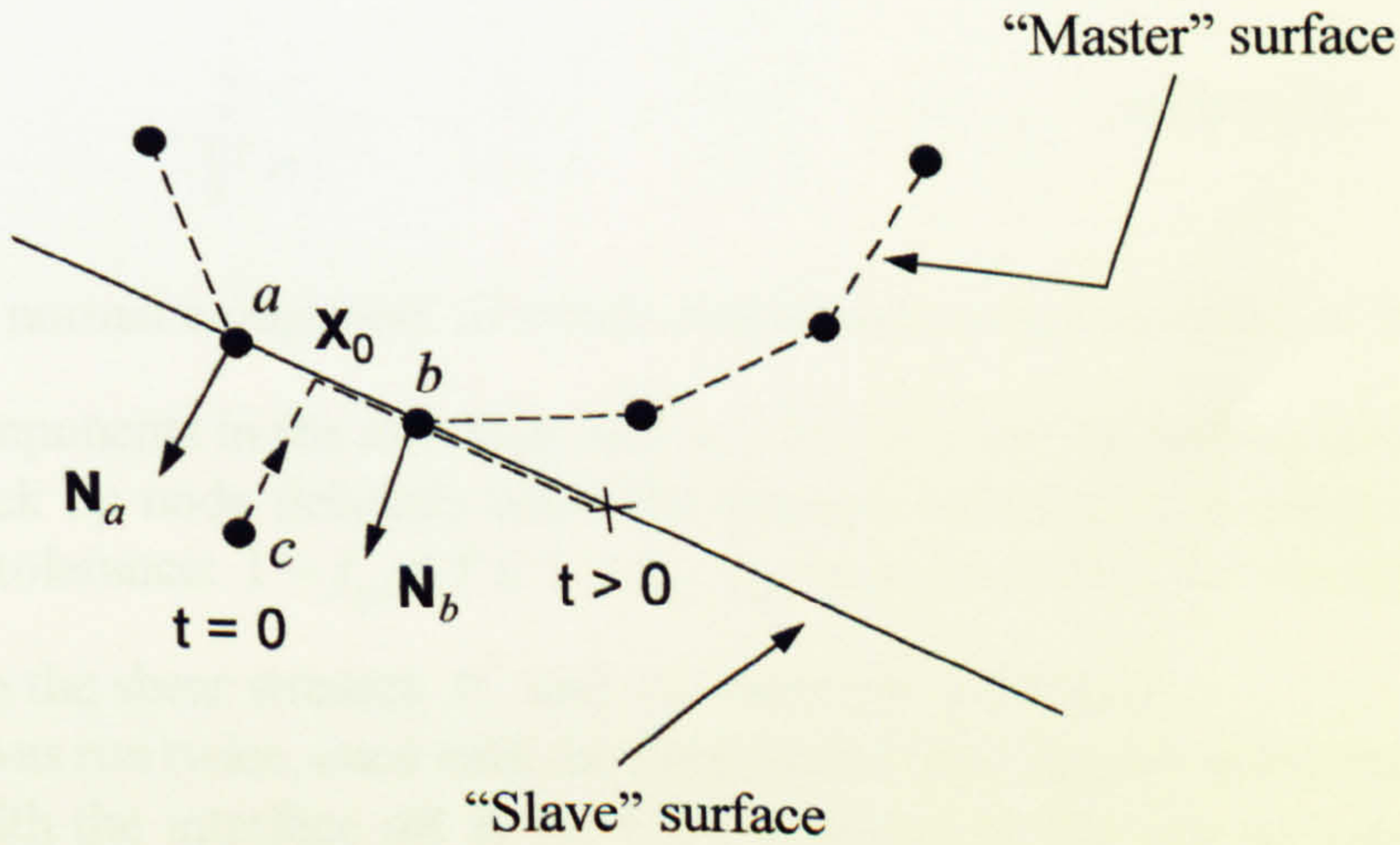

Figure 3: Schematic showing debonding algorithm in *ABAQUS*

algorithm is the same as that of the small sliding and in addition ignores non-linear geometric effects.

All three types of sliding algorithm were incorporated in test models to determine the most appropriate algorithm:

i. *Finite Sliding Algorithm*. Because of the way the finite sliding algorithm works, *ABAQUS* changes the geometry of the model to correctly place nodes along the contact surfaces. Although no undesirable effects should be introduced by these changes in geometry, in practice, for *all* the test models, the algorithm was found to be unstable and gave unreliable stress distribution results compared to the results from small- and infinitesimal-sliding algorithm models. Also this algorithm proved extremely computationally expensive and model runs were very lengthy.
ii. *Small Sliding Algorithm*. This algorithm proved much more stable than the finite sliding algorithm. Compared to identical conventional models of composites, i.e. without any bonded surfaces, the stress distributions were found to be identical.
iii. *Infinitesimal Sliding Algorithm*. The infinitesimal sliding algorithm gave the best results with algorithm stability to near total failure of the composite and the most economic model run time.

Since the infinitesimal sliding algorithm gave the best results in the test models, this was chosen to be used for the rest of the modelling work. Figure 3 shows a schematic describing how the small- and infinitesimal-sliding algorithms work: using initial nodal coordinates, unit normal vectors are first computed for all nodes on the master surface, e.g. $\mathbf{N}_a$ and $\mathbf{N}_b$. These unit normal vectors are used to define a smooth varying normal vector $\mathbf{N}(x)$, at any point, x, on the master surface. The algorithm then determines which master nodes will interact with slave node c for the entire analysis. A point on the surface, $\mathbf{X}_0$, is computed for slave node c such that the vector formed by the slave node and $\mathbf{X}_0$ coincides with $\mathbf{N}(\mathbf{X}_0)$. The example in Figure 3 assumes that $\mathbf{X}_0$ is on the element face with end nodes a and b. A potential contact condition between node c and the line perpendicular to $\mathbf{N}(\mathbf{X}_0)$ will be enforced. At any time $t > 0$, node c is constrained not to penetrate this line. The load transfer always occurs between node c and nodes a and b.

The nodal failure stresses for the fibre/matrix interface were assigned the UTS values of the matrix. Mode I failure of the fibre was set at the UTS of the fibre and similarly mode I failure of the matrix was set at matrix UTS. The failure criterion was established as follows:

$$\sqrt{\left(\frac{\hat{\sigma}_n}{\sigma^f}\right)^2+\left(\frac{\tau_1}{\tau_1^f}\right)^2+\left(\frac{\tau_2}{\tau_2^f}\right)^2}=f\,,\ \hat{\sigma}_n=\max(\sigma_n,0) \qquad (2)$$

where σ_n is the normal component of stress carried across the interface, τ_1 and τ_2 are the shear stress components in the interface, and σ^f, τ_1^f, τ_2^f are the normal and shear failure stresses. A crack tip node debonds when the fracture criterion, f, reaches the value 1.0 within a given tolerance: $1-f_{tol} \le f \le 1+f_{tol}$. f_{tol} was set at 0.05 for the duration of the modelling. Also the shear stresses τ_1^f and τ_2^f were set at 50% σ^f.

The model was run twice, once with the fibre/matrix interface set at the matrix UTS, the second time with the interface set at the UTS obtained by the rule of mixtures (ROM) formula (Table 2):

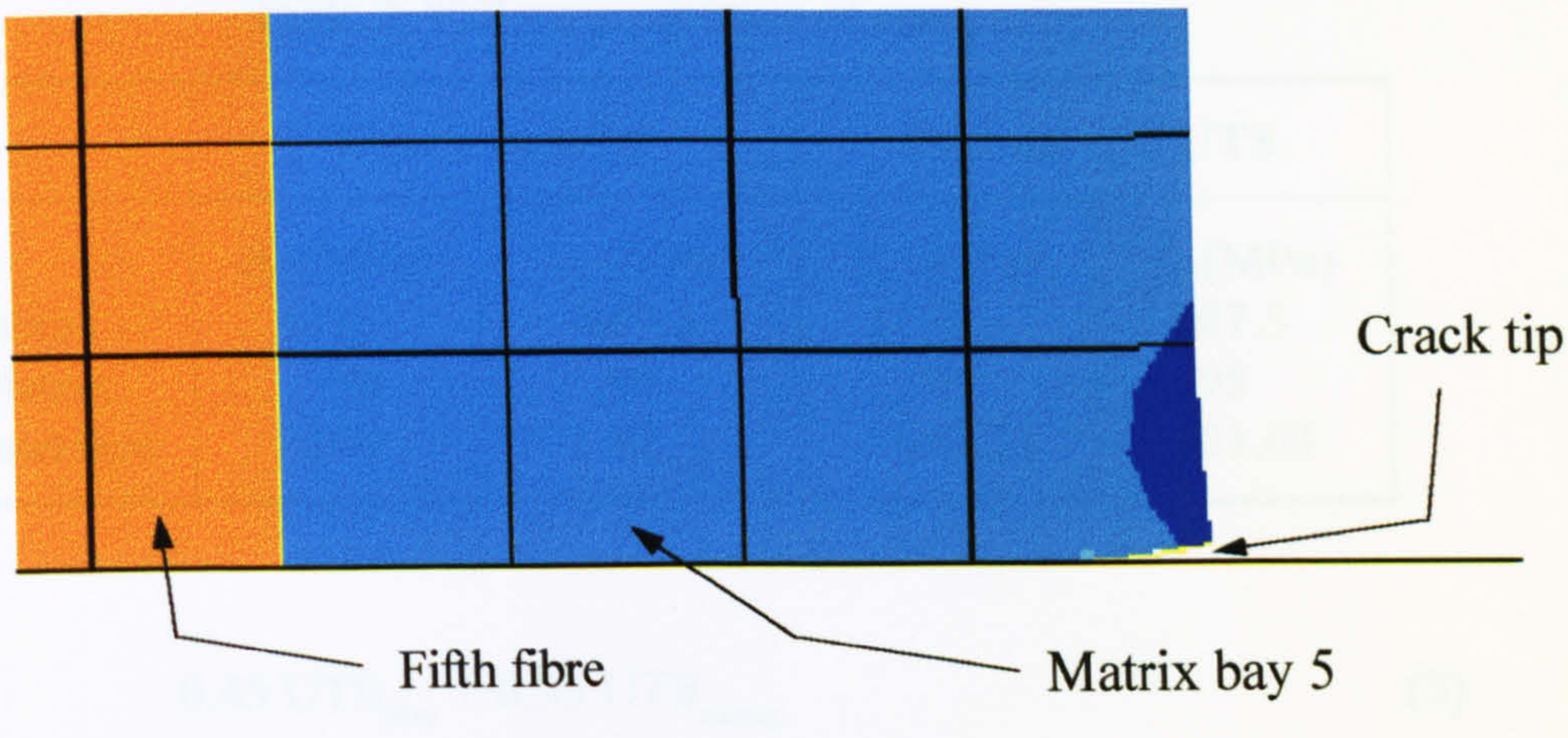

Figure 4: Seed edge crack on right hand side of matrix bay

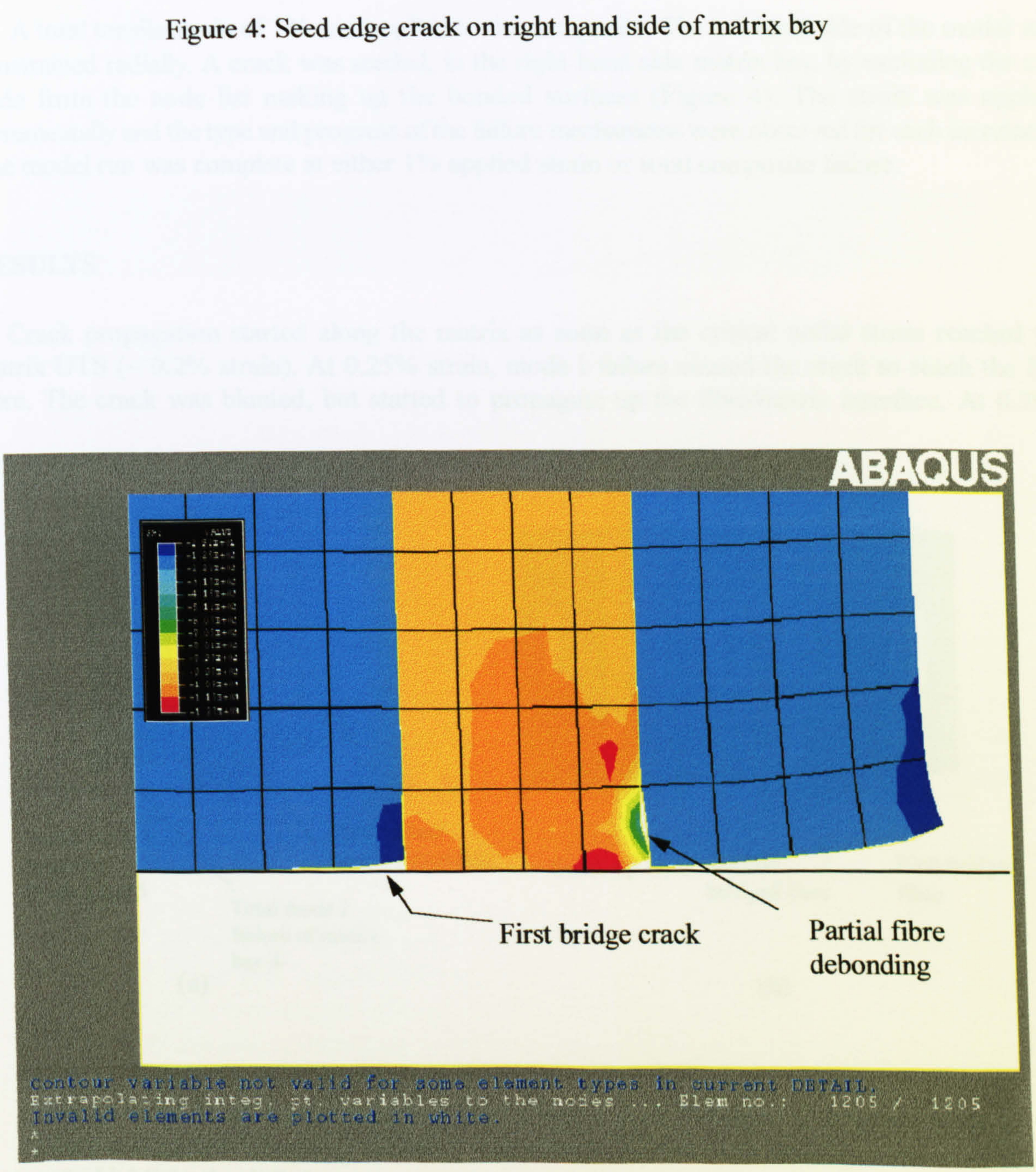

Figure 5: Fibre bridging and partial fibre/matrix debonding

Table 2: Failure properties of composite

	First run UTS		Second run UTS	
	σ_c (MPa)	τ_c (MPa)	σ_c (MPa)	τ_c (MPa)
Fibre	1775	887.5	1775	887.5
Matrix	190	95	190	95
Interface	190	95	903.25	451.63

$$0.45\ UTS_{fibre} + 0.55\ UTS_{matrix} \quad (3)$$

A total tensile strain of 1% was applied to the composite. The left hand side of the model was constrained radially. A crack was seeded, in the right hand side matrix bay, by excluding the end node from the node list making up the bonded surfaces (Figure 4). The strain was applied incrementally and the type and progress of the failure mechanisms were observed for each increment. The model run was complete at either 1% applied strain or total composite failure.

RESULTS

Crack propagation started along the matrix as soon as the critical nodal stress reached the matrix UTS (~ 0.2% strain). At 0.25% strain, mode I failure caused the crack to reach the first fibre. The crack was blunted, but started to propagate up the fibre/matrix interface. At 0.29%

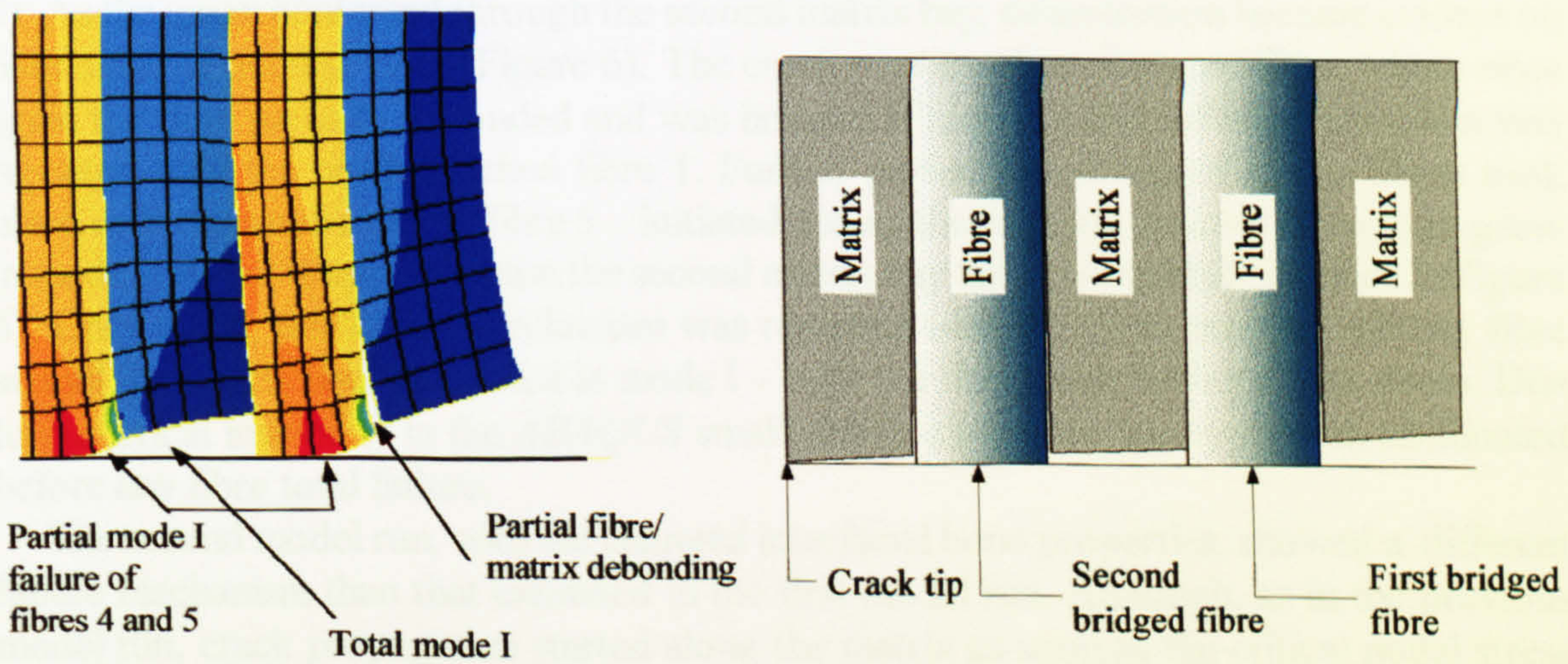

Figure 6: (a) Total mode I failure of matrix bays 4 and 5 together with partial mode I failure and partial debonding of fibre 5 – this model has been distorted by a factor of 10 to highlight the differing types of failure mechanism; (b) schematic diagram of (a) showing how the fibres have been bridged by the matrix

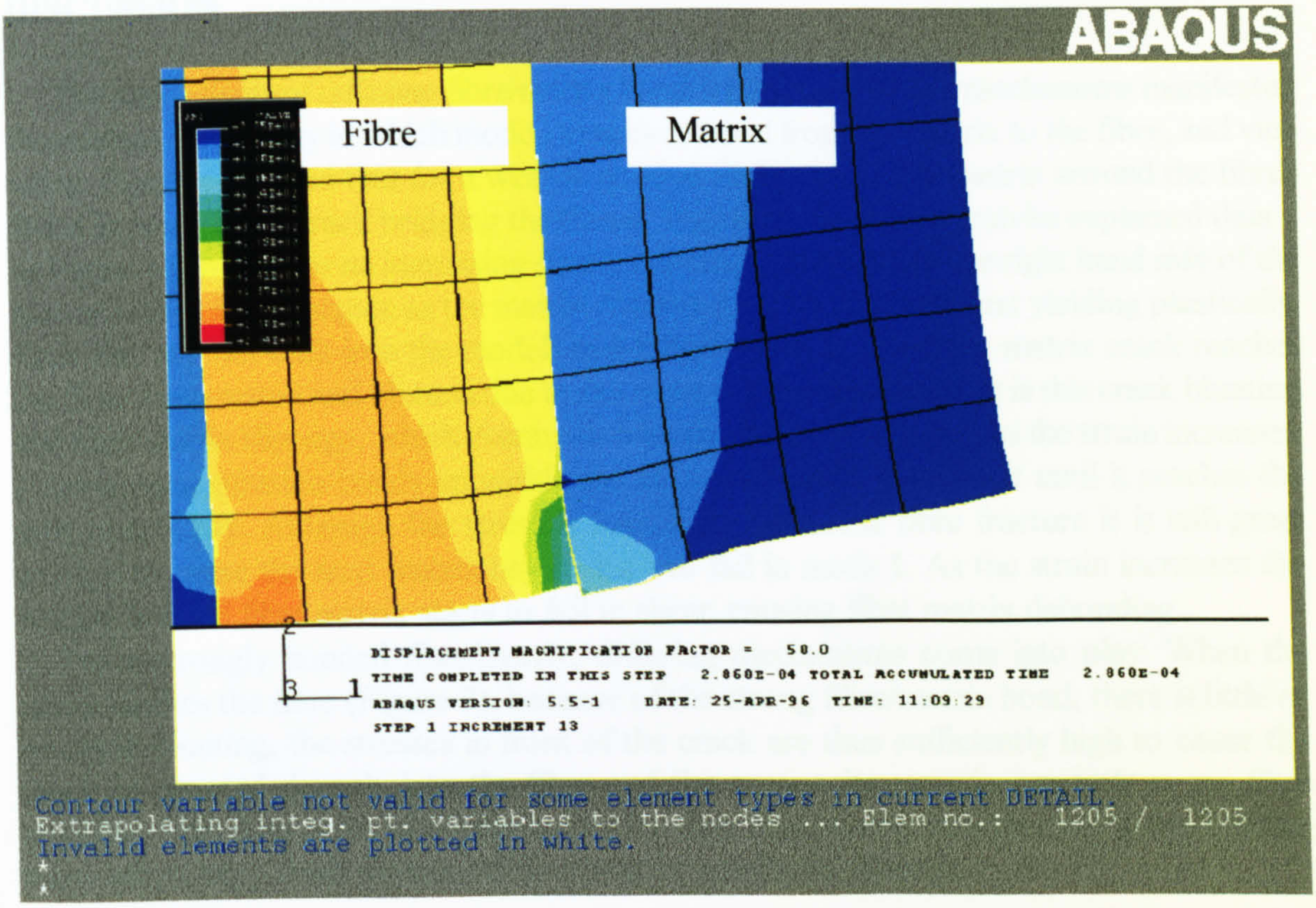

Figure 7: Mode I crack is not arrested at fibre/matrix interface, but continues into the fibre

strain, cracking began in the second matrix bay. Thus the crack bridged the first fibre (Figure 5). As the crack continued through the second matrix bay, delamination became evident on both sides of the first fibre (Figure 6). The crack continued to the next fibre, where once again the fibre partially debonded and was bridged (Figure 6); this failure mechanism was repeated until the crack reached fibre 1. Further partial debonding of all the fibres took place until the small crack in fibre 5 – initiated during the bridging process – began to grow in mode I. At 0.4% applied strain the second matrix bay failed completely in mode I (Figure 6). Once again, this failure mechanism was repeated until the crack reached the last fibre and all the matrix bays had failed in mode I – with the fibres now taking all the strain. Due to numerical instability in the *ABAQUS* small sliding algorithm, the model run terminated before any fibre total failure.

The second model run, with the changed interfacial bond properties, showed a different failure mechanism than that exhibited in the first model run. Although, as in the previous model run, crack propagation started along the matrix as soon as the critical nodal stress reached the matrix UTS, when the mode I matrix crack reached fibre 5, there was no partial debonding and the fibre was not bridged. Instead the crack continued, when the applied strain was 0.48%, to propagate through the fibre (Figure 7). A small amount of fibre/matrix delamination was also apparent at the fibre/matrix interface, where the mode I crack had entered the fibre. Again, due to numerical instability in the *ABAQUS* algorithm, the model run terminated before the fibre completely failed.

DISCUSSION

The main effects of differing fibre/matrix bond strength on failure mechanisms manifested themselves on the way in which mode I cracks crossed from the matrix to the fibre, and vice versa. Figure 6 showed that for a weakly bonded fibre/matrix, the matrix around the fibres failed in mode I, the crack bridging the fibres. The bridging process can be explained thus – as Figure 6 shows – for an increasing strain, the crack (initiated on the right hand side of the picture) starts to propagate as the matrix reaches its UTS (without first yielding plastically, since this was not built into the model) and fails in mode I. When the matrix crack reaches the fibre it is arrested and blunted due to the weak fibre/matrix bond. It is this crack blunting and fibre/matrix slippage, which eventually absorbs energy. However, as the strain increases, a stress concentration builds up within the fibre and passes through it until it reaches the next matrix bay. Although the stress is insufficient to cause fibre fracture it is still great enough to cause the next matrix bay to start to fail in mode I. As the strain increases the weakly bonded fibre matrix starts to fail in shear, causing fibre matrix debonding.

For a strongly bonded fibre/matrix, differing mechanisms come into play. When the crack reaches the fibre (Figure 7), because of the strong fibre/matrix bond, there is little or no crack blunting, the stresses in front of the crack are thus sufficiently high to cause the crack to proceed directly into the fibre and the composite experiences little or no fibre bridging. This does seem to confirmed by the first fibre/matrix interface in Figure 7 which show only a very small amount of fibre/matrix interfacial slippage.

CONCLUSION

A simulation algorithm to model composites failing in several modes, simultaneously, and running in real time was developed using the finite element analysis (FEA) package *ABAQUS*. A small specimen of unidirectional long fibre Al_2O_3/Al composite was modelled in which four and a half fibres situated in five matrix bays were subject to a uniform strain in the longitudinal direction. By comparing two differing fibre/martrix bond strengths, one set at the UTS of the matrix the other set at a rule of mixtures value of the combined UTS properties of both constituent materials, it was found that the weakly bonded fibre/matrix interface led to fibre bridging and fibre/matrix debonding, while the strongly bonded interface led to the composite failing almost completely in mode I with little fibre bridging.

There have been many papers written outlining analytical and semi-analytic methods to predict composite failure. Begley and McMeeking used a complex system of semi-analytic integral equations, to predict the occurrence of fibre bridging. However, while their technique required significantly less computational effort than the FEA method described here, the amount of man hours required to create and implement the solution was at least the same as the time required to create the FEA model, and additionally this approach did not address any other failure mechanisms.

REFERENCES

ABAQUS user's manual, V5.5, Vol 1, 1995.

Aboudi J., 1988, "Micromechanical Analysis of the Strength of Unidirectional Fibre Composites", *Composites Science and Technology*, **33**, pp. 79–86.

Begley M. R., and McMeeking R. M., 1995, "Numerical Analysis of Fibre Bridging and Fatigue Crack Growth in Metal Matrix Composite Materials", *Journal of Materials Science and Engineering*, , **A200**, pp. 12–20.

Datta P. K., Strafford K. N., and Burnell-Gray J. S. (Editors), 1990, *Surface Engineering Practice: Processes, Fundamentals and Applications in Corrosion and Wear*, Ellis Horwood,
pp. 397.

Griffin D., Daadbin A., Datta P. K., and Burnell Gray J. S., 1994, "TheModelling of Crack Propagation Through the Interfacial Region of a SiC/titanium metal matrix composite", *Proceedings of the 10th Irish Materials Forum Conference IMF10, Key Engineering Materials*, Vol. 99–100, pp. 341–346.

Melantis N., Galiotis C., Tetlow P. L., and Davies C. K. L., 1993, "Interfacial Shear Stress Distribution in Model Composites: The Effect of Fibre Modulus", *Composites*, **24**, pp. 459–466.